

ADVANCED LASER DIAGNOSTICS DEVELOPMENT FOR THE  
CHARACTERIZATION OF GASEOUS HIGH SPEED FLOWS

A Dissertation

by

RODRIGO SANCHEZ-GONZALEZ

Submitted to the Office of Graduate Studies of  
Texas A&M University  
in partial fulfillment of the requirements for the degree of

DOCTOR OF PHILOSOPHY

May 2012

Major Subject: Chemistry

Advanced Laser Diagnostics Development for the  
Characterization of Gaseous High Speed Flows  
Copyright 2012 Rodrigo Sanchez-Gonzalez

ADVANCED LASER DIAGNOSTICS DEVELOPMENT FOR THE  
CHARACTERIZATION OF GASEOUS HIGH SPEED FLOWS

A Dissertation

by

RODRIGO SANCHEZ-GONZALEZ

Submitted to the Office of Graduate Studies of  
Texas A&M University  
in partial fulfillment of the requirements for the degree of

DOCTOR OF PHILOSOPHY

Approved by:

Chair of Committee,	Simon North
Committee Members,	Rodney Bowersox
	Jaan Laane
	Robert Lucchese
Head of Department,	David Russell

May 2012

Major Subject: Chemistry

## ABSTRACT

## Advanced Laser Diagnostics Development for the Characterization of Gaseous High Speed Flows. (May 2012)

Rodrigo Sanchez-Gonzalez, B.S., Universidad Autonoma de Queretaro

Chair of Advisory Committee: Dr. Simon North

The study of high-speed flows represents a challenging problem in the fluid dynamics field due to the presence of chemical reactions and non-equilibrium effects. Hypersonic flights, where speeds reach Mach 5 and above, are particularly influenced by these effects, resulting in a direct impact on the flow and consequently on the aerodynamic performance of a vehicle traveling at these speeds. The study of hypersonic flow conditions requires the experimental capability of determining local temperatures, pressures and velocities using non-intrusive techniques. Furthermore, the simultaneous measurement of two or more variables in a complex flow boosts the amount of information that is obtained since valuable correlations can be established.

This research includes the design, construction and characterization of a hypersonic flow apparatus explicitly intended as a tool for advanced laser diagnostics development. This apparatus is characterized by its pulsed operation mode that translates into a significant reduction in mass flow rates and can be operated for long periods at Mach numbers ranging from 2.8 to 6.2. The flow conditions during the uniform flow time interval of each pulse vary by less than 1%, generating a flow of sufficient quality for quantitative measurements.

The development of a laser diagnostic technique, the VENOM technique, which is a non-intrusive method to provide simultaneous 2-D measurements of the mean and instantaneous fluctuations in two-component velocity and temperature is also presented. This technique represents the first single diagnostic capable of instantaneous two-component velocimetry and thermometry in a gaseous flow field by combining two



Nitric Oxide Planar Laser Induced Fluorescence methods: two-component Molecular Tagging Velocimetry and two-line thermometry, employing the nascent  $\text{NO}(v''=1)$  arising from the  $\text{NO}_2$  photodissociation as a molecular tracer. The VENOM technique is expected to be not only applicable to cold high-speed flows, which is the focus of the present work, but also to combustion and other reactive or high-enthalpy flow fields.

## ACKNOWLEDGEMENTS

I would like to thank primarily to my Ph.D. advisor, Dr. Simon North, for his mentorship, his patience, and his enthusiastic support. His love for science and teaching has clearly translated into a leadership that I can only dream to reach one day in the future. His scientific and human standards have set in my life a solid paradigm of the consummate Scientist.

I would also like to thank everyone in the North group for their assistance and their friendship. Thanks to Andrea Hsu for effectively leading my entrance into the laser experimental work and for the certainly difficult endeavor of setting the path of us, chemists, into the hypersonics lab work. I appreciate the help and advice of fellow chemists Kristin Dooley, Buddhadeb Ghosh, and Qingnan Liu. Their skills and different expertise areas provided me with a unique perspective. I also thank the help, the hard work and the friendship of Jacob Dean. I will always remember those memorable CARS experiments that we did together. I also appreciate the healthiest of enmities with Michael Grubb. While leading different experiments we both knew that when "the race was on" there was no truce or any possibility of showing up in the office the next morning without the best of results. I also thank the help and support of Dr. Bowersox and the Aerospace Engineering graduate students at the hypersonics lab. While busy with their own projects they always were willing to share their time and knowledge with me. Thanks to them my work could move forward uninterrupted. I also appreciate the invaluable advice and highly skilled work of the Chemistry Department Machine Shop staff. I owe my little knowledge of machining to Will Seward, as well as the materialization of a now successful Repetitively Pulsed Hypersonic Test facility. Thanks also to Carl Johnson, who built the nozzles. Both of them materialized so many ideas with a talent that made their job look misleadingly easy.

I am so thankful for having a wonderful family. I admire the way my parents clearly envisioned the future of their children in such an early stage of their lives. Their love and lucid guidance have proven rewarding for me, and I hope, for them too. I thank

my brother and sister, for their love and for helping me become, or try to become, patient, and again, for their help to cultivate my stoicism. I thank Jesus Lopez for the insightful and best of comradeships. Our affinities and disagreements have build one of those rare, unique and permanent bonds. I also appreciate the love and the unparalleled friendship of Michelle. The commitment and the innocent virtue of her dedicated soul have been an unexpected and encouraging driving force for me. Thanks also to all my friends back home. I don't want to miss anyone, but for all who were, and all who still are, the distance has grown, but the memories are precious.

I am thankful for every single opportunity that I have had in the United States. I have met fantastic people and I have no complains for how I have been treated. I have always found the occasion of becoming a better scientist, and contrary to my early limited understanding, also a better person. I have learned to embrace a country that has always opened the doors to me.

Finally, I would like to thank CONACYT and the Mexican government. The fighting and strong-willed Mexican people will always arise triumphant over any difficulty. The greatness has a price, and it will certainly be reached at the right moment.

## TABLE OF CONTENTS

	Page
ABSTRACT .....	iii
ACKNOWLEDGEMENTS .....	v
TABLE OF CONTENTS .....	vii
LIST OF FIGURES .....	x
LIST OF TABLES .....	xviii
CHAPTER	
I INTRODUCTION .....	1
I.1 Background and Motivation .....	1
I.2 Research Objectives .....	2
I.3 Literature Survey .....	3
I.3.1 Pulsed Supersonic Facilities .....	3
I.3.2 Velocity and Temperature Measurements in Gaseous Flow Fields .....	4
I.4 Theoretical Background .....	6
I.4.1 Nitric Oxide Laser Induced Fluorescence .....	6
I.4.2 NO Spectroscopy .....	10
I.4.3 Two-line Temperature Measurements .....	17
I.5 Thesis Overview .....	20
II EXPERIMENTAL METHODS: LASER AND IMAGING SYSTEMS, AND DATA ANALYSIS PROGRAM .....	22
II.1 Description of the Laser Systems .....	22
II.1.1 Laser Calibration .....	23
II.2 Imaging System .....	26
II.2.1 Imaging System Resolution .....	27
II.3 Data Analysis Program .....	30
II.3.1 Pre-processing .....	31
II.3.2 Velocimetry .....	37
II.3.3 Thermometry .....	47

III	REPETITIVELY PULSED HYPERSONIC TEST CELL - A TOOL FOR DIAGNOSTIC DEVELOPMENT .....	51
	III.1 Introduction .....	51
	III.2 Design of the Repetitively Pulsed Hypersonic Test Cell .....	52
	III.2.1 The Nozzle Assembly .....	53
	III.2.2 The Test Chamber .....	58
	A. Original Design .....	58
	B. Later Modifications .....	60
	III.3 Operational Details .....	63
	III.4 Characterization of the RPHT Cell .....	65
	III.4.1 Nitric Oxide PLIF Imaging .....	66
	III.4.2 Temporal Characterization: Fast Pressure Measurements .....	68
	III.4.3 CFD Methods .....	75
	III.4.4 Spatial Characterization .....	78
	A. Radial Pitot Surveys .....	79
	B. PLIF Measurements .....	80
	III.5 Flow Visualization Examples .....	86
	III.6 Summary .....	89
IV	EXPERIMENTAL: VELOCITY AND ROTATIONAL TEMPERATURE MEASUREMENTS USING NO <sub>2</sub> PHOTODISSOCIATION .....	91
	IV.1 Instrumentation and Measurement Principle .....	91
	IV.2 Velocity Measurements Using NO <sub>2</sub> .....	93
	IV.2.1 Velocity Measurements Using NO( $v''=1$ ) .....	94
	IV.3 Rotational Temperature Measurements Using NO <sub>2</sub> .....	102
	IV.3.1 Rotational Thermalization Measurements Using NO( $v''=0$ ) and NO( $v''=1$ ) .....	106
	IV.3.2 Temperature Measurement Uncertainties .....	118
	IV.4 Summary .....	122

V	EXPERIMENTAL: SIMULTANEOUS VELOCITY AND TEMPERATURE MEASUREMENTS USING NO <sub>2</sub> PHOTODISSOCIATION - THE VENOM TECHNIQUE .....	123
	V.1 Underexpanded Jet Experiments .....	125
	V.1.1 Instrumentation and Experimental Setup .....	125
	V.1.2 Data Analysis .....	128
	V.1.3 Results .....	130
	V.2 Mach 4.6 Flow Over a Cylinder - Cylinder Wake Measurements.....	131
	V.2.1 Instrumentation and Experimental Setup .....	133
	V.2.2 CFD Simulation.....	138
	V.2.3 Experimental Results.....	141
	A. Near Wake Measurements.....	143
	B. Further Downstream Wake Measurements .....	145
	C. Further Downstream Wake Measurements With Increased Spatial Resolution .....	148
	V.3 Summary .....	153
VI	CONCLUSION AND FUTURE WORK .....	155
	VI.1 Measurement of Acceleration Fields Using the VENOM Technique .....	155
	VI.2 Stereoscopic VENOM Measurements .....	157
	REFERENCES .....	160
	VITA .....	168

## LIST OF FIGURES

FIGURE	Page
1.1 Potential energy diagram of NO and two-level LIF model.....	7
1.2 Energy level diagram for the NO showing rotational transitions for the 12 possible branches in the $A^2\Sigma^+ - X^2\Pi$ system .....	13
1.3 Simulated Nitric Oxide excitation spectrum of $\Sigma^+ (v'=0) - X^2\Pi (v''=0)$ band showing the two different sub-bands corresponding to the two ground state spin-orbit components. The relative intensities reflect the ground state populations at 300 K .....	14
1.4 Simulated Nitric Oxide excitation spectrum showing in detail the 6 branches belonging to each $\Sigma^+ (v'=0) - X^2\Pi (v''=0)$ sub-band. The relative intensities reflect the ground state populations at 300 K .....	15
1.5 Simulated Nitric Oxide excitation spectrum showing the NO(0,0) and NO(1,1) bands at 300 K.....	16
1.6 Nitric Oxide Boltzmann distributions at the lowest (50 K) and highest (300 K) temperatures for the flow fields studied in this thesis .....	19
2.1 Schematic of experimental setup used for the dye laser system calibration.....	24
2.2 Laser Induced Fluorescence excitation spectra for the NO(0,0) band with a resolution of 0.002 nm.....	25
2.3 Laser Induced Fluorescence excitation spectra for the NO(1,1) band with a resolution of 0.002 nm.....	26
2.4 Schematic of the laser diagnostic system and image acquisition setup .....	27
2.5 Edge response and line spread function obtained for the CERCO (a) and the UKA (b) lenses .....	29
2.6 MTFs for the CERCO (a) and UKA (b) lenses obtained from the LSF measurements shown in Fig. 2.5 .....	30
2.7 Fluorescence intensity features in a VENOM image (a). Both	

fluorescence maxima (b) and minima (c) can, in principle, be used to track the flow displacements .....	31
2.8 Common distortions caused by a camera lens. Undistorted image (a), barrel-distorted image (b), and pincushion-distorted image (c) .....	32
2.9 Image alignment through the undistorted centerline .....	33
2.10 Estimation of the average grid size (a) by location of the four nearest intersection centroids (b) around the center point .....	34
2.11 (a) Distorted image, (b) ideal grid synthetically generated by the average grid spacing near the center of the image, and (c) grid intersections in the synthetic grid (red) compared to the real location of the grid intersections (blue) .....	35
2.12 Distorted (a) and corrected (b) dotcard images .....	36
2.13 Field of view correction for two cameras. The identical red square in both images illustrate the need for a translation and scaling correction of (b) with respect to (a) .....	37
2.14 Grid intersection location based on the fluorescence maxima or minima .	38
2.15 Definition of an interrogation area in an initial (left) and a time-delayed image (right) at each grid intersection .....	39
2.16 Grid Discrepancy or zero-velocity map .....	40
2.17 Fitting of the cross-correlation map .....	41
2.18 Velocity map calculation from the local cross-correlation maxima location .....	42
2.19 Estimated velocity uncertainty as a function of signal-to-noise resulting from the data analysis program .....	45
2.20 Instantaneous determination of local velocity in a synthetically generated VENOM data set using maxima/minima tracking (top) 2-D cross-correlation method (middle), and fitted 2-D cross-correlation method (bottom) .....	47
2.21 Image correction for inhomogeneities in the probe lasers. Original fluorescence image (a), correction image (b), and corrected	



image (c). The fluorescence intensity profiles across the corrected and uncorrected images along a row are shown (d) .....	48
2.22 Temperature map obtained without de-warping (b) and after de-warping the time-delayed image (d).....	50
3.1 Nozzle assembly fitted with the Mach 4.6 axisymmetric nozzle .....	53
3.2 Pulsed valve before modification. Before (a) and after opening orifice to 3 mm (b) .....	54
3.3 Ratio of exit flow conditions to input gas conditions, $x/x_0$ , as a function of Mach number calculated with the isentropic flow equations (for air, using $\gamma = 1.4$ ) .....	56
3.4 Nozzle contours calculated by the Method of Characteristics .....	57
3.5 RPHT Cell original design. The nozzle assembly is placed inside of the main chamber (a). Cross-sectional view of the nozzle assembly mounted in the mounting block (b).....	59
3.6 Feeding block designs for the accommodation of six (a) and eight (b) pulsed valves.....	60
3.7 Cross-sectional view of the repetitively pulsed hypersonic test chamber after modifications (a) and view of the removable walls with the quartz window holders (b).....	61
3.8 Photographs of the modified PHAT cell without (a) and with (b) the dismountable side face. Close up of the feeding block fitted with two pulsed valves (c). Mach 4.6 and Mach 6.2 nozzles (d) .....	63
3.9 Gas throughput into the PHAT cell using 4 pulsed valves. The maximum capacity of the pumping system is shown for comparison .....	64
3.10 NO PLIF image sequence of a 12 ms Mach 4.6 flow pulse corresponding to the beginning of the pulse (a), to the fully established flow (b), and to the end of the pulse (c) .....	67
3.11 Composite NO PLIF during the fully established flow stage showing the shear layer growth. Flow is from left to right.....	68
3.12 Photograph indicating the location of the pressure sensors. Zoom-in region shows the formation of a bow shock in front of the	

Pitot using NO PLIF imaging.....	69
3.13 Pressure sensors' calibration to find sensitivity and zero-offsets .....	70
3.14 Absolute percent error values resulting from the estimation of the Mach numbers using polynomial fits 6th order in $p_2/p_0$ .....	71
3.15 Time-resolved pressure measurement of a single pulse along the Mach 4.6 flow axis. Inset shows a series of pulses taken at 1 Hz repetition rate (a). Time-resolved pressure measurement of a single pulse along the Mach 6.2 flow axis (b) .....	73
3.16 Impact pressure shot-to-shot fluctuations shown as a percent between 7 and 8 ms of the stable phase of the pulse .....	75
3.17 Demonstration of grid convergence for the Mach 4.6 nozzle .....	77
3.18 CFD contour results for the Mach 4.6 (a) and Mach 6.2 (b) nozzles.....	78
3.19 Radial Mach number profiles at nozzle exit. Mach 4.6 nozzle (a) and Mach 6.2 nozzle (b).....	80
3.20 Experimental setup of the NO PLIF imaging system (a) and timing schematic for the NO fluorescence MTV experiments (b) .....	82
3.21 Average two-dimensional temperature map of the Mach 4.6 (left) and Mach 6.2 (right) core flow obtained using two-line NO PLIF .....	83
3.22 100-shot fluorescence average images obtained in the Mach 4.6 flow for the velocimetry determination. Initial (a) and 600 ns time delayed image (b) .....	84
3.23 Interpolated average streamwise velocity map for the Mach 4.6 (left) and Mach 6.2 (right) core flow using NO MTV .....	86
3.24 Photographs and NO PLIF images of a sphere (a), a 7 degree half-angle cone (b) and a Mars Phoenix re-entry capsule (c) models used to demonstrate the flow visualization potential of the Repetitively Pulsed Hypersonic Test apparatus .....	87
3.25 NO PLIF images of the Mars Phoenix re-entry capsule (upper panels) and the sphere (lower pannels) models probing two different rotational states in order to obtain temperature maps (right panels) .....	88

3.26	Bow shock stand-off distance for a sphere.....	89
4.1	Composite fluorescence image showing one vertical photolysis line moving with the Mach 4.6 flow. The images were obtained probing the NO( $v''=1$ ) photoproduct as a function of time delay after photodissociation .....	92
4.2	Fluorescence MTV vs NO <sub>2</sub> photodissociation MTV timing schematics ...	94
4.3	NO <sub>2</sub> photodissociation efficiency at varying laser output powers using three methods to direct the beam into the flow field. The photolysis efficiency attained by an unfocused beam is shown for comparison .....	95
4.4	Two different methods to "write" photodissociation lines and the signal structure generated by each of them. (a) shows the microcylindrical lens array and (b) shows the aluminum mesh .....	96
4.5	Fluorescence image obtained under stationary flow conditions (a) and synthetically generated image obtained by fitting the lines in (a) to straight lines (b).....	98
4.6	Single-shot time-delayed images (left panels) and interpolated streamwise velocity maps (right panels) obtained using a single "read" pulse. Image spatial resolution: 52 pixel/mm. Flow direction is from left to right.....	100
4.7	Velocity distribution of fragments produced by NO <sub>2</sub> photolysis using 355 nm. ....	101
4.8	Fluorescence images obtained by probing the NO( $v''=0$ ) photoproduct originated by photodissociation in an N <sub>2</sub> flow seeded with 2.5% of NO <sub>2</sub> and 0.8% of NO.....	103
4.9	Temperature of the Mach 4.6 freestream as a function of seeded-NO <sub>2</sub> percent at a 100% photodissociation efficiency .....	104
4.10	Temperature map of the Mach 4.6 freestream seeding 5% in NO <sub>2</sub> with high fractional photodissociation .....	105
4.11	Boltzmann plots of the vibrational specific nascent NO rotational distributions produced by photodissociation with 355 nm. The experimental distributions were measured in an expansion-cooled NO <sub>2</sub> sample .....	107
4.12	50-shot fluorescence average image showing the area of interest (left).	

Rotational temperature measurements as a function of time after photodissociation for NO( $v''=0$ ) and NO( $v''=1$ ) in an N <sub>2</sub> gas bath at 66.7 Pa and 294 K (right) .....	108
4.13 Rotational temperature thermalization fit after photodissociation with a single exponential temperature decay function for NO ( $v''=1$ ) in an N <sub>2</sub> gas bath at 66.7 Pa and 294 K .....	110
4.14 Rotational temperature thermalization fit after photodissociation with a double exponential temperature decay function for NO ( $v''=0$ ) in an N <sub>2</sub> gas bath at 66.7 Pa and 294 K. The temperature decay cannot be explained by a single exponential.....	111
4.15 Experimental setup for the temperature relaxation experiments in the underexpanded jet flow field .....	114
4.16 Average fluorescence images of the underexpanded jet probing two different rotational states at different times $\tau_1$ after photodissociation .....	115
4.17 Calculated temperature at different times $\tau_1$ after photodissociation. A CFD temperature map is shown for comparison .....	116
4.18 Centerline profiles of the calculated temperature at different times $\tau_1$ after photodissociation. A CFD temperature profile is shown for comparison.....	117
4.19 Measured power fluctuations of the VENOM probe laser systems .....	118
4.20 Measured fluorescence ratio fluctuations(a) and expected temperature uncertainties as a function of measured temperature .....	119
4.21 Mach 4.6 freestream average temperature measurement (left) and measured fluctuations as a percentage of the freestream temperature based on 200 single-shot measurements .....	120
4.22 Measured instantaneous temperature in the Mach 4.6 freestream before and after shot-to-shot fluorescence intensity correction .....	121
5.1 Nitric Oxide spectral line broadening as a function of pressure. The approximate limit for rotational resolution is shown as a red line.....	124
5.2 Experimental schematic of the VENOM experiments on an underexpanded jet (b), and experimental timing schematic .....	126

5.3	Raw VENOM images (100-shot average) probing two different transitions at time delays of (a) 400 ns and (b) 800 ns after photodissociation.....	127
5.4	Fluorescence image taken at $t = 0$ under stationary conditions (a) and synthetic fluorescence image used as reference to estimate the velocity map (b) .....	128
5.5	Intersection location in a time zero fluorescence image (a) and in a time zero synthetic image (b) .....	129
5.6	Interpolated average streamwise velocity map (left) and temperature map (right) shown together with a CFD simulation obtained from 100-shot average images of an underexpanded jet probing two different transitions at 400 ns and 800 ns after photodissociation .....	130
5.7	Schematic of Mach 4.6 flow over a cylinder .....	132
5.8	Regions in the Mach 4.6 flow over a cylinder studied using the VENOM technique.....	133
5.9	Picture showing the experimental setup components including laser alignment.....	135
5.10	Experimental schematic of the VENOM system .....	136
5.11	Grid distribution used in the CFD simulations.....	139
5.12	Density, pressure, velocity and temperature maps obtained by the turbulent CFD simulations .....	140
5.13	Instantaneous images probing the $R_1 + Q_{21}$ ( $J = 1.5$ ) transition of the vibrationally excited NO in the freestream (a), the flow over a 3.2 mm diameter cylinder (b) and the wake further downstream (c). The same sequence is shown (d, e and f) for the $R_1 + Q_{21}$ ( $J = 8.5$ ) transition.....	142
5.14	Instantaneous VENOM images probing the $R_1 + Q_{21}$ ( $J = 1.5$ ) transition of the vibrationally excited NO in the cylinder near wake 2 $\mu$ s after photodissociation (left panel), and $R_1 + Q_{21}$ ( $J = 8.5$ ) transition probed 2.75 $\mu$ s after photodissociation.....	144
5.15	Experimentally obtained average streamwise velocity ( $u$ ) and temperature maps based on 200 single-measurements. Measured streamwise	

velocity (c) and temperature (d) fluctuations shown as rms values .....	145
5.16 Experimentally obtained interpolated average streamwise velocity (u), radial velocity (v) and temperature maps based on 200 single-shot measurements. CFD simulations are shown on left panels for comparison.....	146
5.17 Measured velocity and temperature fluctuations based on 200-single shots normalized to the freestream values. All quantities are shown as a percent .....	147
5.18 Instantaneous VENOM raw images probing the $R_1 + Q_{21}$ ( $J = 1.5$ ) transition of the vibrationally excited NO in the wake further downstream (c'). The same region is shown (f') for the $R_1 + Q_{21}$ ( $J = 8.5$ ) transition. These images were acquired using a finer aluminum mesh to "write" the horizontal photodissociation lines .....	149
5.19 Experimentally obtained interpolated average streamwise velocity (u), radial velocity (v) and temperature maps based on 5000 single-measurements using the fine aluminum mesh to "write" the horizontal photodissociation lines. CFD simulations are shown on left panels for comparison .....	150
5.20 Measured velocity and temperature fluctuations based on 5000-single shots normalized to the freestream values. All quantities are shown as a percent .....	151
5.21 Measured velocity and temperature fluctuation vertical profiles 2 cm downstream from the cylinder based on 5000-single shots normalized to the freestream values .....	152
6.1 Sequential velocity vectors in an underexpanded jet obtained by the current VENOM experimental setup.....	156
6.2 Front view of the stereoscopic VENOM imaging of the flow .....	157
6.3 Top view of the dual-plane stereoscopic VENOM imaging of the flow ...	158
6.4 Dual VENOM system .....	159

## LIST OF TABLES

TABLE	Page
3.1 Specifications of the windows used in the PHAT cell .....	62
3.2 Measured Centerline Properties with Temporal Variances.....	74
3.3 Measured Spatial Averaged Exit Flow Properties with Spatial Variations	80
4.1 Measured NO product distribution resulting from photolysis of NO <sub>2</sub> at 355 nm.....	93
4.2 Uncertainty components associated to the streamwise velocimetry measurements using only $\tau_1$ .....	99
4.3 Fitting parameters associated to a single exponential temperature decay for NO( $v''=1$ ).....	109
4.4 Fitting parameters associated to a double exponential temperature decay for NO( $v''=0$ ).....	110
5.1 Flow conditions used for the VENOM experiments on the Mach 4.6 flow over a cylinder.....	134

## CHAPTER I

### INTRODUCTION

#### **I.1 Background and Motivation**

The Texas A&M University National Aerothermochemistry Laboratory, TAMU-NAL, is an interdisciplinary facility established to advance the fundamental understanding of the coupling of fluid dynamics with chemical reactions and molecular non-equilibrium. These studies include both the experimental characterization of flow fields and theoretical modeling, and are a result of a collaboration between the Chemistry and Aerospace Engineering Departments.

The study of fluid dynamics is often complicated by the influence of chemical reactions and molecular non-equilibrium, which are present in a variety of fields that span energy, environmental, transportation and aerospace applications. Due to these non-equilibrium phenomena, simplifying assumptions are used in the current computational models to predict the basic fluid behavior, i.e. the mean flow properties, but fail to describe in detail the behavior of the flow at a variety of temporal and spatial scales under thermal, chemical, and/or mechanical non-equilibrium conditions. It has been observed that the turbulent properties of a flow field can be explained by thermodynamic variations across the flow, and as a consequence, accurate modeling of turbulence in high-speed aerodynamic flows requires information about the coupling between internal non-equilibrium and basic turbulence processes. A detailed description of the coupling between non-equilibrium effects and turbulence requires systematic integration between theoretical modeling and experimentation that directly relates model parameters to experimental observables for the refinement and implementation of these models [1].

---

This dissertation follows the style of Applied Optics.



There are a limited number of experimental studies that provide an insight into the coupling of the fluid dynamics and the energy transfer, specifically simultaneous measurements of velocity and scalar fields, but these studies mainly involve the combination of different techniques.

This thesis presents the development of a laser diagnostic technique proposed as a non-intrusive method to provide simultaneous 2-D measurements of the mean and instantaneous fluctuations in two-component velocity and temperature. The technique addresses the experimental issues described above and is expected to be not only applicable to cold high-speed flows, which is the focus of the present study, but also to combustion and other reactive or high-enthalpy flow fields.

## **I.2 Research Objectives**

The main objectives of this study were (1) the further development of the Vibrationally Excited Nitric Oxide Monitoring (VENOM) technique, for simultaneous velocity and temperature measurements in gaseous flow fields using Nitric Oxide Planar Laser Induced Fluorescence (NO PLIF) methods, and (2) the design, construction, and full performance characterization of a compact repetitively pulsed hypersonic test facility to enable advanced laser diagnostic development.

The development of a pulsed hypersonic facility intended for diagnostic development is justified when considering the problematic operation of full-scale hypersonic facilities. The limitations such as the excessive operation expense of long duration wind tunnels and the short duty cycles associated with impulse or blow-down wind tunnels are amplified when developing new diagnostic techniques, that require of extensive testing for development and tuning. This facility was conceived as a tool to enable optical diagnostics that utilize pulsed laser such as PLIF and Molecular Tagging Velocimetry (MTV). Specifically, when the pulsed operation of the facility is synchronized to the pulsed laser systems, the operation is essentially continuous. A great advantage of this mode of operation is that the mass flow through the facility is reduced by up to two orders of magnitude as compared to a continuous flow facility.

The development of the VENOM technique represents the first single diagnostic technique capable of instantaneous two-component velocimetry and thermometry in a gaseous flow field. This technique combines two NO PLIF methods: two-component Molecular Tagging Velocimetry (MTV) and two-line thermometry, both using NO originating from NO<sub>2</sub> photodissociation. The two-component MTV using NO from NO<sub>2</sub> photodissociation was demonstrated by Hsu et al. [2] in an underexpanded jet under a variety of quenching environments. The two-line thermometry technique using NO as a tracer is a well-known technique to obtain full frame temperature maps of gaseous flow fields (see section 1.4.3). However, the use NO resulting from NO<sub>2</sub> photolysis for temperature measurements is not as straightforward, and requires the consideration of several issues: (1) the knowledge of the NO nascent rotational distributions resulting from the photodissociation, (2) the increasing thermal effect of the photodissociation process at high NO<sub>2</sub> seeding fractions and high photolysis laser powers, and (3) the times required for the nascent NO distribution to reach the flow field temperature Boltzmann distribution. This study addresses these issues and proposes an implementation scheme to mitigate these effect in order to provide accurate temperature measurements.

### **I.3 Literature Survey**

#### **I.3.1 Pulsed Supersonic Facilities**

The development and use of compact uniform gas expansions, which originated in the high-speed Aerodynamics field, started as an alternative to overcome difficulties imposed by the employment of free gas expansions for the study of chemical reactions, such as the limited temperature range, usually  $< 20$  K, low gas densities,  $< 1 \times 10^{15} \text{ cm}^{-3}$ , and the non-uniformity of the flow. The pulsed supersonic facilities were initially developed in order to study reactions at very low temperature by providing a stringent test of theoretical models, since molecular encounters at low relative velocity are particularly sensitive to the potential energy surface in the entrance channel. Traditional kinetics experiments in static or slow flow reactors are limited to temperatures above 200 K due to condensation of reactants on the walls of the vessel. Initiating reactions in

the uniform flow arising from a converging-diverging, or Laval, nozzle avoids these limitation and the flow is often described as a "wall-less reactor". Initial demonstration and refinement of low temperature uniform supersonic flows originated with Rowe and co-workers [3,4] for the study of ion - molecule reaction rate coefficients in the temperature range 8 - 163 K, for Helium and Nitrogen flows. Their facility generated flows between Mach 2 and Mach 4 using different nozzles. This idea was later taken by Smith and co-workers [5,6] for the study of neutral - neutral reactions in temperatures ranging from 7 K to 295 K. Soon after Smith and co-workers demonstrated a pulsed variant of the technique, which considerably reduced the operational cost due to the lower gas usage, especially important when expensive chemicals are needed, and thus lowered the pumping capacity required to function. This operational model was conveniently matched to pulsed laser systems used for reaction initiation and species detection [7,8,9]. Several other groups have since employed pulsed Laval nozzle systems to study low temperature reactions [10,11,12,13].

### **I.3.2 Velocity and Temperature Measurements in Gaseous Flow Fields**

There are a limited number of experimental studies that provide insight into the coupling of the fluid dynamics and the energy transfer, specifically measurements of velocity and scalar fields. These studies mainly involve the combination of different techniques such as Particle Image Velocimetry (PIV) and Planar Laser Induced Fluorescence (PLIF). Tsurikov and Clemens have reported measurements of velocity and conserved scalar fields combining PIV and acetone PLIF imaging in a gaseous turbulent flow [14]. Also, combined PIV and PLIF imaging of OH and CH radicals in flames have provided simultaneous velocity and location of the reaction zones that can suggest correlations of heat release with the flow behavior [15,16]. In liquids, there are reports of simultaneous velocity and temperature measurements using PIV and PLIF in a water impinging jet [17], and a simultaneous velocity/temperature field estimation using thermochromic liquid crystals [18]. However, the use of particles to determine velocity in the presence of strong gradients, particularly shock waves, results in large errors as

reported by Huffman and Elliott [19], where deviations in velocity using PIV were within 5% near the jet exit using 100 nm particles, but the fidelity of the particle tracking was drastically degraded across a shock with increasing particle size. Koochesfahani and coworkers performed the first solely molecular-based 2-D simultaneous velocity/scalar measurements in a fluid, where a heavy molecule or combination of molecules were seeded upstream in a water flow and later "tagged" with a laser. In one approach a phosphorescent molecule was seeded upstream in a flow and later "tagged" with a laser. Within the phosphorescence lifetime the flow is imaged twice to obtain local displacements in the flow that provide two-component velocity measurements [20]. The temperature dependence of the phosphorescence lifetime permits the determination of the temperature field from the ratio of both images. In a second approach, the two-tracer method, the phosphorescence of one molecule is used to obtain a velocity map as described in the first approach, and a fluorescent molecule is co-seeded and subsequently excited by the same laser pulse to capture a fluorescence image that is used to obtain a concentration field [21]. These techniques, however, rely on the use of water-soluble molecules and depend on larger delay times than those needed in fast gaseous flows. Nevertheless, it was shown that it is possible to use molecular tracers to obtain simultaneous velocity/scalar measurements, simplifying the experimental setup with respect to previous PIV/PLIF experiments. The extension of molecular-based approaches to gaseous flow fields has demanded the use of a tracer suitable to specific applications where the seeding or tracking of particles and large molecules could be problematic.

A brief summary of the molecular tagging velocimetry methods used in gaseous and liquid flowfields can be found in the two-component MTV study by Hsu et al. [22] and in [23], where both seeded and unseeded techniques are discussed. The main focus of the paper by Hsu et al. was the demonstration of two-component velocimetry using NO from the photodissociation of NO<sub>2</sub>. The advantage over the commonly employed NO fluorescence tagging methods is the relative insensitivity to the quenching environment, since the velocity estimation is not based on two images captured within

one single fluorescence lifetime of the electronically excited NO. Since this method uses the vibrationally excited NO photoproduct arising from NO<sub>2</sub> photolysis, it also permits discrimination against natural occurring NO, present in flames or shock tubes [24]. The use of flow tagging using NO<sub>2</sub> photodissociation at 308 nm from a XeCl excimer laser was initially reported by Orlemann [25], and is particularly valuable as an alternative to overcome the short lifetime of highly reactive radicals such as OH, or the short fluorescence lifetime of NO when using NO fluorescence tagging [26]. The photodissociation using 355 nm was initially reported by Nakaya and coworkers [27], and has been used in a number of works to obtain single line velocity measurements in a Mach 5 flow over a cylinder [28], multiple line velocity measurements in a hypersonic boundary layer [29], and full-frame 2-component velocity maps in an underexpanded jet [2].

## **I.4 Theoretical Background**

### **I.4.1 Nitric Oxide Laser Induced Fluorescence**

Laser Induced Fluorescence (LIF) is one of the most extensively used spectroscopic diagnostic techniques based on a light absorption process followed by spontaneous emission. LIF has proved to be useful in the study of gases due to a number of advantages that include high sensitivity and relative simplicity in the experimental setup and data analysis compared to non-linear techniques that usually require the use of multiple high-power laser beams, such as Coherent Anti-Stokes Raman Scattering and other techniques based on the Raman phenomenon. The high sensitivity of LIF processes also permits 2-D measurements by forming the laser beams into sheets for imaging applications, Planar Laser Induced Fluorescence (PLIF), achieving good spatial resolution, as well as temporal resolution when pulsed laser systems are employed.

The LIF process starts with a molecule absorbing a photon of specific energy to excite a particular rovibronic transition, followed by a relaxation of the excited electronic state into the ground state by an spontaneous emission process, or

fluorescence. An schematic of the nitric oxide energy levels showing these processes is shown in figure 1.1.

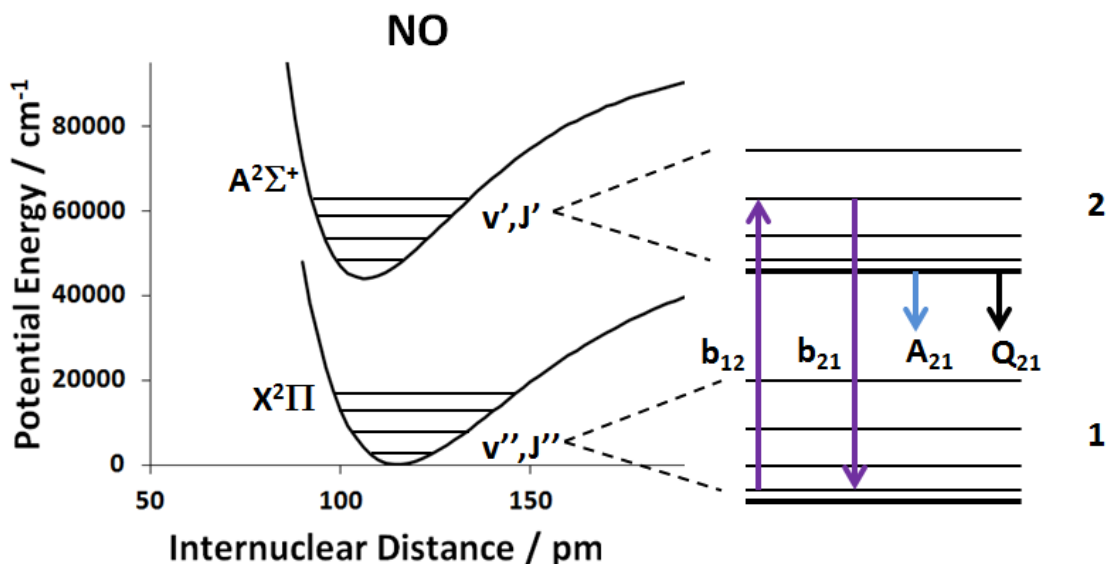


Fig.1.1. Potential energy diagram of NO and two-level LIF model.

The most important processes involved in the LIF technique are shown in figure 1.1 as well as the corresponding rates of stimulated absorption  $b_{12}$ , stimulated emission  $b_{21}$ , spontaneous emission or fluorescence  $A_{21}$ , and collisional quenching  $Q_{21}$ . This model is based on a two-level system and describes the basic NO LIF process for low laser fluences. A more accurate description of this process requires a multi-level fluorescence model to account for Rotational Energy Transfer (RET) processes in both ground and excited states.

The total fluorescence signal collected in an LIF experiment,  $S_{\text{LIF}}$ , is directly proportional to the number density of molecules in the excited state,  $N_2$ , and depends on other factors such as the spontaneous emission rate  $A_{21}$ , the solid angle of collection  $\Omega$ , the emitted photon energy  $h\nu_c$ , and the measurement volume or the collection volume imaged onto the detector  $V$ :

$$S_{LIF} = A_{21} N_2 \frac{\Omega}{4\pi} h\nu c V \quad (\text{Eq. 1.1})$$

The population number densities of the ground ( $N_1$ ) and excited ( $N_2$ ) states can be described by the rate equations:

$$\frac{dN_1}{dt} = -b_{12}N_1 + (b_{21} + A_{21} + Q_{21})N_2 \quad (\text{Eq. 1.2})$$

$$\frac{dN_2}{dt} = b_{12}N_1 - (b_{21} + A_{21} + Q_{21})N_2 \quad (\text{Eq. 1.3})$$

The rates for stimulated absorption and emission,  $b_{12}$  and  $b_{21}$ , are given by the expressions  $b_{12} = B_{12}I_v\Gamma/c^2$  and  $b_{21} = B_{21}I_v\Gamma/c^2$ , where  $B_{12}$  and  $B_{21}$  are the Einstein coefficients for stimulated absorption and emission, respectively, with units of  $\text{m}^3/\text{Js}^2$ ,  $I_v$  is the spectral irradiance in  $\text{W}/\text{cm}^2\text{cm}^{-1}$ ,  $\Gamma$  is the overlap function between the laser line shape and the absorption line, and  $c$  is the speed of light.

For an electronic excitation that requires a wavelength in the UV, as is the case of NO, at  $t = 0$ , the beginning of the laser pulse,  $N_2^0 = 0$ . If the population remains constant,  $N_1 + N_2 = N_1^0$ , and assuming steady state population of the excited state, equation 1.3 can be solved:

$$b_{12}N_1 = (b_{21} + A_{21} + Q_{21})N_2 \quad (\text{Eq. 1.4})$$

Using the definitions of  $b_{12}$  and  $b_{21}$  we have:

$$N_2 = \frac{b_{12}N_1^0}{(b_{21} + b_{12} + A_{21} + Q_{21})} \quad (\text{Eq. 1.5})$$

$$N_2 = N_1^0 \frac{I_v \Gamma}{c^2} \frac{B_{12}}{\frac{I_v \Gamma}{c^2} (B_{21} + B_{12}) + (A_{21} + Q_{21})} \quad (\text{Eq. 1.6})$$

$$N_2 = N_1^0 \frac{I_v \Gamma}{c^2} \frac{B_{12}}{(B_{21} + B_{12})} \frac{1}{\frac{I_v \Gamma}{c^2} + \frac{(A_{21} + Q_{21})}{(B_{21} + B_{12})}} \quad (\text{Eq. 1.7})$$

$$N_2 = N_1^0 \frac{B_{12}}{(B_{21} + B_{12})} \frac{1}{1 + \frac{c^2}{I_v \Gamma} \frac{(A_{21} + Q_{21})}{(B_{21} + B_{12})}} \quad (\text{Eq. 1.8})$$

Defining  $I_v^{sat} = c^2 \frac{(A_{21} + Q_{21})}{\Gamma(B_{21} + B_{12})}$ :

$$N_2 = N_1^0 \frac{B_{12}}{(B_{21} + B_{12})} \frac{1}{1 + \frac{I_v^{sat}}{I_v}} \quad (\text{Eq. 1.9})$$

Introducing this result in eq.1.1 we obtain:

$$S_{LIF} = A_{21} N_1^0 \frac{B_{12}}{(B_{21} + B_{12})} \frac{1}{1 + \frac{I_v^{sat}}{I_v}} \frac{\Omega}{4\pi} h\nu c V \quad (\text{Eq. 1.10})$$

For quantitative LIF measurements that are useful to describe flow field properties eq. 1.10 provides the collected fluorescence signal as a function of the ground state number density. Depending on the laser intensity used in a particular LIF experiment, the fluorescence signal intensity exhibits two different regimes:

\*The saturated regime, for which  $I_v \gg I_v^{sat}$ , and eq. 1.10 results in:



$$S_{LIF} = A_{21} N_1^0 \frac{B_{12}}{(B_{21} + B_{12})} \frac{\Omega}{4\pi} h\nu c V \quad (\text{Eq. 1.11})$$

In this case, the fluorescence intensity does not depend on the laser intensity and quenching. Even when it would be easy to interpret this signal, full saturation is difficult to achieve specially in imaging applications where the laser beam is formed into sheets, and the electronic excitations require the use of wavelengths in the UV where not very high laser powers are available, as it is the case for NO. Also, in a real system, RET processes in the ground state result in a delay to reach the saturated regime.

\*The linear regime, for which  $I_v \ll I_v^{sat}$ , and eq. 1.10 results in:

$$S_{LIF} = A_{21} N_1^0 \frac{B_{12}}{(B_{21} + B_{12})} \frac{1}{1 + \frac{I_v^{sat}}{I_v}} \frac{\Omega}{4\pi} h\nu c V \quad (\text{Eq. 1.12})$$

$$S_{LIF} = A_{21} N_1^0 \frac{B_{12}}{(B_{21} + B_{12})} \frac{1}{1 + \frac{c^2 (A_{21} + Q_{21})}{\Gamma(B_{21} + B_{12}) I_v}} \frac{\Omega}{4\pi} h\nu c V \quad (\text{Eq. 1.13})$$

$$S_{LIF} = N_1^0 B_{12} \frac{A_{21}}{(A_{21} + Q_{21})c} \Gamma I_v \frac{\Omega}{4\pi} h\nu V \quad (\text{Eq. 1.14})$$

The term  $A_{21}/(A_{21} + Q_{12})$  is the quantum yield,  $\phi$ , and expresses the fraction of molecules reaching the excited state that relax through fluorescence. In this regime the fluorescence signal is linear as a function of laser intensity.

#### I.4.2 NO Spectroscopy

In this thesis, only transitions corresponding to the NO  $\gamma$  bands were used, which involve transitions between the ground  $X^2\Pi$  and excited  $A^2\Sigma^+$  states. The fundamentals of NO spectroscopy and related selection rules can be found in the book by Herzberg

[30] but a brief overview is presented here. The electron motion in NO, being a diatomic molecule, is confined to an axial symmetry about the internuclear axis. As a consequence the electronic states are defined by the components of the orbital angular momentum  $L$  and the spin angular momentum  $S$  along the internuclear axis:  $M_L$  and  $\Sigma$ , respectively. For  $M_L > 0$  the inversion of electron motion,  $M_L \leftrightarrow -M_L$ , results in double degenerate states with  $\Lambda = |M_L|$ .

Nitric Oxide is an unusual diatomic molecule that contains an odd number of valence electrons, and that does not show the high reactivity common in other free radicals. Its ground state electronic configuration is  $(\sigma)^2 (\sigma^*)^2 (\sigma)^2 (\sigma^*)^2 (\sigma)^2 (\pi)^4 (\pi^*)^1 (\sigma^*)^0$ . The unpaired electron occupies an antibonding  $\pi^*$  orbital and an electronic excitation promotes this electron to an upper nonbonding orbital, resulting in a shorter bond length of the excited states, as it can be noted in figure 1.1.

The interaction between different angular momenta present in the NO molecule, i.e. nuclear rotation, electron orbit, and electron spin, cause a splitting of the degenerate electronic energy levels as follows:

\*The ground state,  $X^2\Pi$ , shows two types of splitting. The interaction between the electron orbit and the electron spin causes the so called spin-orbit splitting, characteristic of electronic states with  $\Lambda > 0$ . The number of multiplets is equal to  $2S + 1$ , which is 2 for the case of NO:  $^2\Pi_{1/2}$  and  $^2\Pi_{3/2}$ . Furthermore, when  $\Lambda > 0$ , the doubly degenerate states split with increasing rotation speed, i.e. with increasing rotational energy. This splitting is called lambda-doubling and is caused by the interaction between electron orbit and molecular rotation. Compared to spin-orbit coupling, the lambda-doubling splitting is very small, only a fraction of a wavenumber.

\*The first excited state,  $A^2\Sigma^+$ , for which  $\Lambda = 0$ , does not show spin-orbit or lambda-doubling. However, an interaction between the electron spin and the molecular rotation causes a rotational energy dependent splitting between the different  $\Sigma$  terms, the spin-rotation splitting.

The coupling of the different angular momenta is used to classify the electronic states according to the Hund's coupling cases. The ground state, which is a  $\Pi$  state,

shows an intermediate behavior between Hund's a and b cases depending on whether the total angular momentum value  $J$  is low or high. For low- $J$  values ground state NO behaves more like case a and it is employed in this thesis to describe the transitions. The excited state, which is a  $\Sigma$  state, belongs to Hund's case b.

According to Hund's case a, for the  $X^2\Pi$  state, the total angular momentum  $J$  is formed by the electronic angular momentum  $\Omega$  and the nuclear rotation  $N$ . For NO, with one unpaired electron,  $J$  is half-integral and is given by the values  $J = \Omega, \Omega + 1, \Omega + 2, \dots$ , with  $J \geq \Omega$ . In the  $A^2\Sigma^+$  state, the orbital angular momentum  $\Lambda$  and the nuclear rotation  $N$  form a total angular momentum quantum number exclusive of spin,  $K$ , that takes integral values from 0 and up.  $S$  and  $K$  form the total angular momentum quantum number including spin  $J$ , and is given by  $J = (K+S), (K+S-1), (K+S-2), \dots (K-S)$ , with each  $K$  consisting of  $(2S+1)$  components. Figure 1.2 shows a schematic diagram with the rotational energy levels involved in the NO A-X system.

From figure 1.2 and the previous discussion it can be noted that the ground state is quadruple degenerate and the excited state is doubly degenerate. According to the selection rules of total angular momentum  $\Delta J = 0, \pm 1$ , and of symmetry that only terms of different sign can combine,  $+ \leftrightarrow -$ , there are 6 possible branches for each of the two sub-bands of the NO A - X system.

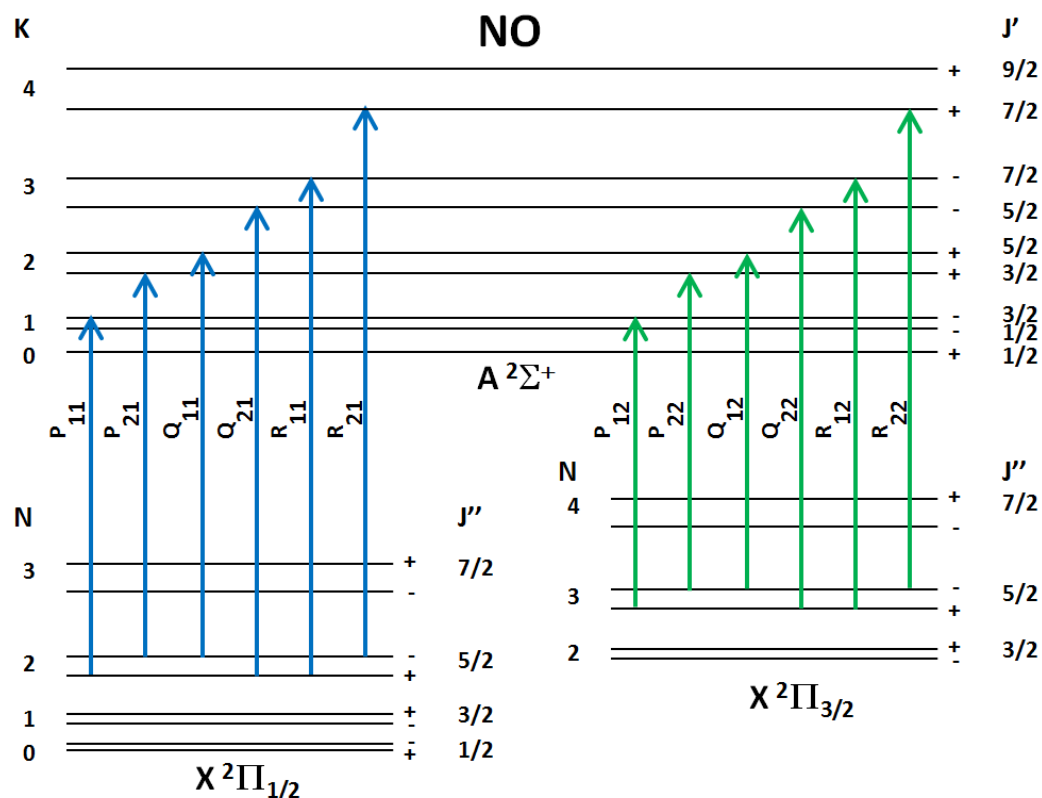


Fig. 1.2. Energy level diagram for the NO showing rotational transitions for the 12 possible branches in the  $A^2\Sigma^+$  -  $X^2\Pi$  system.

The doublet splitting in the  $A^2\Sigma^+$  state shown in figure 1.2 has been exaggerated since, in practice, they are so small that are not resolvable. The 6 branches for the  $A^2\Sigma^+$  ( $v'=0$ ) -  $X^2\Pi_{1/2}$  ( $v''=0$ ) sub-band and the 6 branches belonging to the  $A^2\Sigma^+$  ( $v'=0$ ) -  $X^2\Pi_{3/2}$  ( $v''=0$ ) sub-band are shown in figure 1.3 as a theoretical excitation spectrum for a Boltzmann distribution at 300 K.

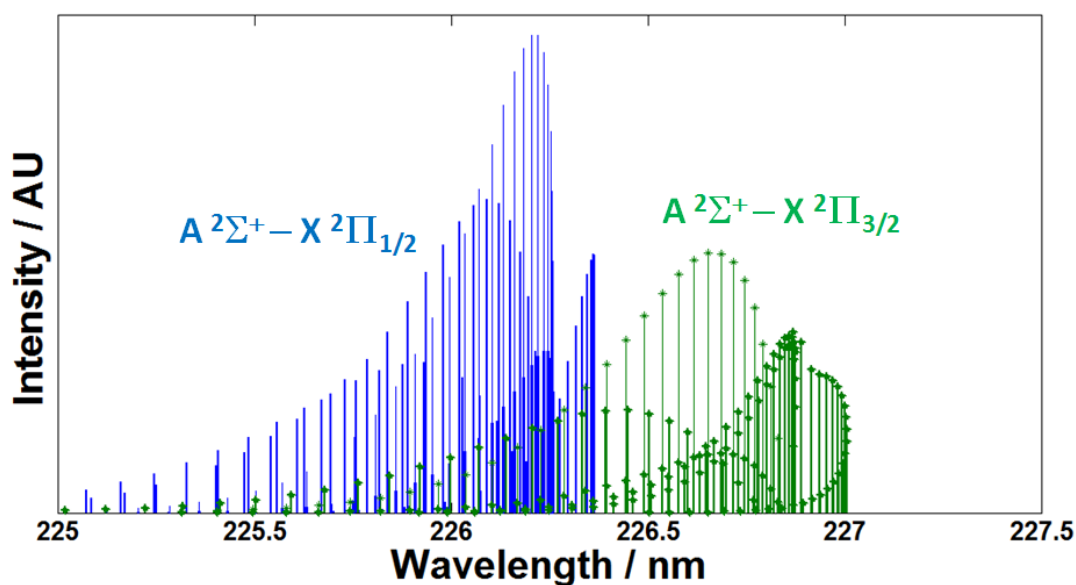


Fig. 1.3. Simulated Nitric Oxide excitation spectrum of  $A^2\Sigma^+ (v'=0) - X^2\Pi (v''=0)$  band showing the two different sub-bands corresponding to the two ground state spin-orbit components. The relative intensities reflect the ground state populations at 300 K.

The branches that differ only in the excited doublet state overlap and the 12 possible branches in the  $A^2\Sigma^+ - X^2\Pi$  system can be reduced to 8 resolvable branches:  $P_{11}$ ,  $P_{21} + Q_{11}$ ,  $Q_{21} + R_{11}$ ,  $R_{21}$ ,  $P_{12}$ ,  $P_{22} + Q_{12}$ ,  $Q_{22} + R_{12}$ , and  $R_{22}$ . Figure 1.4 shows in detail a simulated excitation spectrum of each sub-band with each branch labeled in a different color.

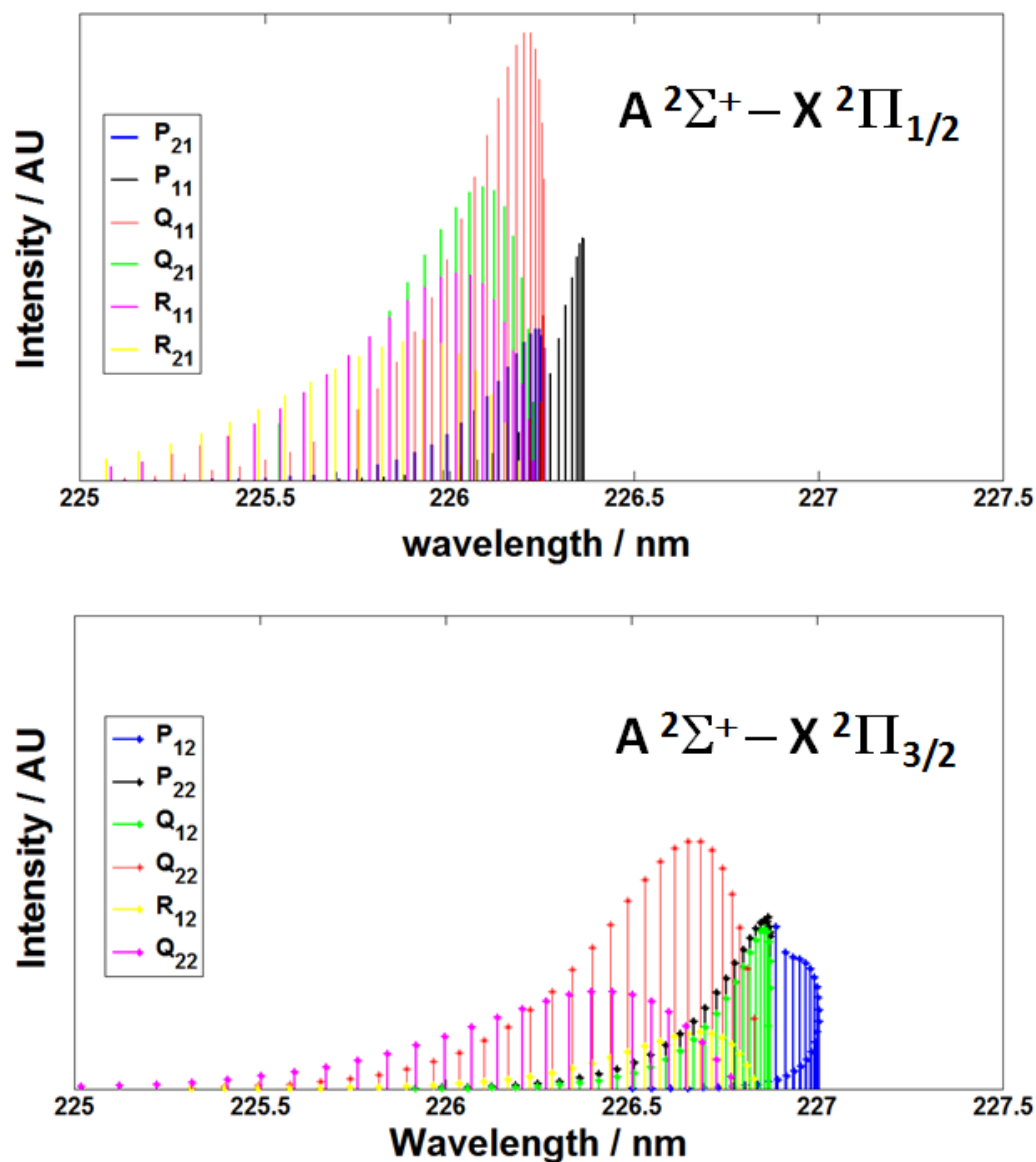


Fig. 1.4. Simulated Nitric Oxide excitation spectrum showing in detail the 6 branches belonging to each  $A^2\Sigma^+ (v'=0) - X^2\Pi (v''=0)$  sub-band. The relative intensities reflect the ground state populations at 300 K.

The experiments described in this thesis employ both the NO(0,0) and the NO(1,1) bands. Although the transitions for the NO(0,0) have been described above, the spectroscopy for the NO(1,1) is very similar. The theoretical excitation spectrum for a mixture of 50% NO( $v''=0$ ) and 50% NO( $v''=1$ ) at 300 K is shown in figure 1.5, looking

at the (0,0) and (1,1) bands. Having an identical composition of the two vibrational states, the intensity difference is due to a larger Franck-Condon factor of the (0,0) band.

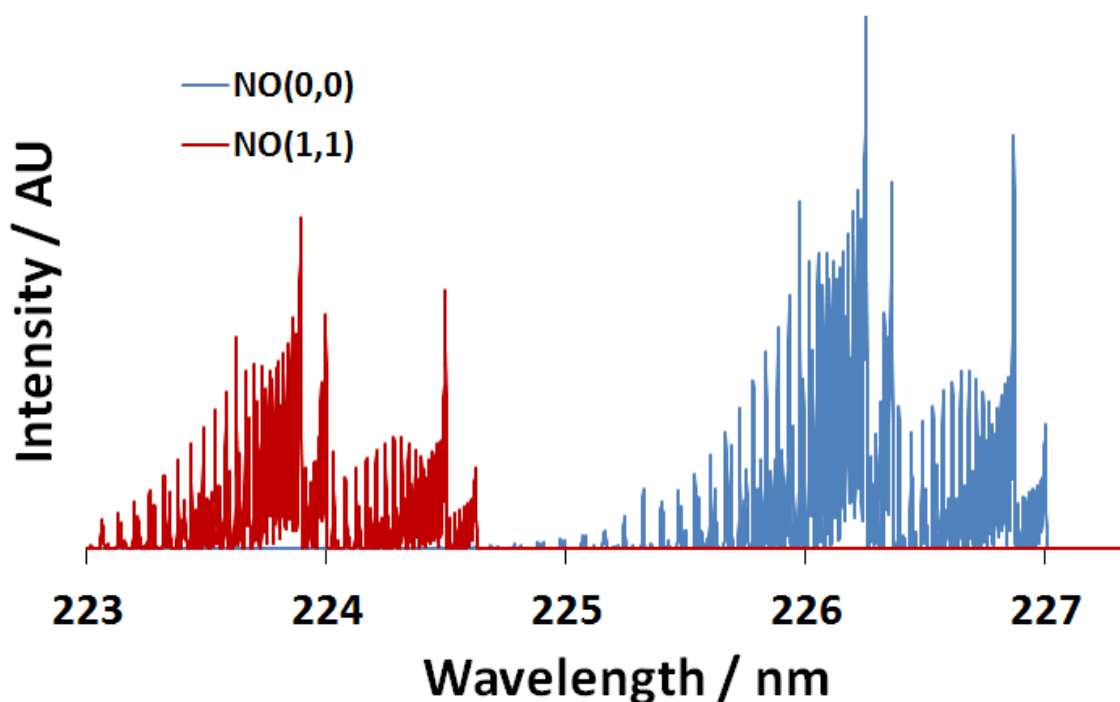


Fig. 1.5. Simulated Nitric Oxide excitation spectrum showing the NO(0,0) and NO(1,1) bands at 300 K.

As mentioned above, the NO A-state has a longer equilibrium internuclear distance than the ground X-state. This results in formation of bandheads in the P-branches, easily noticeable in the blue-degraded structures seen in figures 1.3 - 1.5. Due to the complexity of the NO spectrum, and as described in the following section, the development of a useful quantitative diagnostic technique largely relies in the use of a tunable excitation source with narrow enough linewidth capable of exciting single rotational transitions. Fortunately, such laser systems have been commercially available for decades.

### I.4.3 Two-line Temperature Measurements

As explained above, the fluorescence intensity collected in a LIF experiment for the linear, unsaturated, regime is described by the following expression:

$$S_{LIF} = N_1^0 B_{12} \frac{A_{21}}{(A_{21} + Q_{21})c} \Gamma I_v \frac{\Omega}{4\pi} h\nu V \quad (\text{Eq. 1.15})$$

This equation states that the LIF intensity depends on a number of experimental factors, such as the fluorescence collection optics, but it is also a function of flow-related properties such as the number density of absorbing species and the quenching conditions. By using an excitation source that excites a single rotational state, the LIF signal intensity will reflect the Boltzmann population fraction of that specific state, then we can write:

$$S_{LIF} = f_B N_1^0 B_{12} \frac{A_{21}}{(A_{21} + Q_{21})c} \Gamma I_v \frac{\Omega}{4\pi} h\nu V \quad (\text{Eq. 1.16})$$

where  $f_B$  is the Boltzmann population fraction of the absorbing species given by:

$$f_B = e^{-E_{vib}/kT_{vib}} (2J'' + 1) e^{-E_{rot}/kT_{rot}} \quad (\text{Eq. 1.17})$$

The NO LIF two-line thermometry technique consists in the excitation of two different rotational states,  $J''_1$  and  $J''_2$ , to obtain a ratio of fluorescence intensities [31,32]. Since the LIF intensities can be related to the ground state populations, the rotational temperature can be inferred assuming a Boltzmann distribution. If both transitions originate from the same vibrational level, the fluorescence ratio  $R_{12}$  will only depend the ground state rotational population fractions. The collection system efficiencies, the spectroscopic constants and the laser intensities can be merged into a constant  $C_{12}$ :



$$R_{12} = \frac{S_{f1}}{S_{f2}} = C_{12} \frac{(2J''_1 + 1)}{(2J''_2 + 1)} e^{-\Delta E_{rot}/kT_{rot}} \quad (\text{Eq. 1.18})$$

The constant  $C_{12}$  is experimentally determined by measuring the fluorescence ratio in a point where the temperature is well-known. As described in [31,32], a sensitive temperature measurement is achieved by maximizing the spacing between the probed rotational states as the temperature uncertainty  $\delta T$  scales inversely proportional to  $\Delta E$ :

$$\frac{\partial T}{T} = \frac{kT_{rot}}{\Delta E} \frac{\partial R_{12}}{R_{12}} \quad (\text{Eq. 1.19})$$

As it will be shown in Chapter 4, maximizing the separation between the two transitions benefits the temperature sensitivity. However, a careful selection of the transitions has to be made according to the target temperature range to assure that the population fraction of the high- $J''$  state results in an image with enough signal-to-noise levels. According to equation 1.19,  $\Delta E$  has to be at least of the same order of magnitude than  $kT_{rot}$  for the upper end of the target temperature range. The typical temperature range exhibited by the flow fields studied in this thesis is 50 - 300 K, for which Boltzmann distributions are shown in figure 1.6.

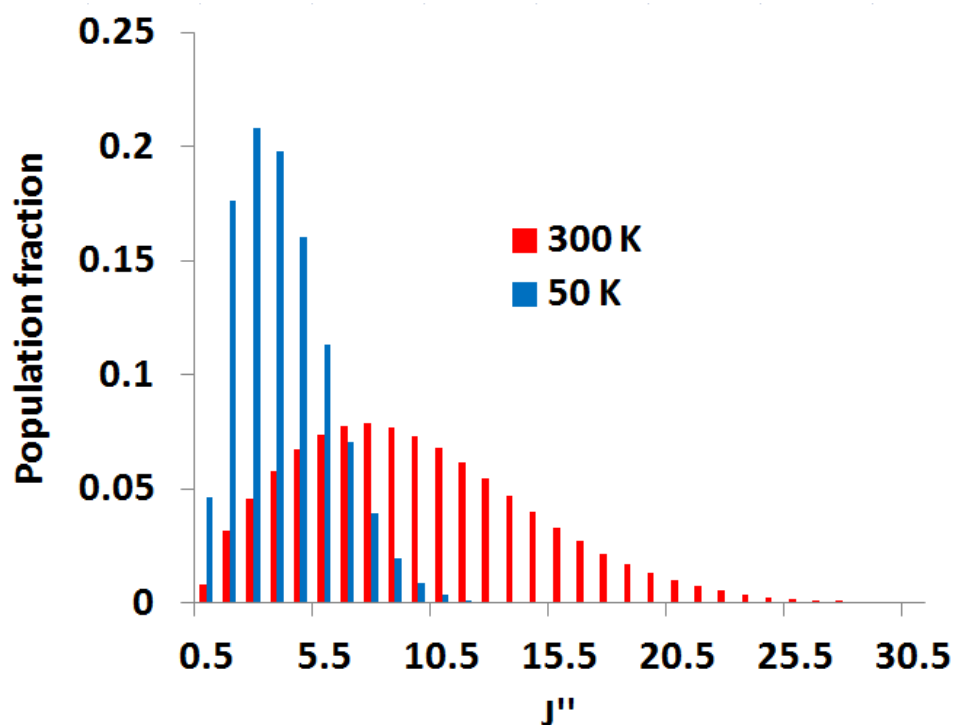


Fig. 1.6. Nitric Oxide Boltzmann distributions at the lowest (50 K) and highest (300 K) temperatures for the flow fields studied in this thesis.

As described above, the fluorescence ratio is a function of temperature, but also a function of pressure that affects the quenching levels across the field of view, especially when two different rotational levels in the emitting excited state are involved. In systems like OH the two transitions can be chosen in such a way that they both share the same upper emitting state [31]. However, the smaller separation between rotational states in NO ( $B = 1.7 \text{ cm}^{-1}$ , compared with  $B = 18.9 \text{ cm}^{-1}$  for OH) necessitates of the excitation of transitions that never lead to the same upper emitting state in order to achieve a good temperature sensitivity. The ratio of quenching rates for the two rotational states is assumed to be independent of the local conditions. In addition, we have performed temperature measurements utilizing two transitions within either the NO  $A \leftarrow X(0,0)$  or the  $A \leftarrow X(1,1)$  band, so there is not any vibrational state dependence of quenching cross sections. There are a number of papers that illustrate the rotational-level independency of collisional quenching of the  $A^2\Sigma^+$  ( $v'=0$ ) state of NO [33,34]. In the case of the VENOM

technique, where the transitions excited are within the  $A \leftarrow X(1,1)$  band, the same rotational-level independency of collisional quenching within the  $A^2\Sigma^+$  ( $v'=1$ ) state has been observed [35,36].

## **I.5 Thesis Overview**

This thesis is organized in six chapters. Chapter 1 has stated the main research goals and provided with enough theoretical background or references necessary to understand the main issues addressed by this work. Mainly, nitric oxide PLIF methods are the foundation for all measurements described herein, and the fundamentals of NO fluorescence as well as the recent accomplishments relevant to the field were presented.

The experimental system employed for most of the experiments deserves a special section on its own. Chapter 2 is dedicated to describe the current laser and image acquisition setup, which represents an upgrade to a previously employed system. The system upgrade has signified an improved efficiency based on long-lasting dye mixtures and an increase in probe laser power by an order of magnitude. This is a critical improvement that has permitted the successful single shot measurements presented in the following chapters. Chapter 2 also describes the basics of the imaging processing methods explicitly developed and written in Matlab to process the fluorescence image pairs that allow the determination of planar velocity and temperature fields.

The main topic of this thesis is the development and demonstration of advanced laser diagnostics to characterize high-speed gaseous flows. However, the development and validation stage of new techniques necessitates of extensive testing periods, which is practically impossible in the existing short-duration hypersonic facilities. Furthermore, the development of useful diagnostic techniques is based on the demonstration of measurement capabilities in environments that resemble an actual problem. For these reasons, the development of a pulsed hypersonic flow apparatus has also been accomplished. Chapter 3 presents the design, construction and full characterization of this facility dedicated to develop and test the laser diagnostics. The flows generated by

this apparatus are repeatable and their properties well-known, and have proven to be an invaluable tool in the diagnostics development.

Chapter 4 describes the measurements of velocity and temperature using nitric oxide originating from nitrogen dioxide photodissociation, as well as the issues involved in order to perform successful measurements. This chapter consists of two main parts. The first part describes the velocity measurements using the vibrationally excited NO photoproduct using two different photodissociation approaches, as well as the uncertainties attainable with each of them. One of those methods proves useful to accomplish simultaneous temperature measurements, which is the topic of the second part of the chapter. In this second part the rotational thermalization of hot NO originating from photodissociation is explored and an implementation scheme is recommended in order to use this NO tracer as a suitable way of measuring rotational temperature in a gaseous flow field.

Chapter 5 represents the culmination of the efforts presented in all previous chapters. It describes a series of measurements performed in the pulsed hypersonic flow apparatus using the NO PLIF methods described in chapter 4 in order to determine simultaneous and instantaneous velocity and temperature maps. These measurements permitted to determine variations in the instantaneous two-component velocity and temperature due to turbulent fluctuations. The first part describes an initial simultaneous measurement of velocity and temperature in an underexpanded jet flow field, obtaining average quantities. The second part describes the instantaneous VENOM measurements in the wake of a Mach 4.6 flow over a cylinder, based on 200 single-shot image pairs. A third set of measurements in the cylinder wake are performed, demonstrating an increase in the spatial resolution of the measurements by using a finer photodissociation grid, resulting in better resolved flow structures. The results from this last set of measurements are based on 5000 single-shot image pairs.

## CHAPTER II

### EXPERIMENTAL METHODS: LASER AND IMAGING SYSTEMS, AND DATA ANALYSIS PROGRAM

The laser diagnostic systems have been installed at the Texas A&M University National Aerothermochemistry Laboratory (TAMU-NAL), conveniently located and surrounded by several facilities and test chambers. The laser experiments reported in this thesis vary in complexity, and are defined by the specific needs of each measurement, allowing flexibility in wavelengths, alignment, and timing schemes. The current experimental setup represents an upgrade from a previous system described elsewhere [2].

#### **II.1 Description of the Laser Systems**

The pulsed laser setup consists of a Spectra Physics LAB-150-10 flashlamp-pumped Nd:YAG laser operated at 10 Hz that produces a maximum power of 200 mJ/pulse when frequency tripled to 355 nm, with a linewidth of  $\sim 1 \text{ cm}^{-1}$ . The laser energies were monitored with a Scientech, Vector H10 (AC2501 head). This beam has a diameter of 9 mm and can be expanded with a 2.5X beam expander before being directed into a test section through mirrors and sheeting optics. Beam splitters are used to optionally split this beam in a variety of splitting ratios in order to generate two 355 nm beams that can be independently aligned.

There are two identical PLIF laser systems that were used for the excitation of nitric oxide, each consisting of an injection seeded Spectra Physics PRO-290-10 Nd:YAG laser operated at 10 Hz, with a linewidth of  $\sim 0.003 \text{ cm}^{-1}$ . The 532 nm output is used to pump a Sirah Cobra Stretch pulsed dye laser to produce a tunable fundamental output beam in the range from 600 to 630 nm using a solution of Rhodamine 610 and Rhodamine 640 in methanol. The dye laser output is mixed with the residual 355 nm beam from the Nd:YAG laser in a Sirah SFM-355 frequency mixing unit to produce a

maximum of 15 mJ/pulse in a range from 223 to 227 nm, with a typical linewidth of 0.08  $\text{cm}^{-1}$  and power fluctuations ranging from 5 to 10%, measured with a Thorlabs PM100D (S314C head).

### **II.1.1 Laser Calibration**

The Sirah dye laser calibration was done by a custom automatic wavelength scanning program written in Labview. The program was originally written for calibration in the wavelength range of  $\sim 223 - 227$  nm required for excitation of the NO(0,0) and NO (1,1) gamma bands. In the past, these wavelengths were generated by frequency doubling (using Coumarin 450 dye in methanol). The Labview scanning program required minor modifications since the current dye laser systems generate wavelengths in the same wavelength range by frequency mixing (dye laser output using a mixture of Rhodamine 610 and Rhodamine 640 in methanol) with the residual 355 nm from the YAG lasers. The program controls the laser systems by accessing the laser's configuration files.

The experimental setup used in the laser calibration is shown in figure 2.1. The calibration required to excite transitions in the NO(0,0) band is straightforward and involves the alignment of the excitation laser along the axis of the calibration cell.

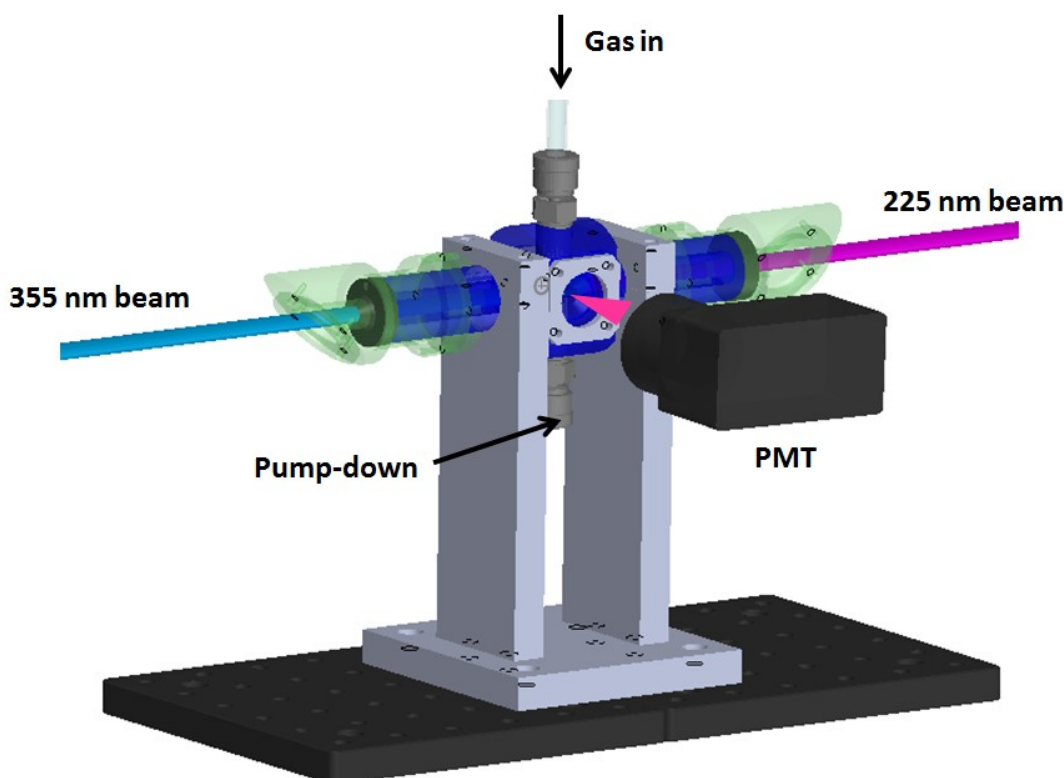


Fig. 2.1. Schematic of the experimental setup used for the dye laser system calibration.

The cell was continuously kept under vacuum by a pumping line, and a slow flow of 1% NO in N<sub>2</sub> is fed to reach constant pressure (usually in the 10 - 50 Torr range). In order to calibrate the laser in the wavelength range required to excite the transitions in the NO(1,1) band, the gas mixture consisted of 1% NO<sub>2</sub> in N<sub>2</sub>. The photolysis laser is also aligned along the axis of the calibration cell entering on the side opposite to the probe laser. Both laser beams overlap, as observed in the figure.

While the laser is tuned to a specific wavelength, the fluorescence generated by each laser pulse is collected at 90 degrees with respect to the laser propagation direction by a Hamamatsu photomultiplier tube R928. The fluorescence trace is received by a PC Gagescope, CompuScope 82G oscilloscope and the signal is integrated and averaged for 10 laser shots.

The previously described procedure generates an intensity associated to the specific wavelength at which the laser is set. The laser then moves to the next wavelength point and the procedure is repeated until the full wavelength range is covered. Parameters such as the step size, the number of shots to average per wavelength point, and the wavelength range to scan were specified in the scanning program's user interface window. The average of 10 fluorescence traces at each wavelength was used to produce a smooth experimental spectrum that was later compared against the LIFBASE spectral simulation program [37] in order to find the shift required to match the theoretical spectrum and then locate the specific desired transitions. Examples of experimental and simulated excitation scans of the NO(0,0) and NO(1,1) bands are shown in figures 2.2 and 2.3, respectively.

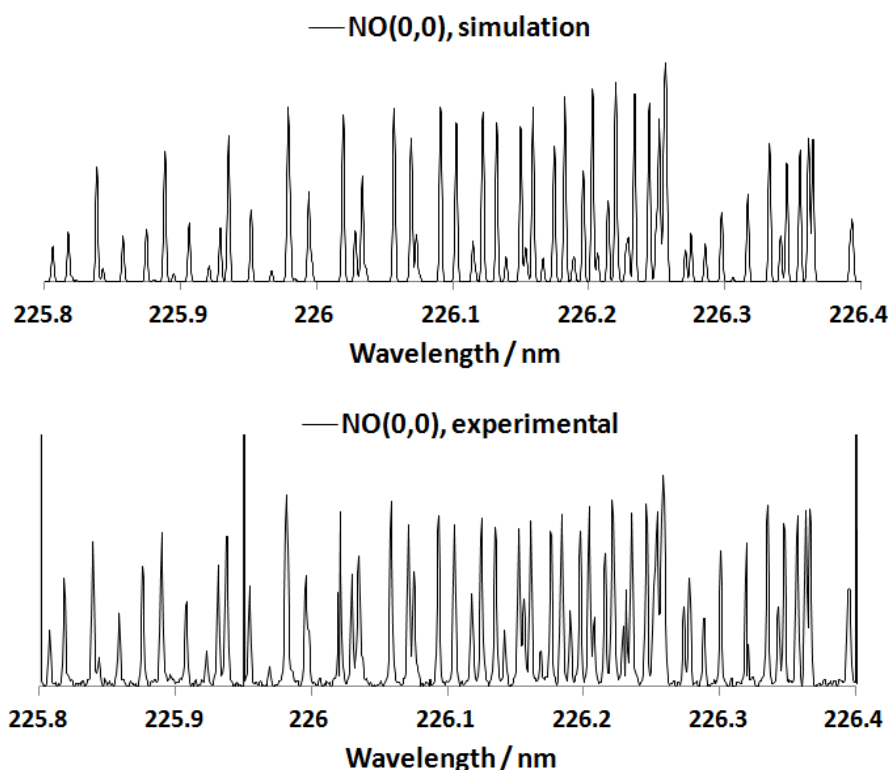


Fig. 2.2. Laser Induced Fluorescence excitation spectra for the NO(0,0) band with a resolution of 0.002 nm.



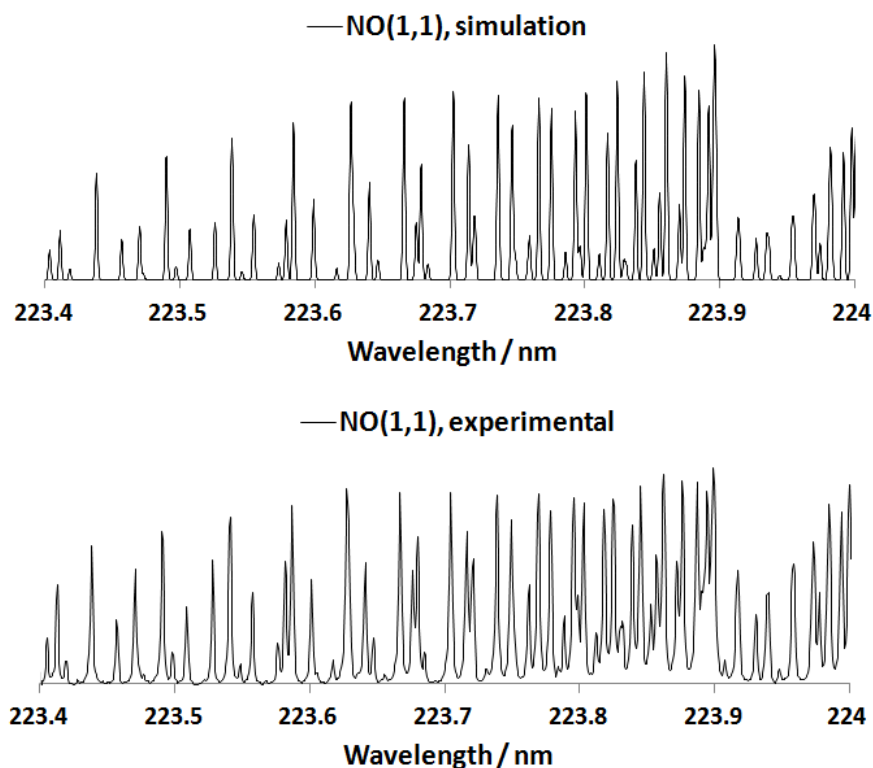


Fig. 2.3. Laser Induced Fluorescence excitation spectra for the NO(1,1) band with a resolution of 0.002 nm.

## II.2 Imaging System

A complete schematic of the laser diagnostic system and image acquisition setup is shown in figure 2.4. The fluorescence images resulting from the laser excitation of nitric oxide - seeded flows were acquired using two Andor iStar DH734 ICCD cameras. The cameras were fitted with either UKA 105 mm F/4.0 UV lenses or CERCO 100 mm F/2.8 UV lenses, and extension rings, employing no optical filters. The timing between the laser systems and the camera gating was controlled using a BNC 575 digital delay/pulse generator.

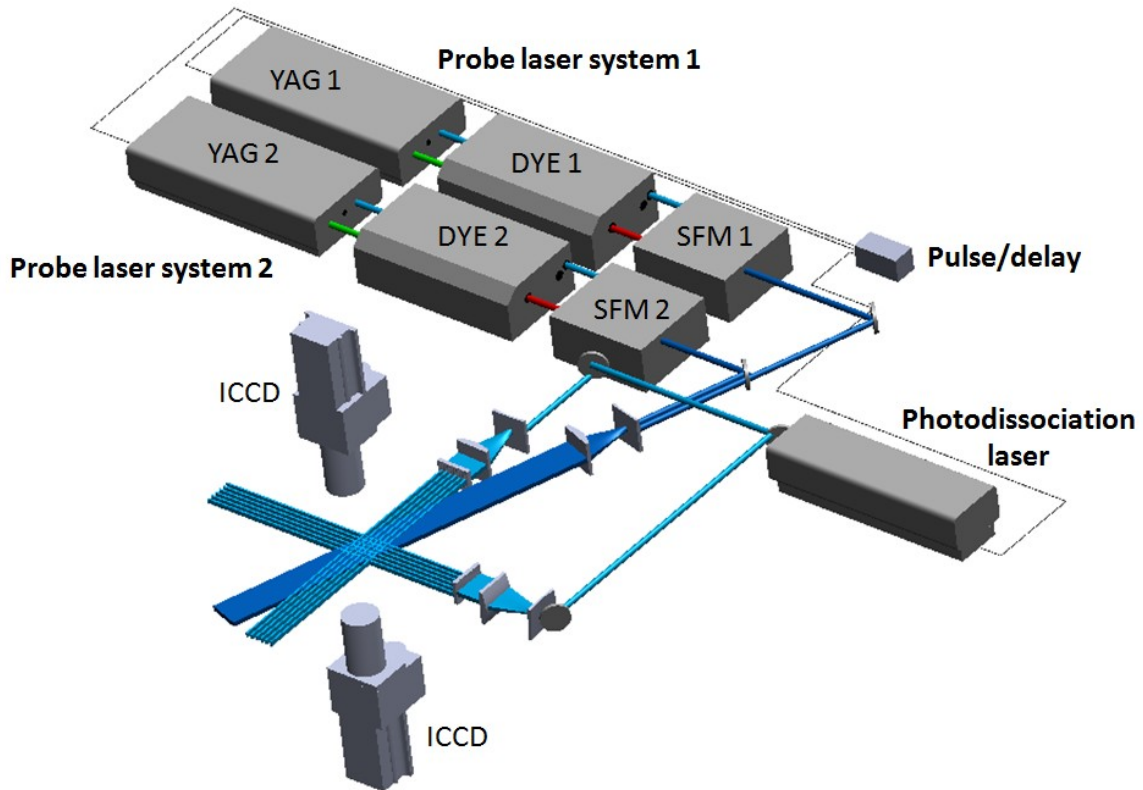


Fig. 2.4. Schematic of the laser diagnostic system and image acquisition setup.

### II.2.1 Imaging System Resolution

In flow imaging applications it is important to perform a precise determination of the optical system's ability to clearly resolve small structures and strong gradients. The theoretical maximum resolution achievable by an optical system is the Nyquist spatial frequency, and is limited by the imaging system pixel size. According to manufacturer specifications, the Andor iStar DH734 ICCD cameras have a pixel width of  $w = 13 \mu\text{m}$ . This resolution limit,  $1/2w$ , is 38.5 line pairs per millimeter, or lp/mm. However, the practical resolution of the system is reduced by a number of factors that include the quality of the lenses, the intensifier, and the fiber optic coupler. The intensifier is the most limiting factor with an estimated resolution of 20 lp/mm [38,39]. Accounting for the combination of these factors, the optical system cut-off frequency is calculated as follows:

$$\frac{1}{f_{system}} = \sqrt{\sum_i \frac{1}{f_i^2}} \quad (\text{Eq. 2.1})$$

where  $f_i$  refers to an specific optical system component such as the lens, the intensifier, the fiber optic coupling, and the CCD array. From eq. 2.1,  $f_{system}$  is estimated to be ~19 lp/mm considering  $f_{intensifier} = 20$  lp/mm and  $f_{array} = 77$  lp/mm (13 $\mu$ m pixel size). For 77 pixel/mm,  $f_{array}$  corresponds to resolvable features of ~4 pixel, or 52  $\mu$ m for both the object and the imaging plane (i.e. a magnification factor of 1).

However, an experimental evaluation of the system's maximum resolution requires a measurement of the modulation transfer function, MTF, which is a parameter that defines the optical system's finite ability to transfer contrast variations in an object to an image. This can be accomplished by measuring the edge spread function (ESF) using the knife-edge technique and calculating its derivative to obtain the line spread function (LSF). Finally, the FT of the LSF results in the MTF.

Figure 2.5 (a) and (b) shows the measured knife edge responses for both the CERCO and UKA lenses. These measurements were obtained by imaging a vertically aligned knife edge illuminated from the back with a mercury lamp placed behind a diffusing screen. The knife edge was translated in 2  $\mu$ m increments and the intensity from a single pixel was monitored and plotted as a function of the knife edge position. The edge response was then fitted with an error function and the fit was differentiated to obtain the Line Spread Function, LSF.

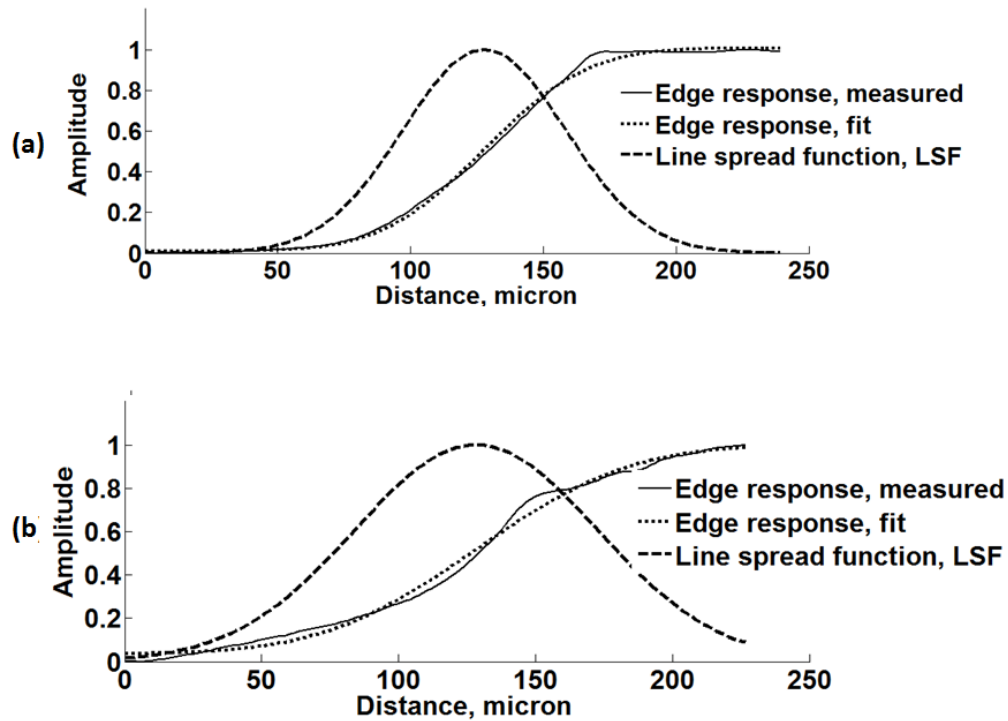


Fig. 2.5. Edge response and line spread function obtained for the CERCO (a) and the UKA (b) lenses.

Figure 2.6(a) and (b) present the corresponding MTFs. The limiting resolution is defined as the frequency corresponding to a 3% of the amplitude of a perfectly modulated signal (amplitude of unity). The reason for this is that human eye is capable of noticing contrast reductions down to 3% percent. The underexpanded jet experiments described in this thesis were performed using the UKA lenses (fig. 2.6 b), for which the imaging system showed a limiting resolution of 8.9 lp/mm, or 112.2  $\mu\text{m}$ . The experiments in the hypersonic pulsed flows were performed using the CERCO lenses (fig. 2.6 a), which resulted in a measured limiting resolution of 14.3 lp/mm, or 70  $\mu\text{m}$ .

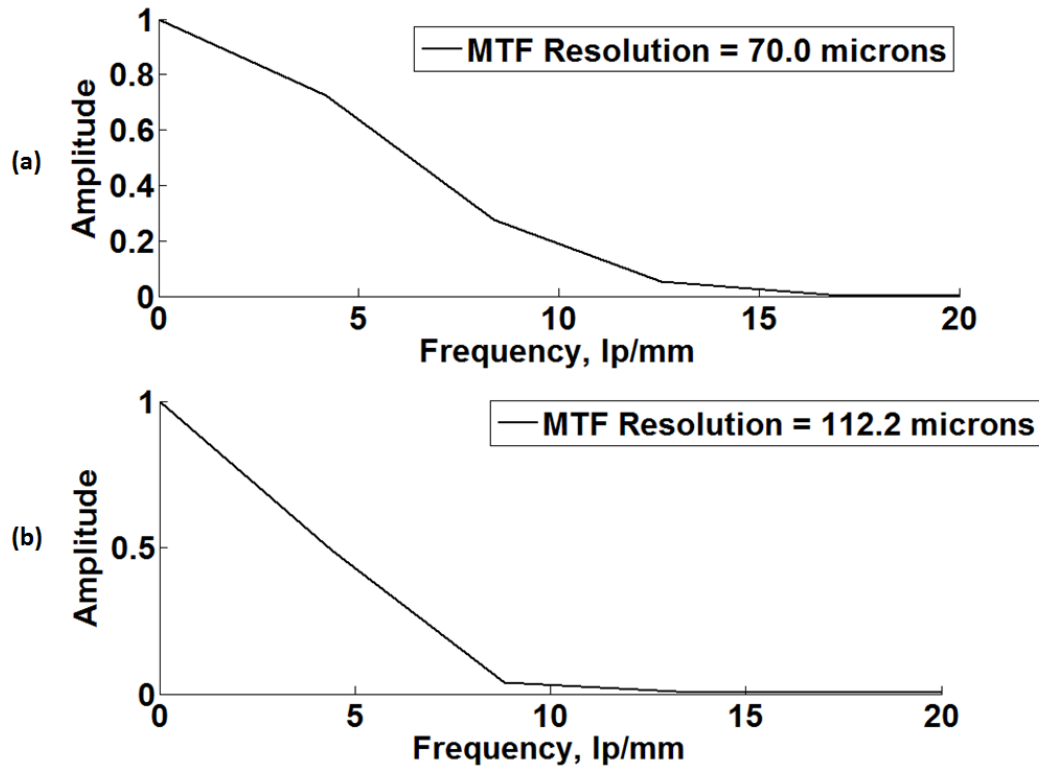


Fig. 2.6. MTFs for the CERCO (a) and UKA (b) lenses obtained from the LSF measurements shown in Fig. 2.5.

### II.3 Data Analysis Program

The data analysis program used to obtain the two-component velocity and temperature maps described in this thesis was written in Matlab. The program consists of several functions that are called by Graphical User Interfaces (GUIs), where several user-defined parameters are specified. This section describes the steps involved in the analysis required to obtain velocity and temperature maps from raw fluorescence images.

The estimation of a velocity map based on VENOM images is based on a procedure that tracks the displacement of fluorescence intersection patterns. The generation of an intensity modulation pattern permits the formation of fluorescence peaks and valleys. These features are illustrated in two and three dimensions in figure 2.7.

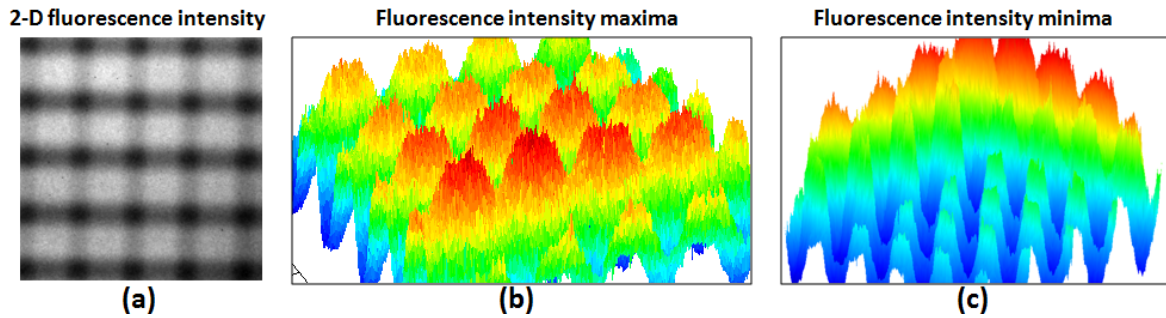


Fig. 2.7. Fluorescence intensity features in a VENOM image (a). Both fluorescence maxima (b) and minima (c) can, in principle, be used to track the local flow displacements.

The program was written in such a way that the intersections of the fluorescence maxima or minima are automatically detected and their displacement tracked. The displacement of these features,  $\Delta x$  and  $\Delta y$ , provide a direct measurement of the local flow movement in two directions.

### II.3.1 Pre-processing

The first step of the image analysis consists of a pre-processing of all raw-images. This pre-processing involves the correction of distortions caused by the camera lenses. The most common distortions caused by lenses are the pincushion and barrel distortions, and some variants of them. For illustration, these distortions were simulated in Matlab using a synthetically generated perfect grid image and are compared to the original undistorted image in figure 2.8.

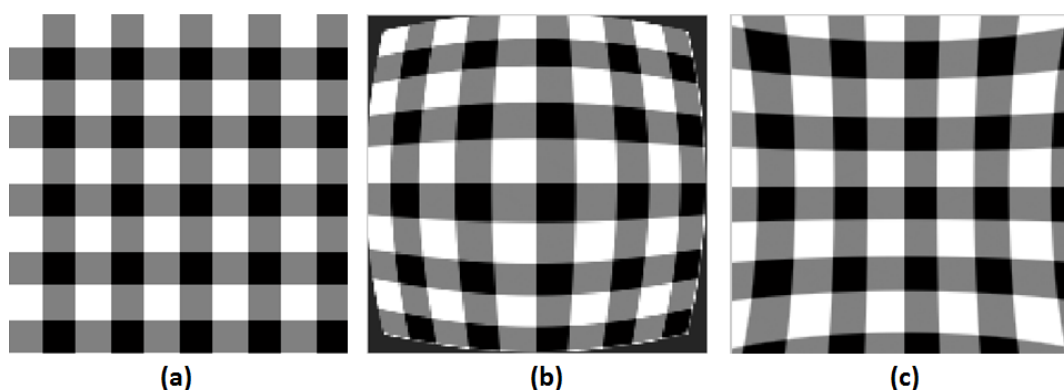


Fig. 2.8 Common distortions caused by a camera lens. Undistorted image (a), barrel-distorted image (b), and pincushion-distorted image (c).

In order to perform the distortion correction of the fluorescence images, an image of a perfect grid with known even spacing is taken with each camera, as seen in figure 2.9. This image corresponds to a glass dotcard with a grid formed by lines separated by 2.54 mm. The lines are printed on one of the surfaces so both cameras situated on each side of the experimental setup can simultaneously acquire an image of it. From figure 2.9, the grid image appears not only distorted, but also misaligned. The image is aligned by picking two points on each end of the image along the horizontal centerline. As observed from figures 2.8 and 2.9, the lines that lay along the center of a distorted image do not bend. These two points can be used to estimate the angle of rotation required for alignment. This procedure is also illustrated in figure 2.9.

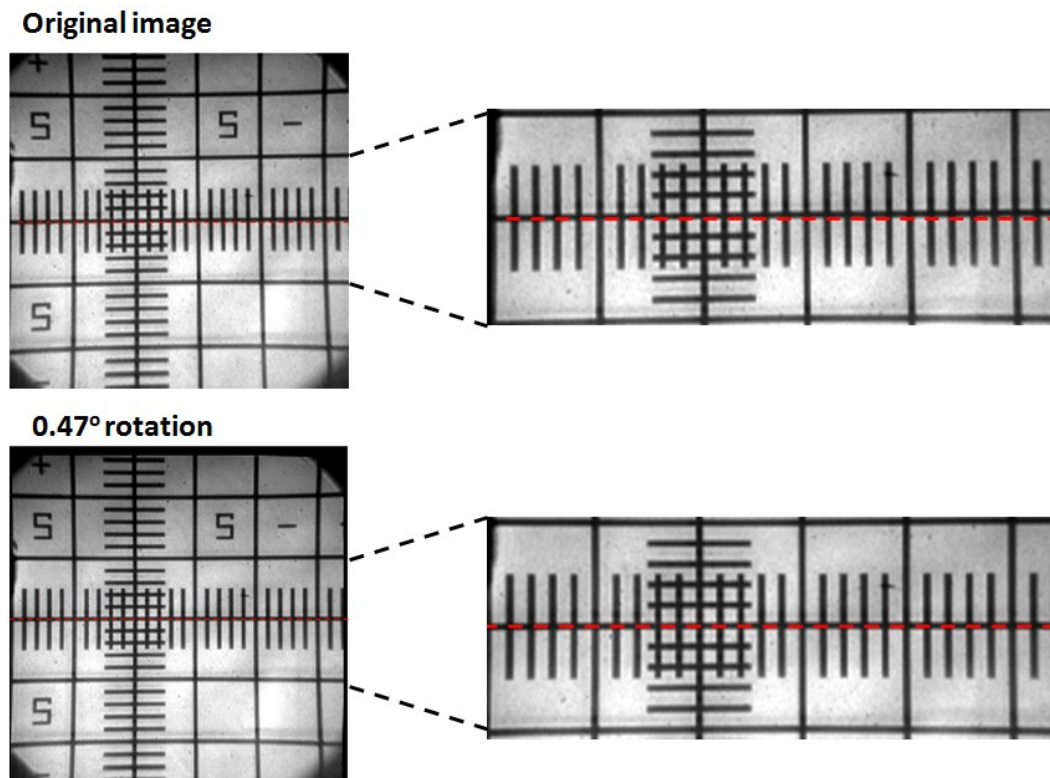


Fig. 2.9. Image alignment through the undistorted centerline.

After the alignment angle has been estimated and used to rotate the image, the lens distortion correction is performed. The distortion correction is based on two facts: (1) the distortion is radially symmetric and affects mainly the regions distant from the center of the image and (2) the lines across the horizontal and vertical axes remain straight. The grid size has to be estimated in order to determine how an undistorted grid image would look like. If the intersection at the center of the image and the nearest four intersections are located, the average grid size can be calculated. This procedure is illustrated in figure 2.10.



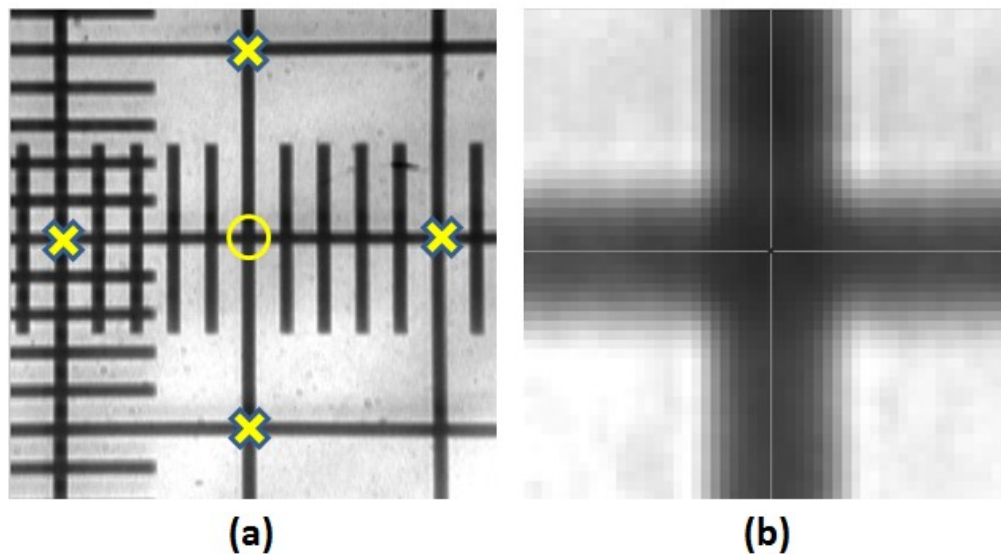


Fig. 2.10. Estimation of the average grid size (a) by location of the four nearest intersection centroids (b) around the center point.

Based on the average grid size calculated in the previous step, a synthetic grid is generated, as shown in figure 2.11(b). This is done by starting at the center of the image and placing evenly spaced intersections in the horizontal and vertical directions. This process does not only allow to visualize how the undistorted grid would look like, but also permits to set reference points for subsequent correction of the distorted image.

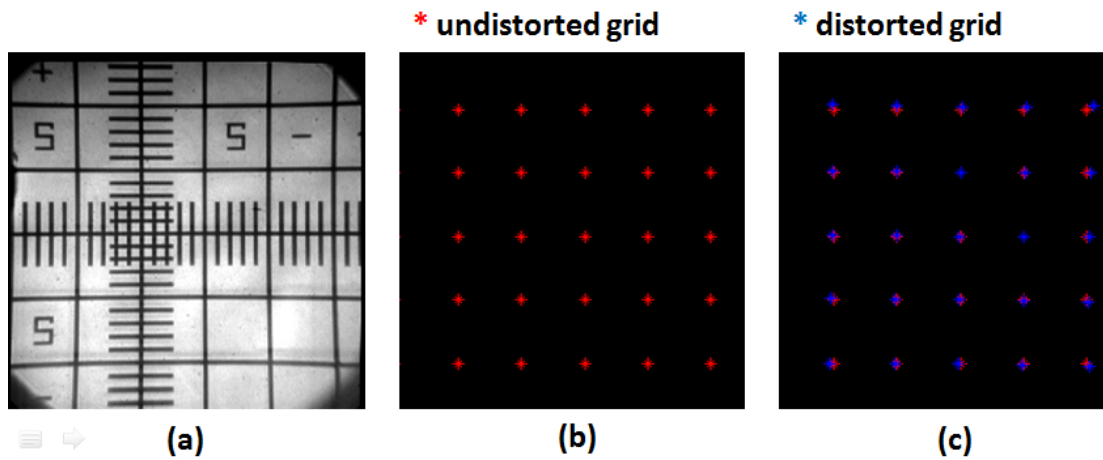


Fig. 2.11. (a) Distorted image, (b) ideal grid synthetically generated by the average grid spacing near the center of the image, and (c) grid intersections in the synthetic grid (red) compared to the real location of the grid intersections (blue).

The grid intersections are located in the distorted image and, at this point, the pairs of coordinates corresponding to the same intersections in the distorted and undistorted grids provide enough information to accomplish a registration of the images. Image registration is the process that compares two images and aligns them to the same field of view by a spatial transformation. This transformation requires mapping intersections in the distorted image to the equivalent pixel positions in the undistorted synthetic grid. Matlab's image processing toolbox contains a series of functions that can perform image registration. Using the intersections' coordinates in the distorted and synthetic grids, the required spatial transformation can be inferred. The use of high-quality lenses resulted in only mild distortions of the images, and consequently only a second or third order polynomial transformation was typically required. This means that polynomial functions of the pixel positions,  $x$  and  $y$ , are automatically determined by Matlab and are used for image mapping. After the transformation, the image results in a homogeneous grid that contains straight lines in the outer regions as seen in figure 2.12.

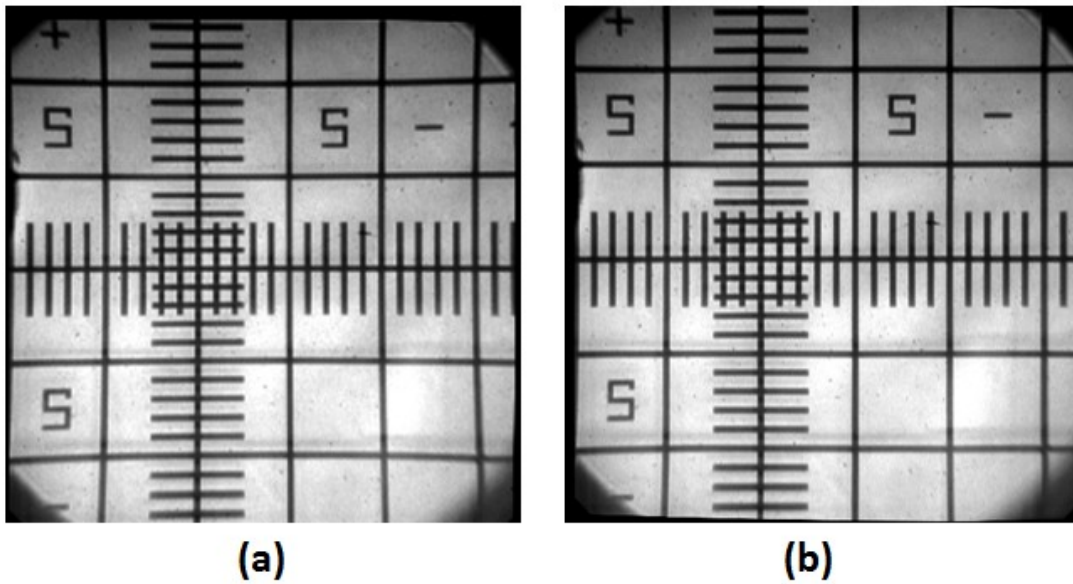


Fig. 2.12. Distorted (a) and corrected (b) dotcard images.

Since the VENOM image pairs are acquired using two different cameras, a correction for a difference in the field of view has to be applied. At this point both images have been independently aligned and corrected for distortions. However there may be discrepancies between both cameras' fields of view and another image registration process is performed. Since both images are now undistorted, only four reference points near the corners of each image are required to correct for translation and scaling.

Figure 2.13 shows two images with different fields of view and zoom levels. The yellow crosses indicate the reference points corresponding to the same intersections in both images, which are used to correct (b) with respect to (a). This procedure is identical to the distortion correction, but requires a much simpler mapping function.

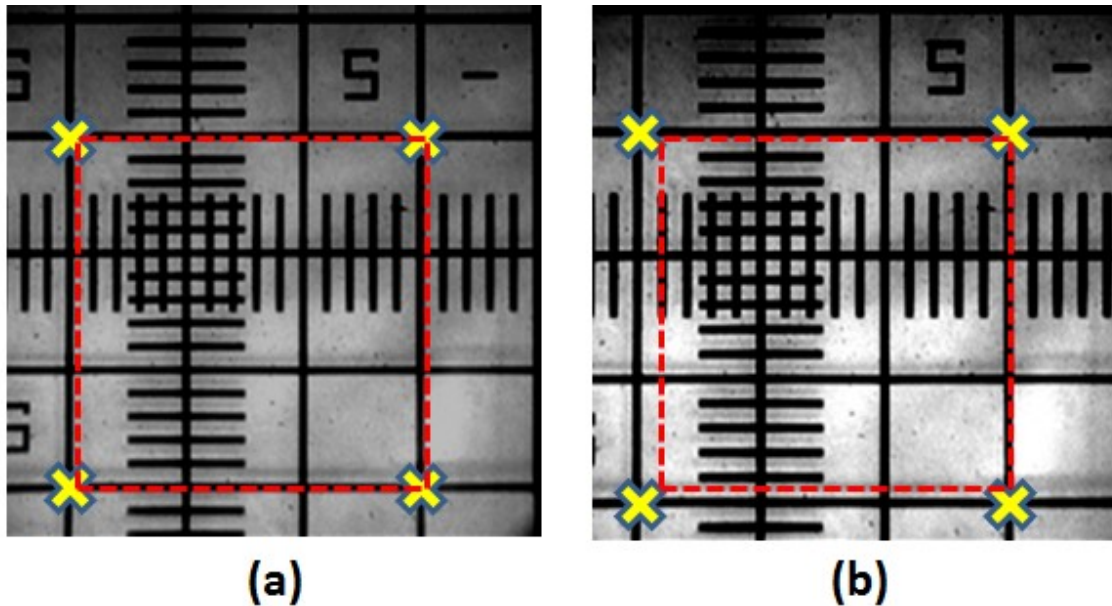


Fig. 2.13. Field of view correction for two cameras. The identical red square in both images illustrate the need for a translation and scaling correction of (b) with respect to (a).

The previous image distortion and field of view correction is independently performed for each camera and subsequently applied to the entire image set acquired with the corresponding camera. After these corrections have been applied, the data set is ready to be processed with the following data analysis method.

### II.3.2 Velocimetry

At this point we assume that two images of the same object obtained with both cameras are identical, given the distortion and field of view correction performed in the pre-processing stage. However, as a safety correction procedure, a multiple-shot average VENOM image is obtained with each camera under stationary conditions, i.e. no flow, with each camera. The use of a multiple-shot average image permits to have clear defined intersections with high signal-to-noise levels. If the cameras are looking at exactly the same object, each intersection should overlap perfectly with its matching intersection in the other image. This means that a zero-velocity map is estimated and used as a discrepancy map to correct the subsequent velocity maps obtained under the

same conditions. A VENOM image is a fluorescence image that shows an intensity modulation pattern that results from high and low NO concentrations generated by photodissociation of  $\text{NO}_2$ . This modulation pattern permits to form grid intersections that are used to visualize and quantify the local flow displacements. The method used to find these intersections starts by extracting the fluorescence local maxima or minima along each row and each column of an image. After this procedure is done, the resulting intersection pattern looks like that shown in figure 2.14 (b). The overlapped grids and intersections extracted from both images look like those shown in figure 2.14 (c) and (d), respectively.

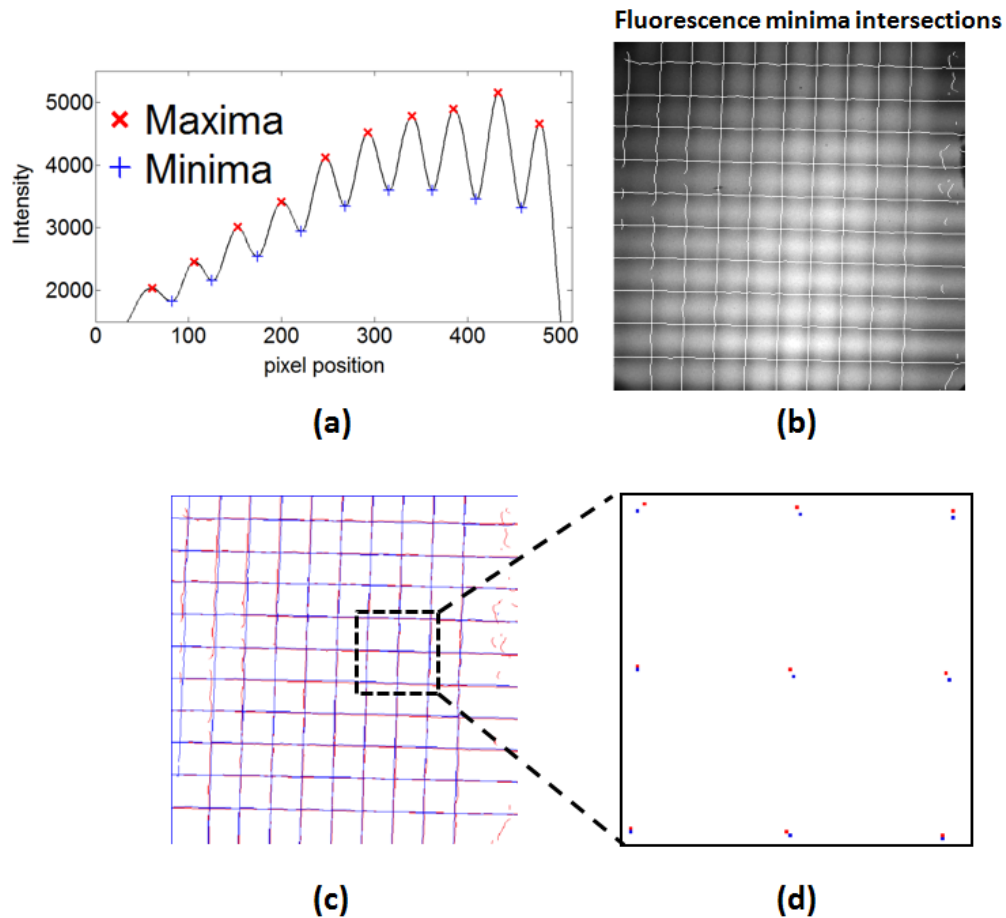


Fig. 2.14. Grid intersection location based on the fluorescence maxima or minima.

Figure 2.14(d) shows that the grid intersection overlap in a zero-velocity field can be imperfect. The imperfect alignment is because the previous distortion and field of view corrections are limited by the finite pixel size or because of an incomplete image de-warping. In order to correct for the difference between the two images, an interrogation area is defined around each intersection and cross-correlated with its counterpart in the second fluorescence image. The 2-D cross-correlation procedure permits a more accurate estimation of the difference in the location of each intersection between the two images, since the comparison is not only based on the absolute intensity maxima of the intersections, but on the entire intensity pattern that shapes the intersection. From the cross-correlation routine at each intersection a new matrix will be generated, the cross-correlation map. This map shows a maximum when the best shape alignment is reached between both original features. The location of the maximum in the cross correlation map indicates the feature displacement  $\Delta x$  and  $\Delta y$ , providing a direct measurement of the two-component local flow displacement in pixels. This procedure is illustrated in figure 2.15.

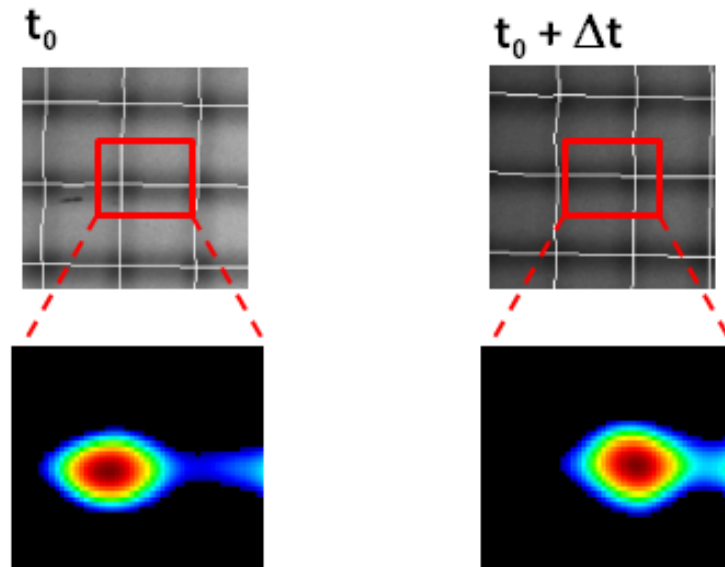


Fig. 2.15. Definition of an interrogation area in an initial (left) and a time-delayed image (right) at each grid intersection.

From the location of the maxima at each intersection cross-correlation map, a discrepancy map between the two cameras is constructed. Using this method, the zero-velocity map based on the fluorescence average images of a static field is estimated and used to correct all the subsequent velocity maps. After completing the previous procedure, a full discrepancy map is constructed and interpolated. An example of a discrepancy map obtained by the previous procedure is shown in figure 2.16.

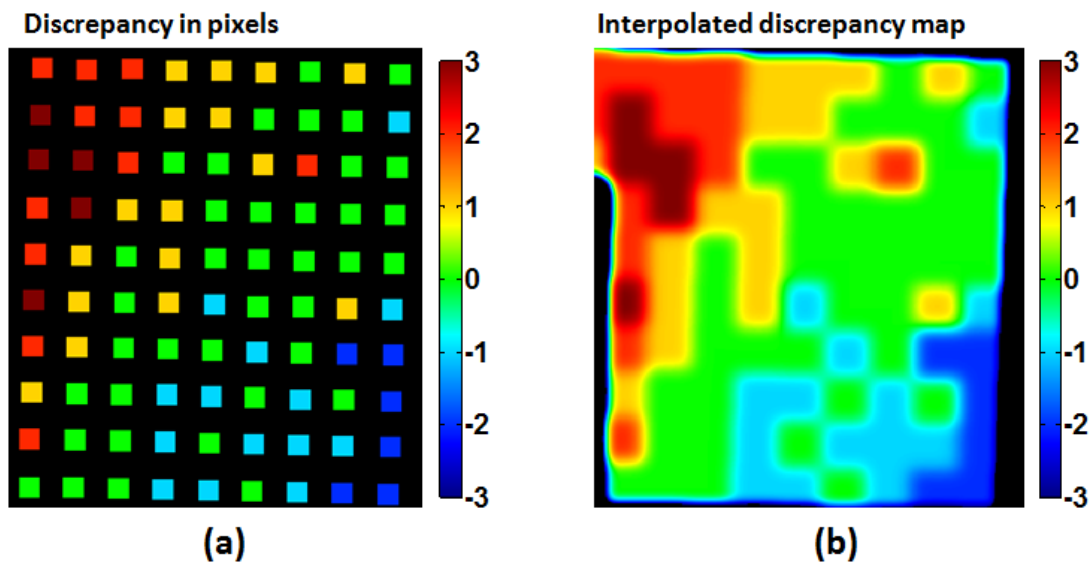


Fig. 2.16. Grid Discrepancy or zero-velocity map.

The accuracy in the estimation of the previous discrepancy map, or zero velocity map, is also limited by the discrete pixel size. Furthermore, the signal-to-noise ratio in the fluorescence images represents a dominant random error source in the instantaneous velocity determination. In order to minimize the effect of these limitations, the flow velocity is calculated based on subpixel fitting of the cross-correlation map, as shown in figure 2.17.

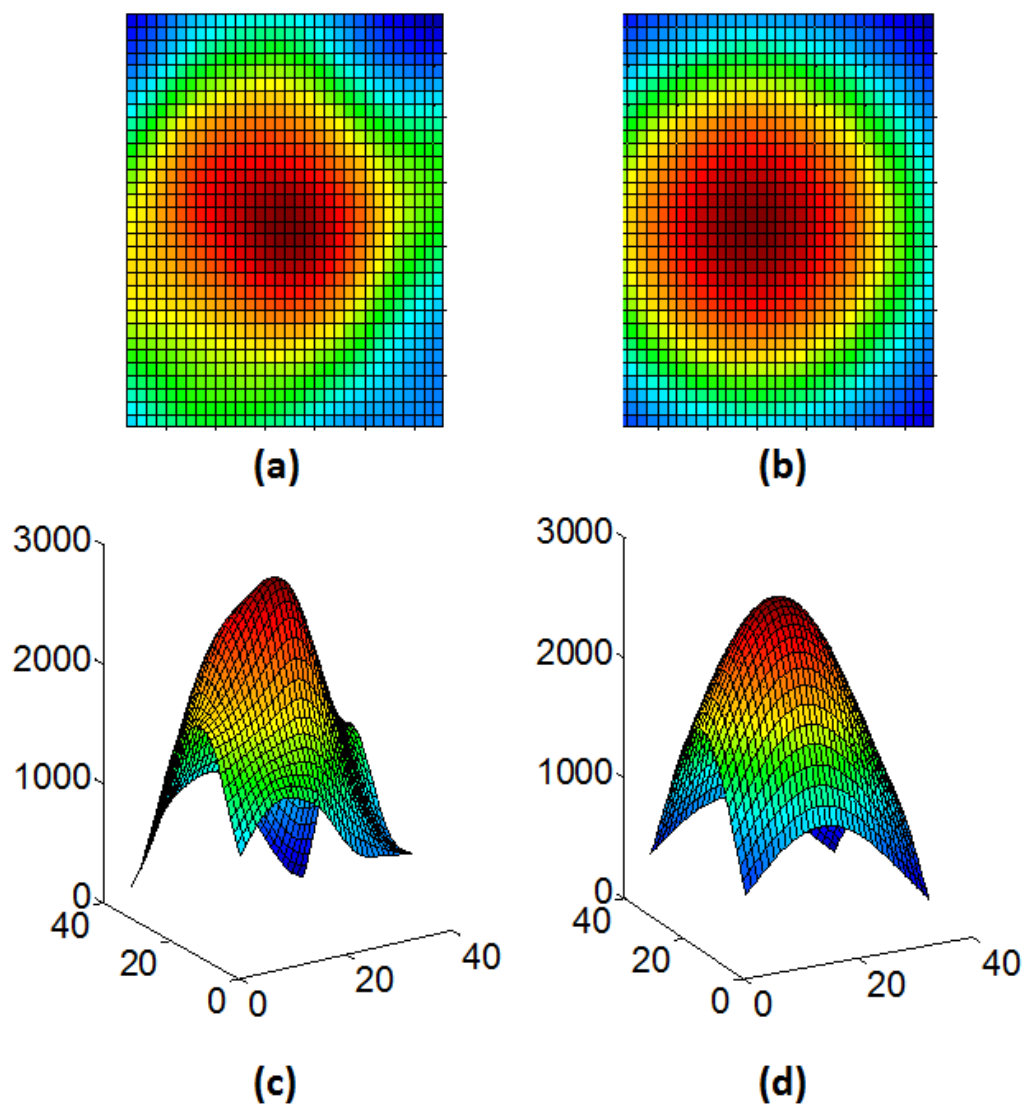


Fig. 2.17. Fitting of the cross-correlation map.

At this point, the estimation of the zero-velocity map has been completed based on the average fluorescence images of the static gas in the cell. The following step is to calculate the velocity map of the flow under study. The analysis of this data starts with an estimation of the velocity map based on an average of all single-shot images taken at each time delay using the exact same procedure used to determine the discrepancy or zero-velocity map. This will not only provide an average velocity map, but also the



average location of the grid intersections which represents essential information for the analysis of the instantaneous velocity fields. After the average location of all intersections is determined, these points can be used to define the location of interrogation areas used in the cross-correlation analysis of the single-shot image pairs. This represents a unique advantage of molecular tagging velocimetry methods compared to PIV, since the intersection location is always the same at time-zero after tagging, and the location after that will only vary closely correlated to the local flow turbulence fluctuations.

Finally, the spatial scale of the experiment is determined using the images of the glass dotcard acquired in the pre-processing stage of the analysis, which in this case had a grid formed by lines separated by 2.54 mm, printed on one of the surfaces. The displacement maps obtained with the previous analysis, shown in figure 2.18(c), is given in units of pixel, and can be converted to a velocity map in m/s by using the conversion factor and dividing by the time delay between the two fluorescence images.

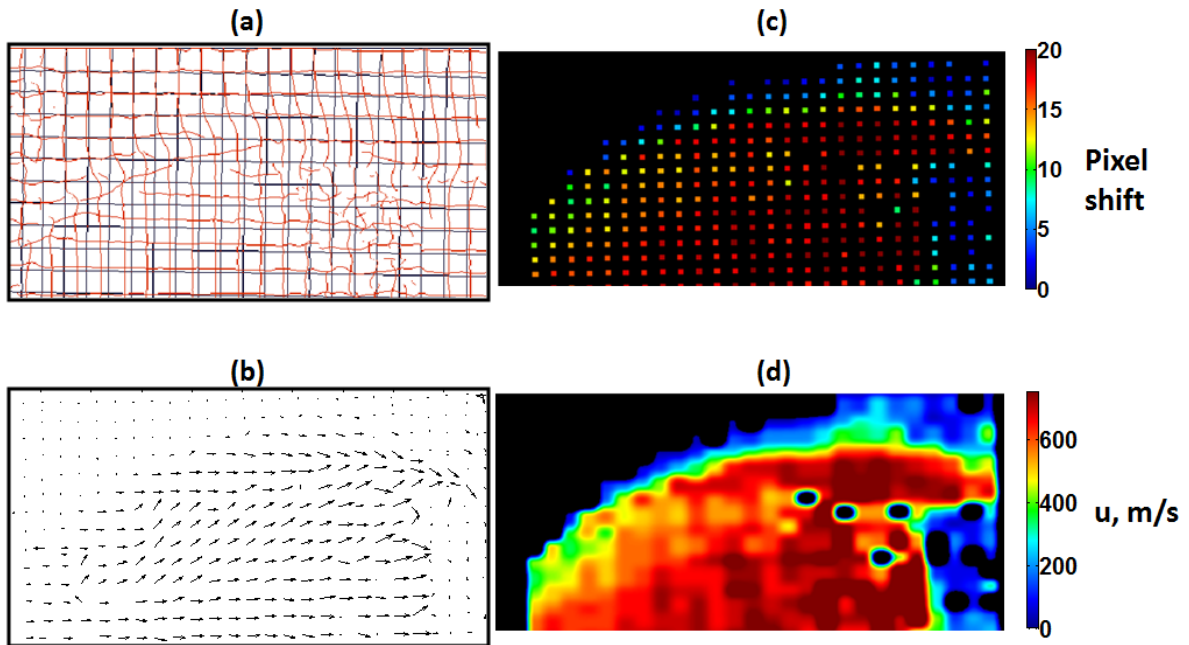


Fig. 2.18. Velocity map calculation from the local cross-correlation maxima location.

One of the primary objectives of this work is to demonstrate the ability of instantaneous velocity and temperature measurements. Although the effect of random error sources is minimized in the averaging process used to determine the mean properties of a flow field, these errors play an important role in the instantaneous VENOM measurements. On the other hand, the presence of a bias in the average measurements does not affect the determination of the overall structure of the flow, since all fluid elements are locally affected by the same bias. The bias in the velocity measurements as well as the magnitude of the random error sources are addressed and estimated in this section.

The possible bias in the velocity measurements can originate from differences in the magnification or shifts in the field of view between the imaging cameras, distortions due to the camera lenses, or the effect of a third velocity component. The effect of all the experimental factors introducing a bias in the measurements can be evaluated, except for the effect of a third velocity component.

As mentioned in the previous section, the grid size was determined at different locations of the image pairs to find distortions after the image correction procedure. It was found that the spatial scale was homogeneous through the entire field of view within 0.5 pixel. The dotcard images were also used to de-warp the images from both cameras to an equivalent field of view accounting for rotation, translation and scaling. However, this error is small, identical for the entire data set, and is completely corrected by the discrepancy map shown previously.

The fluctuations in pressure and temperature in the flow will affect the fluorescence lifetime and hence the effective time measured to calculate the velocity. Bathel et al. have performed an exhaustive investigation of this effect [40], introducing an analysis to evaluate the weighted average of each fluorescence profile as well as a timing correction factor that are particularly relevant for long camera gates and when both images track one single fluorescence event. Since in the present experiments both camera gates are short (typically 50 ns), and are used to capture images from two different fluorescence events, such corrections are not significant, and are not applied.

The dominant random error source in the velocity determination is the signal-to-noise ratio of the fluorescence images. Given that an accurate determination of the intersection location depends on the quality, or cleanliness, of these features, the signal-to-noise is defined in terms of the amplitude of the fluorescence modulation pattern rather than the overall fluorescence signal. This amplitude depends on the size of the mesh used to “write” the photodissociation lines as well as on the quality of the optical system used to capture the images. A test was performed in order to quantify the uncertainty in the velocity measurements at different signal-to-noise levels using the data analysis program. Based on the grid size used in our experiments, sets of 200 single-shot images with varying signal-to-noise-levels were synthetically generated. The experimental signal-to-noise is  $\sim 2$  for the velocity measurements. All synthetic image sets were processed in order to calculate the velocity uncertainty, based on the experimental spatial resolution and time delay, employing the same in-house data analysis code used to process the experimentally obtained images. The calculation was performed for the velocity determination with an experimental spatial resolution of 36 pixel/mm and time delay  $\tau_2 = 1250$  ns. The velocity uncertainties using synthetic images with signal-to-noise of 2 were within 1.6% in the freestream of a Mach 4.6 flow, or about 11 m/s in a 700 m/s flowfield. This uncertainty due to the data analysis code is shown as a function of signal to noise in figure 2.19.

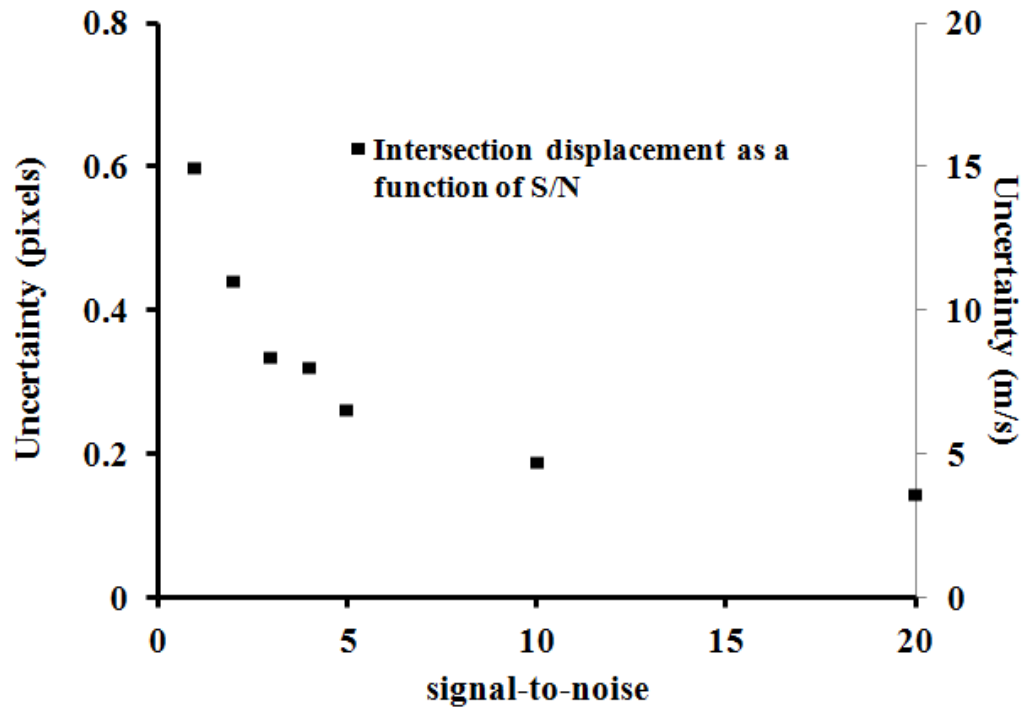


Fig. 2.19. Estimated velocity uncertainty as a function of signal-to-noise resulting from the data analysis program.

The previous calculation represents the ideal velocity uncertainty obtainable from a VENOM experiment. However, the measured random uncertainties in the two-component velocity determinations are larger, and are attributable to a number of factors such as the time jitter in the delay generator, the lasers and the cameras, as well as the effect of the shot-to-shot signal-to-noise fluctuations on the intersection tracking procedure. The estimated uncertainties introduced by the equipment timing jitter are identical in the 1-component and the 2-component velocimetry experiments. The combined effect of the timing factors and the data processing algorithm was experimentally evaluated in the chamber under stationary conditions using a gas mixture of 0.6%  $\text{NO}_2$  in  $\text{N}_2$  maintained at 133 Pa. The measured intersection displacement uncertainty in this case was 1.3 pixel, corresponding to 30 m/s, based on the experimental spatial resolution of 36 pixel/mm and time delay  $\tau_2 = 1250$  ns.

As mentioned above, the 2-D cross correlation analysis of the VENOM data analysis represents an improvement to the simple fluorescence maxima/minima tracking routine employed in the past. Currently, the maxima/minima tracking procedure is only the first step in the cross correlation analysis, since once the maxima/minima are found in the average fluorescence images, interrogation windows are defined to perform the cross-correlation procedure using the entire fluorescence intersection patterns. The cross-correlation procedure not only permits a more accurate estimation of the flow displacements by comparing the full intensity pattern and not only the location of the absolute maxima/minima, but also permits the analysis of single-shot image pairs that are characterized by low signal-to-noise levels. The analysis of noisy image pairs using the simple maxima/minima tracking results in higher uncertainties since the local maxima/minima position fluctuates due to the image noise. It has to be noted that the automated procedure used to locate the maxima/minima can locate multiple maxima/minima points in a single intersection. When this occurs, the measurement at this location has to be rejected to avoid confusion of the algorithm that could result in a wrong velocity measurement. A test aimed to compare the performance of the maxima/minima tracking procedure compared to the cross-correlation method was performed, and consisted of the analysis of the 200 synthetic single-shot images using both methods, for the typical signal-to-noise levels of 2 in a zero-velocity field. The results are summarized in figure 2.20.

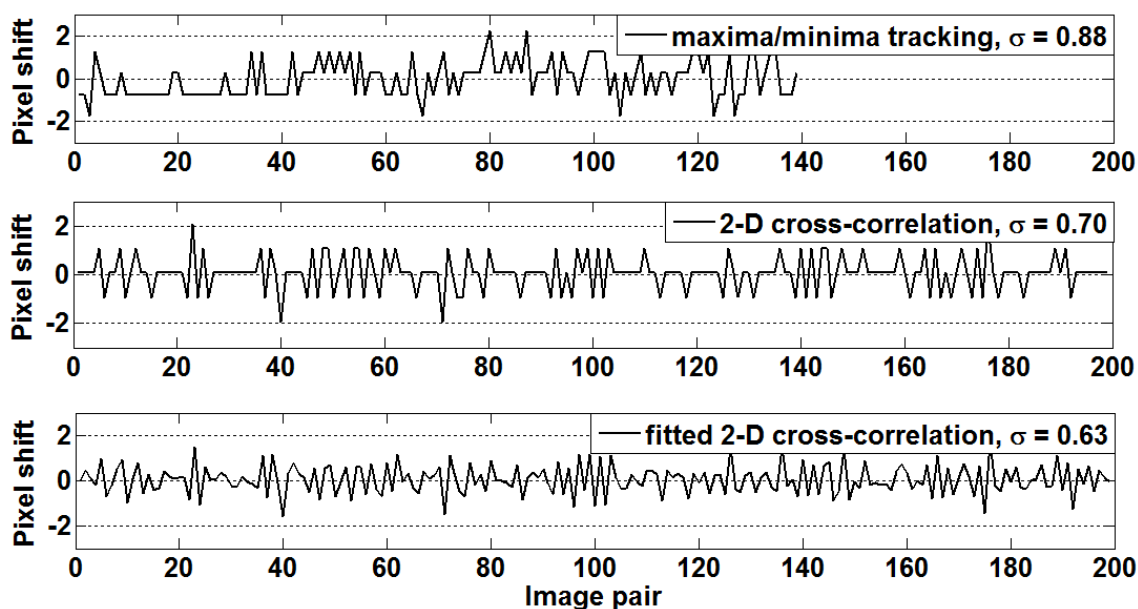


Fig. 2.20. Instantaneous determination of local velocity in a synthetically generated VENOM data set using maxima/minima tracking (top) 2-D cross-correlation method (middle), and fitted 2-D cross-correlation method (bottom).

Figure 2.20 shows the intersection displacements in units of pixels for the maxima/minima tracking method, the 2-D cross-correlation method, and the fitted 2-D cross-correlation method. It is noticeable that the fitted cross-correlation does not only provide a more accurate location of the intersection displacement, but it also results in the lowest data rejection due to low signal-to-noise levels. Using the maxima/minima tracking in the synthetically generated data set consisting of 200 single-shot pairs led to a rejection of 30% of the intersections, while the entire data set could be successfully processed by cross-correlation method.

### II.3.3 Thermometry

The temperature data analysis follows after completion of the velocimetry analysis detailed in the previous section. This implies that all images are aligned, corrected for distortions, and images acquired using different cameras have been corrected for field of view discrepancies. The temperature analysis is based on fluorescence intensity and, ideally, a homogeneous temperature field should result in

homogeneous fluorescence images when probing a specific rotational state. However, there are inherent inhomogeneities associated to each "read" laser sheet. These defects translate into an inhomogeneous fluorescence image as shown in figure 2.21(a). If a VENOM image is acquired using the same conditions as (a), but removing the aluminum mesh, the laser sheet intensity pattern can be obtained (b), normalized, and used to correct the original image to produce an intensity-corrected image (c). This process is repeated for all images contained in the data set and is independently performed for each camera associated to a probe laser.

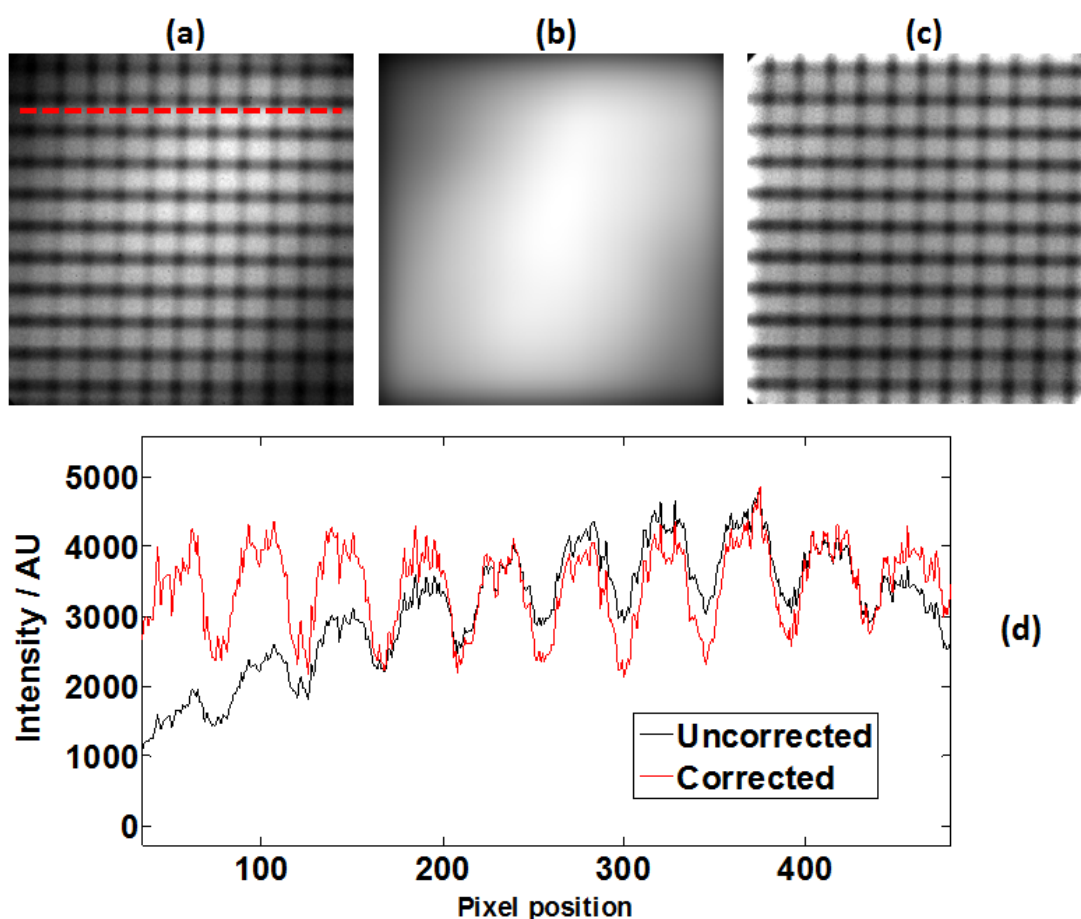


Fig. 2.21. Image correction for inhomogeneities in the probe lasers. Original fluorescence image (a), correction image (b), and corrected image (c). The fluorescence intensity profiles across the corrected and uncorrected images along a row are shown (d).

Prior to the acquisition of a data set, a single temperature calibration constant  $C_{12}$  is determined based on a fluorescence ratio measured in the chamber under static conditions at room temperature, using the same pressure and gas composition used in the experiment.  $C_{12}$  is evaluated averaging a large area within the camera field of view, with the same camera gain levels as those used to acquire the experimental images. As stated in Chapter 1 the fluorescence ratio, which also is a function pressure that affects the quenching levels across the field of view, would be expected to interfere when two different rotational levels in the emitting state are involved. However, rotational-level independency of collisional quenching of both the  $A^2\Sigma^+$  ( $v'=0$ ) and the  $A^2\Sigma^+$  ( $v'=1$ ) states has been observed. Determining a single constant  $C_{12}$  based on intensity-corrected images suffices to estimate the temperature of the entire field of view.

After the calibration constant has been determined under stationary conditions, the sequential flow field imaging performed to obtain the velocity measurements using the VENOM technique provides enough information to de-warp the second time-delayed fluorescence image. This is important since estimating fluorescence intensity ratios that correspond to the same flow elements will decrease the occurrence of grid artifacts in the temperature map. By employing the information contained in the velocity vectors, a second spatial transformation or de-warping of the time-delayed image proportional to the local flow velocity is performed. The effect of such transformation can be observed in figure 2.22(d). The difference with respect to the temperature map estimated without de-warping can be observed in (b). As a consequence of the image de-warping, which is proportional to the local flow velocity, the temperature measurement is averaged over the local spatial displacements of the flow, determined by the chosen time delay  $\tau_2$ .



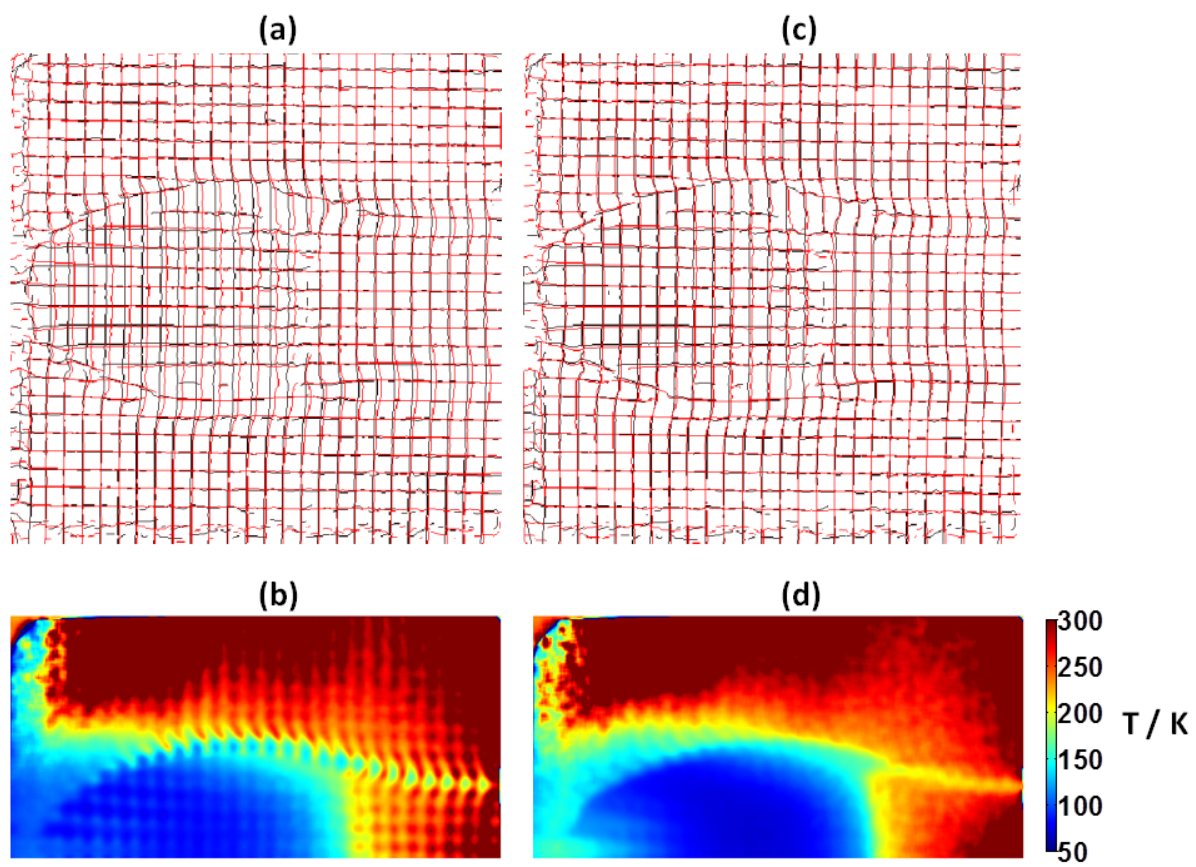


Fig. 2.22. Temperature map obtained without de-warping (b) and after de-warping the time-delayed image (d).

## CHAPTER III

### REPETITIVELY PULSED HYPERSONIC TEST CELL - A TOOL FOR DIAGNOSTIC DEVELOPMENT

#### **III.1 Introduction**

The complexity and limited understanding of hypersonic flows necessitate of experimentation as the primary source of knowledge. Ground testing is the main research tool in the hypersonic flow regime due to the excessive costs involved in hypersonic flight testing, which makes it virtually unavailable. Current experimental studies in existing hypersonic facilities are characterized by the high operation expense of long duration wind tunnels and the short duty cycles associated with impulse or blow-down wind tunnel facilities. These limitations make existing facilities far from ideal to develop, test, and tune new diagnostic techniques. Considering these limitations, a compact repetitively pulsed hypersonic flow apparatus was designed, constructed, and characterized as a tool for advanced laser diagnostics development. The reduction in mass flow rates, and therefore pumping speed requirements, make a pulsed nozzle system more compact and ideal for applications where toxic chemicals used either as reactants or flow tracers in continuous flows can be both a safety issue and prohibitively expensive. In addition, such systems can be operated during long periods in contrast to shorter run blow down and impulse facilities. The design of the Repetitively Pulsed Hypersonic Test Cell, or RPHT cell (previously named PHAT or Pulsed Hypersonic Ablation Test cell), is based on the work of Atkinson and Smith [7,8]. The primary application of this facility is to serve as a laser diagnostic development tool. However, as shown below, the flow quality has proved to be sufficient for future quantitative measurements in a variety of hypersonics experiments, including, but not limited to, boundary layer studies and low temperature ablation.

This facility is particularly well suited for development of optical diagnostics that utilize pulsed lasers such as planar laser induced fluorescence (PLIF) and molecular

tagging velocimetry (MTV). Specifically, when the pulsed operation of the facility is synchronized to the pulsed laser systems, the operation is essentially continuous. A key advantage of this model of operation is that the mass flow through the facility is reduced by several orders of magnitude as compared to a continuous flow facility.

The design of the RPHT cell has been intended for cold flow generation, providing simulation of Mach number and Reynolds number. The Mach number is defined as the ratio of the flow velocity to the local speed of sound. The Reynolds number expresses the ratio of the inertial forces to viscous forces in the flow. These two quantities, also called similarity parameters, are widely used in the Aerodynamics field since they define the aerodynamic forces experienced by a vehicle, and are important at the moment of scaling an Aerodynamics problem, thus the term *similarity parameters*. The Mach number expresses the degree of compressibility of the flow while the Reynolds number is defined by the viscosity, or "stickiness", of the gas. For a diagnostic technique to be useful in a larger hypersonic facility, the same flow conditions have to be replicated in the development and testing stage.

### **III.2 Design of the Repetitively Pulsed Hypersonic Test Cell**

The RPHT cell is housed with the National Aerothermochemistry Laboratory located at Texas A&M University. This apparatus is based on other relatively recent cold-flow supersonic pulsed facilities [7,8]. It was designed in Solidworks, and consists of two main elements: the nozzle assembly and the test chamber. The principal factors considered to design the RPHT cell were (1) the main chamber had to provide ample optical access to permit flexibility in the alignment of multiple laser beams and enough optical access for imaging cameras, (2) allow a variety of flow conditions through easily exchangeable converging-diverging nozzles designed to produce flows of different Mach numbers, and (3) a pumping system with enough capacity to keep up with the pulsed gas flowing into the chamber.

### III.2.1 The Nozzle Assembly

The nozzle assembly is shown in Figure 3.1 and consists of an aluminum feeding block fitted with up to 4 solenoid pulse valves and a screw-in aluminum axisymmetric converging-diverging nozzle.

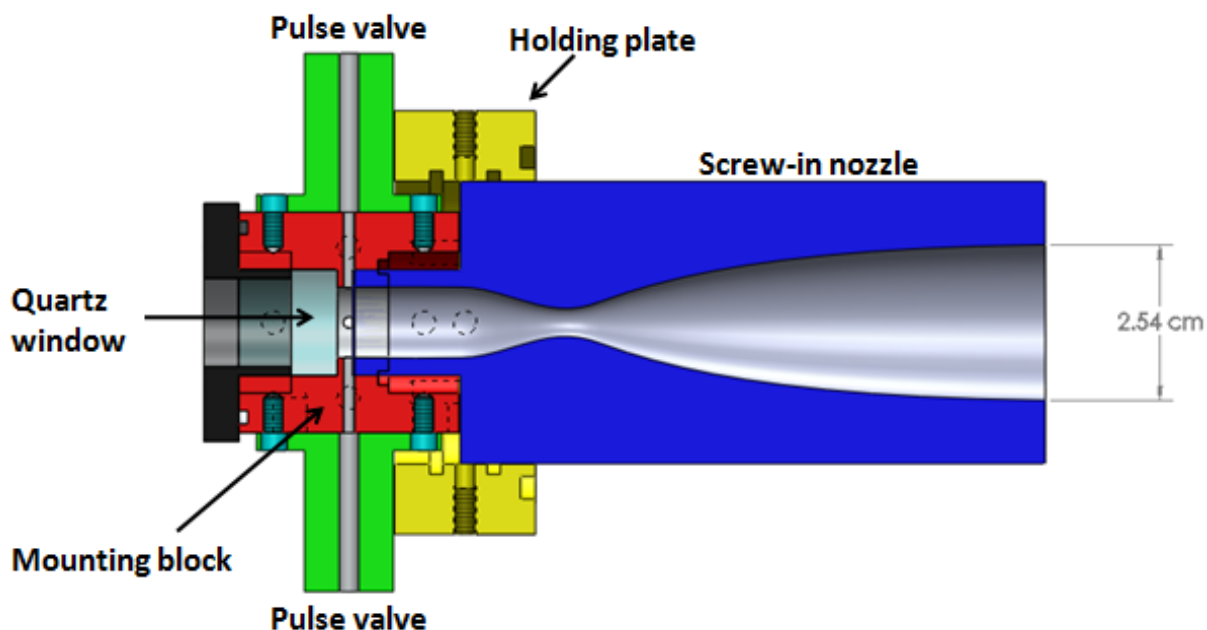


Fig. 3.1. Nozzle assembly fitted with the Mach 4.6 axisymmetric nozzle.

The gas mixtures are supplied radially to a settling chamber volume located in the center of the feeding block using four Parker General Valve Series 9 pulsed valves. According to manufacturer specifications, the pulsed valves can operate at temperatures up to 400 K, pressures up to 85 atm, and repetition rates up to 120.0 Hz. The settling chamber region was intentionally designed small,  $2.25 \text{ cm}^3$ , since continuum stable flow generated by a nozzle requires a balance between inflow and outflow, and thus constant pressure.

The back of the feeding block has optical access via a 25.4 mm diameter quartz window to permit laser photolysis of precursors, if necessary. The pulsed valves are

manufactured with an exit orifice diameter of 1 mm. In order to achieve the mass flow required to run higher Mach number flows, each pulse valve was modified to have a 3 mm diameter exit orifice that was sealed with a Viton® gasket as a substitute to the standard Teflon® poppet (Figure 3.2). We observed no change in valve performance other than increase in the mass flow as a result of this modification.

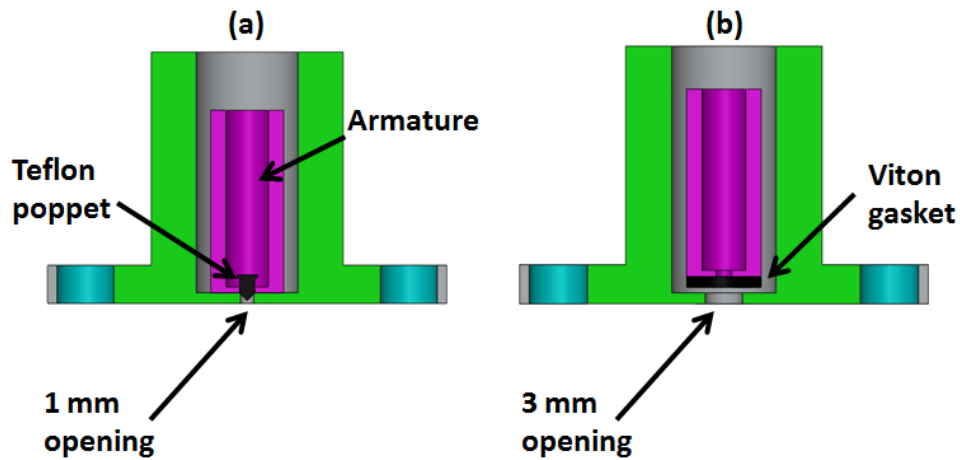


Fig. 3.2. Pulsed valve before modification. Before (a) and after opening orifice to 3 mm (b).

The pulse valves pulse length is adjustable, and is controlled by a custom built valve driver circuit [41], which provides externally triggered 1.0 ms – 20.0 ms long pulses with  $\sim 250$   $\mu$ sec opening times.

Four axisymmetric aluminum nozzles, Mach 6.2, 4.6, 4.0, and 3.0 were designed. The converging-diverging design was chosen in order to generate homogeneous flows, with constant exit pressure, density, temperature and velocity. This is achieved by a short initial narrowing, or converging, region where the gas experiences a subsonic acceleration to maintain a constant mass flow rate. The converging region is followed by a minimum cross-section region, the throat, where the gas becomes sonic if there is enough mass flow through the nozzle. Finally, the flow is accelerated at supersonic speeds by a controlled expansion of the gas in a diverging region that defines the final

properties of the flow. The gas within the nozzle is subject to a gradual compression and a subsequent gradual expansion that is thermodynamically reversible, and consequently, the flow can be described by isentropic flow equations [42]:

$$\frac{T}{T_0} = \left(1 + \frac{\gamma - 1}{2} M^2\right)^{-1} \quad (\text{Eq. 3.1})$$

$$\frac{p}{p_0} = \left(1 + \frac{\gamma - 1}{2} M^2\right)^{\frac{-\gamma}{\gamma - 1}} \quad (\text{Eq. 3.2})$$

$$\frac{\rho}{\rho_0} = \left(1 + \frac{\gamma - 1}{2} M^2\right)^{\frac{-1}{\gamma - 1}} \quad (\text{Eq. 3.3})$$

$$\frac{A}{A^*} = \left[\frac{(\gamma + 1)}{2}\right]^{\frac{-(\gamma + 1)}{2(\gamma - 1)}} \left[\frac{1 + \frac{(\gamma - 1)}{2} M^2}{M}\right]^{\frac{(\gamma + 1)}{2(\gamma - 1)}} \quad (\text{Eq. 3.4})$$

where:

T = temperature

p = pressure

$\rho$  = density

A = nozzle cross sectional area

M = Mach number

$\gamma$  = ratio of specific heat capacities,  $C_p/C_v$

A\* is the nozzle cross sectional area at the throat and the subscript 0 denotes the input conditions at the stagnation region.

For a nozzle designed to generate a flow at a nominal Mach number, these equations express that the ratio of the pressure, temperature, and density between the gas at the nozzle exit and the input gas are exclusive function of the Mach number. Based on this fact, the exit conditions of a flow in a properly designed and constructed nozzle can

be well-determined if the input conditions are known. Also, a nozzle can be designed to generate any desired exit flow conditions. The calculated ratios of exit flow conditions to input gas conditions for a given Mach number nozzle using the isentropic flow equations are shown in Figure 3.3.

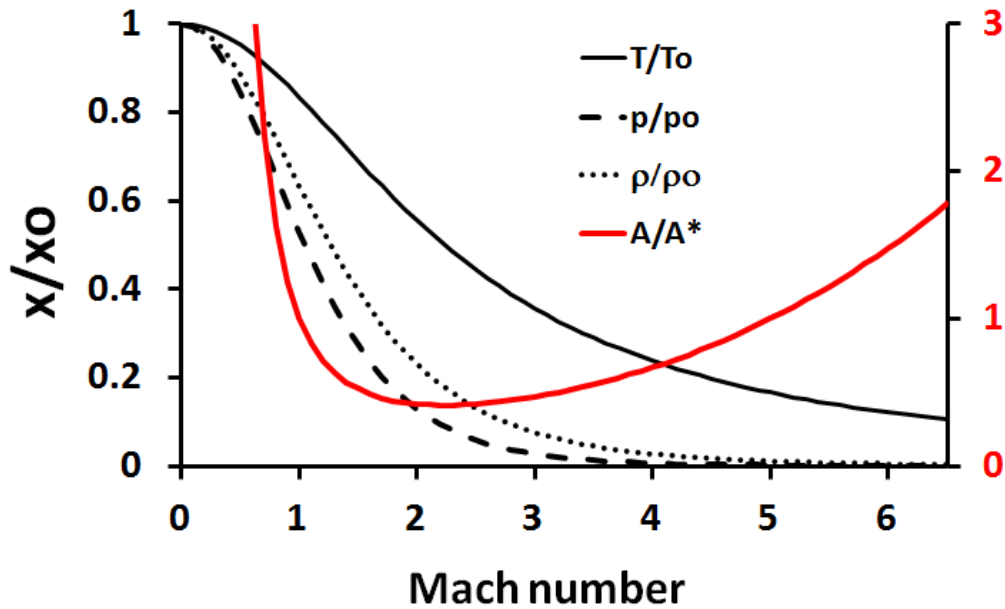


Fig. 3.3. Ratio of exit flow conditions to input gas conditions,  $x/x_0$ , as a function of Mach number calculated with the isentropic flow equations (for air, using  $\gamma = 1.4$ ).

The isentropic flow equations describe the ideal gas behavior within the nozzle and are a good guidance to estimate the nozzle behavior. However, there are a number of phenomena that affect the actual performance of the nozzle, mainly factors involving the presence of a wall, such as viscosity and heat transfer effects that have a critical role in the diverging region of the nozzle. In order to account for wall effects, the nozzles were designed using the Method of Characteristics (MOC) [7]. The design was performed classically using the MOC with an ad-hoc Mach number increase to account for boundary layer displacement effects as estimated using simple integral methods assuming turbulent flow. Figure 3.4 shows the nozzle contours obtained from such

calculations for the Mach 3, 4, 4.6, and 6.2 nozzles. These contours were employed to generate Solidworks models that were built from aluminum blocks using Computer Numerical Control (CNC) machining.

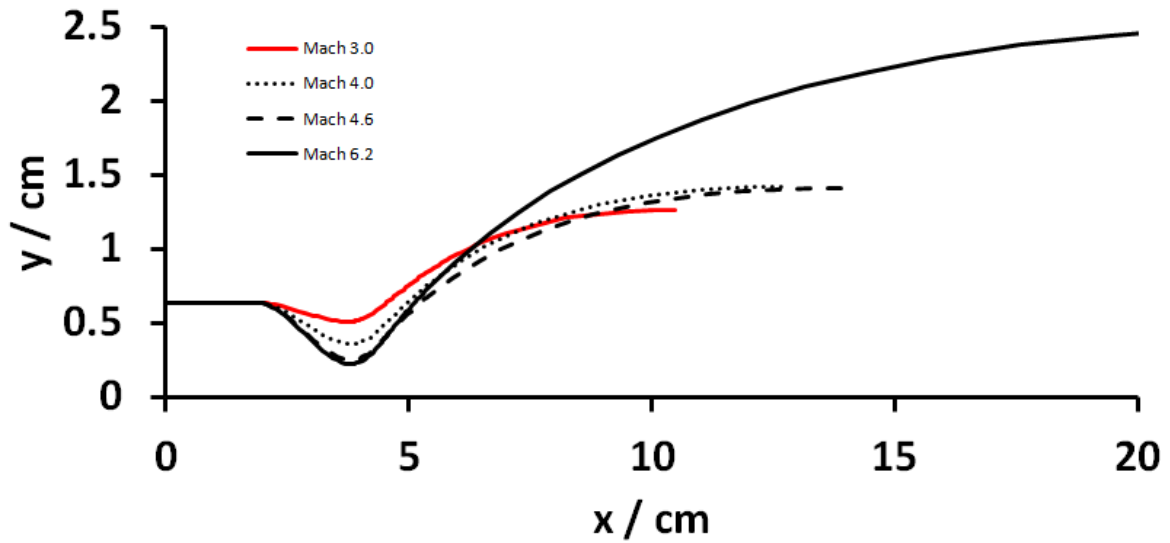


Fig. 3.4. Nozzle contours calculated by the Method of Characteristics.

The original target Mach numbers for the built nozzles were 3.0, 4.0, 5.0, and 7.0. The nozzle inviscid shape was designed for uniform flow using the method of characteristics. However, viscous boundary layers result in reduced effective area ratios, which then result in reduced Mach numbers. This effect is quantified by the displacement thickness:

$$\delta^* = \int_0^1 \left[ \left( 1 - \frac{\rho U}{\rho_e U_e} \right) d(r/\delta) \right] \quad (\text{Eq. 3.5})$$

where  $\rho_e$  and  $U_e$  are the density and velocity in the freestream,  $r$  is the normal distance from the nozzle surface moving toward the center,  $\delta^*$  corresponds to the effective reduction in the exit nozzle radius. The area reduction can be severe under the expected



operating conditions because (1) the static pressures are low ( $\sim 1$  Torr) and (2) the nozzle wall temperature ( $\sim 300$  K) is high compared to the gaseous freestream, as predicted by the  $T/T_0$  curve in figure 3.3. The low pressures result in low density, which then translates into low Reynolds numbers, and the boundary layer thickness goes with the Reynolds number to the  $-n$  power, where  $n = 1/2$  for laminar flow and  $\sim 1/5$  for turbulent flow. The large temperature ratio across the boundary layer results in a low-density ratio, hence  $\rho/\rho_e \ll 1$ , and as the above equation indicates,  $\delta^* \sim \delta$ .

In summary, for high-speed, hot-wall, low-density flows, the nozzle performance is strongly influenced by viscous effects as observed in this study. As comparison, for low-speed cold-wall flows,  $\delta^*$  is usually a small fraction of  $\delta$  (in the order of the  $1/10$  for incompressible flow) and hence this effect is often secondary.

### **III.2.2 The Test Chamber**

#### **A. Original Design**

The original design of the RHPT cell is shown in figure 3.5. The RPHT cell was designed to maximize optical access in order to accommodate a variety of laser diagnostic experiments. The test chamber was constructed from welded 12.5 cm thick aluminum plates and has dimensions 25 cm x 25 cm x 63.5 cm for a total volume of approximately 40 L. The square design of the chamber was preferred over the cylindrical design due to the difficulty in the machining of the window slots that this shape would implicate.

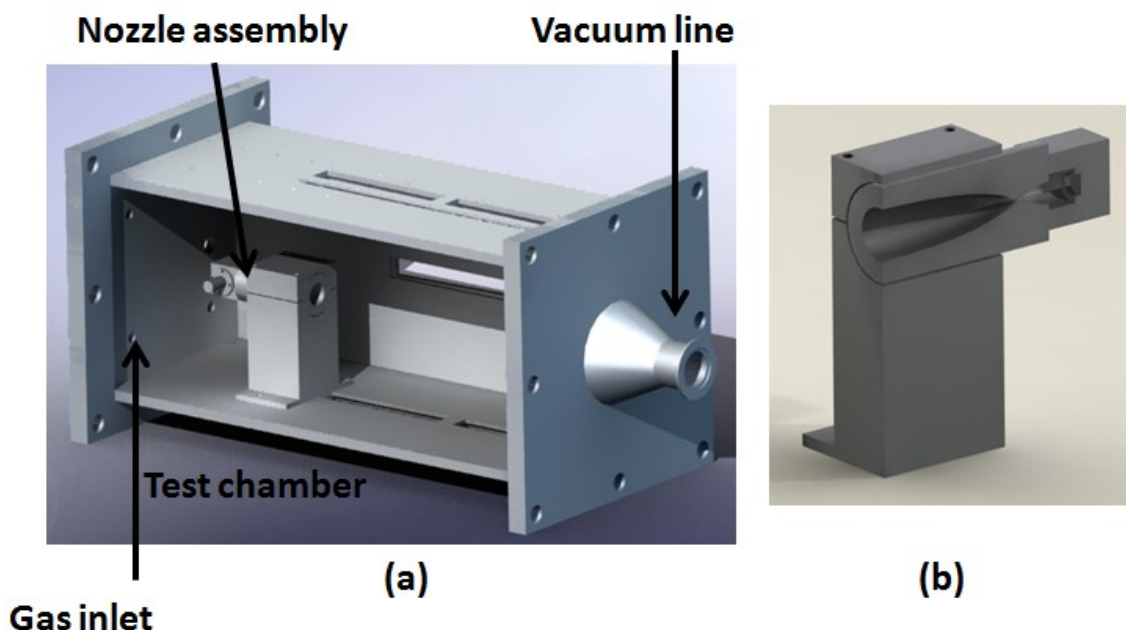


Fig. 3.5. RPHT Cell original design. The nozzle assembly is placed inside of the main chamber (a). Cross-sectional view of the nozzle assembly mounted in the mounting block (b).

The primary optical access was originally provided by two 17.8 cm x 2.54 cm fused silica windows centered on each of the top and bottom faces (for multiple laser beams), and on each side of the cell (for imaging cameras). The nozzle assembly was held inside of the main chamber by a mounting block that could optionally be mounted on a stepper motor - driven rail. As seen in Figure 3.5, the test chamber is coupled to a vacuum line via a liquid nitrogen trap where seeded chemicals used as diagnostic tracers or tracer precursors can be condensed to avoid damage to the pump assembly and minimize toxic exhaust. The test gas was fed into the pulsed valves by 1/4" tubing running through Ultra-Torr vacuum fittings in the gas inlet ports located behind the nozzle assembly, as seen in figure 3.5.

The feeding block was originally designed in three different versions to accommodate four, six, and up to eight pulsed valves (figure 3.6). The four pulsed valve version was chosen because, as explained below, this is the maximum number of pulsed

valves allowed by the current system's pumping capacity. However, an upgrade in the pumping system would allow the use of any of the alternative designs.

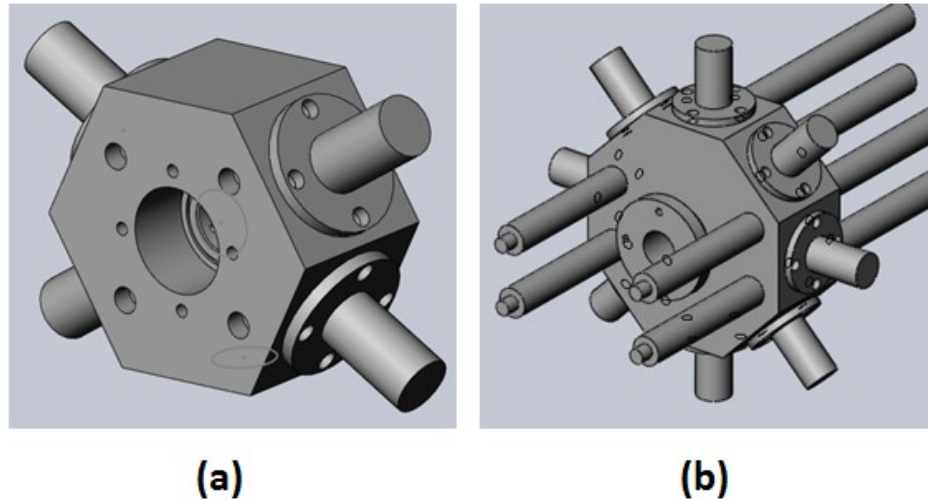


Fig. 3.6. Feeding block designs for the accommodation of six (a) and eight (b) pulsed valves.

Test models can be mounted using an array of  $\frac{1}{4}$ -20 tapped holes located on the chamber floor and ceiling. The entire chamber is mounted to a rail system on an optical table that allows the laser mirrors, the sheeting optics and the ICCD cameras to remain fixed, and aligned, while the chamber is moved horizontally in order to probe the flow at different downstream locations.

### **B. Later Modifications**

The original design of the PHAT cell presented some difficulties for an efficient operation. It was learned that constant access to the inside of the chamber was needed in order to place or adjust test models, pressure transducers and the aluminum grids used in the velocimetry experiments. In addition, sometimes the pulsed valves require of minor adjustments to maintain proper operation. Although this adjustments are simple and quick to do, at this stage the only physical access to the main chamber internal components was accomplished by removing the cover held by eight bolts located at each

end of the main chamber. These problems were solved by two later modifications. The first modification consisted of making easily dismountable side faces, as seen in figure 3.7. One of the window slots on each dismountable side wall was enlarged so that each side has now a 17.8 cm x 2.54 cm and a 17.8.0 cm x 5.08 cm fused silica windows centered on each side face of the cell for imaging cameras.

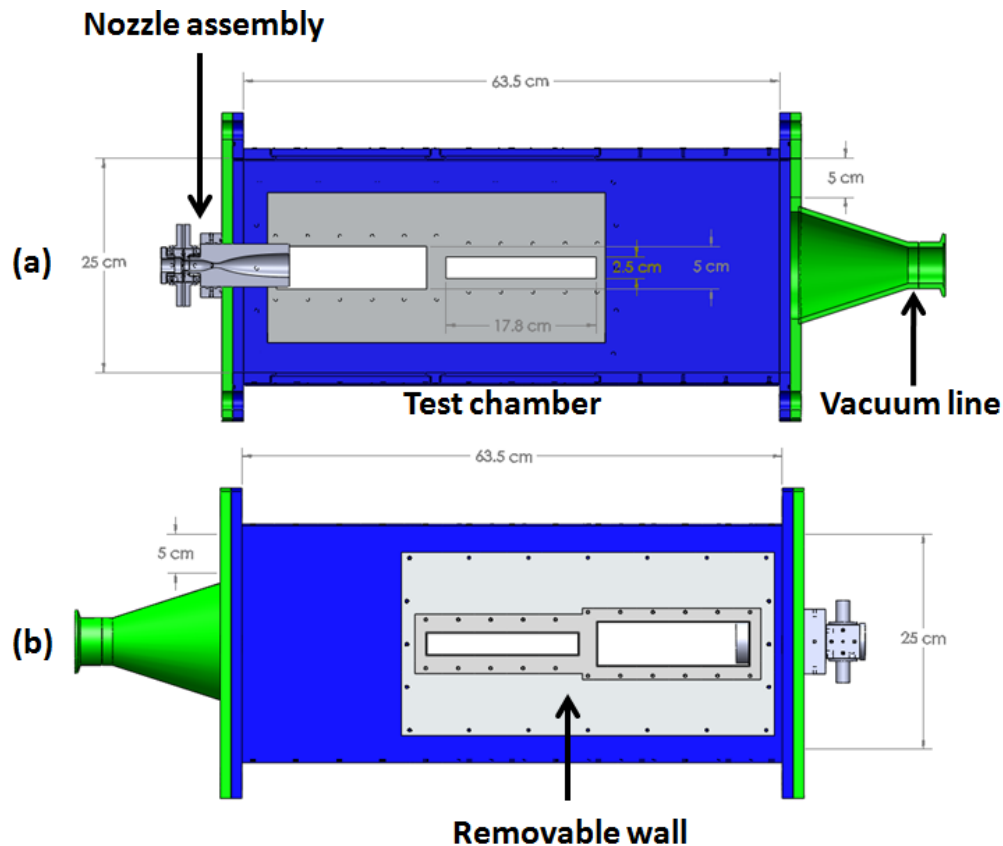


Fig. 3.7. Cross-sectional view of the repetitively pulsed hypersonic test chamber after modifications (a) and view of the removable walls with the quartz window holders (b).

The quartz window thickness was chosen based on a stress analysis calculation done for a simply supported rectangular window [43], based on the largest window in the test chamber (17.8 cm x 5.08 cm). Assuming a tensile strength of 6500 psi, considering an external pressure of 14.7 psi and the internal pressure a total vacuum, a

rectangular quartz window designed with a factor of safety of 10 should have a minimum thickness of 6.5 mm. For convenience, windows with a standard thickness of 3/8" were purchased. The full characteristics of the windows used in the RPHT cell main chamber are shown in Table 3.1.

Table 3.1. Specifications of the windows used in the PHAT cell.

<b>Material</b>	UV fused silica
<b>Thickness</b>	9.53 mm
<b>Tolerance in each dimension</b>	$\pm 0.15$ mm
<b>Clear aperture</b>	90 %
<b>Polishing</b>	
Flatness	1 lambda
Surface quality	60/40
<b>Parallelism</b>	3 arc minute

The second modification consisted in eliminating the mounting block to hold the nozzle assembly inside the chamber. The nozzle assembly is currently mounted on the external end of the chamber using a removable aluminum plate as shown in 3.7. The necessary minor adjustment of the pulsed valves can now be performed during operation. Figure 3.8 shows photographs of the modified RPHT cell, including the removable side walls, the external feeding block, and the rail system.

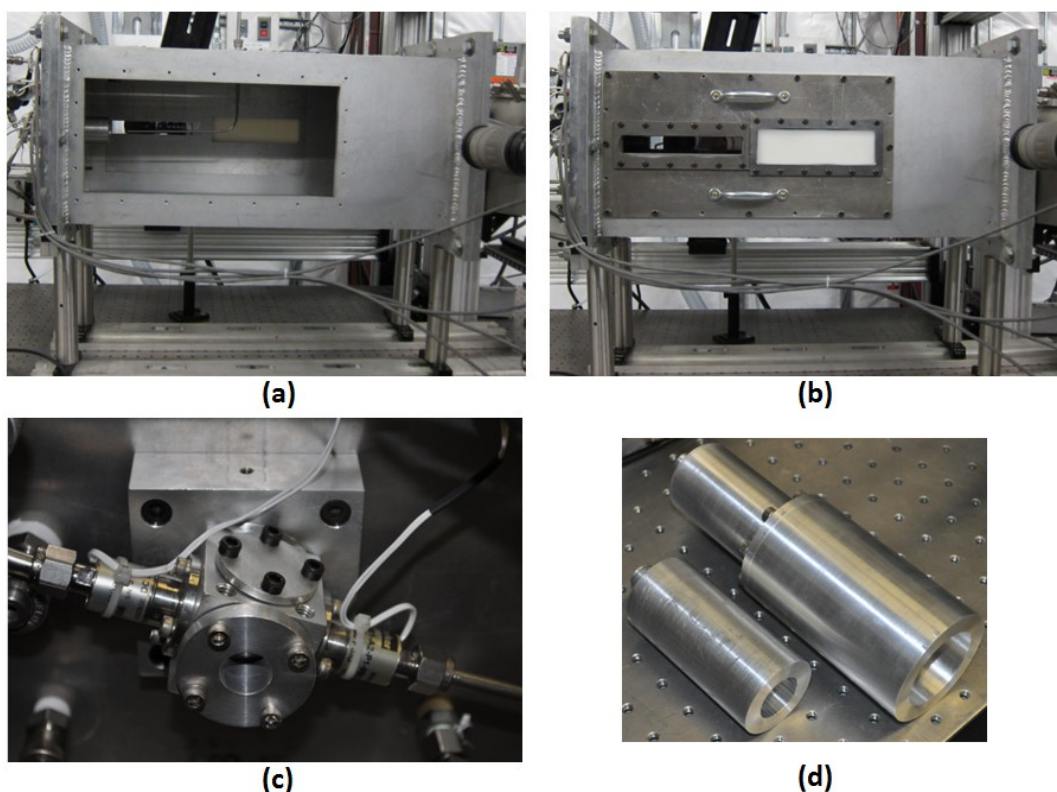


Fig. 3.8. Photographs of the modified RPHT cell without (a) and with (b) the dismountable side face. Close up of the feeding block fitted with two pulsed valves (c). Mach 4.6 and Mach 6.2 nozzles (d).

### III.3 Operational Details

The main chamber is evacuated using a pump assembly that consists of a Leybold E250 rotary pump and a roots blower that provides a combined pumping speed of  $70 \text{ l s}^{-1}$ . The pump assembly is located outside of the laboratory and is connected to the RPHT cell through 20 m of 7.62 cm i.d. pipe and 4 m of a 5.08 cm i.d. flexible hose, resulting in an effective pumping speed of  $48.3 \text{ l s}^{-1}$ . In order to maintain a pressure of 1 Torr inside the chamber, the maximum gas throughput into the chamber cannot exceed  $48.31 \text{ Torr-ls}^{-1}$ . Flow conductance calculations were performed for the use of the modified pulsed valves with 3 mm diameter orifices feeding the nozzles, assuming molecular flow due to the thin wall of the pulse valves' orifices. From equation 3.2, the pressure ratios required to run the Mach 4.6 and Mach 6.2 nozzles are 328 and 1933,

respectively. If these pressures are used to calculate the gas flow into the RPHT cell, using the maximum gas feeding capacity, i.e. four pulsed valves, the results are those plotted in Figure 3.9 as a function of pulsed valve pulse length. Since the gas consumption for the Mach 6.2 nozzle is expected to be larger than for any of the other lower Mach number nozzles, the calculations were performed for repetition rates of 0.5 Hz for this high Mach number nozzle. The calculation for the Mach 4.6 nozzle was performed with for a pulse repetition rate of 1 Hz.

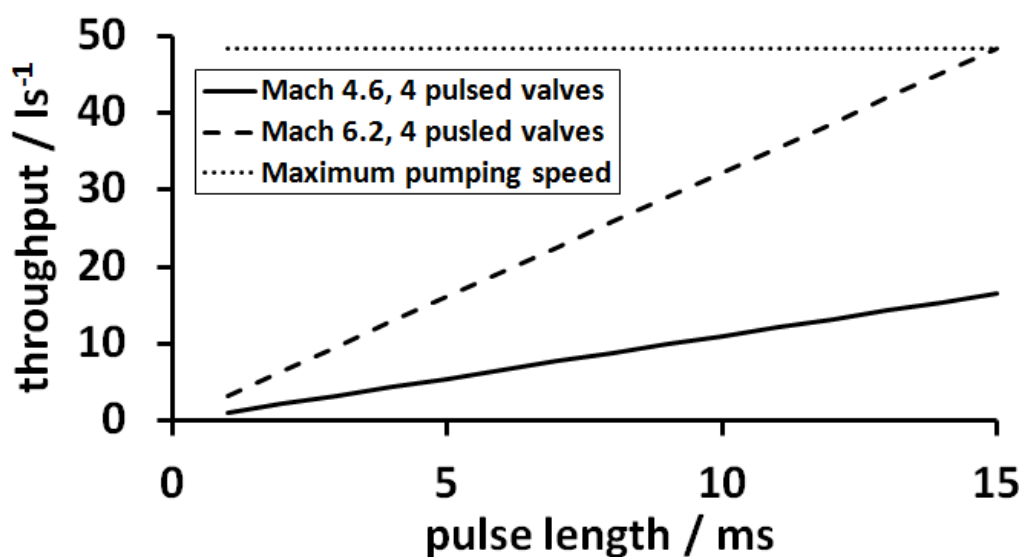


Fig. 3.9. Gas throughput into the RPHT cell using 4 pulsed valves. The maximum capacity of the pumping system is shown for comparison.

Figure 3.9 shows that the Mach 4.6 nozzle can be operated using four pulsed valves and pulse lengths well above 15 ms. On the other hand, the operation of the Mach 6.2 nozzle has to be limited to pulse lengths below this value. The calculations were performed to estimate the limitations and operational conditions of the RPHT cell using the two highest Mach number nozzles since they were expected to require the highest gas loads. These calculations did not take into account the pressure drop through the pulsed valve itself, and did not consider the finite thickness of the pulse valve orifices.

The real limitations of the RPHT cell required to be experimentally determined through a detailed performance study. The performance of the apparatus and the resulting flow uniformity were thoroughly characterized using a combination of NO PLIF flow imaging, pressure, temperature and velocity measurements. These results are presented in the following section.

The pressure inside the chamber is continuously monitored using a calibrated pressure transducer (MKS Series 902). Under static, i.e. no flow, conditions the pressure in the chamber is typically  $\sim 0.2$  Torr. During operation, a needle valve connected to the chamber allows tuned pressure matching between the gas exiting the nozzle and the chamber static gas.

As mentioned above, the pulse times are restricted to a few milliseconds at repetition rates of 0.5 and 1 Hz, allowing proper operation with the currently available pumping capacity. The pulsed flow is easily synchronized with the laser systems and ICCD cameras using a BNC 575-8C digital delay/pulse generator and a frequency divider. The entire nozzle assembly can be heated up to 400.0 K in order to avoid test gas liquefaction during expansion at high Mach numbers.

### **III.4 Characterization of the RPHT Cell**

The challenge of pulsed Laval nozzle systems is ensuring that the flows are stable during a single gas pulse and that the individual gas pulses are reproducible. Confirmation of both issues requires diagnostics for flow characterization. The operation of the pulsed flow was initially examined through NO PLIF imaging. There is another flow visualization technique widely used in gaseous flows, the schlieren technique, based on light deflection by the refractive index gradients existing in the flow. This technique, in a relatively easy to implement configuration, can provide useful qualitative information about the distribution of the density field and the presence of shocks. However, schlieren photographs were not attempted because the expected flow densities, in the order of  $0.01 \text{ kg/m}^3$ , are at the very low bound of conventional schlieren sensitivity [44], and because of the small-scale and short duration of the flow. NO PLIF



imaging was used to examine the complete temporal behavior of the flow pulses. Furthermore, NO PLIF techniques were used to obtain detailed temperature and velocity (MTV) measurements. Finally, point-wise time-resolved pressure measurements were provided by miniature fast-response pressure sensors. While the time-resolved pressure measurements allow a precise measurement of both the fluctuations within a single pulse and shot-to-shot stability in the flow behavior, the NO PLIF/MTV measurement of average velocity and temperature maps provide supporting evidence of a spatially uniform flow. This is important since the spatial and temporal uniformity are key parameters to define the applicability of these flows in future studies.

#### III.4.1 Nitric Oxide PLIF Imaging

PLIF imaging techniques are sensitive enough to reveal important flow features, such as weak shocks. The time behavior of the pulsed flow generated in the RPHT cell was explored by flowing nitrogen seeded with 1% NO, and running 12 ms length pulses at 1 Hz. The 226 nm beam from a dye laser system was passed through a lens system to form a 20 mm wide sheet approximately 150  $\mu\text{m}$  in thickness. PLIF images were obtained probing the  $A^2\Sigma^+ (v' = 0) \leftarrow X^2\Pi (v'' = 0)$  band of NO on the  $R_1 + Q_{21}(8.5)$  transition. Probing this transition allows to obtain contrast between the warm background gas and shear layer growth and the cold core flow in the center. In this way the presence of shocks can be easily observed when the exit flow pressure is not matched to the chamber background pressure. This is the case at the beginning and end of each pulse. At the end the pulse valve has closed and the residual gas is being evacuated from the nozzle. This is evident in the structure of the time-dependent impact pressure measurements shown in figure 3.10(c). The following PLIF images (figure 3.10) captured 2'' downstream of the Mach 4.6 nozzle exit show a non-pressure matched flow at the beginning of the pulse (a), a fully developed flow (b), and a clear diamond shock structure at the end of the gas pulse (c).

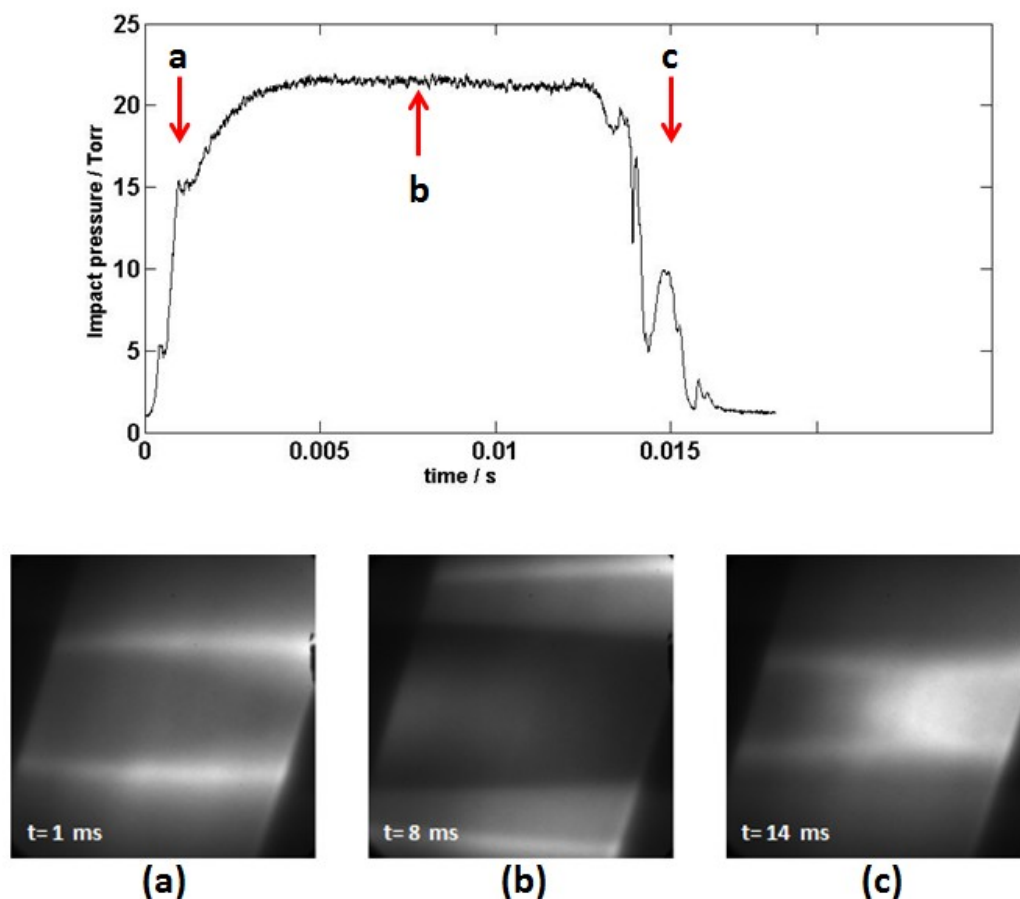


Fig. 3.10. NO PLIF image sequence of a 12 ms Mach 4.6 flow pulse corresponding to the beginning of the pulse (a), to the fully established flow (b), and to the end of the pulse (c).

During the fully developed flow stage there is a core region in the center surrounded by shear layer growth which begins to be significant after 2 or 3 nozzle diameters downstream. This is illustrated by a composite NO PLIF image obtained by imaging the flow at different regions downstream of the nozzle, shown in figure 3.11.

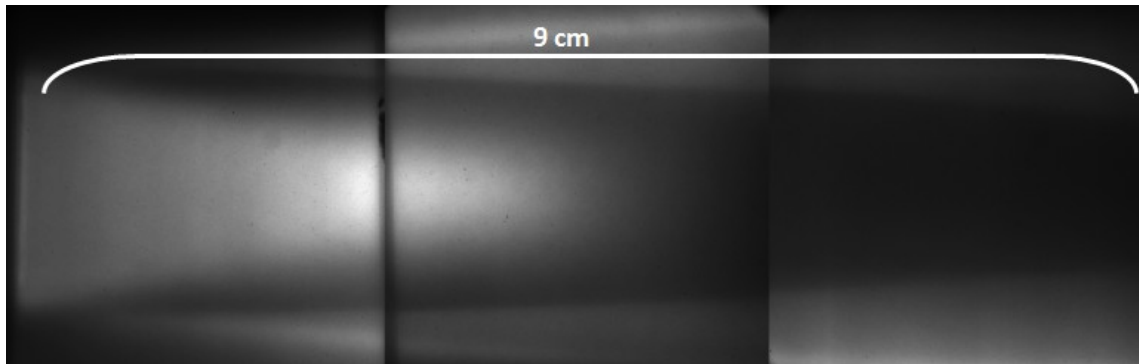


Fig. 3.11. Composite NO PLIF during the fully established flow stage showing the shear layer growth. Flow is from left to right.

### III.4.2 Temporal Characterization: Fast Pressure Measurements

Miniature fast-response pressure sensors permitted measurements of the freestream pressure and Mach number. The location of the pressure sensors is shown in figure 3.12. In the settling chamber upstream of the nozzle throat, Endevco model 8540-15 and 8540-100 absolute piezoresistive pressure sensors were used. These sensors have diaphragm-resonance frequencies of 140 and 350 kHz and full-scale pressures of 15 and 100 psia, respectively. The sensing diaphragms are flush-mounted to the tip of the sensor and covered with a screen, leaving a small dead-air volume of under  $0.005 \text{ cm}^3$ , maximizing transient response. Downstream of the nozzle exit, a Kulite XCEL-100-5A sensor was flush-mounted into the tip of a pitot tube. This sensor has a resonant frequency of 150 kHz and a 5 psia full-scale pressure. The overall outer diameter of the assembled pitot tube was 0.343 cm.

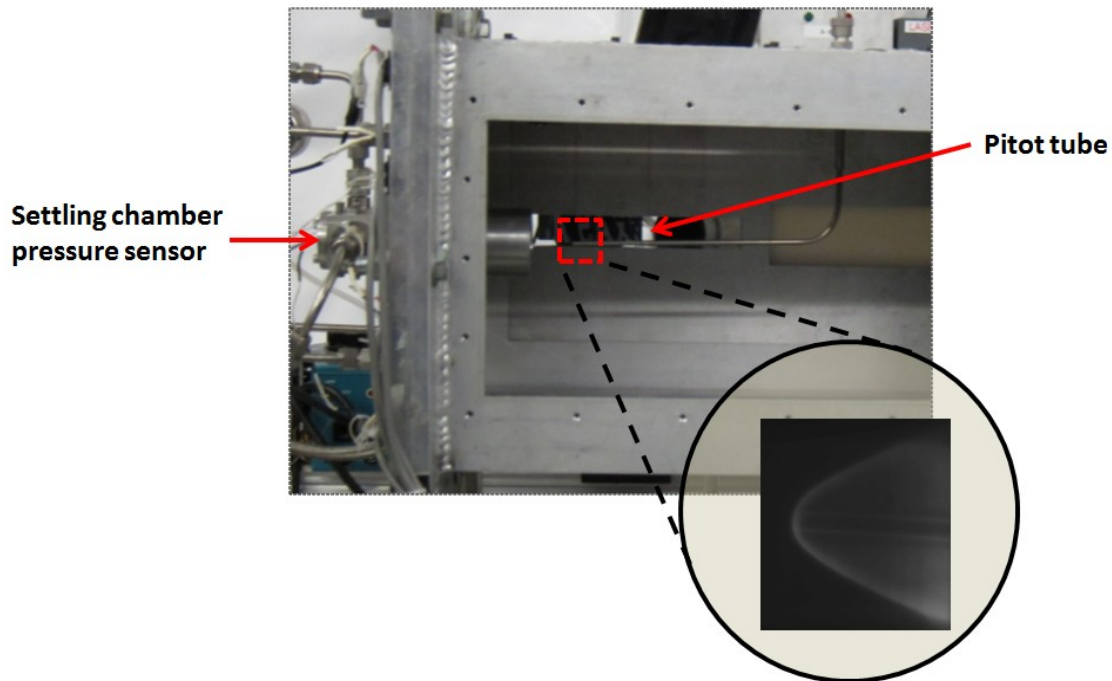


Fig. 3.12. Photograph indicating the location of the pressure sensors. Zoom-in region shows the formation of a bow shock in front of the Pitot using NO PLIF imaging.

An Endevco Model 136 signal conditioner supplied a steady 10V DC excitation voltage to both sensors and amplified their millivolt-level output to a 10V full-scale signal. The amplification circuitry in the Model 136 had a 200 kHz bandwidth (-3 dB). The output of the signal conditioner was sampled at 500 kHz using two fully-independent channels on a 16-bit data acquisition board. The data were then digitally low-pass filtered at 100 kHz to remove the non-physical high-frequency content near the sensors' resonant frequencies. These transducers were statically calibrated immediately prior to the measurements against an MKS Baratron 631C capacitance manometer. They are known to have an excellent linear response, and therefore a simultaneous calibration of all transducers was performed between 1 and 100 Torr to determine their sensitivities and zero-offsets. Figure 3.13 shows a calibration plot for the Endevco 8540-100 and the Kulite XCEL-100-5A pressure sensors.

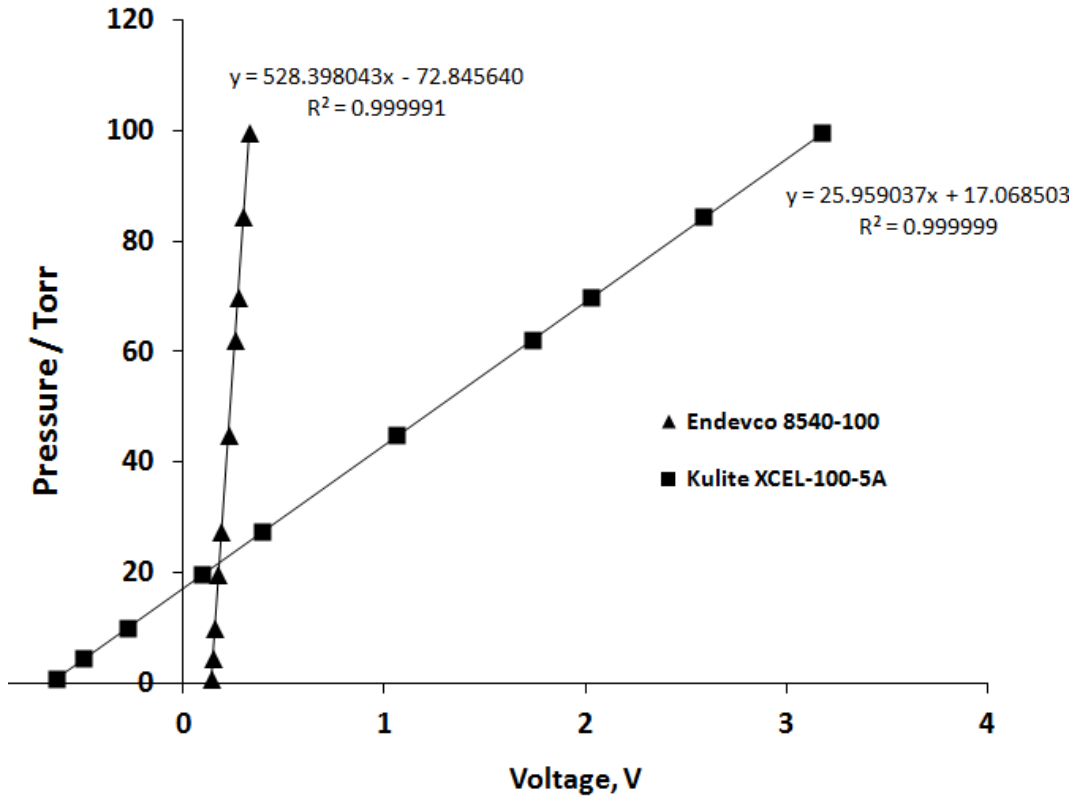


Fig. 3.13. Pressure sensors' calibration to find sensitivity and zero-offsets.

According to equation 3.2, The Mach number of the flow can be easily calculated from the pressure ratio between the settling chamber pressure and the nozzle exit pressure,  $p_0/p$ . However, as shown in figure 3.12, the presence of the Pitot tube generates a shock in the flow, and as a consequence, the Pitot tube measures the total pressure behind the shock wave  $p_2$ . The ratio between the total pressure measured by the Pitot tube behind the shock wave and the settling chamber pressure,  $p_2/p_0$ , can be expressed as a function of the flow's Mach number:

$$\frac{p_2}{p_0} = \left[ \frac{(\gamma + 1)M^2}{(\gamma - 1)M^2 + 2} \right]^{\frac{\gamma}{\gamma - 1}} \left[ \frac{(\gamma + 1)}{2\gamma M^2 - (\gamma - 1)} \right]^{\frac{1}{\gamma - 1}} \quad (\text{Eq. 3.6})$$

The Mach number time histories along the nozzle centerline can be determined using this equation. The time-resolved measurements performed to examine the pressure fluctuations in the flow require a real time estimation of the Mach number. As mentioned above, the data sampling frequency was 500 kHz, and since equation 3.6 cannot be explicitly solved for Mach number, the times required to reach a solution cannot match the sampling frequency. For this reason, a polynomial curve fit, 6th order in  $Pr = p_2/p_0$ , was used for a much faster inverse solution for Mach number. It was observed that the Mach number error resulting from the use of this method was very sensitive to the Mach number range used for the 6th order polynomial fit. Figure 3.14 illustrates this effect, showing that the error decreases as the Mach number range included in the fit gets shorter.

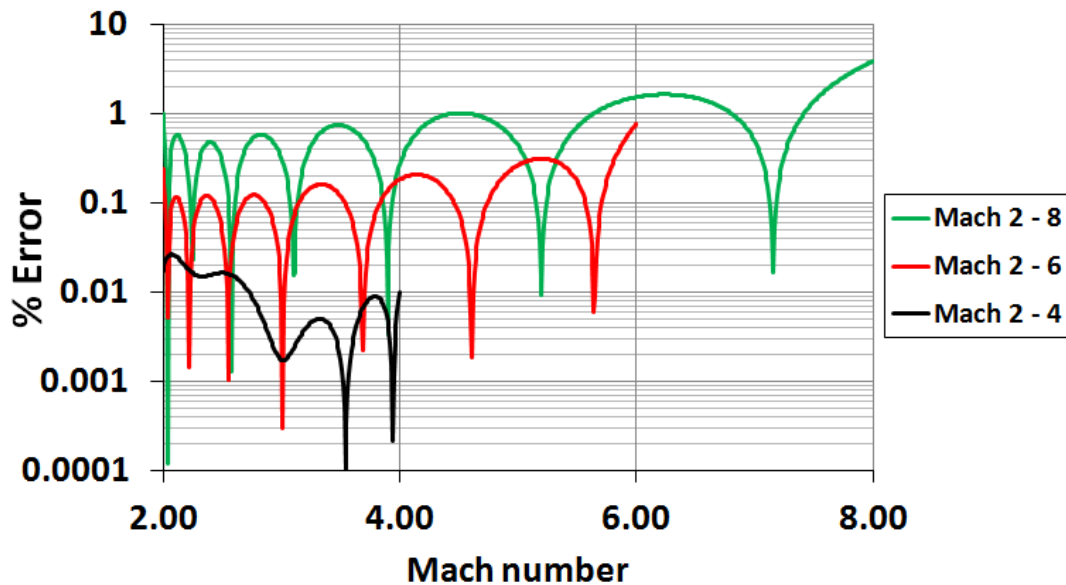
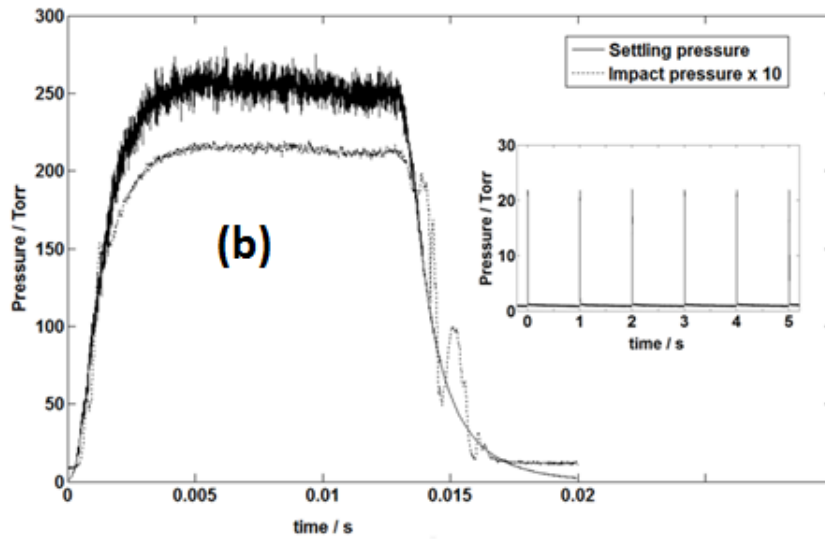


Fig. 3.14. Absolute percent error values resulting from the estimation of the Mach numbers using polynomial fits 6th order in  $p_2/p_0$ .

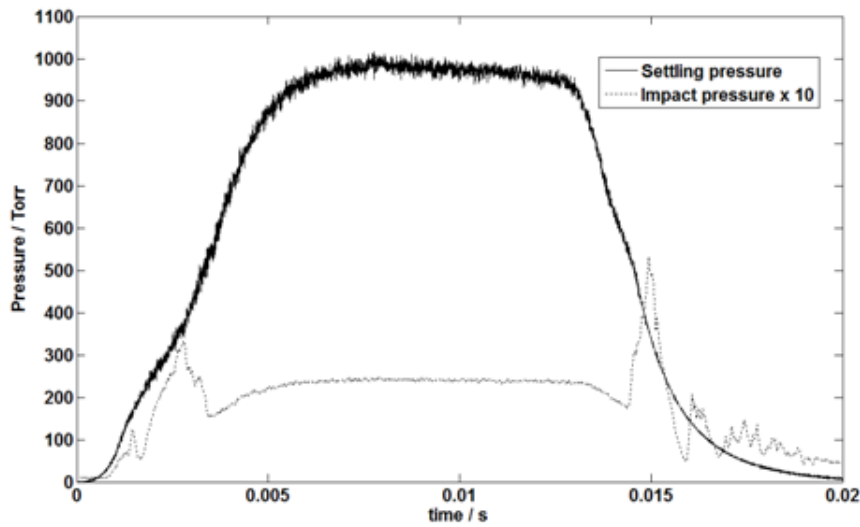
As noticed from figure 3.14, the percent error obtained by calculating the Mach number using the polynomial fit decreases about one order of magnitude by reduction of

the fit range in 2 Mach number units. Since each of the nozzles was designed to generate a flow with a specific Mach number the data analysis was performed by using an appropriate polynomial fit that spanned 3 Mach number units around the nozzle's design Mach number in order to keep the Mach number calculation errors within 0.05%.

Shown in figure 3.15 is the time-dependent impact pressure profile of a single pulse with a 10.0 ms pulse valve opening time using the Mach 4.6 nozzle and  $N_2$  as the test gas. The data shown in the figure was taken using a pulsed valve repetition rate of 1 Hz. From the pulse structure, it can be inferred that there is an induction time to generate a stable flow. This induction period results from a combination of the pulse valve opening time, which is estimated to be about 250  $\mu s$ , and the time required to fill the settling chamber region, about 1.2 ms. The figure shows a region of 10.0 ms of stable flow established after 3.0 ms of the trigger signal. The sharp features in the impact pressure before and after the stable flow region are due to shock waves, which arise from non-pressure matched expansion as the flow is established and after the valves have closed and the pressure in the settling chamber decreases. The presence of these shocks is observed in NO PLIF images acquired at times corresponding to the beginning and the end of the pulse, as previously shown in figure 3.10. The inset in Fig. 3.15(a) shows a series of 6 consecutive 10 ms duration pulses at a 1 Hz repetition rate. We find excellent stability from shot to shot with average pressure differences of 0.8%. Shorter and longer pulse valve opening times result in similar pressure profiles, differing only in the magnitude of stable flow times. However, given that the induction time to stable flow when operating the Mach 4.6 nozzle is 3 ms, a total pulse valve opening time below 5 ms should be avoided.



**(a) Mach 4.6 operation**



**(b) Mach 6.2 operation**

Fig. 3.15. Time-resolved pressure measurement of a single pulse along the Mach 4.6 flow axis. Inset shows a series of pulses taken at 1 Hz repetition rate (a). Time-resolved pressure measurement of a single pulse along the Mach 6.2 flow axis (b).

The measured centerline flow properties of the Mach 6.2 nozzle were obtained at 0.5 Hz and pulse valve opening times of 15 ms. The time-resolved pressure profile for a single flow pulse is shown in figure 3.15(b).



Using identical operation conditions as those employed with the Mach 4.6 nozzle, the same measurements were performed with the Mach 4 and Mach 3 nozzles. The centerline properties for all nozzles are summarized in Table 3.2.

Table 3.2. Measured Centerline Properties with Temporal Variances.

Nozzle	$p_0$ (Torr)	$p_2$ (Torr)	M
Mach 6.2	$964 \pm 12.7$	$23.8 \pm 0.2$	$6.20 \pm 0.02$
Mach 4.6	$256 \pm 5.6$	$21.5 \pm 0.16$	$4.61 \pm 0.03$
Mach 4.0			3.75
Mach 3.0	$86.2 \pm 4.41$	$34.7 \pm 0.62$	$2.74 \pm 0.06$

The nozzles were designed using a cubic polynomial to describe the contracting region. The settling chamber diameter was 1.3 cm, which resulted in area contraction ratios of 6.5 and 7.9 for the Mach 4.6 and the Mach 6.2 nozzles, respectively. Additional screens and flow conditioning were deemed unnecessary as it was expected that the large-scale motions would be damped during the contraction. During the uniform flow time interval using the Mach 4.6 nozzle, the settling pressure rms was 5.6 Torr, that is 2.2%, and the impact pressure was observed to vary 0.7%. This reduction is expected due to the stabilizing effect of the favorable pressure gradient during the acceleration within the nozzle. This fact is experimentally demonstrated in figure 3.15, where the impact pressure fluctuations are about an order of magnitude lower than those measured in the settling region. These results are also stated in table 3.2. As mentioned above, the shot-to-shot fluctuations are also an important factor that determines the repeatability of the flow. Figure 3.16 shows the shot-to-shot fluctuations as a percent of the average pressure obtained from 100 flow pulses using the Mach 4.6 nozzle. The pressure fluctuations from shot-to-shot are below 1% for all nozzles.

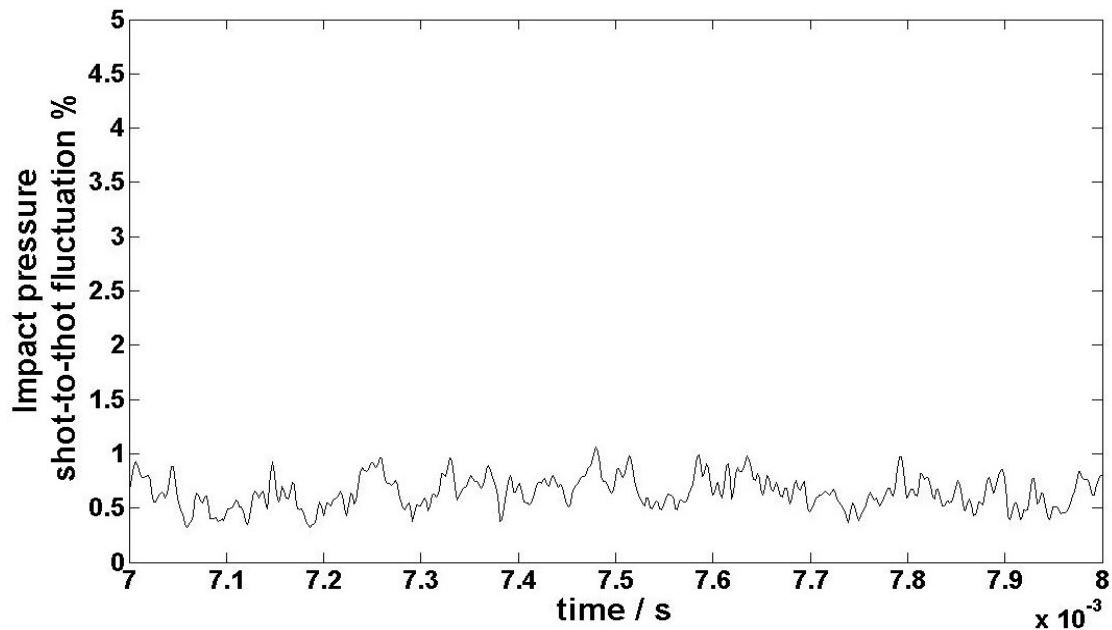


Fig. 3.16. Impact pressure shot-to-shot fluctuations shown as a percent between 7 and 8 ms of the stable phase of the pulse.

### III.4.3 CFD Methods

The construction of a near-hypersonic nozzle, Mach 4.6, was selected as it provides a reasonable margin (25 K) of operation without having to heat air in the settling region to avoid liquefaction at the highest available total pressure. The Mach 6.2 nozzle was arbitrarily selected since it matches other facilities within the laboratory. The inviscid supersonic nozzle contours were designed with the method of characteristics [45]. The Mach 4.6 and Mach 6.2 nozzles have exit diameters of 2.8 cm and 5.05 cm, respectively. However, at the present Mach numbers and wall temperatures, isothermal at room temperature, viscous effects were a significant factor in the exit flow. Hence, detailed CFD computations for the Mach 4.6 and Mach 6.2 nozzles were also performed as part of the nozzle design. The computations help to verify Mach number exit uniformity and to ensure that shock waves were not generated within the nozzle.

The numerical simulations were performed using the GASP [46] flow solver. The flow solutions were converged to steady state using the implicit Gauss-Seidel method. Inviscid fluxes were computed using third-order accurate MUSCL [47]

interpolation and the Roe approximate Riemann solver [48]. Viscous fluxes were computed to second-order accuracy. Both laminar and turbulent simulations were performed. First-order closures such as k-omega [49] and Menter's shear-stress transport (SST) [50] models produced results very similar to the laminar solutions. The turbulent flow results presented in this work were obtained using the Baldwin-Lomax model [51].

The measured stagnation values of the pressure and temperature were used as inflow conditions to the nozzle. Viscous wall conditions were specified along with a wall temperature ( $T_w = 290$  K) at the nozzle surface. Initial iterations of the simulations were performed with a specified low backpressure at the exit. Once the flow reached supersonic conditions at the exit, the boundary condition was switched to extrapolation and the solution was restarted and ran until convergence. At each grid level, the L2 norms of the residuals were reduced by at least 4 orders of magnitude.

A cubic-spline fit of the nozzle coordinates output from the design code was used for the profile of the nozzles. Given the axi-symmetric nature of the nozzles, a two-dimensional grid was used in the simulations. Grid convergence was demonstrated utilizing three structured grids. The fine grid had 641 points in the axial direction, 513 of which were in the diverging section of the nozzle, and 129 points in the wall-normal direction. The medium and coarse grids consisted of 321 x 65 and 161 x 33 points, respectively. Example grid convergence study results for the fine and medium grids are shown in figure 3.17 for the Mach 4.6 nozzle. The Mach number across nozzle exit is plotted versus radial distance. As indicated medium and fine grid results are similar, with a maximum Mach number difference of 2% in the viscous shear layer. The corresponding Mach 6.2 grid convergence was similar, where the grid densities were matched to the ones stated above.

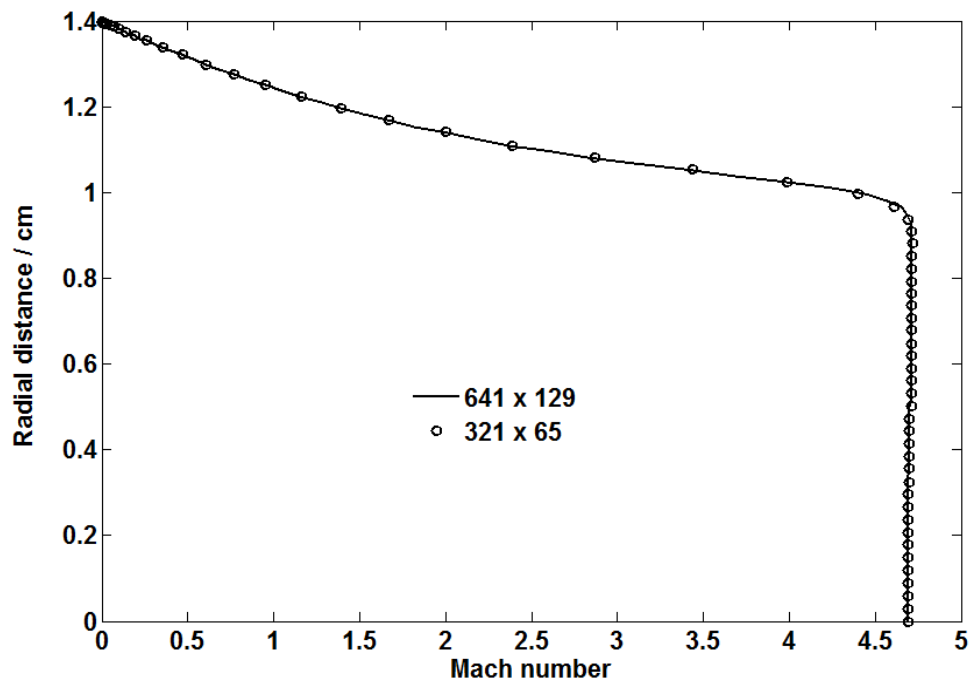


Fig. 3.17. Demonstration of grid convergence for the Mach 4.6 nozzle.

As mentioned above, the viscous effects play an important role in nozzle design at high Mach numbers. This is evident in the CFD simulation results shown in figure 3.18, where the viscous boundary layers are seen to occupy a significant fraction of the exit flow. However, the simulations demonstrated shock wave free flow in the nozzle, and hence the designs were not changed as a result of the CFD.

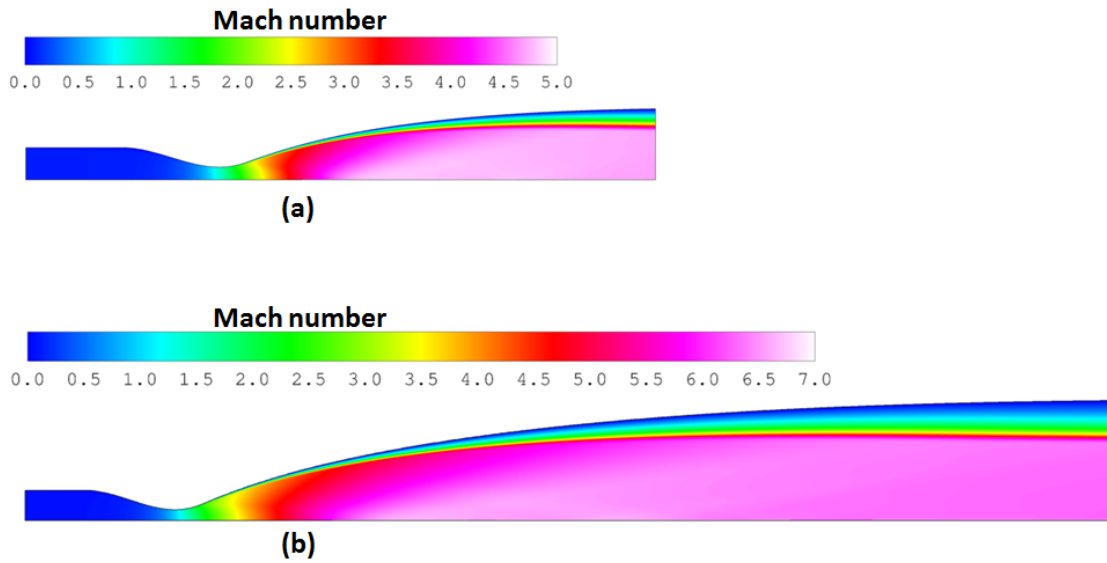


Fig. 3.18. CFD contour results for the Mach 4.6 (a) and Mach 6.2 (b) nozzles.

While the flow stability and repeatability were assured by the previously described pressure measurements, the resulting freestream properties downstream from the nozzle exit that define the flow quality are also important. These measurements are described in the following section.

#### III.4.4 Spatial Characterization

The spatial flow properties downstream from the nozzle exit were quantified by performing different measurements that included (1) radial pitot pressure surveys across the nozzle exit, (2) two-line NO PLIF temperature measurements, (3) 1-component molecular tagging velocimetry measurements and (3) VENOM [28] measurements for simultaneous thermometry and velocimetry.

### A. Radial Pitot Surveys

To obtain exit Mach number profiles, pitot pressure surveys across the exit of the nozzle were performed, where the test chamber and nozzle exit pressure were matched based on the centerline Mach numbers listed in table 3.2. Hence, the Rayleigh-pitot formula was used to compute the Mach number, given the static pressure and measured pitot pressures. The results are shown in figure 3.19 (a) and (b) for the Mach 4.6 and 6.2 nozzles, respectively. Laminar and turbulent CFD simulation results are shown for comparison purposes. The state of the boundary layer, laminar or turbulent, along the nozzle wall is uncertain due to the low Reynolds numbers and strong favorable pressure gradients. Hence, both laminar and turbulent simulations were performed. Albeit the differences are subtle, the boundary layers appear to be turbulent. For both nozzles, the measured exit profiles are in reasonable agreement with the CFD results, where the measured Mach numbers were approximately 2% lower than predicted. The uniform, or inviscid, core regions were approximately 57% and 65% of the exit diameters for the Mach 4.6 and 6.2 nozzles, respectively. The measured spatial variations across the uniform core region are summarized in Table 3.3. The static temperature and velocity across the nozzle exit were estimated from the Mach number data assuming a constant total temperature, in this case room temperature. The results are also summarized in Table 3.3.

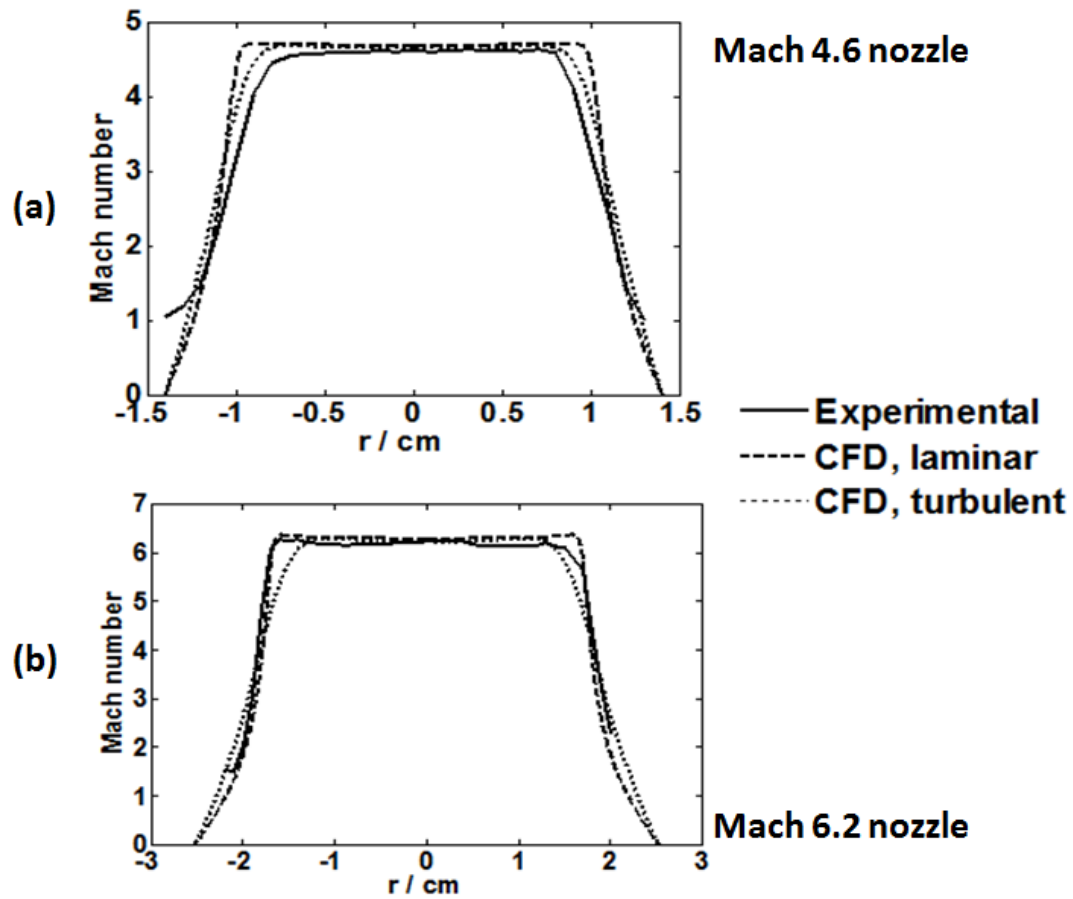


Fig. 3.19. Radial Mach number profiles at nozzle exit. Mach 4.6 nozzle (a) and Mach 6.2 nozzle (b).

Table 3.3. Measured Spatial Averaged Exit Flow Properties with Spatial Variations.

Nozzle	$P_2$ (Torr)	M	U (m/s)	T (K)
Mach 4.6	$21.5 \pm 0.2$	$4.61 \pm 0.02$	$703 \pm 3$	$55.8 \pm 0.4$
Mach 6.2	$23.7 \pm 0.3$	$6.2 \pm 0.04$	$760 \pm 5$	$34 \pm 0.4$

## B. PLIF Measurements

A mixture of 1% NO in N<sub>2</sub> was used as a test gas for the PLIF experiments. The PLIF laser system, shown in figure 3.20, consisted of an injection seeded Spectra Physics PRO-290-10 Nd:YAG laser operated at 10 Hz pumping a Sirah Cobra Stretch

pulsed dye laser at 532 nm to produce 621 nm output using a mixture of Rhodamine 610 and Rhodamine 640 in methanol. The dye output was mixed with the residual 355 nm from the Nd:YAG laser in a Sirah SFM-355 frequency mixing unit to produce approximately 10 mJ/pulse near 226 nm. The 226 nm beam was passed through a lens system to form a 20 mm wide sheet approximately 150  $\mu\text{m}$  in thickness. Two-dimensional temperature maps of the flow were obtained using the 2-line PLIF technique [52,53]. The PLIF images were obtained probing the  $A \ ^2\Sigma^+ (v' = 0) \leftarrow X \ ^2\Pi (v'' = 0)$  band of NO on the  $R_1 + Q_{21}(1.5)$  and the  $R_1 + Q_{21}(8.5)$  transitions. These rotational states were chosen to provide sensitive temperature measurements at the low temperatures expected in these flows. Fluorescence images were captured using an Andor iStar DH734 ICCD camera mounted perpendicular to the laser sheet. The camera was fitted with a UKA 105 mm F/4.0 UV lens and extension rings to capture images with a resolution of  $\sim 72$  pixel/mm. All the fluorescence images obtained for this study were acquired in the fluorescence linear regime as confirmed by measurements of the fluorescence intensity captured by the ICCD camera as a function of laser power for both probe transitions. It has to be noted that there are about 80 – 90% of laser power losses from the dye laser exit to the exit of the nozzle due to the optics, absorption of background NO in the chamber, and an iris used to “clean” irregularities in the beam before it goes through the sheeting optics.



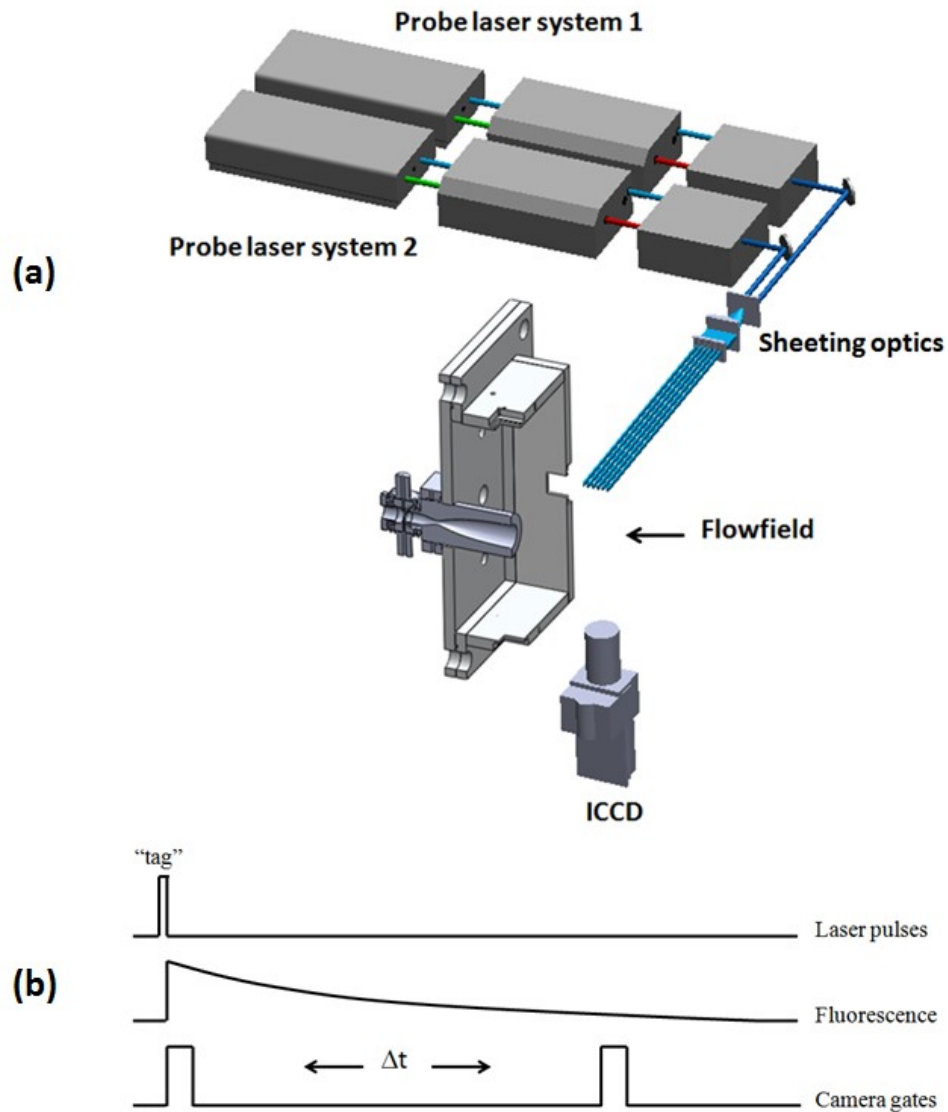


Fig. 3.20. Experimental setup of the NO PLIF imaging system (a) and timing schematic for the NO fluorescence MTV experiments (b).

The 2-dimensional temperature maps are obtained by comparison of images obtained probing the two NO rotational states. In principle, the fluorescence signal intensity is a complicated function of the initial population of the probed state, the stimulated absorption Einstein coefficient, the saturation and laser intensity, the fluorescence yield, and collection optics efficiency [54]. However, the ratio of two

fluorescence signals obtained in the linear fluorescence regime by probing two rotational states can be directly used to determine the rotational temperature, provided that the coefficient  $C_{12}$  is known; that is,  $S_{f2}/S_{f1} = C_{12}\exp[-\Delta E_{21}/kT_{rot}]$ . For the current experiments  $C_{12}$  was determined by collecting image pairs without pulsed flow. This was achieved by running the imaging system at twice the pulsed valve repetition rate, so every other image pair produced a fluorescence ratio to calculate  $C_{21}$  at the known temperature inside the chamber measured using a thermocouple. Figure 3.21 shows the 2-dimensional temperature map of the core flow using the Mach 4.6 nozzle (left) and the Mach 6.2 nozzle (right). For the analysis 100 images of each rotational state were averaged. Pulse-to-pulse intensity variation of individual images was corrected for laser power and spatial profile. The average rotational/translational temperature in the Mach 4.6 flow core was found to be 56.2 K with a spatial  $T_{rms}$  of  $\pm 1.2$  K. The temperature of the flow can be estimated assuming adiabatic flow in the nozzle [55], and yields a value of 55.8 K, which is within the measurement uncertainty associated with NO PLIF thermometry. These results are summarized in Table 3.3. The measured temperature for the Mach 6.2 nozzle core flow was 38.8 K with a spatial  $T_{rms}$  of  $\pm 0.8$  K, close to the estimated temperature of 34 K.

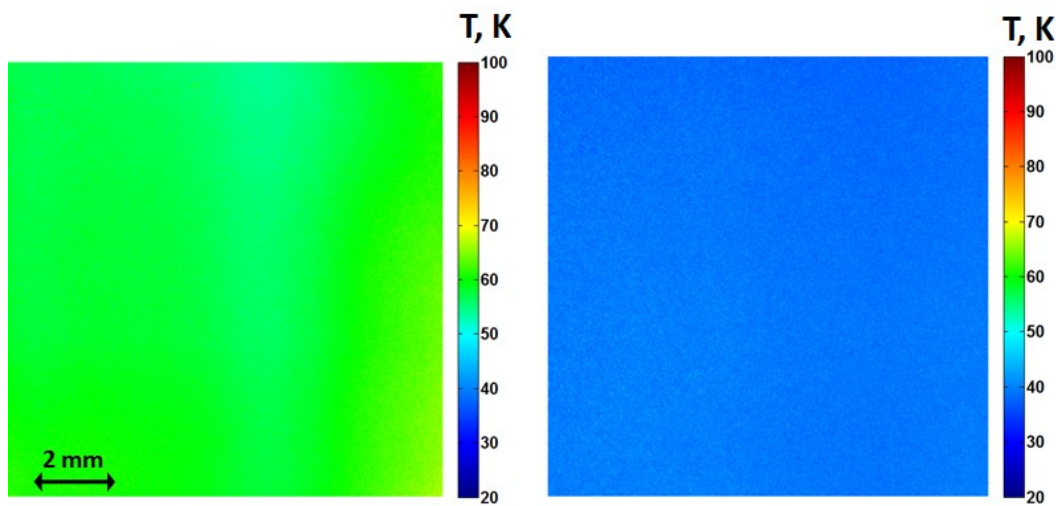


Fig. 3.21. Average two-dimensional temperature map of the Mach 4.6 (left) and Mach 6.2 (right) core flow obtained using two-line NO PLIF.

In cases where the NO fluorescence lifetime is long relative to fluid displacement Molecular Tagging Velocimetry (MTV) can be used to obtain streamwise velocity maps "writing" a set of vertical NO excitation lines onto the flow field with the PLIF lasers [56,57]. The laser sheet was directed through an array of ten 300 mm focal length, 2 mm wide micro-cylindrical lenses, following the approach reported by Pitz and co-workers [58,59]. The lens array results in higher laser energy density in the probing region, greater fluorescence signals, and hence permits longer time delays critical for MTV measurements, compared to the use of an aluminum mesh which provides a modulated fluorescence intensity pattern based on partial blockage of the laser sheet. The narrower "written" regions attained with the focusing due to the lens array permit more accurate line location, resulting in an improved determination of the velocity field (figure 3.22). Two time delayed images acquired with 50 ns camera gates were collected within the NO fluorescence lifetime, the first 10 ns after the excitation pulse and the second following a 600 ns time delay. The streamwise velocity was calculated by measuring the displacement of the "write" lines and dividing this value by the known time delay between the two images, correcting for the finite gate times.

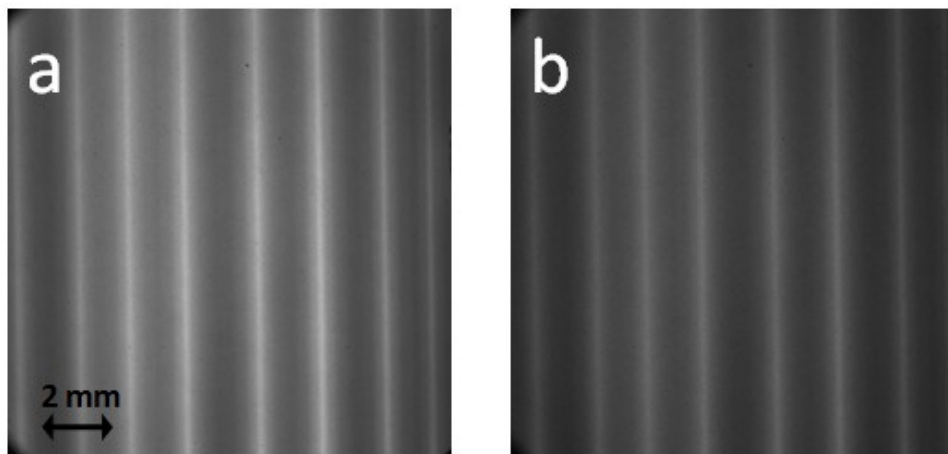


Fig. 3.22. 100-shot fluorescence average images obtained in the Mach 4.6 flow for the velocimetry determination. Initial (a) and 600 ns time delayed image (b).

The velocity determination was performed using an in-house data analysis code written in MATLAB. The first step in the analysis involves the location of the fluorescence maxima along each row of the initial and time-delayed images, followed by a cross-correlation line-tracking sub-routine that determines the displacement of the same line in the streamwise direction within a user-defined region that depends on the time delay used in the experiment. A single camera arrangement was employed due to its simplicity, particularly in terms of minimizing the image processing required in a two camera configuration. Figure 3.23 shows the average streamwise velocity map of the Mach 4.6 flow (left), and the Mach 6.2 flow (right) obtained from the analysis of 100 time-delayed image pairs in each case. The spatially averaged streamwise velocity is  $u = 716 \text{ m/s} \pm 7 \text{ m/s}$  in the Mach 4.6 flow very close to the velocity of 703 m/s calculated using the measured Mach number and thermometry results. For this case, the line displacement uncertainty across the entire field of view was determined to be 0.5 pixels. We have found the line location routine to be the dominant source of uncertainty in the velocity determination, corroborated by the same uncertainty measured under stationary conditions, i.e. using a gas mixture of 1% NO in N<sub>2</sub> in the chamber maintained at 1 Torr, that generates a homogeneous velocity field of 0 m/s. The variations in the average velocity are consistent with the errors of the 1-component MTV measurements estimated to be  $\sim 1.5 \%$ . An average, streamwise velocity of  $757 \text{ m/s} \pm 8 \text{ m/s}$  was determined from MTV measurements of the Mach 6.2 flow, which compares favorably with the value predicted from the pitot pressure, which was 760 m/s.

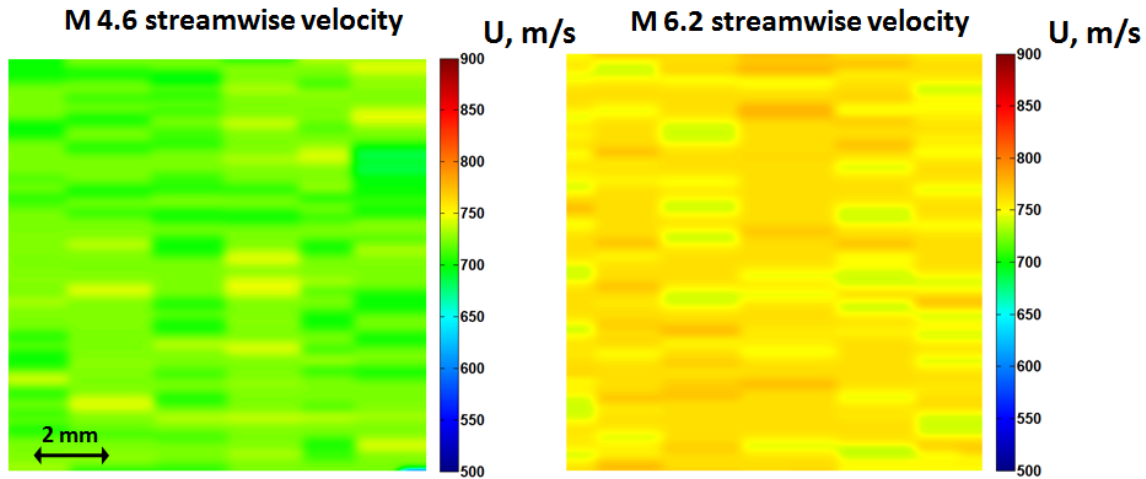


Fig. 3.23. Interpolated average streamwise velocity map for the Mach 4.6 (left) and Mach 6.2 (right) core flow using NO MTV.

We also employed the recently developed VENOM technique as a confirmation of the Mach 4.6 flow field velocity and temperature fields [25,60,61]. The average streamwise velocity determined for the Mach 4.6 flow using the VENOM technique yielded an average velocity of  $700 \pm 5$  m/s, consistent with the results obtained using NO PLIF. A comparison of image pairs acquired  $1.5 \mu\text{s}$  after the photolysis pulse yielded an average temperature of  $59.6 \pm 2.3$  K, consistent with NO PLIF measurements.

A more detailed treatment of the data analysis required to obtain temperature and velocity maps is presented in chapters 2, 4 and 5.

### III.5 Flow Visualization Examples

As mentioned above, the Repetitively Pulsed Hypersonic Test apparatus design includes the possibility of mounting test models on an array of  $\frac{1}{4}$ -20 tapped holes located on the chamber floor and ceiling. Having demonstrated the flow repeatability and low freestream turbulence intensities at a variety of Mach numbers, this apparatus represents a valuable tool that generates flows of sufficient quality to permit qualitative and quantitative observations in diverse flow field structures. As an example, three different test models were used to demonstrate the potential of flow structure

visualization using PLIF imaging, and the option of qualitative measurements by performing two-line thermometry mapping of the same flow fields. These models were a 4.74 mm diameter sphere, a 7 degree half-angle cone, and a Mars Phoenix re-entry capsule. An photograph of these test models is shown in figure 3.24 (upper panels).

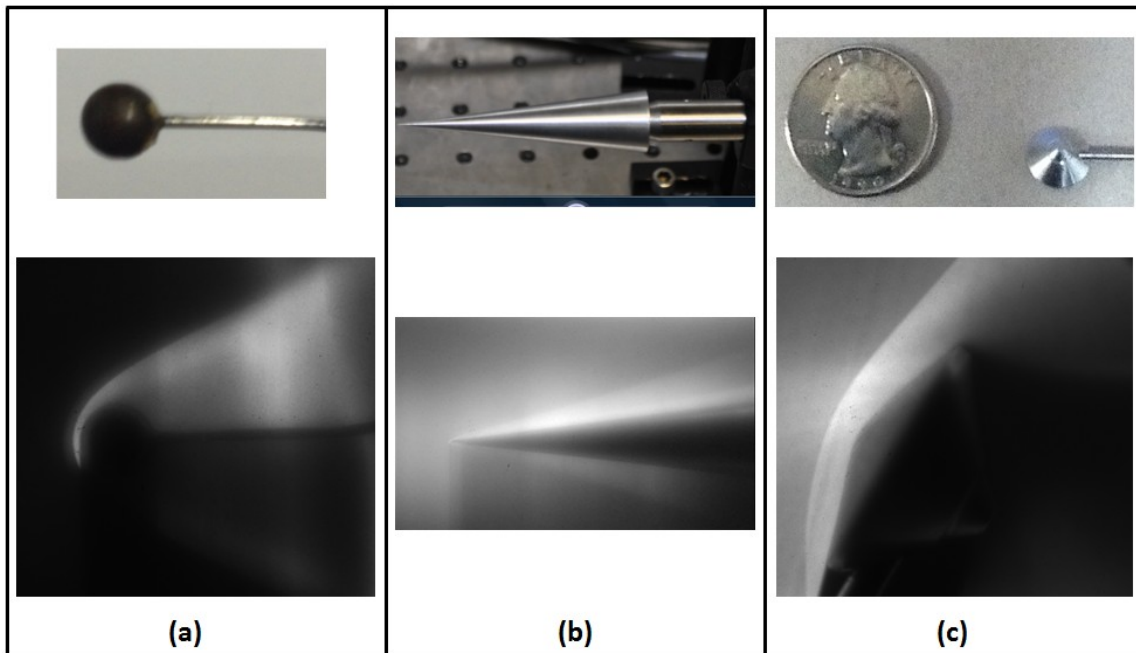


Fig. 3.24 Photographs and NO PLIF images of a sphere (a), a 7 degree half-angle cone (b) and a Mars Phoenix re-entry capsule (c) models used to demonstrate the flow visualization potential of the Repetitively Pulsed Hypersonic Test apparatus.

Figure 3.24 (lower panels) also shows averaged NO PLIF images of the models held in place 1 cm downstream from the nozzle exit in the Mach 4.6 flow using 1% NO in  $N_2$ . The images clearly reveal the formation of bow shocks (a and c) or an oblique shock (b). Since the gas pressure, density, and temperature rapidly raise across a shock wave, these structures are usually distinguishable by probing a specific rotational state in order to provide contrast with respect to the cold freestream.

Figure 3.25 shows NO PLIF images of the Mars Phoenix re-entry capsule and the sphere models obtained by probing the  $R_1 + Q_{21}$  (1.5) and  $R_1 + Q_{21}$  (8.5) transitions in the  $A^2\Sigma^+(v' = 0) \leftarrow X^2\Pi(v'' = 0)$  band.

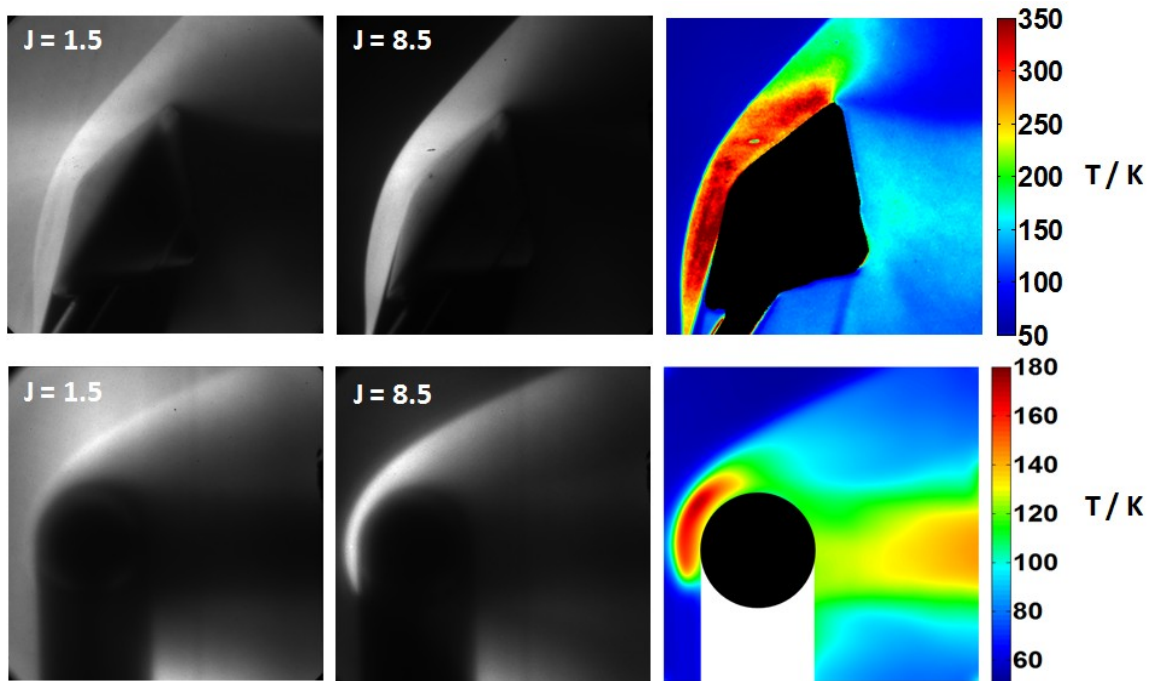


Fig. 3.25. NO PLIF images of the Mars Phoenix re-entry capsule (upper panels) and the sphere (lower pannels) models probing two different rotational states in order to obtain temperature maps (right panels).

Using these images the temperature maps can be calculated with the two-line PLIF technique, as shown in the right panels of the same figure. It can be observed that the stagnation points right behind the shock waves show the largest temperature, and the cold freestream at 56 K and the warmer wake regions are revealed as well. The timing between the pulsed valves and laser/camera system ensured that all fluorescence images were taken during uniform stable phase of the flow.

From the previous PLIF images of the sphere, additional information can be obtained. The bow shock created in front of a blunt body detaches from the body's

surface. The shock stand-off distance for a spherical body exposed to a supersonic flow has a well-known and relatively simple dependence on the freestream Mach number and the sphere diameter for a non reactive flow.

The ratio between the stand-off distance and the sphere diameter was measured using an NO fluorescence image, as shown in figure 3.26, resulting in a value of  $\Delta/D = .087 \pm .007$ . This result can be compared with numerical predictions.

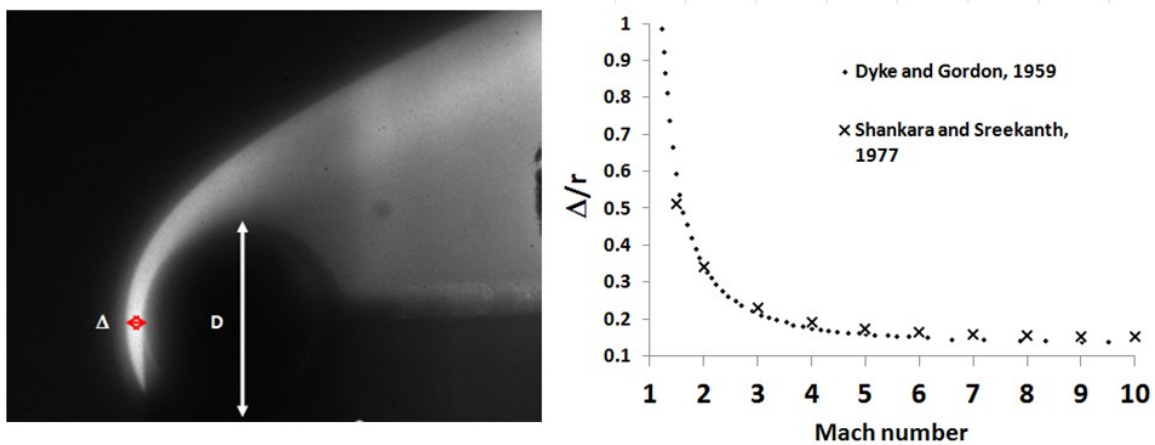


Fig. 3.26. Bow shock stand-off distance for a sphere.

A plot of these calculations is also shown in figure 3.26. The measured value of 0.087 falls within the value range predicted by different sources [62,63].

### III.6 Summary

The design, construction and full characterization of a compact Repetitively Pulsed Hypersonic Test chamber was accomplished at the National Aerothermochemistry Laboratory located at Texas A&M University. The system was designed to utilize relatively modest laboratory scale infrastructure to facilitate advanced high-energy pulsed laser diagnostic development for hypersonic flows as well as exploratory work in ablating boundary layers. The facility can operate stable 2-20 ms length flow pulses of uniform axisymmetric supersonic flow at Mach 2.74, Mach 3.75,



Mach 4.6 and Mach 6.2 for operation times exceeding 8 hours with no change in flow behavior. The nozzle assembly permits facile exchange of converging-diverging nozzles to achieve a variety of exit Mach numbers. The pulsed flow output can be easily synchronized with laser and camera systems using conventional digital delay generators. The system is particularly well suited to the long time operation often required for diagnostic development and/or optimization, and for use with toxic chemical tracers, which can be cryogenically trapped at the modest mass flows employed. In principle, the apparatus can operate over a unit Reynolds numbers ranging between  $6.0 \times 10^4 \text{ m}^{-1}$  and  $3.0 \times 10^6 \text{ m}^{-1}$ . The nozzle flows were characterized by using both fast response pressure sensors and nitric oxide MTV/PLIF imaging for two-dimensional temperature and 1-component velocity measurements. During the uniform flow time interval, the pressure at the nozzle exit was observed to vary by less than 1%. These values correspond to fluctuations in exit flow velocity and temperature within 1% as well. Velocity and temperature measurements at Mach 4.6 and Mach 6.2 using MTV/PLIF measurements were in excellent agreement with predicted values. Observed rms values exceeded the magnitude of the fluctuations indicated by the pressure measurements providing an estimate of the intrinsic uncertainties associated with the MTV/PLIF techniques. The utility of the apparatus was demonstrated by performing NO PLIF flow imaging experiments in a variety of models that included a sphere, a 7 degree half angle cone, and a Mars Phoenix re-entry capsule. Qualitative measurements employing these models were also demonstrated by obtaining average temperature maps of these flow fields as well as a measurement of the bow shock stand-off distance for a sphere in a Mach 4.6 flow.

## CHAPTER IV

### EXPERIMENTAL: VELOCITY AND ROTATIONAL TEMPERATURE MEASUREMENTS USING NO<sub>2</sub> PHOTODISSOCIATION

#### IV.1 Instrumentation and Measurement Principle

The use of molecular tracers for velocity measurements utilizing Molecular Tagging Velocimetry (MTV) techniques has been justified in Chapter 1. The use of NO as a molecular tracer has unique and well-documented advantages in MTV experiments performed in gas phase such as its thermal stability, the natural occurrence of NO in some flow fields such as combustion and high enthalpy hypersonic flows, the virtually identical heat capacity ratios of air and NO ( $\gamma = 1.405$  for air compared to  $\gamma = 1.394$  for NO), which represents a negligible influence in the flow properties especially at the low seeding or natural occurring fractions usually present in the flows, and the well-studied spectroscopy of this molecule.

Despite the previously mentioned advantages of NO as a molecular tracer, the limitations of using NO fluorescence for MTV experiments have been clearly demonstrated in high quenching environments, where the NO fluorescence lifetime can be reduced significantly [2]. The solution proposed to overcome this limitation was the utilization of seeded NO<sub>2</sub> instead of NO, employing a photolysis laser to generate NO *in situ*. The localized NO photoproduct is then "read" by two sequential electronic excitations and the resulting fluorescence from each excitation event is captured by an ICCD camera. Since each image is obtained capturing light originating from an independent fluorescence event the technique is useful to determine velocity in flow fields characterized by high fluorescence quenching conditions. This principle is illustrated in figure 4.1, where a photolysis laser is vertically aligned at the Mach 4.6 nozzle exit running a nitrogen flow seeded with 1% NO<sub>2</sub>. The NO( $v=1$ ) photoproduct is then excited by a probe laser tuned to excite the  $R_1 + Q_{21}$  ( $J = 8.5$ ) transition in the (1,1) band at different time delays after photodissociation. The vibrationally excited NO is

long-lived and remains in the flow for several tens of microseconds, as opposed to the fluorescence lifetime of NO, which is about 200 ns [2,64].

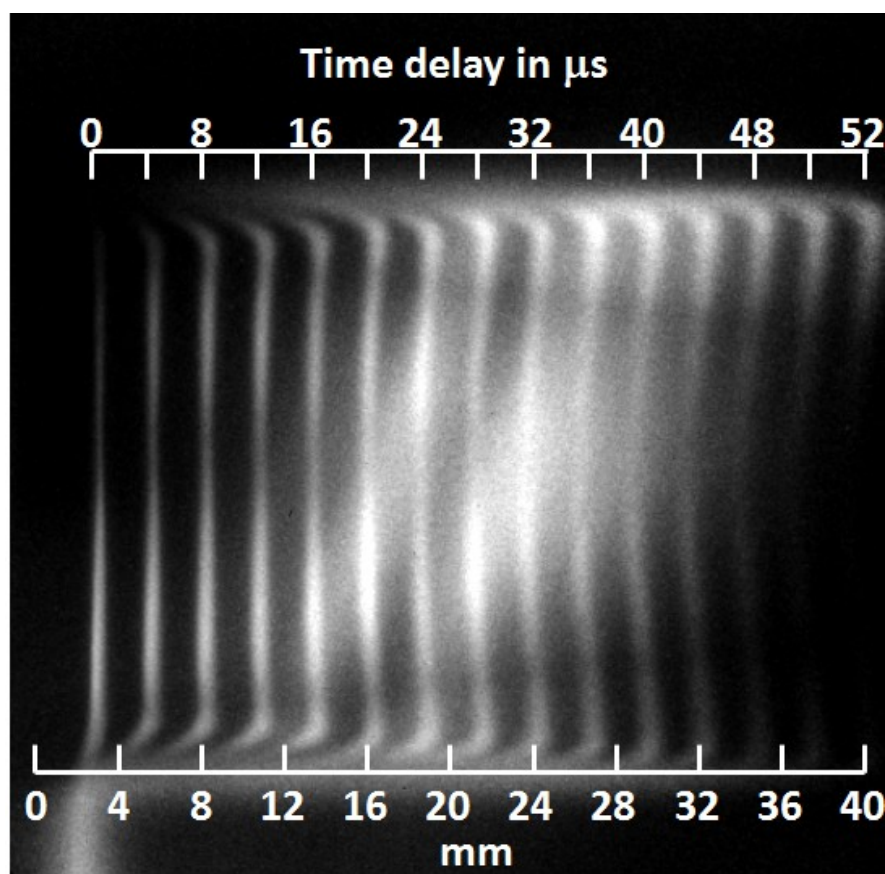
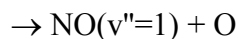


Fig. 4.1. Composite fluorescence image showing one vertical photolysis line moving with the Mach 4.6 flow. The images were obtained probing the NO( $v''=1$ ) photoproduct as a function of time delay after photodissociation.

The experiments described in this work have employed the third harmonic of an Nd:YAG laser at 355 nm to photodissociate NO<sub>2</sub>. This process can be described by the following equation:





The vibrational distributions for the nascent NO originating from NO<sub>2</sub> photodissociation have been experimentally studied using different wavelengths [65]. In general, the photodissociation of NO<sub>2</sub> results in a fixed ratio of NO(*v*''=0) and NO(*v*''=1) photoproducts that shows a strong wavelength dependence. The photolysis of NO<sub>2</sub> is a unimolecular reaction system in chemical dynamics that has been extensively studied [65]. According to those studies, the unimolecular decomposition of NO<sub>2</sub> at 355 nm results in the product distribution shown in table 4.1.

Table 4.1. Measured NO product distribution resulting from photolysis of NO<sub>2</sub> at 355 nm [65].

NO( <i>v</i> ''=0)		NO( <i>v</i> ''=1)	
Π <sub>1/2</sub>	Π <sub>3/2</sub>	Π <sub>1/2</sub>	Π <sub>3/2</sub>
41.0 ± 6.2 %	18.8 ± 2.7 %	29.2 ± 4.4 %	12.0 ± 1.8 %

## IV.2 Velocity Measurements Using NO<sub>2</sub>

As revealed by figure 4.1, the NO<sub>2</sub> photodissociation MTV technique not only facilitates obtaining a full velocity map that includes the high quenching regions of the flow field, but also an increased accuracy in the velocity measurement by permitting larger time delays between both captured images that result in larger line or intersection displacements. However, the use of NO<sub>2</sub> photodissociation MTV methods requires a more intricate experimental setup. The simplest NO<sub>2</sub> photodissociation MTV experiment requires one photolysis laser, one probe laser, and one camera in order to obtain average velocity fields. If an instantaneous velocity measurement is desired, the minimum requirements are one photolysis laser, two probe lasers (or one high-repetition probe laser), and two cameras (or one high repetition rate camera). The measurements described in this work are aimed to obtain time-resolved measurements using 10 Hz laser systems, and consequently the three-laser, two-camera setup is employed to

measure instantaneous velocity fields. Figure 4.2 shows the timing schematics for NO fluorescence MTV and NO<sub>2</sub> photodissociation MTV for comparison.

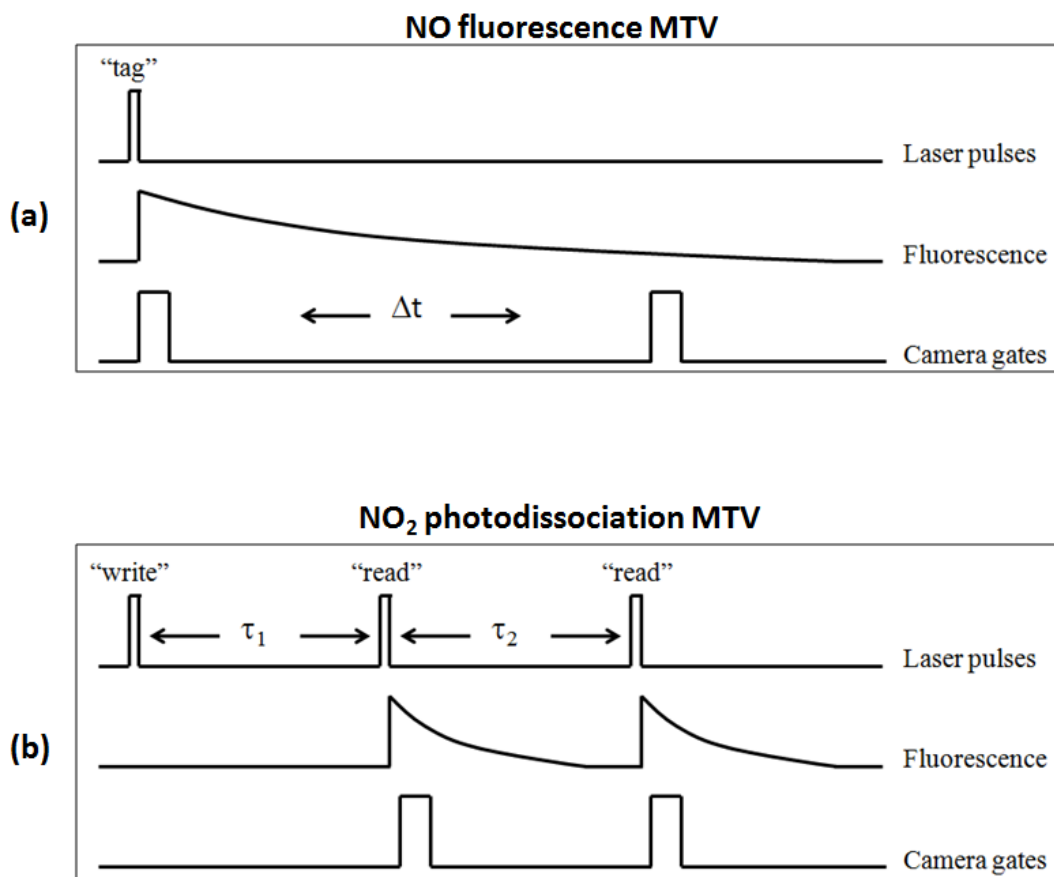


Fig. 4.2. Fluorescence MTV vs NO<sub>2</sub> photodissociation MTV timing schematics.

#### IV.2.1 Velocity Measurements Using NO( $v''=1$ )

A review of the MTV methods used in gas phase was provided in Chapter 1. Most of these methods have in common the utilization of laser focusing in order to attain high energy densities to tag the flow regions of interest, with the possibility of tagging multiple lines onto the flow if a laser sheet is sent through a series of microcylindrical lenses. The experiments described in this section are aimed to explore the performance of two different approaches used to "write" an initial photodissociation transient grid

onto the flow field. These experiments are illustrative and involve the determination of the streamwise velocity in a homogeneous pulsed Mach 4.6 flow. These two approaches are (1) the use of an aluminum mesh previously employed in the original demonstration of the  $\text{NO}_2$  photodissociation velocimetry technique to obtain two velocity components [2], and (2) the use of a microcylindrical lens array.

The first, approach I, employed an aluminum mesh to write a periodic set of photodissociation lines. In practice, the aluminum mesh provides a modulation pattern of high and low tag density regions, permitting the measurement of velocity and full-frame temperature maps [22,61]. The second approach, approach II, employed a microcylindrical lens array to attain higher laser energy density and narrower “written” regions via focusing [66,67]. This second approach results in higher NO photoproduct densities and hence improved signal-to-noise levels. An estimation of the photodissociation efficiencies obtained by these two approaches is shown in figure 4.3, where the photodissociation efficiency is plotted as a function of laser output from the 355 nm beam.

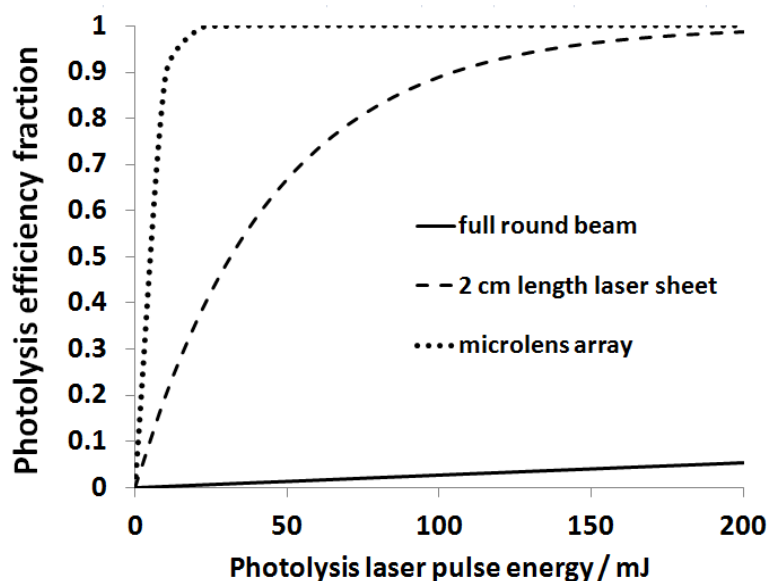


Fig. 4.3.  $\text{NO}_2$  photodissociation efficiency at varying laser output powers using three methods to direct the beam into the flow field. The photolysis efficiency attained by an unfocused beam is shown for comparison.

The photolysis efficiencies shown in figure 4.3 were calculated for a mixture of 1% NO<sub>2</sub> in N<sub>2</sub>. The NO<sub>2</sub> absorption cross-section at 355 nm is  $4.9 \times 10^{-19}$ . The photolysis laser attenuation by the background gas stagnant in the hypersonic apparatus is about 0.2 % based on the same gas composition as the Mach 4.6 freestream. These photolysis efficiencies were estimated assuming a 355 nm beam with an exit diameter of 9 mm expanded to a diameter of 2 cm before being formed into a 200  $\mu$ m thickness sheet. From this figure we can deduce that using a microlens array permits the highest photolysis efficiencies that will lead to higher signal-to-noise levels and, in addition, the narrower grid lines intended for a velocimetry experiment would result in more accurate determination of velocity.

Figure 4.4 shows pictures of 10 2-mm-wide microcylindrical lenses stacked into an array (a) and the aluminum mesh (b) used for "writing" photodissociation lines onto the flow. These photodissociation lines were written in a 1% NO<sub>2</sub> in N<sub>2</sub> Mach 4.6 flow.

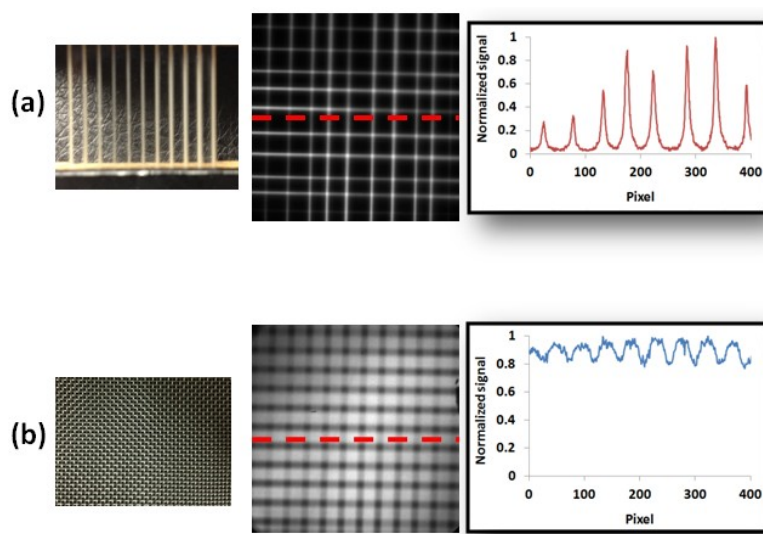


Fig. 4.4. Two different methods to "write" photodissociation lines and the signal structure generated by each of them. (a) shows the microcylindrical lens array and (b) shows the aluminum mesh.

The lines were "written" in vertical and horizontal directions with respect to the flow axis in order to generate intersections to be later "read" by an NO PLIF system. The use of a lens array leads to higher photoproduct density which translates in high signal-to-noise fluorescence images. The NO lines are sharp and well-defined, and most of the flow field lacks of fluorescence signal. On the other hand, the photolysis pattern "written" by using the aluminum mesh leads to an NO photoproduct density modulation, and the resulting fluorescence images exhibit the same modulation pattern. The darker regions contain relatively large amounts of fluorescence signal compared to the bright regions. While the intersection features are not as sharp as those resulting from the use of a lens array, they can be easily visualized and used to track the local flow displacements. Furthermore, the presence of fluorescence signal across the entire field of view can be exploited to extract additional qualitative information about the flow field, as it will be demonstrated in the following sections.

In addition to variations in the optical preparation of the "write" regions there are several timing schemes that can be employed in order to obtain velocity information. Based on the VENOM timing schematic shown in figure 4.2(b), only the first "read" pulse is required to obtain a velocity measurement, since the position of the initial "write" lines can be easily determined in the chamber in the absence of flow and then processed to generate a synthetic initial image for comparison [68,61]. For the present study, a synthetic image was generated based on the best linear fits of the "written" regions, constraining the photodissociation regions to straight lines, as they are generated by the photodissociation beam aligned through the flow. This scheme limits the uncertainty of the velocity estimation to the uncertainty in the location of the "written" lines in the time-delayed image. This principle is shown in figure 4.5.



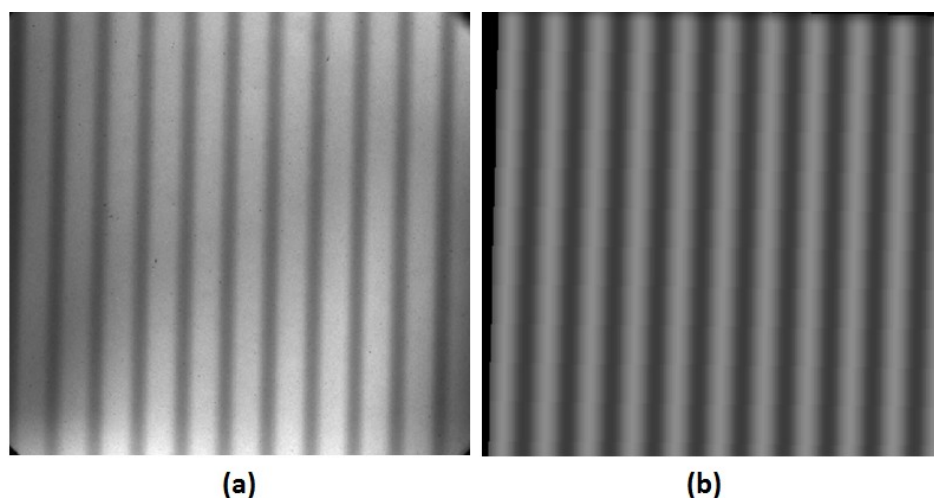


Fig. 4.5. Fluorescence image obtained under stationary flow conditions (a) and synthetically generated image obtained by fitting the lines in (a) to straight lines (b).

Shown in figure 4.6 are raw single-shot time-delayed images (left panels) employing the aluminum mesh (top) and the micro-lens array (bottom). The fluorescence images were obtained probing the  $R_1 + Q_{21}$  ( $J=1.5$ ) transition in the  $A^2\Sigma^+$  ( $v' = 1$ )  $\leftarrow X^2\Pi$  ( $v'' = 1$ ) band  $1.2 \mu\text{s}$  ( $\tau_1$ ) after the photodissociation pulse using camera gates of 50 ns, resulting in images with a spatial resolution of 52.5 pixel/mm. It is observed that in the case of the aluminum mesh employed previously by Hsu et al. [22] tracking dark regions rather than the fluorescence maxima results in the same determination of the line displacements. This is a consequence of using an aluminum mesh with 50% transmission that generates identical widths of bright and dark regions. If a higher transmission aluminum mesh is used, tracking the dark regions results in more accurate velocity determination than tracking the wider fluorescence maxima. For the current work an aluminum mesh that generates bright regions of 0.84 mm width and dark regions of 0.25 mm width was employed. The signal-to-noise levels in the single shot images obtained using approach II are a factor of two higher than those obtained using approach I, and although this impacts the accuracy of the line location, the full width at half maximum (FWHM) of the fluorescence minima using approach I is equivalent to that of the fluorescence maxima in approach II, 20 pixel, resulting in very

similar uncertainty values in the displacement determination as seen in Table 4.2, with  $\sigma = 0.4$  pixel for both approaches.

Table 4.2. Uncertainty components associated to the streamwise velocimetry measurements using only  $\tau_1$ .

<b>Timing</b>		
Delay generator jitter		$\pm 0.5$ ns
Laser pulse jitter (injection seeded)		$\pm 1$ ns
Camera gate jitter		$\pm 0.03$ ns
Gate duration		$\pm 0.03$ ns
<b>Measured uncertainty</b>		
Approach I (aluminum mesh)	$\pm 0.43$ pixels	$\pm 7$ m/s
Approach II (microlens array)	$\pm 0.37$ pixels	$\pm 6$ m/s

It may be expected that approach II would result in dramatically smaller FWHM of the “written” lines since the micro-lens array tightly focuses the photodissociation beam. However, the 355 nm photodissociation of  $\text{NO}_2$  results in high velocity NO fragments, which broaden the “written” lines during the first 100 ns after photodissociation. The nascent velocity distribution of the photolysis fragments using 355 nm are plotted in figure 4.7.

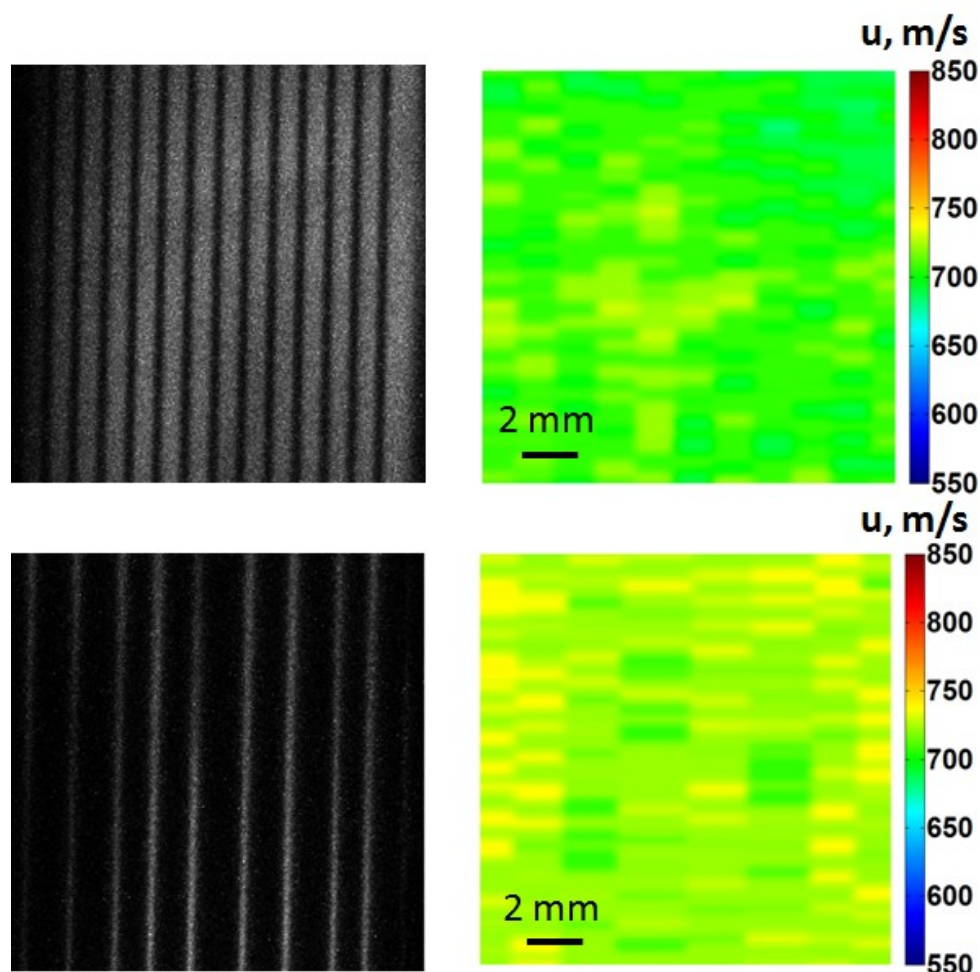


Fig. 4.6. Single-shot time-delayed images (left panels) and interpolated streamwise velocity maps (right panels) obtained using a single “read” pulse. Image spatial resolution: 52 pixel/mm. Flow direction is from left to right.

The velocity in either MTV or PIV is, in essence, non-local due to the spatial displacements over the employed time delays. Therefore, the magnitude of the molecule or particle displacement determines the spatial resolution of the velocity field and the extent of averaging over the particle trajectory. The right panels of figure 4.6 show the derived instantaneous streamwise velocity maps using  $\tau_1$  of 1.2  $\mu\text{s}$ . Although the velocity determinations are discrete, the velocity maps shown in the figure represent interpolations of the data. The determined velocity was 705 m/s, with a spatial resolution of 850  $\mu\text{m}$ , averaged along the streamwise direction due to the flow displacement. The

experimental determination of the resolution of the optical system using the "knife edge response" technique, has been addressed in Chapter 2. Considering a laser sheet thickness of 200  $\mu\text{m}$ , the overall resolution limit of the experiments is 200 x 70 x 70  $\mu\text{m}$ . This would permit using shorter time delays to increase the spatial resolution of the velocity measurements, currently averaged across a maximum of 850  $\mu\text{m}$ , at the expense of an increased velocity uncertainty.

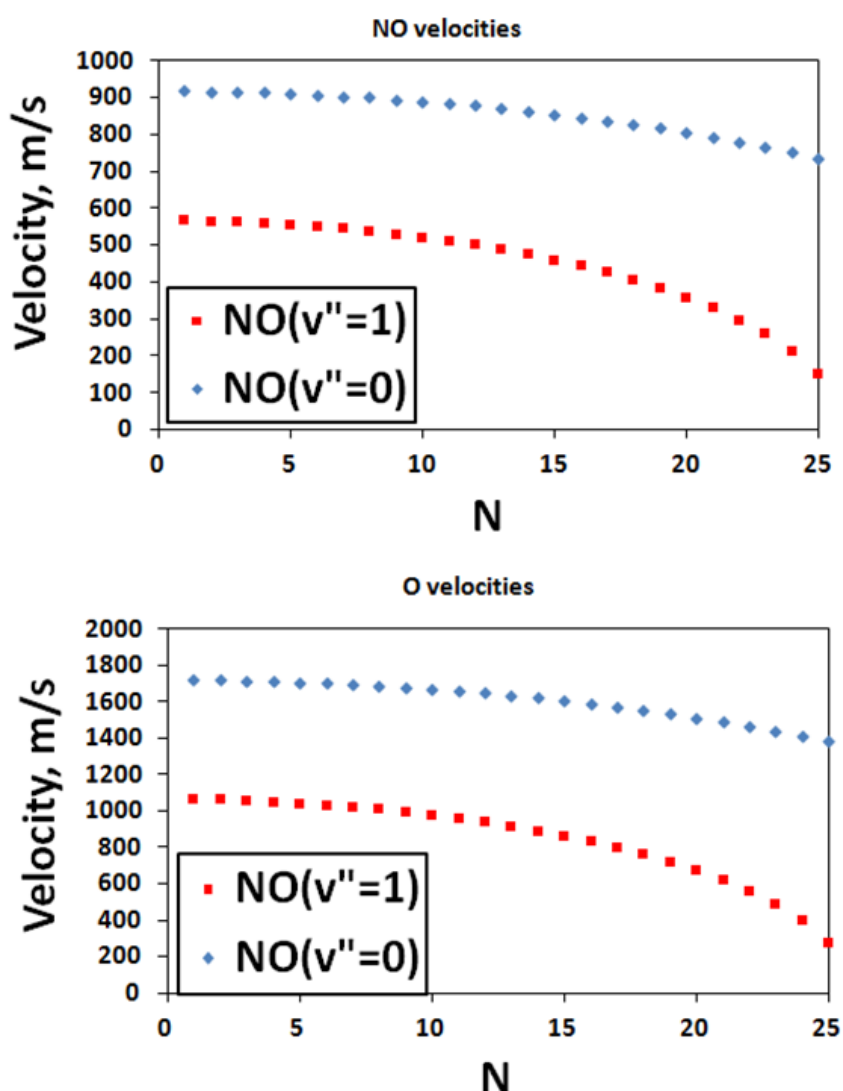


Fig. 4.7. Velocity distribution of fragments produced by  $\text{NO}_2$  photolysis using 355 nm.

### IV.3 Rotational Temperature Measurements Using NO<sub>2</sub>

A two-line PLIF temperature measurement in an NO-seeded flow is straightforward, and it has been explained in Chapter 1. The measurement of temperature fields in NO<sub>2</sub>-seeded flows follows the same principle, with the difference of NO being generated *in situ* by NO<sub>2</sub> photolysis. As demonstrated in the previous section, the velocity measurement approach using the aluminum mesh generates full-frame fluorescence images, which can simultaneously provide a temperature map. On the other hand, the narrow “write” lines associated with the use of a microcylindrical lens array to obtain velocity measurements would limit the temperature determinations to these bright regions. In principle, this limitation can be overcome if trace NO is co-seeded in the NO<sub>2</sub>-seeded flow and the “read” lasers tuned to probe the NO ( $v''=0$ ) photoproduct via transitions in the  $A^2\Sigma^+ (v' = 0) \leftarrow X^2\Pi (v'' = 0)$  band, thus providing a full temperature map. Since the photodissociation of seeded NO<sub>2</sub> results in a local increase in NO concentration, the “write” laser still provides a detectable modulation signal that can be discriminated against the initially co-seeded NO background. Co-seeding of NO would be unnecessary in flames and other flow fields where natural occurring NO is present. This principle is shown in figure 4.8, where two fluorescence images were acquired at 50 ns and 1050 ns after photodissociation by probing the NO( $v''=0$ ) photoproduct in a Mach 4.6 flow field seeded with 2.5 % of NO<sub>2</sub> and 0.8% of NO in N<sub>2</sub>.

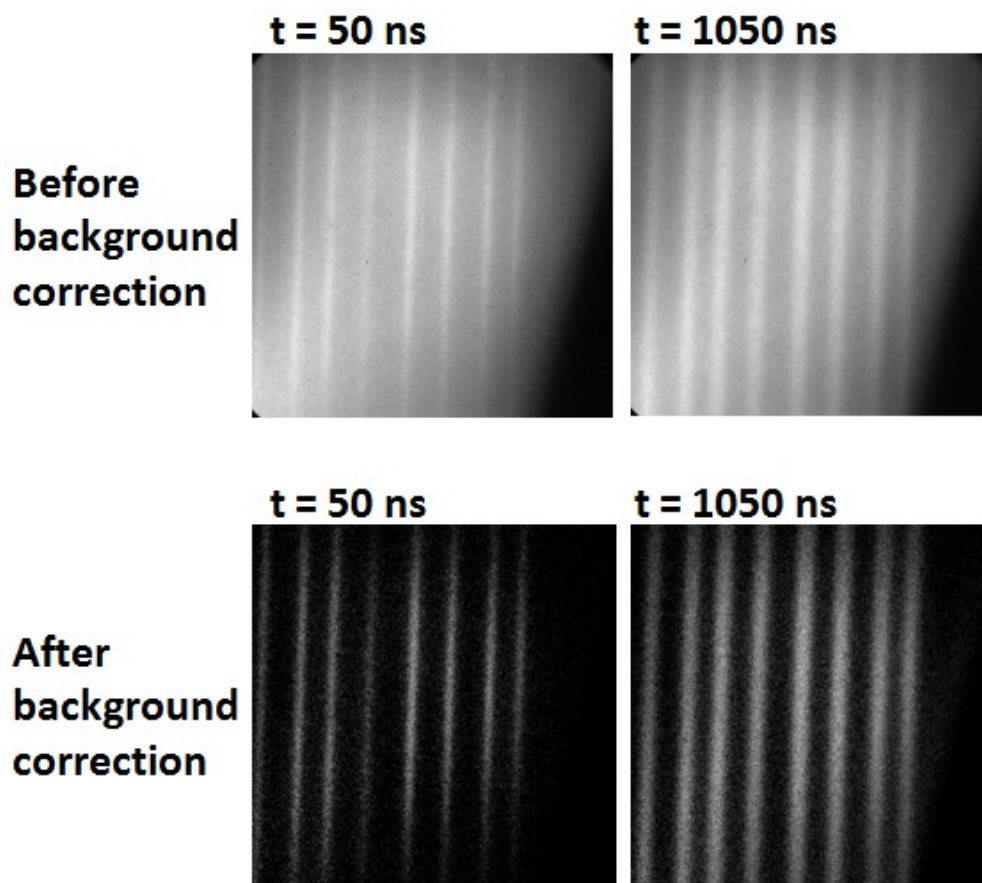


Fig. 4.8. Fluorescence images obtained by probing the  $\text{NO}(v''=0)$  photoproduct originated by photodissociation in an  $\text{N}_2$  flow seeded with 2.5% of  $\text{NO}_2$  and 0.8% of  $\text{NO}$ .

Background subtraction is achieved by acquiring a background fluorescence image with the photolysis laser blocked. Following the previous idea, the background-subtracted images shown in figure 4.8 can be processed to obtain a velocity map, while the fluorescence images before background correction can be used to provide a full-frame temperature map. However, it should be noted that the photodissociation of  $\text{NO}_2$  can have a thermal effect on the flow field.

The use of  $\text{NO}$  originating from the photolysis of  $\text{NO}_2$  for qualitative purposes requires a fundamental understanding of the unimolecular decomposition process, especially if such source of  $\text{NO}$  is intended for use in a temperature measurement of the flow. A common sense understanding of the energetics involved in the photolytic

decomposition of  $\text{NO}_2$  leads to think that the thermal properties of the flow may be altered by this process, particularly when an energy excess is involved. This thermal effect is proportional to the fraction of  $\text{NO}_2$  seeded in the flow as well as to the wavelength and energy density of the photolysis laser. Given the available energy for the fragments arising from  $\text{NO}_2$  photolysis at 355 nm and assuming that vibrational relaxation is insignificant over the time scale of the velocity/temperature measurement, which occurs within the first few microseconds after photodissociation, one can estimate the energy imparted to the flow.

As observed in figure 4.9, a photodissociation efficiency of 100% with no thermal diffusion or turbulence effects, and a 1%  $\text{NO}_2$  seeded in the Mach 4.6 nitrogen flow at 60 K results in a temperature increase of approximately 10 K.

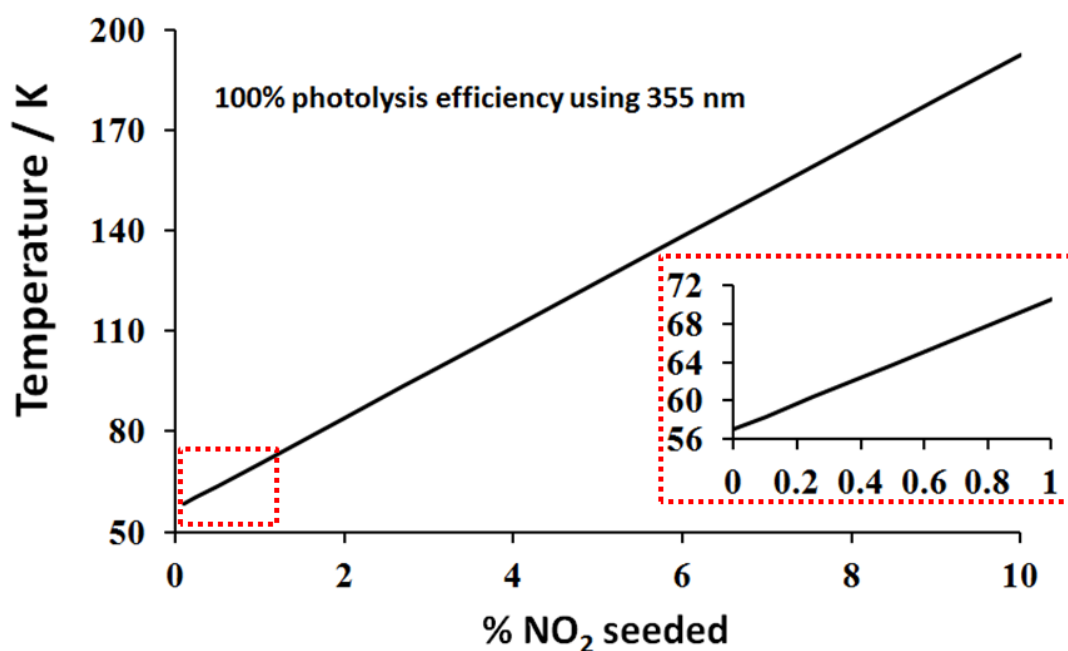


Fig. 4.9. Temperature of the Mach 4.6 freestream as a function of seeded- $\text{NO}_2$  percent at a 100% photodissociation efficiency.

Figure 4.10 illustrates the combined effect of using high  $\text{NO}_2$  seeded fractions with a high photodissociation efficiency on an NO PLIF two-line temperature measurement. The measurement in the Mach 4.6 freestream using 5%  $\text{NO}_2$  and the full 355 nm laser power directed in the vertical direction through an aluminum mesh results in temperatures ranging from 75 K to 95 K for the non-attenuated and attenuated regions, respectively.

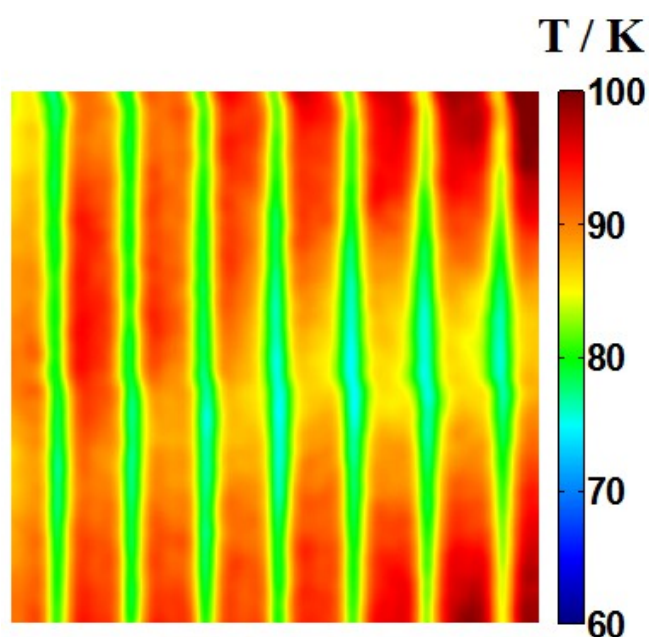


Fig. 4.10. Temperature map of the Mach 4.6 freestream seeding 5% in  $\text{NO}_2$  with high fractional photodissociation.

In practice, the photodissociation efficiency is not 100%, and the photolysis beam is divided into vertical and horizontal components to "write" a full grid. In the following sections it will be demonstrated that using low  $\text{NO}_2$  seeding fractions in the measurements results in perturbations considerably less than 10 K in the Mach 4.6 freestream.



### IV.3.1 Rotational Thermalization Measurements Using $\text{NO}(v''=0)$ and $\text{NO}(v''=1)$

The translational and rotational degrees of freedom are assumed to be strongly coupled so that seeded, or naturally occurring, NO is in local thermodynamic equilibrium with the flow. However, if NO is photolytically generated from seeded  $\text{NO}_2$ , it is initially not in local thermodynamic equilibrium. Since the two-line PLIF thermometry technique utilizes rotational temperatures as a proxy for local rotational/translational temperature it is critical that rotational thermalization via collisional energy transfer occurs prior to such measurements.

The nascent ro-vibrational state distributions of the NO products have been characterized and are well described by microcanonical statistical models for energy partitioning of the excess energy, i.e. the photon energy minus the bond dissociation energy. The  $\text{NO}_2$  bond dissociation energy is  $25130 \text{ cm}^{-1}$ , while the 355 nm photon energy is  $28169 \text{ cm}^{-1}$ . After photodissociation, the available energy for the  $\text{NO}(v''=0)$  and  $\text{NO}(v''=1)$  photoproducts is  $3039 \text{ cm}^{-1}$  and  $1164 \text{ cm}^{-1}$ , respectively. Assuming an equipartition of this excess energy ( $3/2 kT + kT$ ), and a Boltzmann distribution,  $\text{NO}(v''=0)$  is produced at a rotational temperature of  $\sim 1775 \text{ K}$ , while  $\text{NO}(v''=1)$  is produced at a rotational temperature of  $\sim 690 \text{ K}$ . In reality, the rotational distributions are predicted by Phase Space Theory (PST) while variational Rice-Ramsperger-Kassel-Marcus theory or the Separate Statistical Ensembles Method describes the vibrational distributions [69, 70, 71]. The vibrational distributions which in this case include only two states,  $v''=0$  and  $v''=1$ , can be described by a Boltzmann temperature, while the rotational distributions are non-Boltzmann and therefore cannot be assigned an effective temperature. The vibrational specific NO rotational distributions arising from the 355 nm photolysis of  $\text{NO}_2$  at 300 K [65] are shown in the form of Boltzmann plots in figure 4.11. For comparison, Boltzmann NO rotational distributions at 300 K are provided (dashed lines). For reference and better understanding of this figure, the plot also includes the best fit rotational temperatures to the nascent NO ( $v''=1$ ) and NO ( $v''=0$ ) distributions (solid lines), which result in 850 K and 1400 K, respectively. It has been previously demonstrated that the nascent NO rotational distributions reflect the

wavelength-dependent photolysis of the seeded  $\text{NO}_2$  rather than the temperature of the flow field [65].

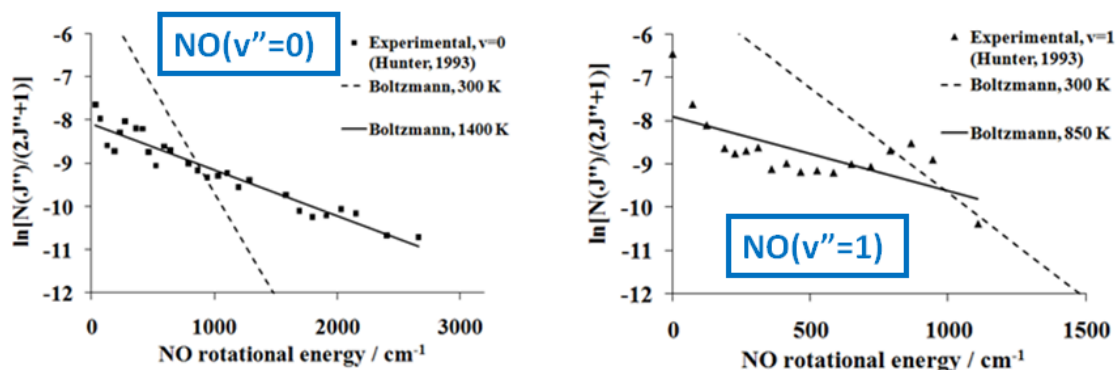


Fig. 4.11. Boltzmann plots of the vibrational specific nascent NO rotational distributions produced by photodissociation with 355 nm. The experimental distributions were measured in an expansion-cooled  $\text{NO}_2$  sample.

Rotational energy transfer (RET) via collisions between the nascent NO from  $\text{NO}_2$  photolysis and bath gas serve to thermalize the rotational distributions. There are several models for state-to-state ( $J_i \rightarrow J_f$ ) RET cross sections [72,73,74], and optical-optical double resonance experiments have provided direct measurement of these values for specific systems [75,76]. Transitions between small values of  $\Delta J$  are efficient, often exceeding the hard-sphere collision rates.

For temperature determinations using the  $\text{NO}_2$  photodissociation, the concern is how long it is required to wait in order to reach the temperature of the flow field. For this purpose, a series of experiments were performed in order to find the thermalization times required when probing the two NO products generated by 355 nm photolysis:  $\text{NO}(v''=0)$  and  $\text{NO}(v''=1)$ . These experiments were performed in an aluminum cell with a 10 sccm flow of 2.5%  $\text{NO}_2$  in  $\text{N}_2$  at 294 K and a total pressure of 66.7 Pa. After producing  $\text{NO}_2$  photolysis with a 355 nm laser sheet, the rotational temperatures were determined using two-line PLIF by probing the  $R_1 + Q_{21}$  ( $J=1.5$ ) and  $R_1 + Q_{21}$  ( $J=17.5$ ) transitions, in the  $^2\Sigma^+ (v' = 0) \leftarrow X^2\Pi (v'' = 0)$  band in order to estimate the rotational temperature of

NO( $v''=0$ ) and the same transitions in the  $^2\Sigma^+ (v' = 1) \leftarrow X^2\Pi (v'' = 1)$  band in order to estimate the rotational temperature of NO( $v''=1$ ). Fifty single-shot images were acquired and averaged at each time after photodissociation using camera gates of 25 ns. The temperatures of a 1 cm x 1 cm area were averaged and then plotted as a function of time after photodissociation. This results are summarized in Figure 4.12.

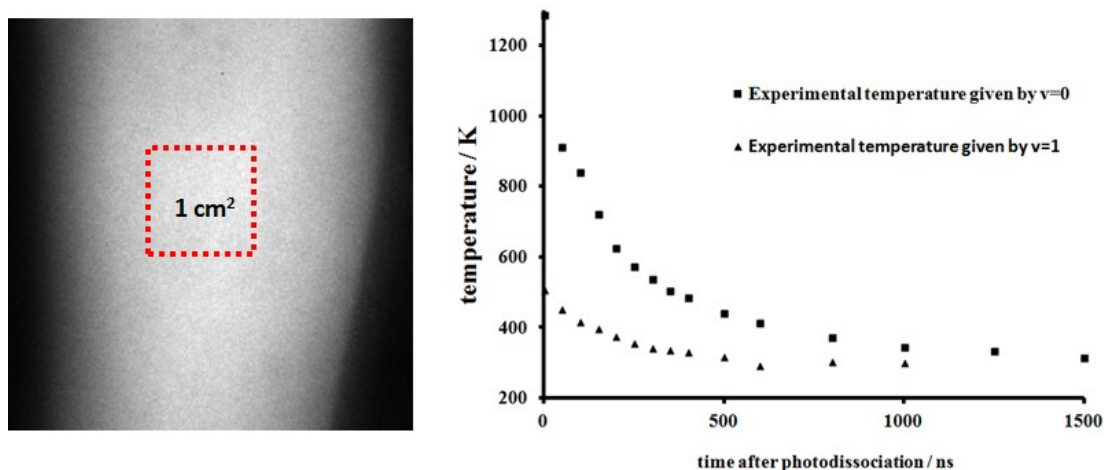


Fig. 4.12. 50-shot fluorescence average image showing the area of interest (left). Rotational temperature measurements as a function of time after photodissociation for NO( $v''=0$ ) and NO( $v''=1$ ) in an N<sub>2</sub> gas bath at 66.7 Pa and 294 K (right).

In order to find a time constant for each thermalization process, the temperature decay was fitted with the following equation:

$$T = a + b * \exp [-c * (t + d)] \quad (\text{Eq. 4.2})$$

where

T = measured temperature

t = time at which T was measured

a = shift from zero temperature (should be  $\sim$  near 296 K. It could be fixed to the measured room temperature, but it was left as an extra fitting parameter)

b = initial temperature after photodissociation ( + a)

c = decay constant in  $\text{ns}^{-1}$

d = shift from t, (t + d) is the real time at which T was measured, just added as a “safety/consistency” extra factor, should be within 10 ns of the probe laser shot to take into account the small shift of the camera gates to avoid scattered light.

It can be observed in figure 4.13 that the measured temperature at time zero after photodissociation is above 500 K for  $\text{NO}(v''=1)$ , and the rotational thermalization for this vibrationally excited photoproduct could be properly described by the previous equation. The fitting parameters are summarized in table 4.3. Thermalization of  $\text{NO}(v''=1)$  with the bath gas occurred, under the described experimental conditions, with a time constant of  $354 \pm 45$  ns.

Table 4.3. Fitting parameters associated to a single exponential temperature decay for  $\text{NO}(v''=1)$ .

Species	$\text{NO}(v''=1)$
$X_{\text{NO}_2}$	0.025
$[\text{I}] / \text{cm}^{-3}$	$1.64 \times 10^{16}$
T / K	294
a	298.6
b	209
c	0.002822
d	11.35
$k[\text{A}] / \text{s}^{-1}$	$2.822 \times 10^6$
$k / \text{cm}^{-3} \text{s}^{-1}$	$1.72 \times 10^{-10}$

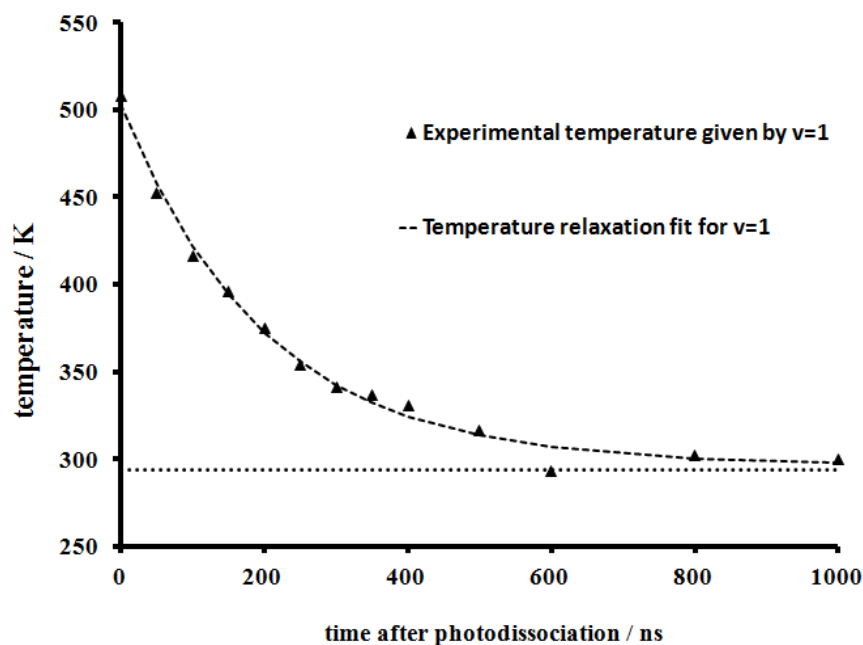


Fig. 4.13. Rotational temperature thermalization fit after photodissociation with a single exponential temperature decay function for NO ( $v''=1$ ) in an  $N_2$  gas bath at 66.7 Pa and 294 K.

The measured temperature at time zero after photodissociation for NO( $v''=0$ ) was above 1200 K, and the experimentally obtained rotational thermalization shown in Figure 4.12 could not be fit using equation 4.2. The thermalization plot exhibits an initial short-time behavior and, as a consequence, a two exponential temperature decay fit was performed. Figure 4.14 shows the two exponential fitting and table 4.4 shows a summary of the resulting fitting parameters.

$$T = 296 + b * \{\exp[-c * (t + d)] + \exp[-e * (t + d)]\} \quad (\text{Eq. 4.3})$$

Table 4.4. Fitting parameters associated to a double exponential temperature decay for NO( $v''=0$ ).

Species	NO( $v''=0$ )
$X_{NO2}$	0.025

Table 4.4. Continued.

Species	NO( $v''=0$ )
$X_{\text{NO}_2}$	0.025
$[\text{I}] / \text{cm}^{-3}$	$1.64 \times 10^{16}$
T / K	295.7
a	296
b	620.3
c	0.00278
d	22.06
e	0.01996

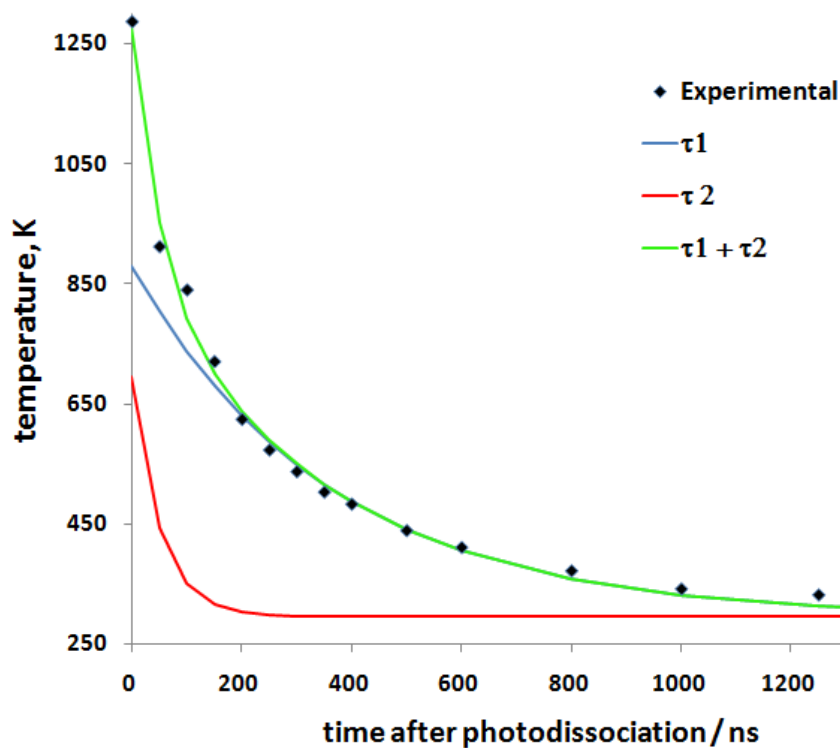


Fig. 4.14. Rotational temperature thermalization fit after photodissociation with a double exponential temperature decay function for NO ( $v''=0$ ) in an  $\text{N}_2$  gas bath at 66.7 Pa and 294 K. The temperature decay cannot be explained by a single exponential.

Thermalization of NO( $v''=0$ ) with the bath gas occurred with a time constant of  $360 \pm 27$  ns and, compared to NO( $v''=1$ ), the times required to reach within 3% of the

bath gas temperature of 294 K, are about 500 ns longer under this conditions. This is due to the higher average nascent rotational energy which requires more collisions to reach a room temperature Boltzmann distribution. In addition, for  $\text{NO}(v''=0)$ , the double exponential fitting is needed because the short-time behavior, with a time constant of  $50 \pm 8$  ns, is result of the higher average velocity (up to 900 m/s for low rotational states, as seen in figure 4.7) which decreases the time to the first hard sphere collision. Although there are only two points associated to the short-time behavior (Figure 4.14), an extrapolation of the  $v''=0$  data to time zero yields a rotational temperature inconsistent with the known nascent rotational temperature ( $> 1200$  K) originating from photodissociation using 355 nm.

Given the gas density in these experiments, the rotational thermalization times for  $\text{NO}(v''=0)$  and  $\text{NO}(v''=1)$  correspond to effective rate constants of  $1.69 \times 10^{-10}$  molecule  $\text{cm}^3 \text{s}^{-1}$  and  $1.72 \times 10^{-10}$  molecule  $\text{cm}^3 \text{s}^{-1}$  for  $\text{N}_2$  as the bath gas, and cross sections of  $2.56 \times 10^{-15}$   $\text{cm}^2$  and  $2.60 \times 10^{-15}$   $\text{cm}^2$ . In general, for pressures of several Torr, delay times on the order of few hundreds of nanoseconds are sufficient to ensure complete rotational thermalization.

The previous measurements were performed in a homogeneous room-temperature static field. However, a real flow field is composed by regions of varying temperature and gas density conditions. For this reason, temperature measurements were performed in an underexpanded jet flow field at varying times after photodissociation. Briefly, an underexpanded jet is produced when a gas is allowed to escape through a nozzle from a region where the gas pressure is  $p_o$  into a region with  $p_a$ , where the jet pressure ratio, JPR,  $p_o/p_a \geq 2$ . For a highly underexpanded jet, the flow is initially confined by a barrel shock structure surrounding an interior where the gas expands and cools to be then suddenly recompressed by a strong shock normal to the flow direction, called the Mach disk. The use of such a complicated flow field is justified by the fact that it is very well documented in the literature (see for example reference [77]) and it shows a wide variety of pressure, temperature and velocity conditions, offering a

challenging, yet well-characterized, environment to test experimental diagnostic techniques.

The thermometry experiments were performed in the RPHT apparatus described in Chapter 3. In order to generate an underexpanded jet flow field, the converging-diverging nozzle was replaced by an aluminum 1 inch i.d. cylindrical nozzle with a 1 mm pinhole plate on the exit end, and the armature and spring systems were removed from the interior of the pulsed valves in order to permit continuous flow into the cylindrical nozzle. As explained earlier, the aluminum mesh used to provide a photodissociation modulation pattern of high and low NO photoproduct density regions, would permit the measurement of velocity and full-frame temperature maps. To prove this principle, two 355 nm laser sheets aligned orthogonal to each other were used to photodissociate the seeded  $\text{NO}_2$ . This setup as well as the laser alignment configuration are shown in figure 4.15. The gas mixture in the stagnation region had a composition of 6.3% of  $\text{NO}_2$  in  $\text{N}_2$ , a temperature of 294 K, and a pressure of 59.3 kPa, and was expanded through a pinhole nozzle of 1 mm diameter into an evacuated chamber maintained at 253 Pa, to produce an underexpanded jet with a jet pressure ratio (JPR) of 234. The laser alignment configuration used in these experiments is shown in figure 4.15.



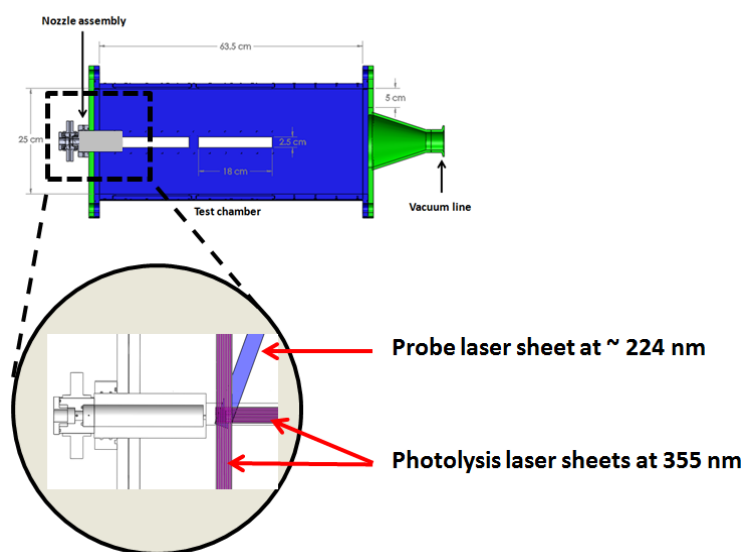


Fig. 4.15. Experimental setup for the temperature relaxation experiments in the underexpanded jet flow field.

The NO grid was “written” via the 355 nm laser with a total power of 100 mJ per pulse. The 9 mm diameter beam was expanded by a 2.5X beam expander and split with a 50:50 beam splitter into the vertical and horizontal laser sheets aligned through the centerline of the flow. The orthogonal photodissociation sheets were passed through an aluminum mesh to produce a grid of nascent NO. The experimental timing followed that shown in figure 4.2 where  $\tau_1$  ranged from 250 to 2000 ns and  $\tau_2$  was zero. The laser systems were tuned to probe the  $A^2\Sigma^+ (v' = 1) \leftarrow X^2\Pi (v'' = 1)$  band on the  $R_1 + Q_{21}$  (1.5) and the  $R_1 + Q_{21}$  (8.5) transitions. The temperature was estimated at each time delay based on 100 fluorescence single-shot average images acquired sequentially with each probe laser while the other remained blocked. The constant  $C_{12}$  was experimentally determined assuming a temperature of 294 K on the image area corresponding to the exterior of the underexpanded jet structure. Figure 4.16 shows the average image pairs obtained at each time delay.

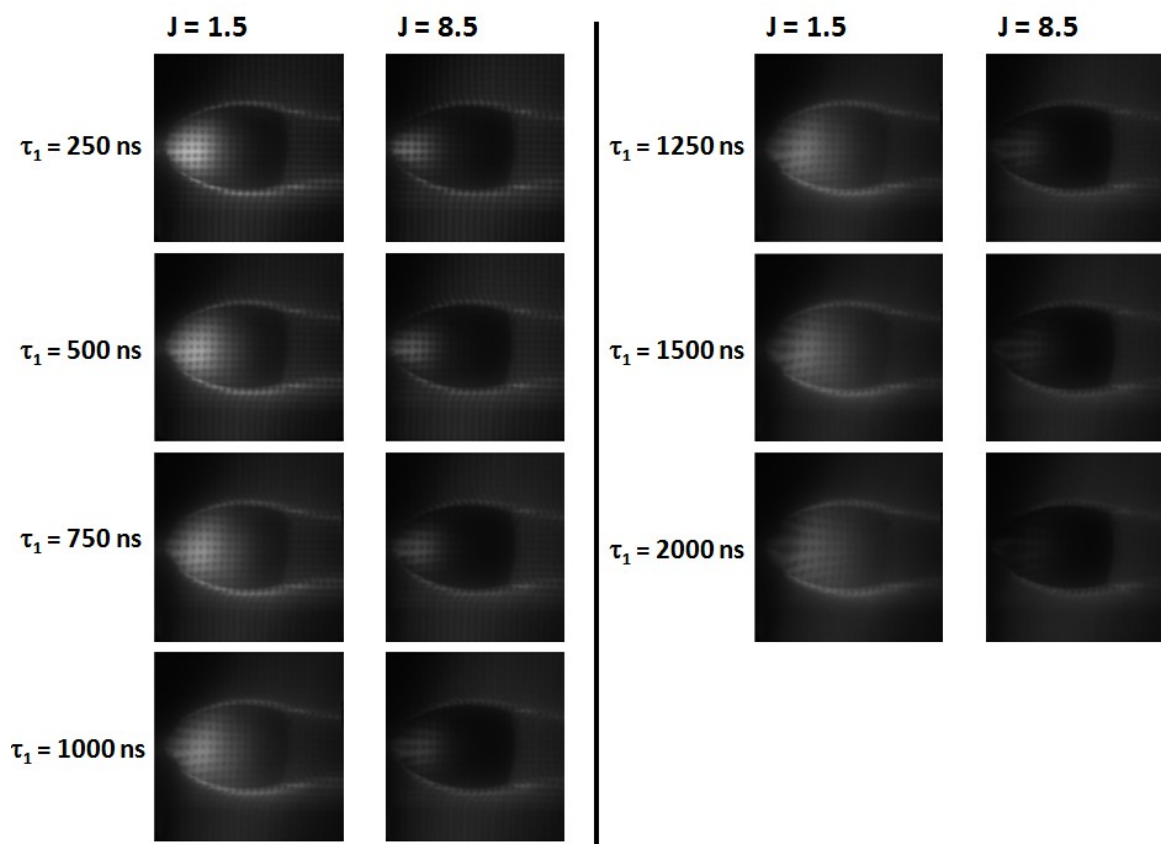


Fig. 4.16. Average fluorescence images of the underexpanded jet probing two different rotational states at different times  $\tau_1$  after photodissociation.

The temperatures in the underexpanded jet under the experimentally tested conditions range from approximately 40 to 300 K. It can be observed in figure 4.16 how the fluorescence intensities in different regions of the flow field change as a function of time after photodissociation as a result of redistribution of the rotational populations. The most remarkable change is observed in the region immediately upstream of the Mach disk. This is the region of the flow field with the lowest expected temperature, and over time it shows an increase in fluorescence intensity for the  $J=1.5$  images. On the other hand, the same region in the  $J=8.5$  images show a drastic decrease in intensity. These changes reveal that, over time, the photodissociation-generated rotational populations shift from the high rotational states to low rotational states. Figure 4.17

shows the temperature maps estimated from the fluorescence image pairs shown in figure 4.16.

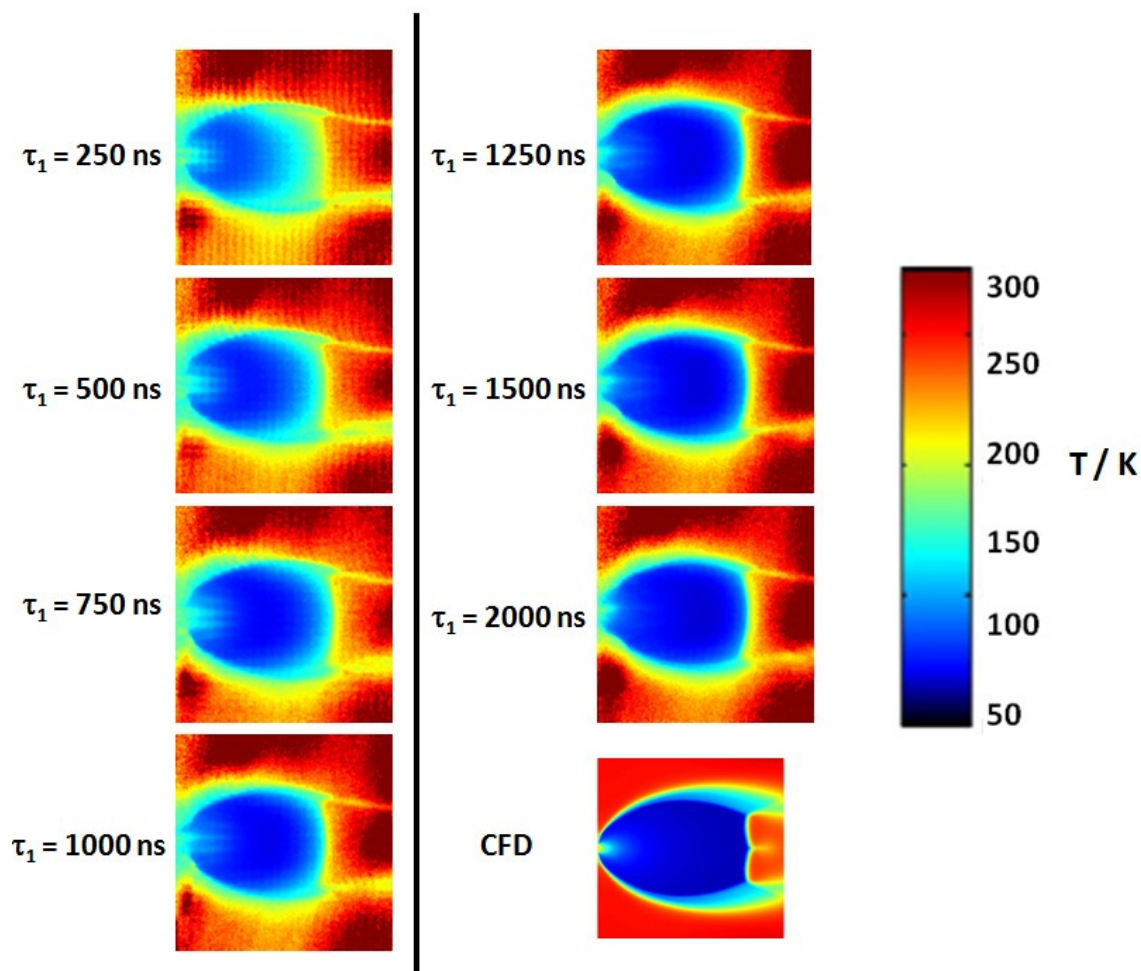


Fig. 4.17. Calculated temperature at different times  $\tau_1$  after photodissociation. A CFD temperature map is shown for comparison.

As observed in figure 4.17, at  $\tau_1=500$  ns the temperature derived from the measurements is close to the CFD predictions in the relatively high density regions, i.e. the nozzle exit and downstream of the Mach disk. In the lower density region before the Mach disk, however, the derived temperature is significantly higher than predicted.

These observations can be quantitatively visualized if the temperature profiles across the centerline are plotted as shown in figure 4.18.

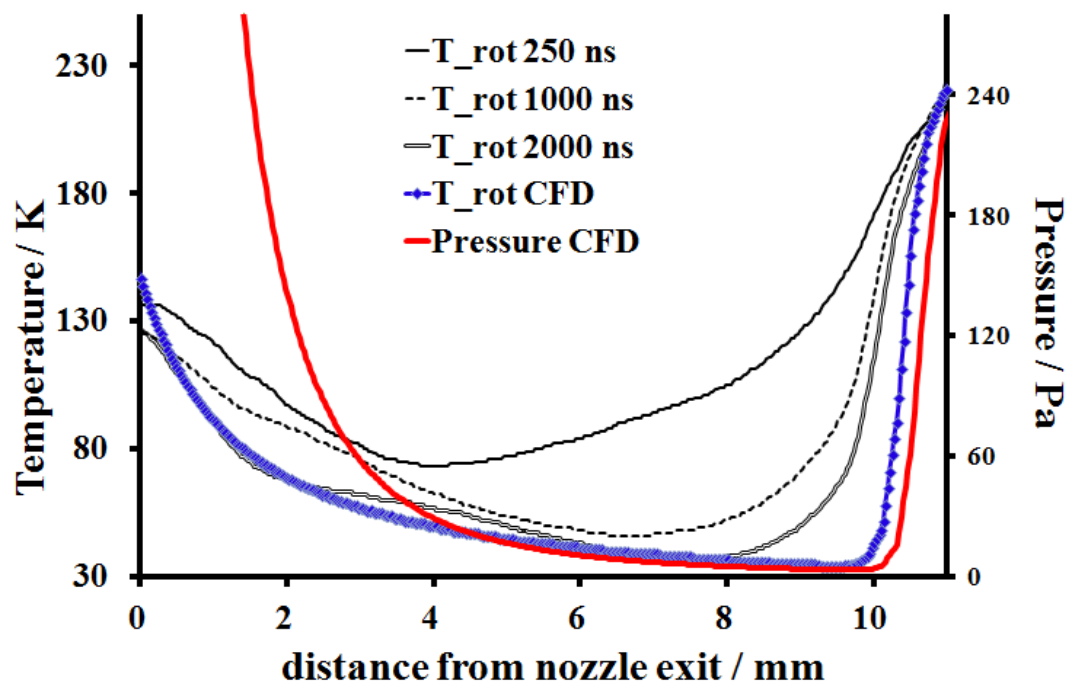


Fig. 4.18. Centerline profiles of the calculated temperature at different times  $\tau_1$  after photodissociation. A CFD temperature profile is shown for comparison.

For clarity, only the experimentally obtained temperature profiles at  $\tau_1 = 250$ , 1000 and 2000 ns have been plotted in figure 4.18. At early times after photodissociation, the overestimation of temperature right before the Mach disk reflects incomplete thermalization of the nascent rotational distribution arising from  $\text{NO}_2$  photolysis since there are few collisions prior to the read laser sequence. At longer time delays between the “write” and “read” pulses, lower temperatures are measured in this region, consistent with rotational relaxation. It should be noted that given the streamwise velocity, delay times of  $\tau_1 > 1\mu\text{s}$  correspond to spatial displacements on the order of the jet structure and so the derived temperature reflects both the rotational relaxation and the transit from higher density regions upstream.

### IV.3.2 Temperature Measurement Uncertainties

A set of temperature measurements in the uniform Mach 4.6 flow were performed, using a gas composition of 0.6% NO<sub>2</sub> diluted in N<sub>2</sub> and time delays of  $\tau_1$  2000 ns and  $\tau_2$  of 950 ns. One of the primary objectives of this work is the estimation of instantaneous temperature fields, and this is only achieved by single-shot experiments. The main source of temperature uncertainty when using the two-line thermometry technique for instantaneous measurements is attributable to the probe laser shot-to-shot fluctuations. Measured fluctuations for both probe lasers were acquired and are plotted for 200 shots in figure 4.19.

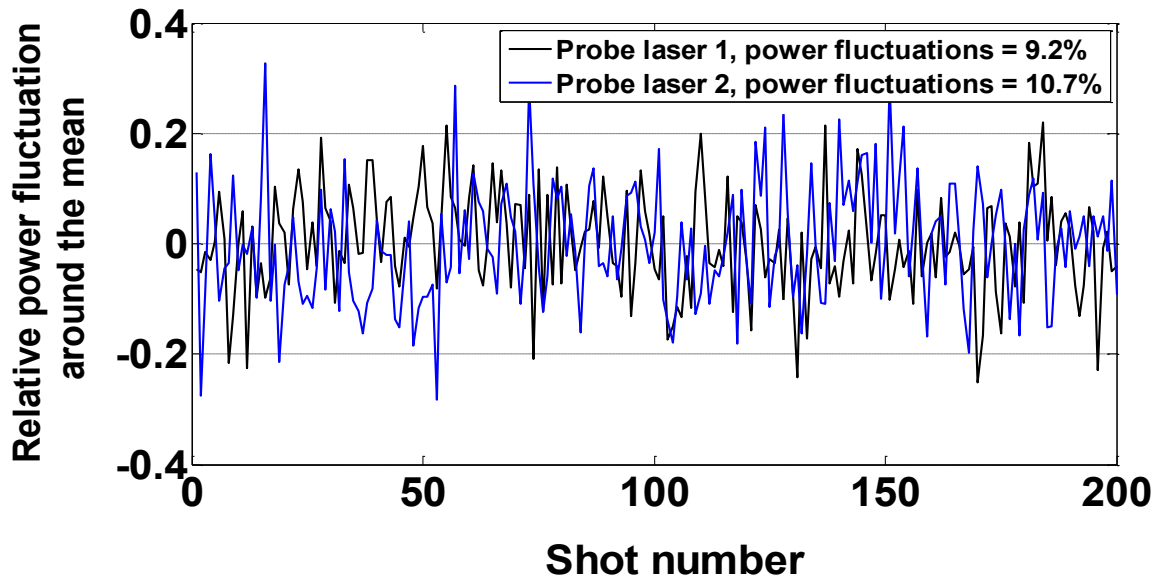


Fig. 4.19. Measured power fluctuations of the VENOM probe laser systems.

The measurement of the power fluctuations resulted in a maximum of 10% from shot to shot. Recalling equation 1.19,  $\frac{\partial T}{T} = \frac{kT_{rot}}{\Delta E} \frac{\partial R_{12}}{R_{12}}$ , the temperature uncertainty,  $dT/T$  will scale with the uncertainty in the measured fluorescence ratio  $dR_{12}/R_{12}$ . For a maximum of 10% power fluctuations of each probe laser, the uncertainty in the measured fluorescence ratio is 14%. Figure 4.20 shows the measured fluorescence ratio

based on the power fluctuations shown in figure 4.19 as well as the corresponding temperature uncertainties,  $dT/T$ , when probing the  $J = 1.5$  and  $J = 8.5$  transitions of NO.

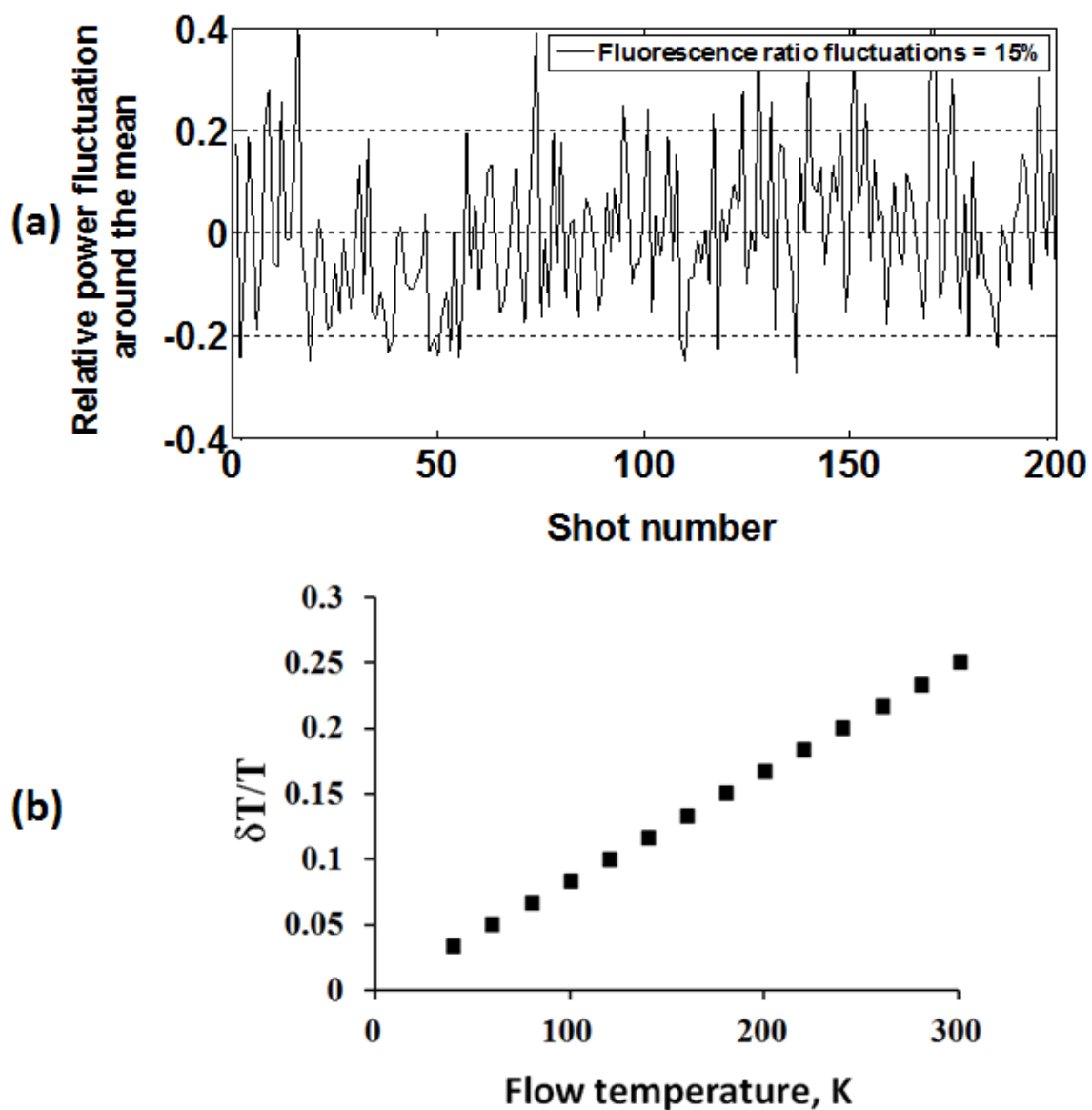


Fig. 4.20. Measured fluorescence ratio fluctuations (a) and expected temperature uncertainties as a function of measured temperature.

From the plot shown in figure 4.20, for a temperature measurement of the Mach 4.6 freestream at 56 K by using the  $R_1 + Q_{21}$  ( $J=1.5$ ) and  $R_1 + Q_{21}$  ( $J=8.5$ ) transitions, the uncertainty of a single-shot temperature measurement due to 10% laser shot-to-shot fluctuations is 5%. In order to confirm these estimations, the temperature of the Mach 4.6 freestream was calculated from experimental fluorescence images. Figure 4.21 shows an average temperature map of the Mach 4.6 freestream obtained from 200 instantaneous image pairs as well as a temperature fluctuation map as a percentage of the freestream temperature. These results are close to the uncertainty limit reported using the two-line NO thermometry technique for instantaneous measurements in gaseous flow fields [78].

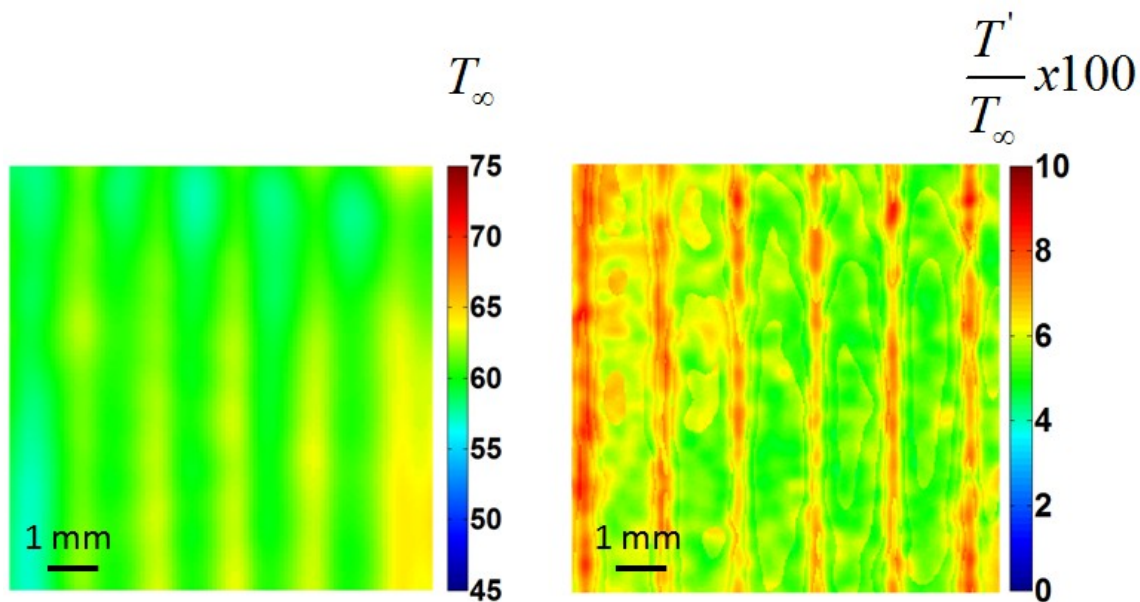


Fig. 4.21. Mach 4.6 freestream average temperature measurement (left) and measured fluctuations as a percentage of the freestream temperature based on 200 single-shot measurements.

The measured fluctuations range from 5% to 7% indicating that laser power fluctuations are the dominant factor limiting the uncertainty of the thermometry measurements using the VENOM technique. These uncertainties can be reduced if a

fluorescence intensity correction accounting for the probe laser shot-to-shot fluctuations is applied to all instantaneous fluorescence images. As explained earlier, the fluorescence images were acquired in the fluorescence linear regime, and thus, a fluorescence intensity correction is straightforward based on the measured laser shot-to-shot fluctuations.

After the shot-to-shot intensity fluctuation corrections there was a reduction in the percent fluctuations with respect to the mean temperature, from 5.5% in the uncorrected images down to 3.4 % in the intensity-corrected images, as observed in figure 4.22. The shot-to-shot corrections only account for the signal shot noise, however, the noise present in the fluorescence images also includes dark noise and readout noise, which cannot be easily accounted for.

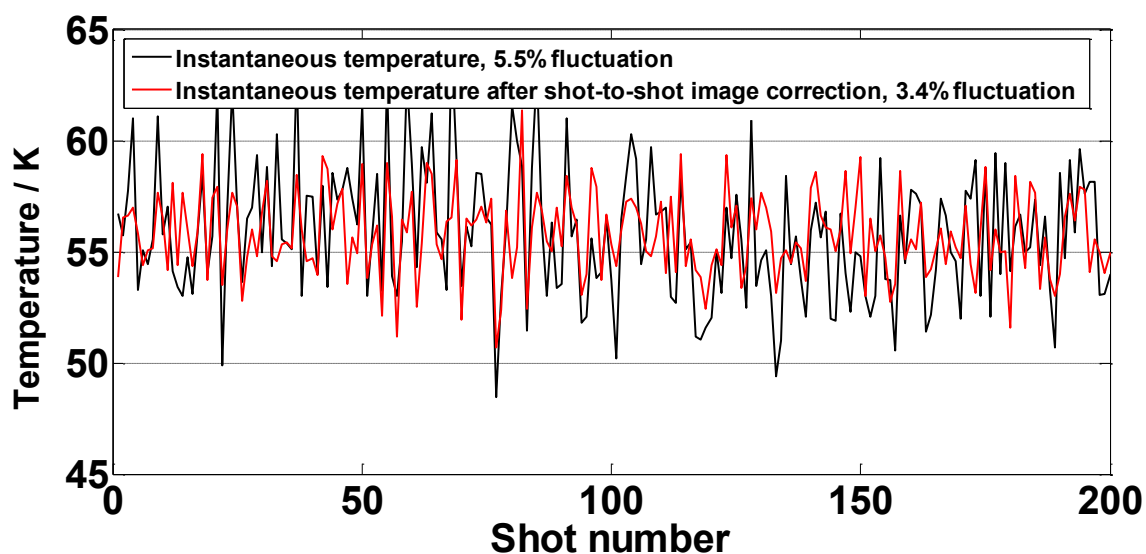


Fig. 4.22. Measured instantaneous temperature in the Mach 4.6 freestream before and after shot-to-shot fluorescence intensity correction.



#### IV.4 Summary

In this Chapter two different photodissociation schemes intended for velocity measurements were investigated, employing different methods to “write” a transient NO grid in the flow using the 355 nm photolysis of NO<sub>2</sub>, which was subsequently probed by planar laser induced fluorescence imaging to extract velocity maps. It was found that only one scheme provides full-frame temperature maps in an NO<sub>2</sub> seeded flow. The most accurate velocity measurement was attained by writing an NO pattern in the flow using a micro-lens array and then comparing the line displacement with respect to a reference image. The demonstrated uncertainty of this approach was 1.0 % corresponding to 7 m/s in a 705 m/s uniform flow.

The time needed for the collisional relaxation of the nascent NO distribution was also characterized and defined the timing scheme of the VENOM measurements. For the measurements in the Mach 4.6 flow we find that times  $>1 \mu\text{s}$  are sufficient for thermalization of the nascent NO at pressures of 1 Torr, and thus, a reliable temperature measurement can be performed.

We found that the uncertainty associated with the instantaneous temperature measurements using the NO two-line thermometry technique was largely determined by the shot-to-shot power fluctuations of the probe lasers, and for the flows employed in this work were determined to range from 5% to 7% of the mean freestream temperature. These fluctuations can be reduced if the laser power fluctuations are recorded and later used to correct the intensity of the fluorescence images acquired in the linear regime.

Ultimately, for a simultaneous velocity and temperature measurement using the VENOM technique, a mesh capable of generating a modulation in the photodissociation pattern is desired in order to obtain a full temperature map. However, a tradeoff between velocity accuracy and a full temperature map is expected based on the feature sharpness ( $\text{SNR}_v$ ) and the overall signal-to-noise ( $\text{SNR}_T$ ) achieved by the grid.

CHAPTER V

EXPERIMENTAL: SIMULTANEOUS VELOCITY AND TEMPERATURE  
MEASUREMENTS USING NO<sub>2</sub> PHOTODISSOCIATION  
- THE VENOM TECHNIQUE

The Vibrationally Excited Nitric Oxide monitoring, or VENOM, technique is proposed as a non-intrusive method to provide simultaneous 2-D measurements of the mean and instantaneous fluctuations in two-component velocity and temperature using NO as a tracer generated from the photodissociation of seeded NO<sub>2</sub>. This technique is the result of combining the two-component Molecular Tagging Velocimetry and the two-line thermometry methods discussed in Chapter 4. The VENOM technique employs the nascent NO( $v''=1$ ) arising from NO<sub>2</sub> photodissociation as a molecular tracer. The use of NO( $v''=1$ ) over NO ( $v''=0$ ) can provide discrimination in the presence of large NO background levels common in combustion systems, shock tunnels, and arcjet facilities. The feasibility of extending the NO<sub>2</sub> photodissociation velocimetry technique to simultaneously obtain 2D temperature fields in a gaseous flow field was initially demonstrated in an underexpanded jet flow field as explained in the following section. The VENOM technique is inherently well suited for simultaneous velocimetry and thermometry measurements by simply probing two different rotational states of NO with each “read” laser.

The technique is not only applicable to cold high-speed flows, which is the focus of the present study, but it is also expected to be useful in combustion and other reactive or high-enthalpy flow fields. However, the possibility of performing temperature measurements is limited by the ability of probing single rotational transitions, which does not only depend on the probe lasers' spectral linewidths, but also on the magnitude of the collisional broadening of the absorption spectral lines under the test gas conditions. In the binary collision regime, the collisional broadening at constant temperature can be expressed as:

$$\Delta\nu_c = \sum_i 2\gamma_i(T)p_i \quad (\text{Eq. 5.1})$$

where  $\Delta\nu_c$  is the collisional broadening in  $\text{cm}^{-1}$ ,  $2\gamma_i$  is the broadening coefficient defined as the NO collision width per unit pressure of the  $i^{\text{th}}$  component at constant temperature, and  $p_i$  is the partial pressure of the  $i^{\text{th}}$  mixture component.

In order to understand the effect of the pressure broadening on the absorption lines of NO, as well as the limit of a temperature measurement using the VENOM technique, figure 5.1 shows the magnitude of the line broadening as a function of pressure at 50, 300 and 1500 K.

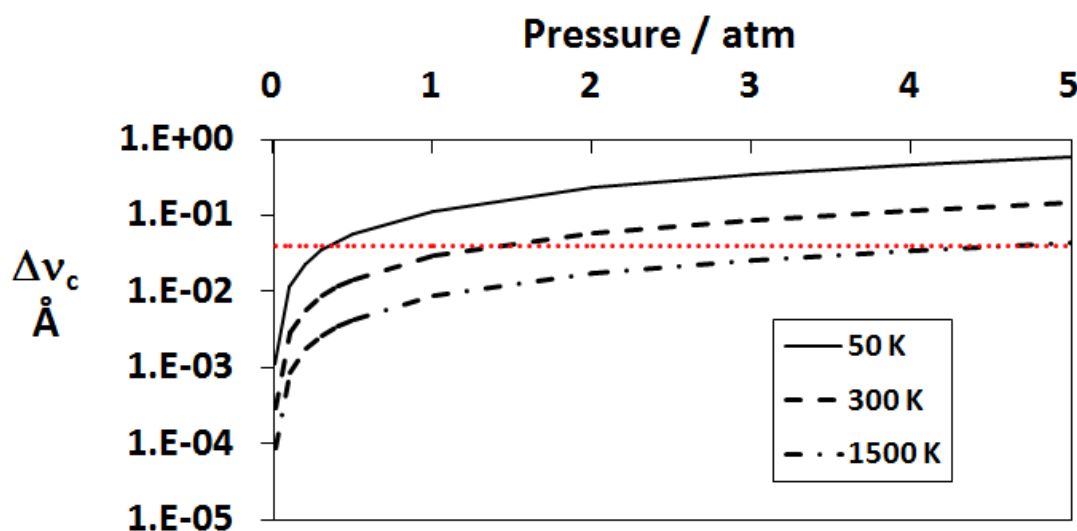


Fig. 5.1. Nitric Oxide spectral line broadening as a function of pressure. The approximate limit for rotational resolution is shown as a red line.

These broadening curves were calculated for NO diluted in air using equation 5.1 and the experimental parameters reported in [79,80]. The absorption line broadening limit for rotational resolution is approximately 0.04 Å. From the figure, it can be deduced that the measurements at low temperatures, i.e. < 100 K, can only be accomplished at

pressures well below one atmosphere. The measurements presented in this work do not suffer from significant collisional broadening effects, since the temperatures typically range from 50 to 300 K and are performed at pressures of few Torr. Nevertheless, an implementation of the VENOM technique to perform measurements in a high-pressure environment would be limited to pressures of not more than a few atmospheres in the high-temperature limit.

## **V.1 Underexpanded Jet Experiments**

The first set of experiments intended to demonstrate the feasibility of the simultaneous measurement of two-component velocity and temperature using the VENOM technique were performed in an underexpanded jet flow field. As described previously, this technique permits two-component velocity measurements in an NO<sub>2</sub>-seeded flow by tracking the fluorescence of an NO grid “written” with a high energy 355 nm photodissociation laser using two temporarily separated “read” lasers tuned to probe two different rotational states. The intensity ratio of the two fluorescence images provides a spatially resolved rotational temperature map. It should be noted that, as opposed to conventional two-line thermometry measurements, the simultaneous acquisition of a velocity map provides sufficient information to locally de-warp the second fluorescence image, generating a ratio of fluorescence intensities that correspond to identical fluid elements.

### **V.1.1 Instrumentation and Experimental Setup**

The experimental setup used for these experiments was described in detail in chapter 2. Briefly, a highly underexpanded jet flow field was generated in the RPHT cell apparatus by replacing the converging-diverging nozzle by a 1 inch i.d. cylindrical nozzle with a 1 mm pinhole plate on the exit and the pulsed valves permanently open to achieve uninterrupted gas flow. The gas mixture in the stagnation region consisted of 6.3% NO<sub>2</sub> in N<sub>2</sub> at 445 Torr and 294 K, and was expanded into the RPHT cell's main chamber maintained at a constant pressure of 1.9 Torr, resulting in an underexpanded jet

with a jet pressure ratio (JPR) of 234. The NO grid was written using 100 mJ per pulse at 355 nm. This beam was initially expanded with a 2.5X beam expander and subsequently split with a 50:50 beam splitter in order to "write" the vertical and horizontal photodissociation patterns. These orthogonal laser sheets were sent through an aluminum mesh that generated equally spaced photodissociation lines every 0.28 mm. The NO photoproduct grid was sequentially probed by two identical dye laser systems tuned to probe the  $A^2\Sigma^+ (v' = 1) \leftarrow X^2\Pi (v'' = 1)$  band on the  $R_1 + Q_{21}$  (1.5) and the  $R_1 + Q_{21}$  (8.5) transitions for the first and the second time-delayed images, respectively. A schematic of the experimental setup and the timing scheme employed to perform these experiments is shown in figure 5.2.

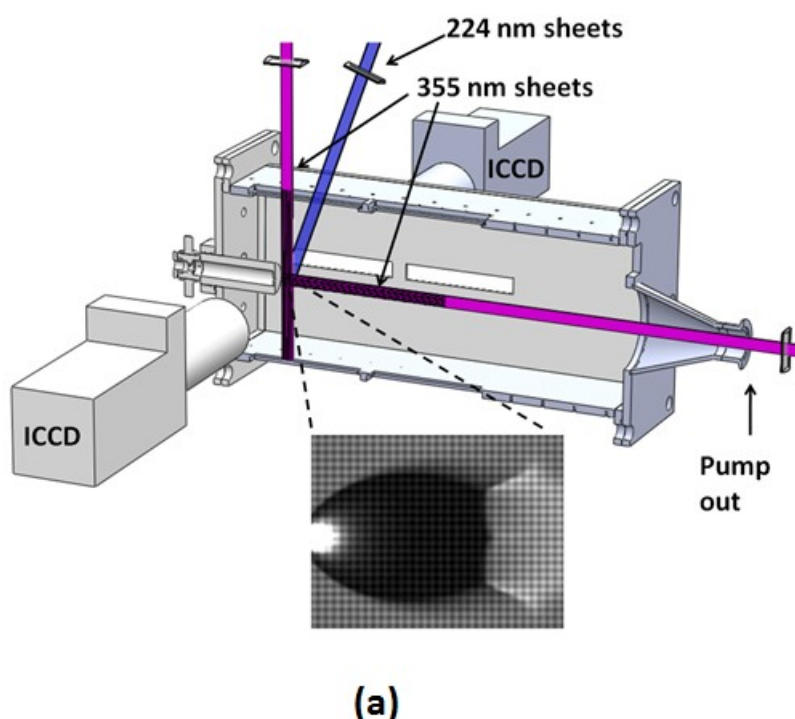
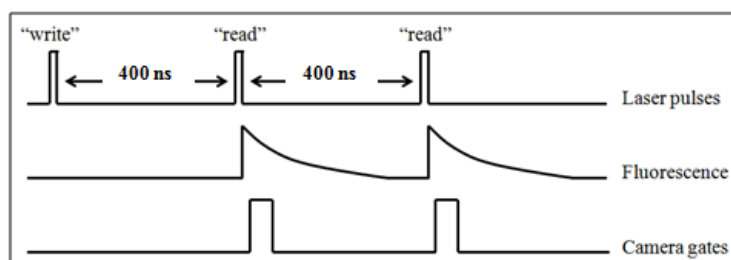


Fig. 5.2. Experimental schematic of the VENOM experiments on an underexpanded jet (b), and experimental timing schematic.



(b)

Fig. 5.2. Continued.

The fluorescence images were captured using two Andor iStar DH734 ICCD cameras situated on both sides of the vacuum chamber perpendicular to the laser sheets. The cameras were fitted with UKA 105 mm  $F = 4.0$  UV lenses and extension rings. At each time delay, 100 single-shot images were acquired at full resolution and then averaged. Figure 5.3 shows the acquired raw average images with a spatial resolution of 66 pixel per mm.

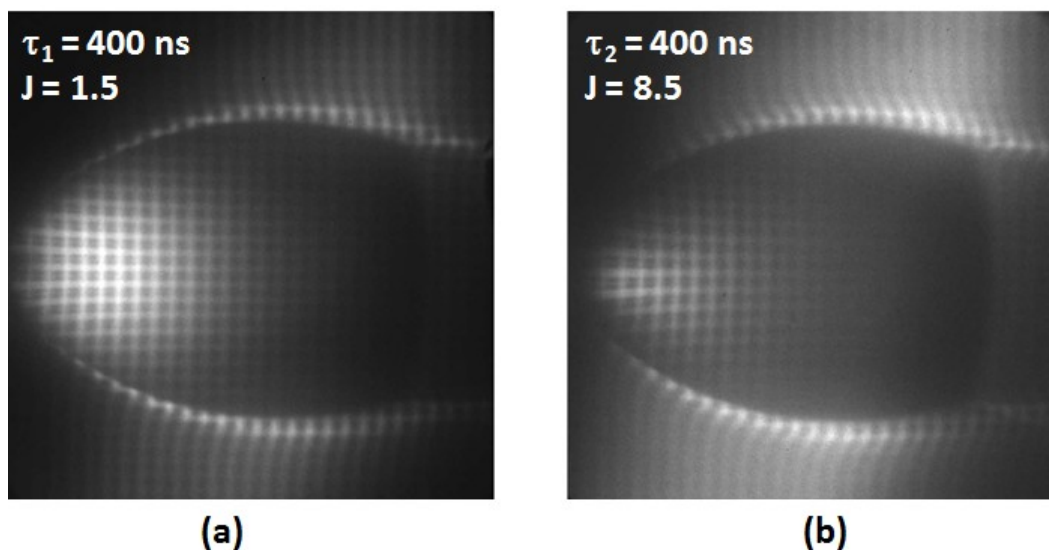


Fig. 5.3. Raw VENOM images (100-shot average) probing two different transitions at time delays of (a) 400 ns and (b) 800 ns after photodissociation.

### V.1.2 Data Analysis

It has been explained in chapter 1 that sensitive temperature measurements require maximizing the energy difference between the two probed rotational states, and higher rotational states are not significantly populated in the low temperature region before the Mach disk. The signal-to-noise levels range from 2 to 17 in the low-J image and from 1.5 to 8 in the high-J image for the data shown in figure 5.3. The low signal in the second, high-J, time-delayed image limits the accurate grid intersection location especially in the coldest region of the flow field. For this reason, only the first time-delayed image was used to obtain the velocity map, evaluating the grid intersection displacements with respect to a fitted time zero grid image exploiting the well-known periodicity of the initial photodissociation pattern. The velocity analysis of this data follows the procedure described in Chapter 2, only differing in the use of a synthetically generated image as a time-zero image.

An experimentally obtained fluorescence image of the grid under stationary conditions is shown in figure 5.4 (a) next to the synthetic image (b) generated in Matlab employed as the  $t = 0$  ns image.

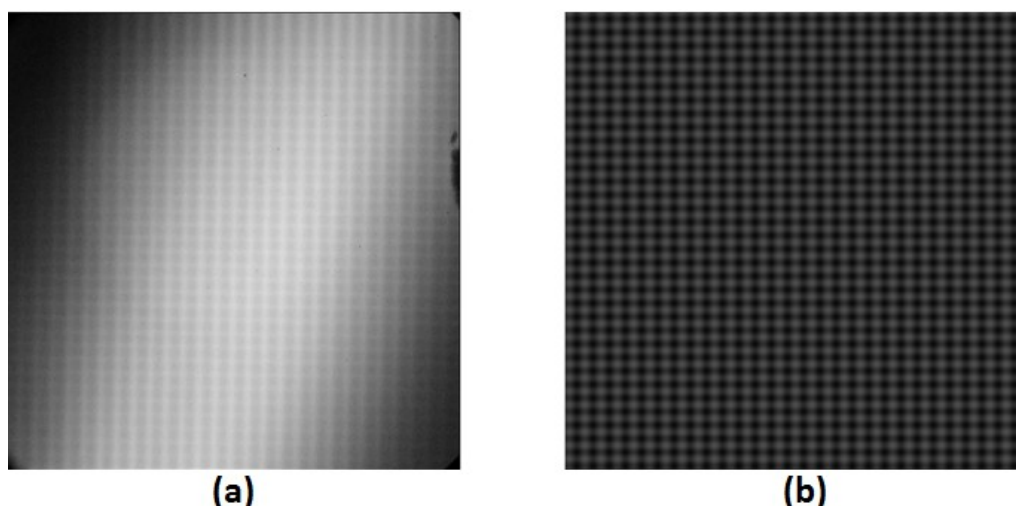


Fig. 5.4. Fluorescence image taken at  $t = 0$  under stationary conditions (a) and synthetic fluorescence image used as reference to estimate the velocity map (b).

The time zero grid was acquired in stationary conditions in the same chamber using 6.63% of  $\text{NO}_2$  in  $\text{N}_2$  at a total pressure of 5 Torr. The grid intersections are well-known at time zero, and the employment of a synthetic image for the intersection location at time zero reduces the uncertainty of the velocity measurement to the uncertainty in the location of the time-delayed image intersections. Due to spatial fluctuations in the signal-to-noise levels in a real fluorescence image, the location of the fluorescence local maxima or minima does not always result in straight lines, as shown in figure 5.5, even at time zero.

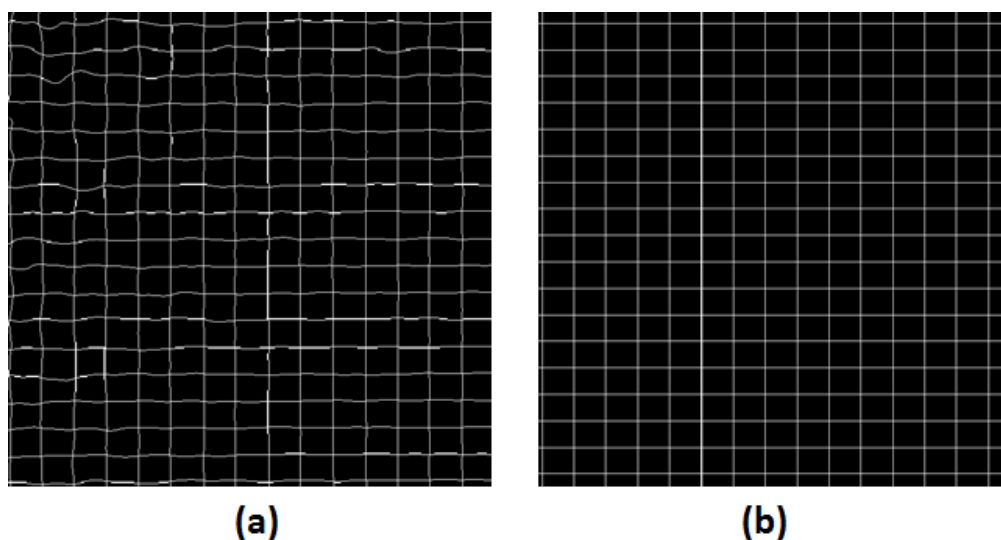


Fig. 5.5. Intersection location in a time zero fluorescence image (a) and in a time zero synthetic image (b).

In the limit of small displacements the velocimetry analysis provides the transformation matrix needed to warp the time-delayed grid back onto the initial grid. Once the grids are aligned between the two images, extraction of rotational/translational thermometry information is possible, because the ratio of the fluorescence images directly reflects the spatially resolved internal temperature [3,4]. Such analysis is robust, provided that the time delays are not sufficiently long to be affected by diffusion, out-of-plane transport, and complex quenching over the flow trajectory.



### V.1.3 Results

The derived 2D streamwise velocity map is shown in figure 5.6 (left, upper panel) as well as a comparison to a computational fluid dynamics (CFD) simulation (left, lower panel). The overall agreement in velocity magnitudes is good for most regions of the flow. Figure 5.6 (right, upper panel) shows the temperature map derived from the data presented in figure 5.3. The lower panel shows a CFD simulation for comparison. In regions of the flow characterized by higher density, the experimental temperature results are in good agreement with the CFD results. In the lower density regions, and particularly in the region before the Mach disk, the experimental temperatures are significantly overestimated.

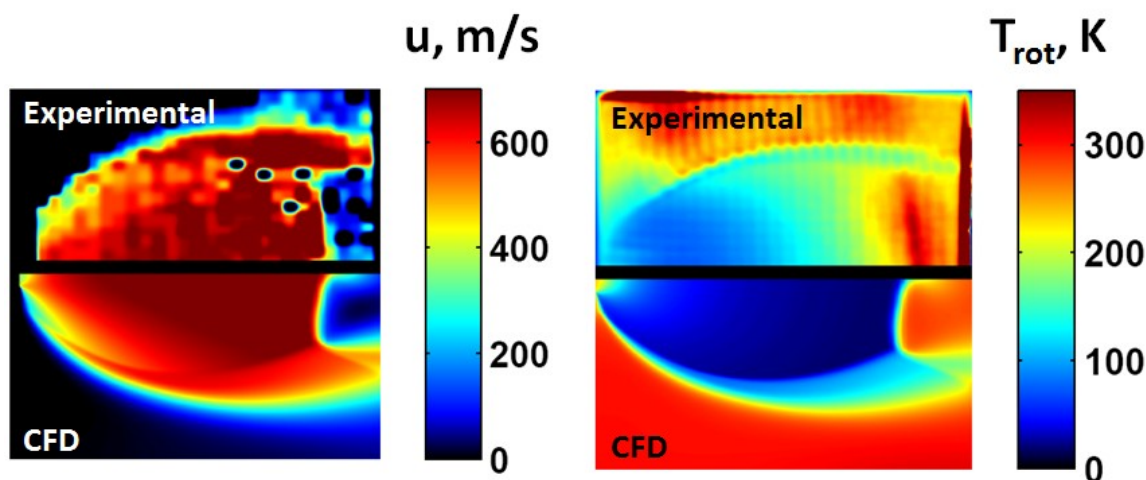


Fig. 5.6. Interpolated average streamwise velocity map (left) and temperature map (right) shown together with a CFD simulation obtained from 100-shot average images of an underexpanded jet probing two different transitions at 400 ns and 800 ns after photodissociation.

The temperature overestimation is due to insufficient collisional relaxation of the nascent  $\text{NO}(v''=1)$ , produced with a rotational temperature of  $> 500$  K after  $\text{NO}_2$  photolysis using 355 nm, during the write-read delay time. This issue has been addressed in Chapter 4 and, in order to measure correct temperatures using the VENOM

technique, several hard sphere collisions must occur prior to the PLIF read sequence. Given a time delay of 400 ns between the “write” and initial “read” pulse, incomplete thermalization is expected at pressures less than 1 Torr. The feasibility of single-shot velocity measurements using VENOM has been discussed previously [2], where rms velocity uncertainties for 1-component velocimetry were about 10% in the high signal-to-noise regions of the fluorescence images. Because the uncertainties are highly dependent on signal-to-noise levels the same constraint applies when two rotational states are probed to obtain temperature information. Given the current choice of rotational states, the measured rms temperature uncertainties ranged from 9% in the exit of the jet to 35% before the Mach disk.

The underexpanded jet was initially chosen to demonstrate the feasibility of performing temperature measurements associated to a two-component velocity determination. However, as shown previously, rotational thermalization did not occur within a practical time scale to perform a velocity measurement, usually of few  $\mu\text{s}$  for high-speed flows, due to the extremely low pressures encountered before the Mach disk ( $< 1 \text{ Pa}$ ). For this reason, a Mach 4.6 flow field was chosen to evaluate the performance of the combined velocity/temperature instantaneous VENOM measurements.

## **V.2 Mach 4.6 Flow Over a Cylinder - Cylinder Wake Measurements**

The VENOM measurements described in the previous section employed only the first time-delayed fluorescence image to obtain a velocity map by comparing the intersections displacements against a synthetically generated grid image. The uncertainties in the velocity measurements using that approach are lower, however, a true simultaneous velocity/temperature measurement is only possible when the velocity is determined by using the instantaneous images generated by both sequentially acquired fluorescence images. This section demonstrates true simultaneous velocity/temperature measurements using the VENOM technique in the wake of a Mach 4.6 flow over a 3.2 mm diameter cylinder.

The importance of flow fields involving the wake formed behind objects exposed to high-speed flows originates in the study of the performance of intercontinental ballistic missiles and high-speed vehicles re-entering the atmosphere. The exposure of a blunt body to a hypersonic flow leads to the formation of a prominent bow shock in the object's front. The flow field's structure of a Mach 4.6 flow over a cylinder is illustrated in figure 5.7.

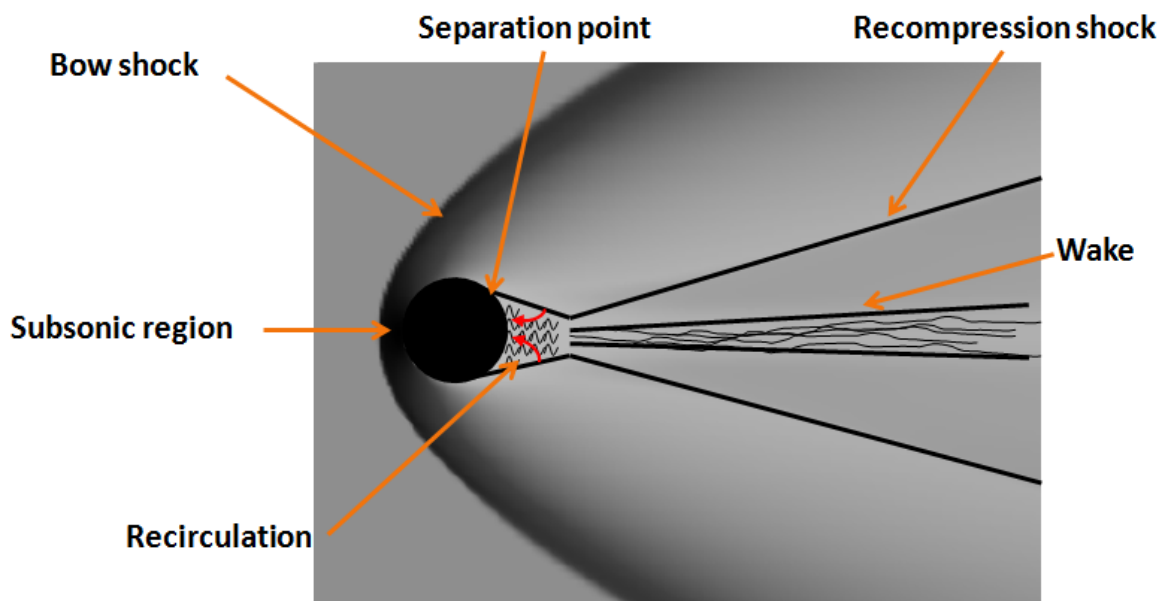


Fig. 5.7. Schematic of Mach 4.6 flow over a cylinder.

The flow, moving from left to right, traversing the shock right in front of the object becomes subsonic and reaches a stagnation region characterized by the highest temperatures and densities in the entire flow field. The boundary layer after the separation point behind the cylinder forms a free shear layer. The inner part of this shear layer reaches the reattachment point that turns back and recirculates, while the outer part continues to flow downstream until it reattaches and experiences a recompression.

The VENOM measurements were performed in three different regions of the described flow field. These regions are depicted in figure 5.8 and are: (1) the undisturbed

freestream, (2) the near-wake, and (3) the wake further downstream. The characterization of the freestream using NO MTV and NO two-line thermometry, as well as the VENOM technique were completed earlier to evaluate the properties of the Mach 4.6 flow, as presented in Chapter 3. These flow properties are spatially homogeneous and well-known and therefore are not of presented in this section.

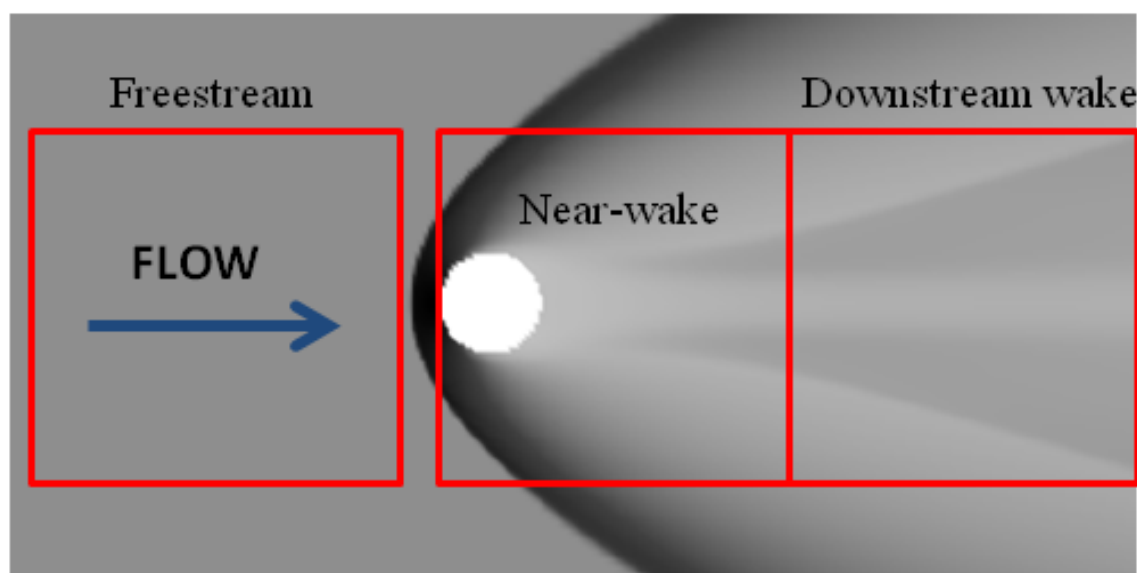


Fig. 5.8. Regions in the Mach 4.6 flow over a cylinder studied using the VENOM technique.

### V.2.1 Instrumentation and Experimental Setup

The VENOM experiments to characterize the flow over a cylinder were carried out in a uniform flow generated in the RPHT cell facility located at the National Aerothermochemistry Laboratory at Texas A&M University, which was described in detail in Chapter 3. The facility was operated at a Mach number of 4.6. Table 5.1 summarizes the flow conditions employed for these experiments. The Mach 4.6 axisymmetric converging-diverging nozzle has an exit diameter of 2.8 cm. The main chamber has a total volume of approximately 40 l and is evacuated by a Leybold E250 rotary pump and a roots blower combination coupled to a vacuum line through a liquid nitrogen trap used to condense the seeded tracers. The pressure in the main chamber is

continuously monitored by an MKS Series 902 calibrated pressure transducer. The chamber is mounted to a rail system on an optical breadboard to allow movement with respect to the fixed laser alignment and cameras to probe the flow at the different locations shown in figure 5.8. The screw-in exchangeable axisymmetric aluminum converging-diverging nozzle was fitted to a block containing a settling volume of 2.25 cm<sup>3</sup>. The gas was supplied radially to the settling region by four Parker General Series 9 pulse valves.

Table 5.1. Flow conditions used for the VENOM experiments on the Mach 4.6 flow over a cylinder.

<b>Mach number</b>	4.61
<b>Pressure Ratio, <math>p_0/p</math></b>	331.6
<b>Temperature Ratio, <math>T_0/T</math></b>	5.25
<b>Stagnation Temperature, <math>T_0</math></b>	294 K
<b>Stagnation Pressure, <math>p_0</math></b>	256 Torr
<b>Exit Pressure, <math>p</math></b>	0.77 Torr
<b>Exit Temperature, <math>T</math></b>	56 K
<b>Freestream Speed of Sound, <math>c</math></b>	150.4 m/s
<b>Exit Flow Velocity</b>	694 m/s
<b>Viscosity</b>	$3.56 \times 10^{-10} \text{ Kg m}^{-1} \text{ s}^{-1}$
<b>Gas Density</b>	$1.33 \times 10^{-17} \text{ cm}^{-3}$
<b>Reynolds number</b>	$1.20 \times 10^6 \text{ m}^{-1}$

The pulsed flow was operated at 1 Hz with a pulse valve opening time of 10 ms. According to previous flow characterization measurements performed on this nozzle, steady flow in the freestream is established 2 ms after the initial pulse valve opening. The pressure and temperature in the settling region were 34.1 kPa and 293 K, respectively, resulting in an exit flow with a streamwise velocity of 693 m/s and a temperature of 56 K. These freestream conditions propagate 2 – 3 nozzle diameters

downstream before significant shear layer growth occurs. This flow was pressure-matched with the background gas in the chamber to obtain a collimated freestream with a zero radial velocity component. During operation, the pressure matching between the nozzle exit and the chamber was controlled by a needle valve. The gas mixture consisted of 1%  $\text{NO}_2$  diluted in  $\text{N}_2$  and was prepared in a 150 l cylinder using a stainless steel mixing manifold.  $\text{NO}_2$  supplied by Sigma Aldrich (>99.5% purity) and dry compressed  $\text{N}_2$  supplied by Brazos Valley Welding were employed. After evacuating the mixing manifold and the cylinder the  $\text{NO}_2$  partial pressure was measured using a calibrated a MKS Piezo Vacuum Transducer. The total mixture pressure was 2.07 MPa. A photograph of the experimental setup is shown in figure 5.9.

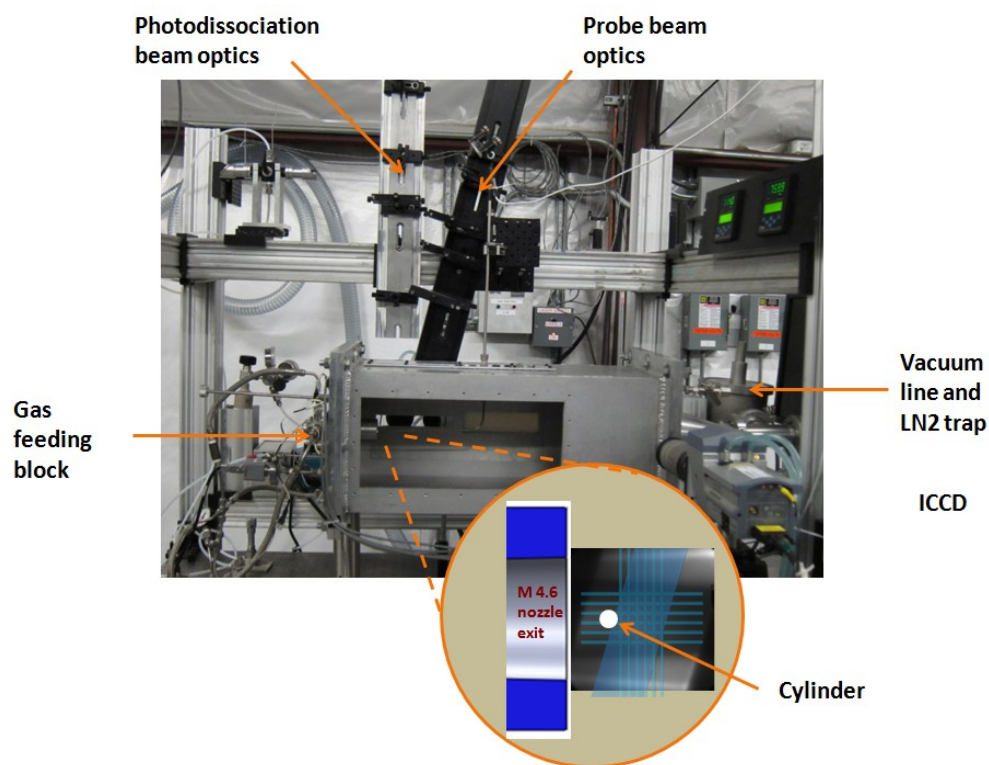


Fig. 5.9. Picture showing the experimental setup components including laser alignment.

The VENOM experimental setup is shown schematically in figure 5.10. The system consists of a Spectra Physics LAB-150-10Nd:YAG laser operated at 10 Hz producing a total power of 150 mJ/pulse at 355 nm. The 9 mm diameter laser beam was expanded with a 2.5X beam expander and directed into the chamber perpendicular to the flow axis through sheeting optics. A 40:60 beam splitter was used to optionally split the 355 nm beam to direct a second “write” laser sheet parallel to the flow axis to obtain the two-component velocity measurements of the flow field. Both photodissociation laser beams were directed through an aluminum mesh to produce a periodic modulated pattern of NO photoproducts in the flow. Each photodissociation laser sheet with a thickness of 200  $\mu\text{m}$  had an energy density of  $\sim 1.75 \text{ J/cm}^2$  at the imaging region resulting in photolysis efficiencies near 70%. For the one-component velocity measurements, where there is no splitting of the 355 nm laser, the photodissociation efficiencies ideally approach 100%.

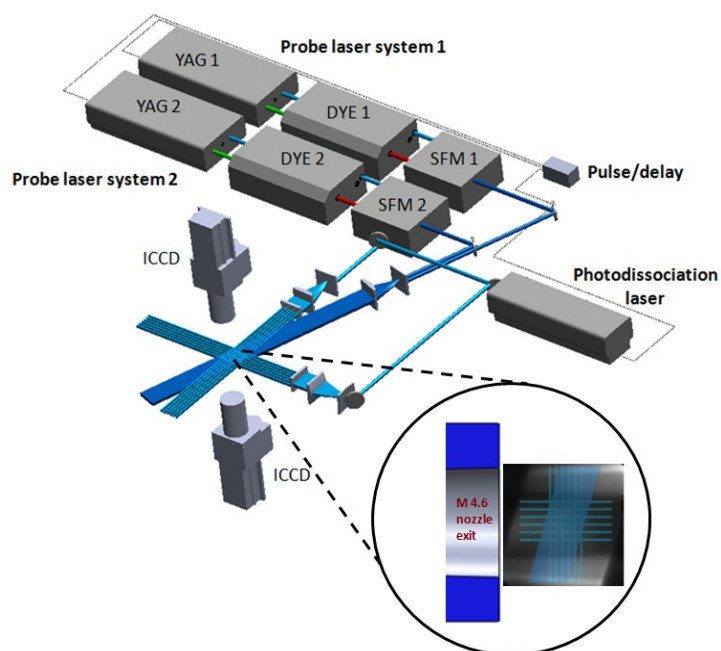


Fig. 5.10. Experimental schematic of the VENOM system.

Each of the two identical PLIF laser systems consists of an injection seeded Spectra Physics PRO-290-10 Nd:YAG laser operated at 10 Hz. The 532 nm output is used to pump a Sirah Cobra Stretch pulsed dye laser to produce a tunable output beam in the range from 600 to 630 nm using a solution of Rhodamine 610 and Rhodamine 640 in methanol. The dye laser output is mixed with the residual 355 nm beam from the Nd:YAG laser in a Sirah SFM-355 frequency mixing unit to produce approximately 10 mJ/pulse in a wavelength range of 223 to 227 nm, with a typical linewidth of  $0.08 \text{ cm}^{-1}$  and power fluctuations ranging from 5 to 10%. This output wavelength range permits probing transitions corresponding to both the  $A^2\Sigma^+ (v' = 0) \leftarrow X^2\Pi (v'' = 0)$  and the  $A^2\Sigma^+ (v' = 1) \leftarrow X^2\Pi (v'' = 1)$  bands. For these VENOM experiments both probe laser sheets were directed into the chamber at an angle of  $70^\circ$  with respect to the streamwise flow direction in order to avoid the aluminum mesh employed for the vertical “write” laser sheet. The fluorescence images were acquired using two Andor iStar DH734 ICCD cameras mounted on each side of the chamber perpendicular to the laser sheets. The cameras were fitted with CERCO 100 mm F/2.8 UV lenses and extension rings. No optical filters were employed. The timing between the pulsed flow, the laser systems, and the camera gating was controlled using a BNC 575 digital delay/pulse generator.

All VENOM measurements were performed during the steady flow phase of the pulsed flow. The basic timing sequence employed in these measurements consisted of an initial laser pulse, the “write” pulse, that photodissociates  $\text{NO}_2$  using 355 nm. After a time delay  $\tau_1$  a first “read” dye laser excites a specific rotational state of the nascent  $\text{NO}(v''=1)$  photoproduct and an associated ICCD camera captures a fluorescence image of the flow. Finally, after a second time delay  $\tau_2$  the second “read” system excites a different  $\text{NO}(v''=1)$  rotational state in order to capture a second fluorescence image. The first time delay,  $\tau_1$ , has to be long enough to ensure complete thermalization of the hot NO distribution produced by the photodissociation (see below), and  $\tau_2$  must be long enough to capture fluorescence from only the second “read” laser. The second time delay,  $\tau_2$ , defines the resolution of the velocity measurement by controlling the extent of



displacement of the tagged lines between the capture of both images.  $\tau_1$  was set to 2000 ns and  $\tau_2$  was 1250 ns.

### **V.2.2 CFD Simulation**

Two-dimensional steady state computational fluid dynamics (CFD) simulations of the cylinder in a Mach 4.6 flow were performed using the Cobalt [81] Navier-Stokes flow solver for comparison with the experimental results. The underlying algorithm is fundamentally based on Godunov's first-order accurate, cell-centered, finite volume, exact Riemann solution method [82]. Second-order spatial accuracy is achieved via an upwind-biased reconstruction based on least-squares gradients. Total variation diminishing limiters are used to ensure stability of the inviscid flux reconstruction. The solution is advanced in time by solving the implicit system of equations using either the Gauss-Seidel or the Jacobi iterative methods. The 2D grid used in the simulations had 81920 quadrilateral cells. Grid cells were clustered near the cylinder surface to capture viscous effects due to the solid wall. In the inviscid region of the flow, cells were clustered in the region upstream and downstream of the cylinder to adequately resolve the bow shock and the aft wake. A representative grid distribution is presented in figure 5.11.

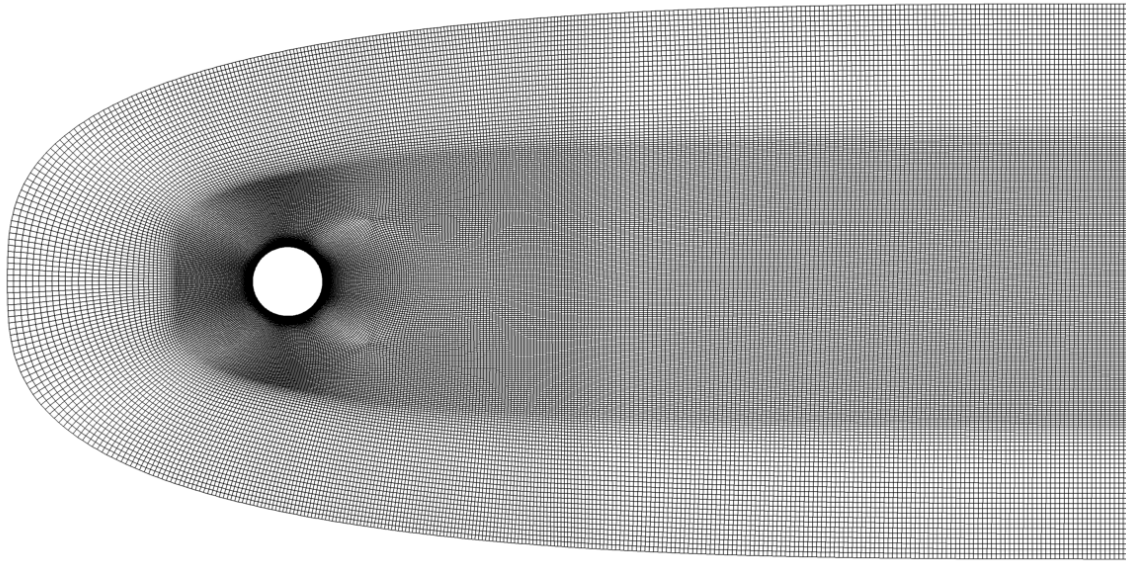


Fig. 5.11. Grid distribution used in the CFD simulations.

The freestream conditions were applied at the outer boundary of the domain. At cell faces where the flow is crossing into the domain, supersonic conditions were specified and at cell faces with outflow, flow quantities were extrapolated from the interior of the domain. Adiabatic viscous wall boundary conditions were specified at the surface of the cylinder. Laminar and turbulent simulations were performed with different wall-normal grid distributions at the cylinder surface. Menter's two-equation SST [83] model was used in the turbulence simulations. The results between laminar and turbulent simulations did not produce appreciable different results. The resulting CFD density, pressure, velocity and temperature maps are shown in figure 5.12.

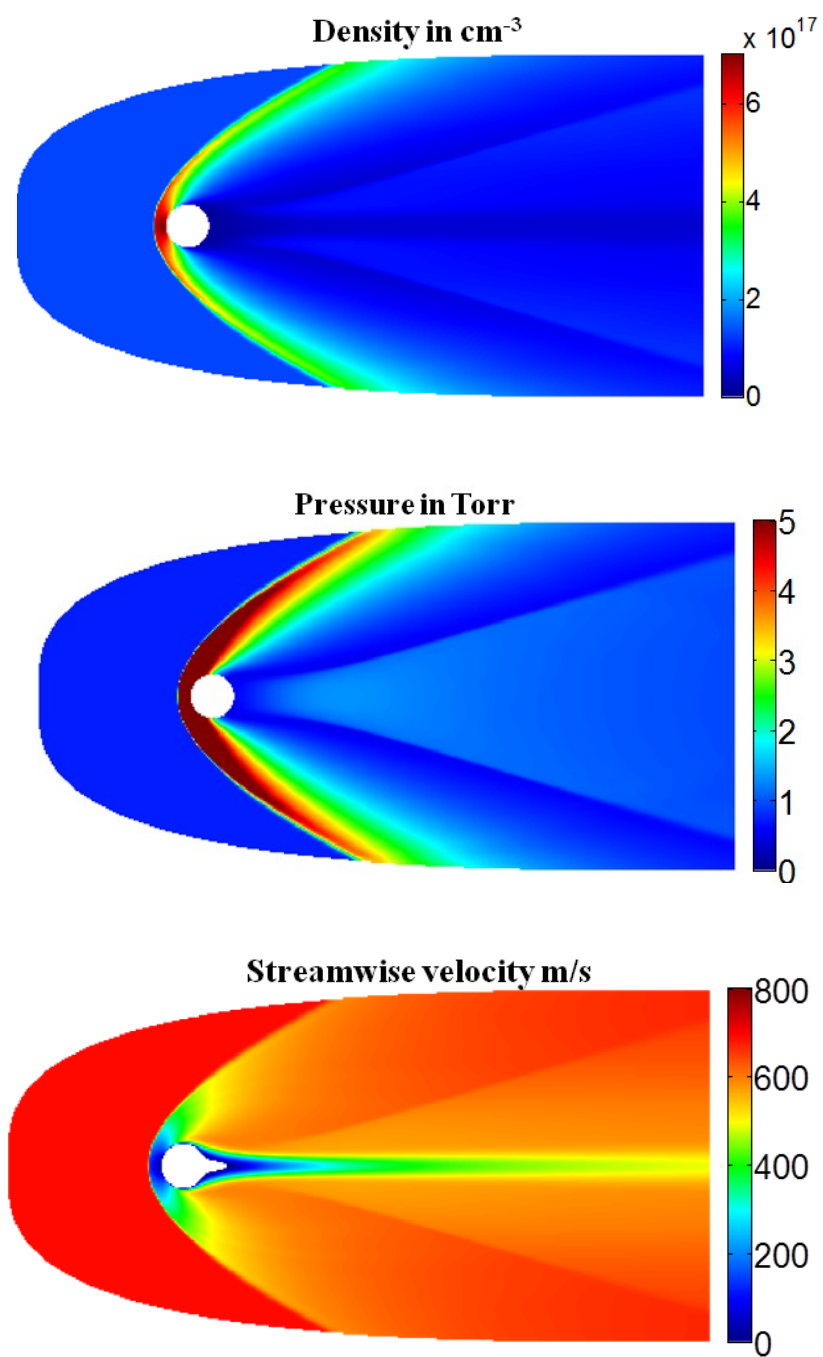


Fig. 5.12. Density, pressure, velocity and temperature maps obtained by the turbulent CFD simulations.

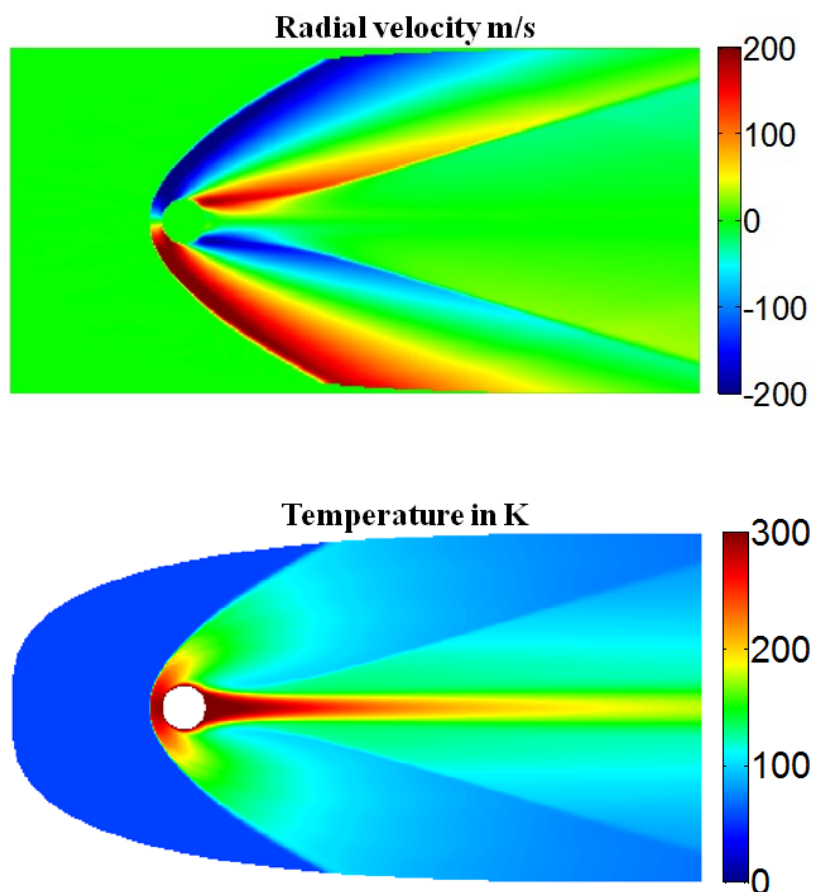


Fig. 5.12. Continued.

### V.2.3 Experimental Results

The goal of these experiments was to demonstrate the simultaneous and instantaneous determination of two-component velocity and temperature maps in a Mach 4.6 flow over a cylinder wake. As mentioned earlier, the measurement of two-component velocity fields using the VENOM technique requires the alignment of two orthogonal photodissociation laser sheets through the flow field. Figure 5.13 shows instantaneous raw fluorescence image pairs acquired using  $\tau_1 = 2000$  ns and  $\tau_2 = 1250$  ns. The images were taken using a magnification factor of 1 at a distance ranging from 1.25 to 3.75 cm downstream of the nozzle exit using camera gates of 50 ns and looking at a field of view of 1.4 cm x 1.4 cm, corresponding to 36 pixel/mm.

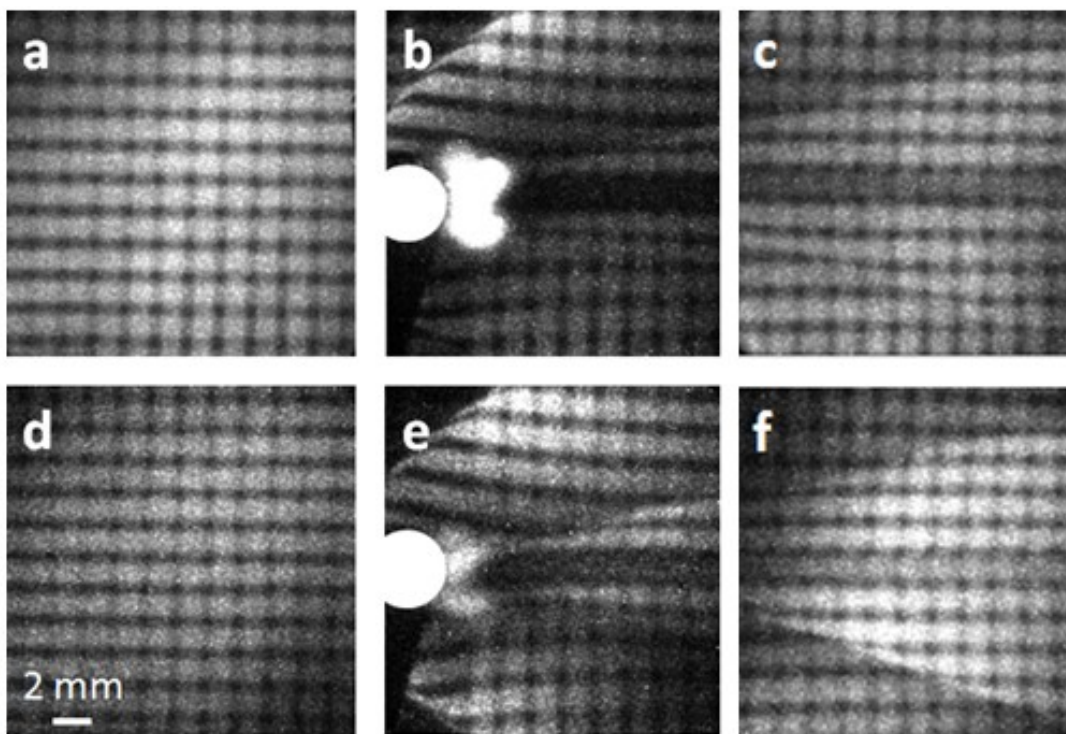


Fig. 5.13. Instantaneous images probing the  $R_1 + Q_{21}$  ( $J = 1.5$ ) transition of the vibrationally excited NO in the freestream (a), the flow over a 3.2 mm diameter cylinder (b) and the wake further downstream (c). The same sequence is shown (d, e and f) for the  $R_1 + Q_{21}$  ( $J = 8.5$ ) transition.

The image pairs in figure 5.13 are instantaneous fluorescence shots captured from the excitation of the  $R_1 + Q_{21}$  ( $J = 1.5$ ) (images a, b, and c) and the  $R_1 + Q_{21}$  ( $J = 8.5$ ) (images d, e, and f) transitions in the NO  $A^2\Sigma^+ (v' = 1) \leftarrow X^2\Pi (v'' = 1)$  band. The flow movement is from left to right, and the image pairs represent the spatial sequence of the flow at different positions downstream from the nozzle exit. The first image pair, (a) and (d) corresponds to the undisturbed freestream flow 1.25 cm downstream of the nozzle exit, and 1.25 cm upstream of the cylinder. The homogeneous streamwise displacement of the flow can be observed by comparing the horizontal shift of image (d) with respect to image (a), which is 0.88 mm, with no axial flow movement or spatial distortions. The second image pair, (b) and (e), corresponds to instantaneous VENOM images of the flow over the cylinder, 2.5 cm downstream of the nozzle exit. The cylinder

position is shown as a white circle. Other than the bright region behind the cylinder due to ablation of the cylinder surface by the horizontal focused photodissociation laser sheet, the tagged lines clearly reveal the local flow movement and the different features of the flow. On the left-top and left-bottom corners of these images the bow shock is clearly distinguished from the darker freestream. The curvature of the horizontal lines near the cylinder reveals the flow moving across the bow shock and around the cylinder. The darkest horizontal strip located in the center of the images corresponds to the wake formed after the flow separation from the cylinder surface. This region shows the shortest flow displacements and a consequential temperature increase as revealed by the lowest fluorescence intensity due to the low- $J$  states probed to capture the images. The third image pair, (c) and (f), shows the cylinder wake 3.75 cm downstream from the nozzle exit. Here, the flow experiences a recompression shock, depicted by the diagonal fluorescence patterns, and characterized by the flow on the top and bottom of the images turning towards the centerline to continue in the streamwise direction.

### A. Near Wake Measurements

The analysis of the wake directly behind the cylinder, or near wake, was affected by ablation due to the focused 355 nm laser sheet, as shown in figure 5.13 (b) and (e), and therefore only the vertical photodissociation beam was employed to acquire additional VENOM images, resulting in only 1-component velocity determinations and full temperature maps for this region.

Figure 5.14 shows single-shot fluorescence raw images of the cylinder near-wake region captured by exciting the  $R_1 + Q_{21}$  ( $J = 1.5$ ) (left panel) and the  $R_1 + Q_{21}$  ( $J = 8.5$ ) (right panel) transitions, respectively, in the  $\text{NO } A^2\Sigma^+ (v' = 1) \leftarrow X^2\Pi (v'' = 1)$  band.

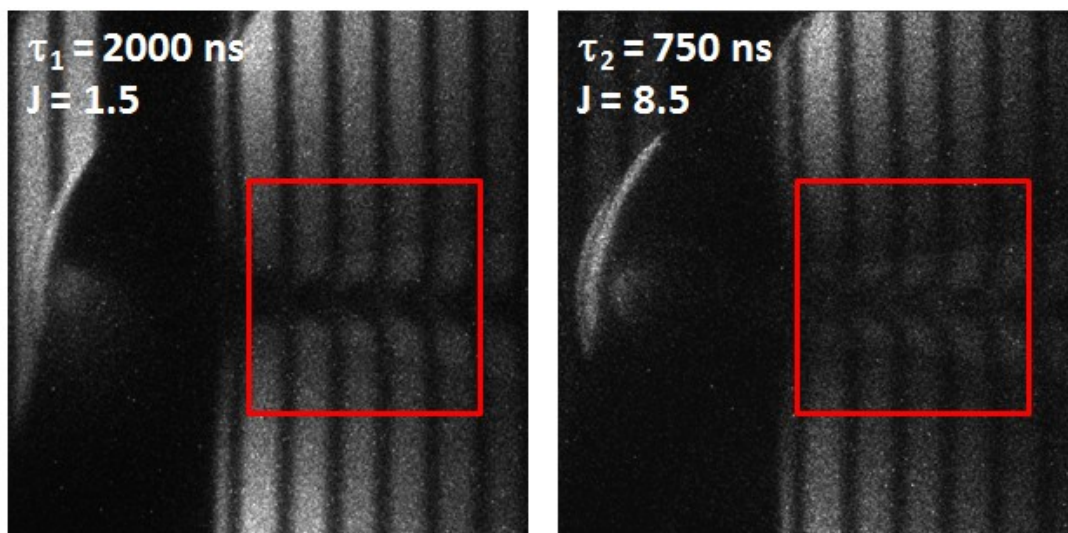


Fig. 5.14. Instantaneous VENOM images probing the  $R_1 + Q_{21}$  ( $J = 1.5$ ) transition of the vibrationally excited NO in the cylinder near wake 2  $\mu$ s after photodissociation (left panel), and  $R_1 + Q_{21}$  ( $J = 8.5$ ) transition probed 2.75  $\mu$ s after photodissociation.

The vertical dark strip located on the left half of the images corresponds to the shade produced by blocking the photolysis laser sheet in order to avoid ablation of the cylinder. Tracking the horizontal displacement of the tagged lines permits to obtain an estimation of the streamwise velocity component. Figure 5.15 shows the experimentally derived 200-single-shot-based average streamwise velocity map, as well as the measured rms, both in m/s. The regions shown in these maps correspond to the red squares depicted in figure 5.14.



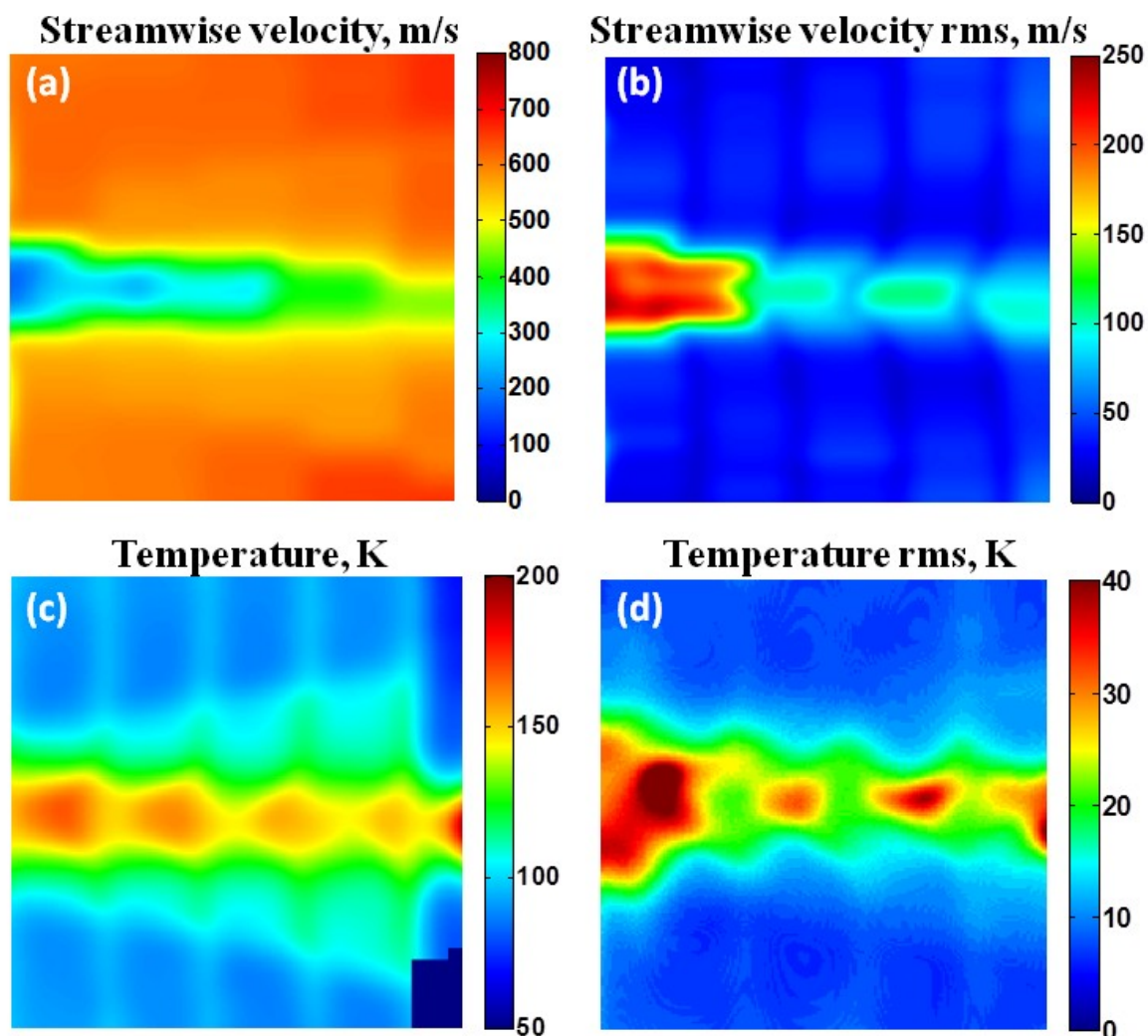


Fig. 5.15. Experimentally obtained average streamwise velocity ( $u$ ) and temperature maps based on 200 single-measurements. Measured streamwise velocity (c) and temperature (d) fluctuations shown as rms values.

### B. Further Downstream Wake Measurements

The experiments performed in the cylinder wake, downstream region shown in figure 5.13(c) and (f), were not affected by the horizontal photodissociation laser sheet ablation of the cylinder, and consequently, the measurement of the two velocity components was possible. The mean streamwise and radial velocity and temperature maps derived from the downstream cylinder wake are shown in the right panels of



figure 5.16, corresponding to the regions illustrated in figure 5.13 (c) and (f). The CFD simulations are shown in the left panels for comparison.

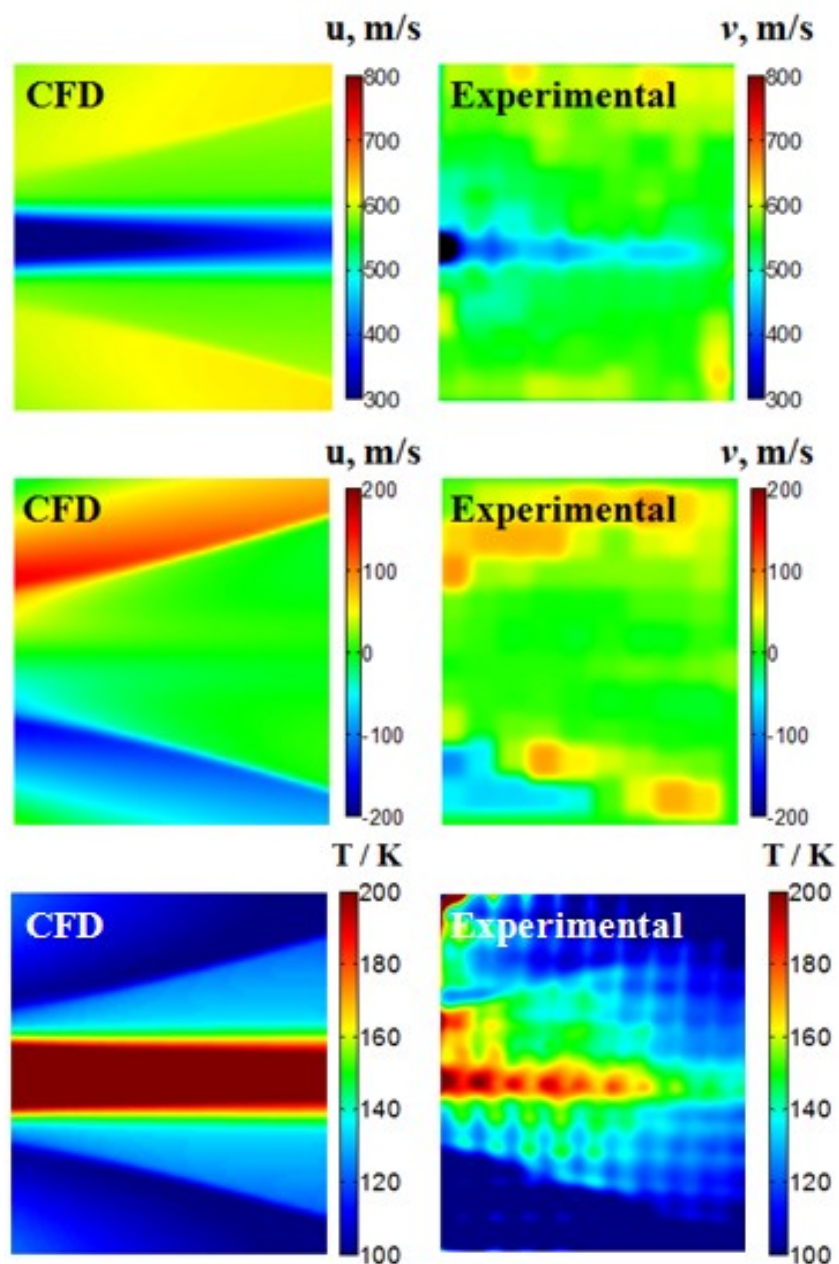


Fig. 5.16. Experimentally obtained interpolated average streamwise velocity ( $u$ ), radial velocity ( $v$ ) and temperature maps based on 200 single-shot measurements. CFD simulations are shown on left panels for comparison.

The overall agreement between the experimental average velocity and temperature maps and the CFD results is good, with deviations of  $< 10\%$  for most of the flow field. The main flow structures are well-resolved, including the diagonal gradients indicating the recompression shock and the wake. The largest differences, however, correspond to the wake region. These differences are attributable to the turbulence present in the experimental results, which do not affect the CFD calculations since any vortex shedding will not be captured by the steady-state CFD solutions. Another reason for the large differences in this region is the relatively low experimental spatial resolution, which particularly is expected to affect the velocity maps. The measured turbulent fluctuations based on the single-shot image pairs are shown in figure 5.17.

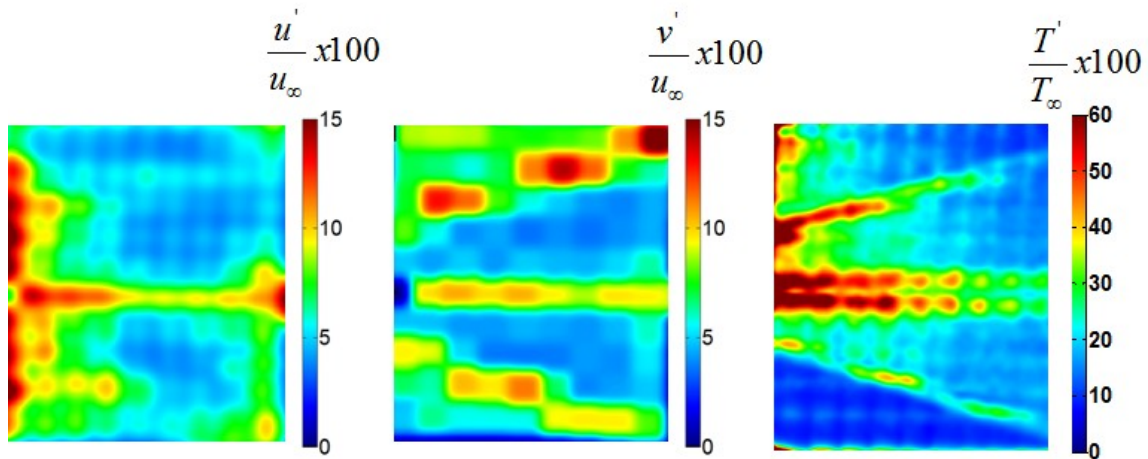


Fig. 5.17. Measured velocity and temperature fluctuations based on 200-single shots normalized to the freestream values. All quantities are shown as a percent.

### **C. Further Downstream Wake Measurements With Increased Spatial Resolution**

The relatively large grid size used in the VENOM experiments described in the previous section can be visually compared to the wake size in figure 5.13. It is noticeable that only two horizontal grid lines were "written" in the flow along the wake region. Since the velocity maps shown in figure 5.16 are results of an interpolation procedure, the lowest velocity region of the wake is not captured, and as a consequence of the interpolation procedure, is over-estimated. This effect is also visible in the temperature fluctuation map shown in figure 5.17, where the largest fluctuations appear along the wake borders and are a visual artifact with an structure corresponding to the grid intersection locations.

The previous limitation can be overcome if the spatial resolution of the experiment is increased. This is achieved if a finer photodissociation grid is written onto the flow. The VENOM images shown in figure 5.18 correspond to the further downstream wake region (the same region shown in figure 5.13 (c) and (f) ) acquired under the same experimental conditions, but substituting the aluminum mesh that generates the horizontal photodissociation lines by a finer mesh. The use of this finer mesh resulted in the generation of photolysis lines equally spaced by 0.28 mm, instead of the previous mesh that generated bright regions of 0.84 mm width and dark regions of 0.25 mm width.

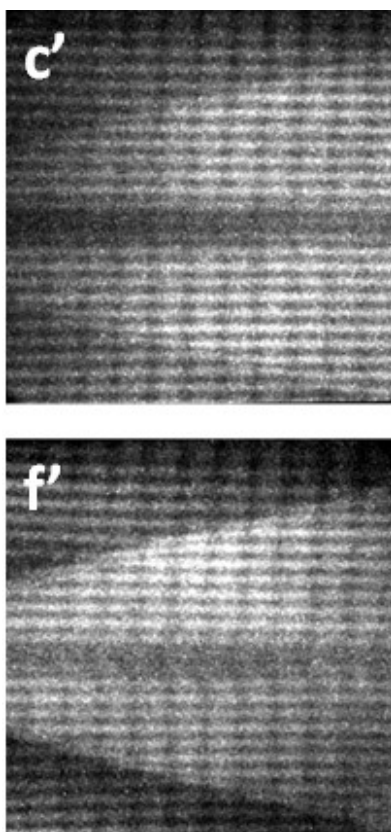


Fig. 5.18. Instantaneous VENOM raw images probing the  $R_1 + Q_{21}$  ( $J = 1.5$ ) transition of the vibrationally excited NO in the wake further downstream (c'). The same region is shown (f') for the  $R_1 + Q_{21}$  ( $J = 8.5$ ) transition. These images were acquired using a finer aluminum mesh to "write" the horizontal photodissociation lines.

The use of a finer aluminum mesh to "write" the horizontal photolysis patterns permitted to obtain twice as many intersection points across the regions that require a better spatial resolution in the radial direction. Using this setup, 5000 single-shot VENOM image pairs were captured, in sets of 200 image pairs at a time. This allowed the computer to handle the file writing procedure at the end of each acquisition cycle, and also allowed to obtain multiple fluorescence images of the static background as temperature reference for the two-line thermometry measurements in order to calculate the calibration constant  $C_{12}$ . This is important because the laser power stability cannot be assured for long periods of time, and acquiring an independent set of reference fluorescence images for each 200 VENOM image pairs provided good results. Figure

5.19 shows the mean velocity and temperature maps computed from the 5000 single-shot measurements.

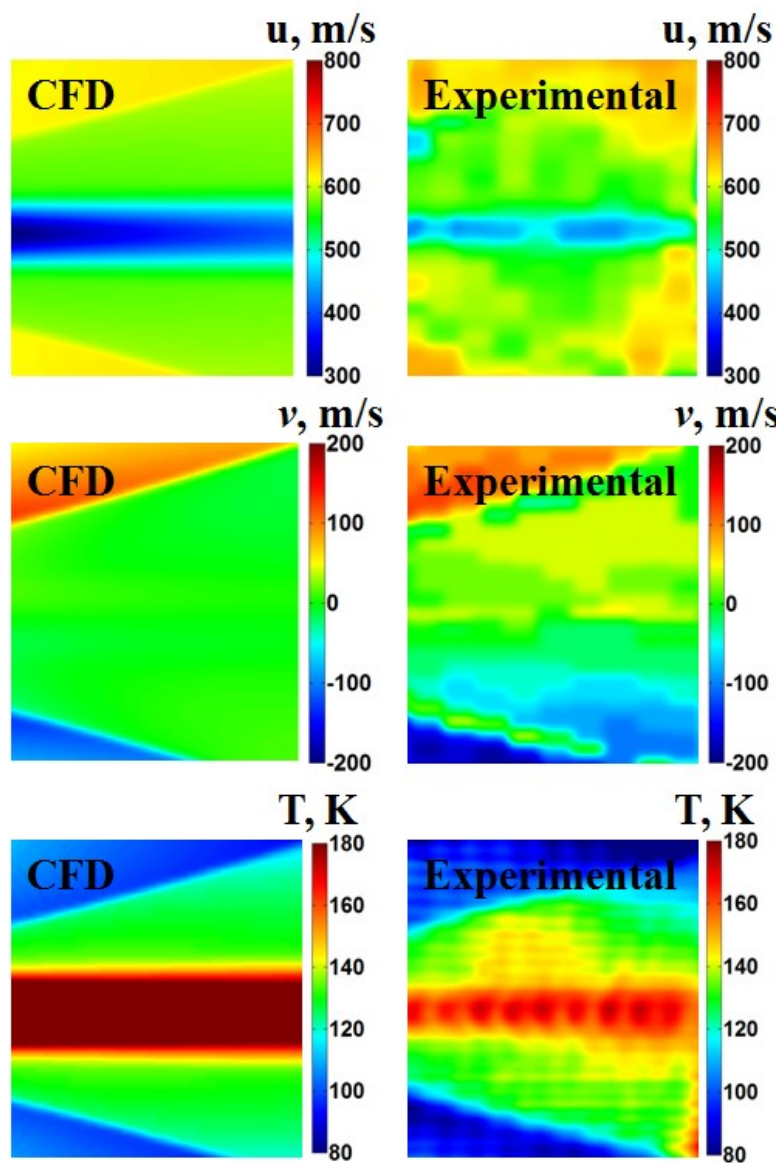


Fig. 5.19. Experimentally obtained interpolated average streamwise velocity ( $u$ ), radial velocity ( $v$ ) and temperature maps based on 5000 single-measurements using the fine aluminum mesh to "write" the horizontal photodissociation lines. CFD simulations are shown on left panels for comparison.

The overall agreement between the experimental results and the CFD simulations is good, showing differences of <10% for most of the flow field. The streamwise velocity component along the centerline, however, shows again the largest deviations: as high as 30%. These deviations are due to a number of reasons, which again include the effects of turbulence that were not considered in the steady state solutions achieved by the CFD simulations. For the current setup the maximum error due to the data processing algorithm was experimentally determined under stationary conditions to be 25 m/s for the entire field of view considering the experimental spatial resolution of 36 pixel/mm and  $\tau_2 = 1250$  ns.

The fluctuations measured in the cylinder wake using the 5000 single-shot VENOM measurements are shown in figure 5.20, normalized by the freestream values to obtain  $u'/u_\infty \times 100$ ,  $v'/u_\infty \times 100$ , and  $T'/T_\infty \times 100$ .

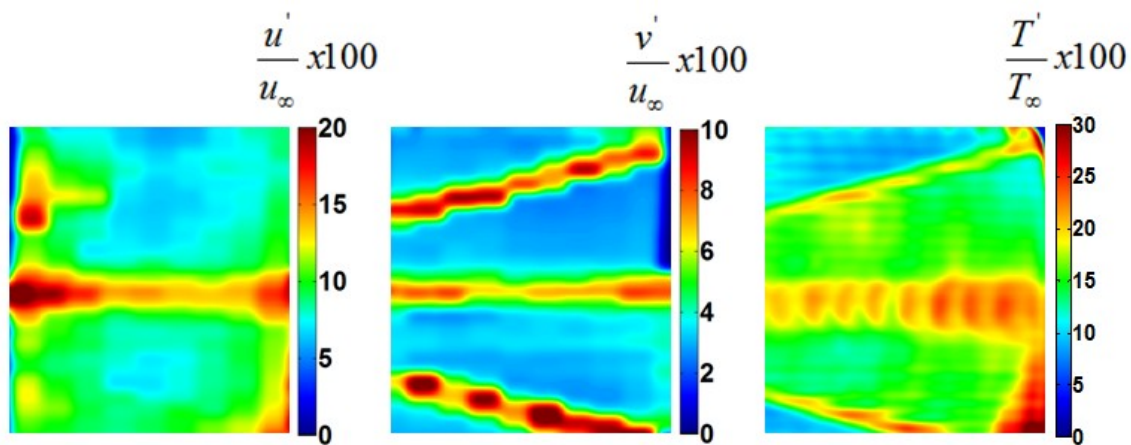


Fig. 5.20. Measured velocity and temperature fluctuations based on 5000-single shots normalized to the freestream values. All quantities are shown as a percent.

The fluctuations  $u'$  and  $v'$  in the cylinder wake are significantly higher than the measurement uncertainties, suggesting that these quantities result from turbulent fluctuations. Furthermore, they are consistent with the mean structure for the

downstream cylinder wake. The velocity and temperature fluctuation vertical profiles measured 2 cm downstream from the cylinder are shown in figure 5.21.

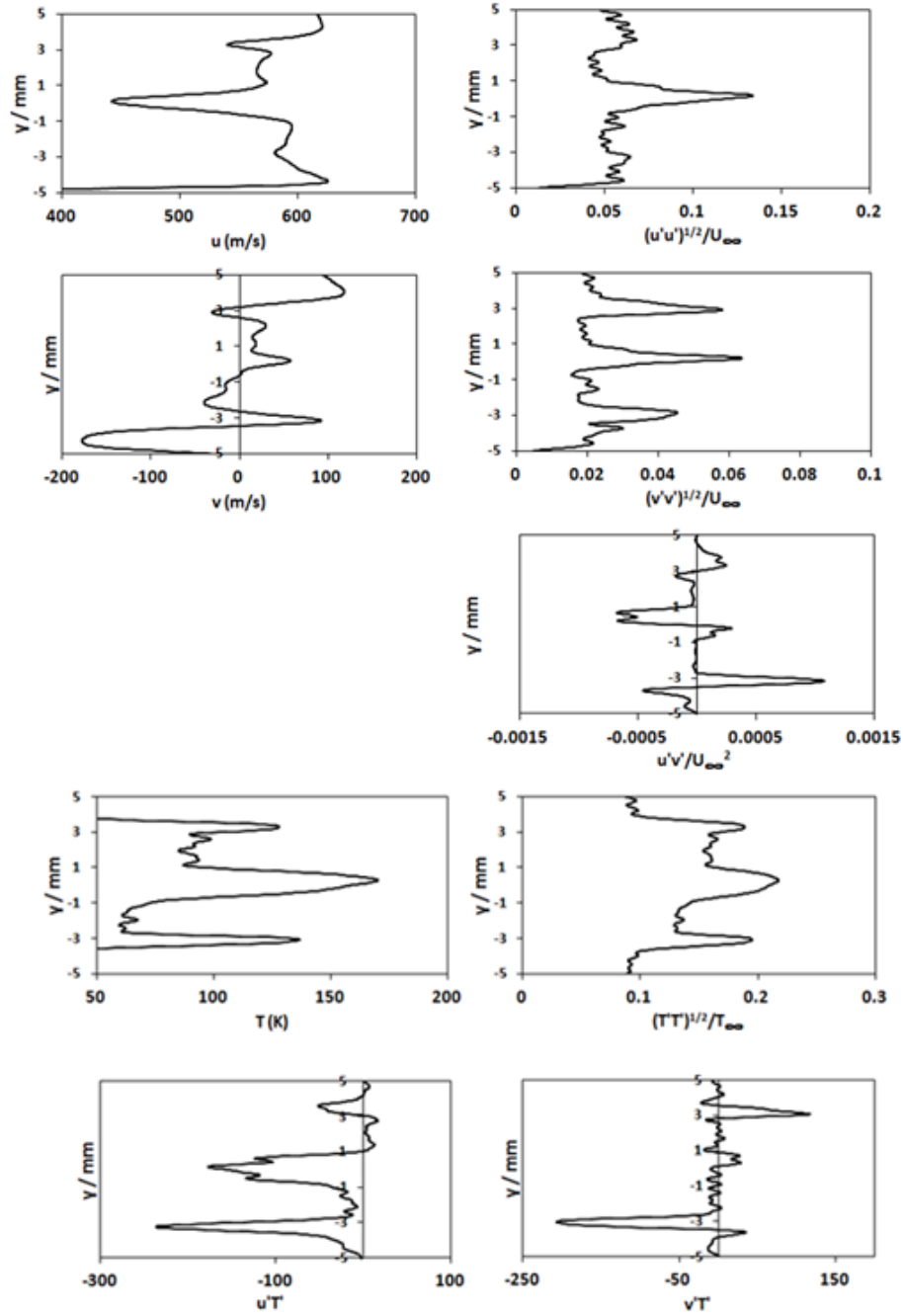


Fig. 5.21. Measured velocity and temperature fluctuation vertical profiles 2 cm downstream from the cylinder based on 5000-single shots normalized to the freestream values.

### V.3 Summary

The performance of the Vibrationally Excited Nitric Oxide Monitoring, or VENOM, technique for simultaneous velocity and temperature measurements in gaseous flow fields was demonstrated and the technique was successfully implemented. In the current implementation of the VENOM technique the initial "read" pulse, which provides measurement of one rotational state for thermometry, is delayed typically  $>1 \mu\text{s}$  from the 355 nm "write" pulse. The second "read" pulse, which provides the second rotational state measurement, occurs at an additional  $>500 \text{ ns}$  delay to avoid collection of fluorescence originated from the first "read" pulse. For most flows the chosen time delays represent a compromise between spatial resolution, velocity resolution, and accurate thermometry.

The initial VENOM experiments intended to demonstrate the possibility of simultaneous measurement of two-component velocity and temperature were performed in an underexpanded jet flow field. The results consisted of average temperature and velocity maps. While the overall agreement with CFD simulations was good, the results showed a significant overestimation in temperature in the lowest density regions of the field due to incomplete thermalization of the hot NO photoproducts resulting from  $\text{NO}_2$  photodissociation. These initial VENOM measurements demonstrated the possibility of obtaining velocity and temperature measurements in a challenging flow field such as the underexpanded jet. The impact of using a rotationally hot photoproduct to obtain temperature information in a gaseous flow field, as discussed in chapter 4 leads to an overestimation of temperature in the lowest density regions of a flow field. A second set of measurements using a different flow field were performed in order to address this issue and demonstrate an implementation scheme aimed to mitigate this effect in order to provide more accurate temperature measurements associated to a velocity measurement. These simultaneous and local velocity/temperature measurements were performed in the wake of a cylinder in a uniform Mach 4.6 flow field. The mean and fluctuation velocity and temperature maps were computed from 5000 single-shot VENOM image pairs. The wake temperature and velocity fluctuations, with respect to the freestream values, were 15% – 30% and 5% – 20%, respectively. The mean velocity and temperature maps were



compared to CFD simulations, resulting in a good agreement, within 10% for most of the flow field. The fluctuations  $u'$ ,  $v'$ , and  $T'$  in the wake are higher than the measurement uncertainties, and thus, are regarded as turbulent fluctuations. The spatial distributions agree with the results of CFD simulations. The results suggest that the VENOM technique holds promise for interrogating high-speed unsteady flow fields.

## CHAPTER VI

### CONCLUSION AND FUTURE WORK

#### **VI.1 Measurement of Acceleration Fields Using the VENOM Technique**

The aerodynamic behavior of an object is a direct result of the pressure distribution on its surface. These pressures are a consequence of the different acting forces in the flow, and a reliable method to determine their magnitude and distribution by non-intrusive methods is particularly required in compressible flows. It has been previously demonstrated how the pressure distributions in an gaseous flow could be estimated without employing pressure sensors, and it has been suggested that they can be obtained from just flow information (velocity and acceleration fields) for both compressible and incompressible flows [84].

The first VENOM experiments performed in the underexpanded jet flow field described in chapter 5 employ only the first time-delayed fluorescence image to derive a velocity field by comparing the location of the grid intersections to their counterparts in a zero-time grid obtained under static conditions, or in a zero-time synthetic grid image. This is possible due to the well-known periodicity of the initial photodissociation grid, a unique advantage of MTV methods. Using this configuration to measure the flow velocity, the second “read” pulse could be employed to provide a second velocity determination, and thus, the rate of change in velocity, or acceleration. If the “read” lasers are tuned to probe two different transitions, this second velocity measurement can also provide a simultaneous temperature measurement in the sense that both measurements interrogate the same fluid elements.

The measurement of acceleration using the current experimental setup is straightforward and only requires the measurement of two consecutive velocity fields. This information can be derived from the two VENOM images and the zero-grid as explained above. The acceleration is calculated as :

$$acceleration = \frac{u_2 - u_1}{t_2 - t_1} \quad (\text{Eq. 6.1})$$

where  $t_1$  and  $t_2$  are the times at which the two velocity fields were acquired. Figure 6.1 shows two sequentially obtained velocity vectors in an underexpanded jet that would lead to an estimation of the acceleration field.

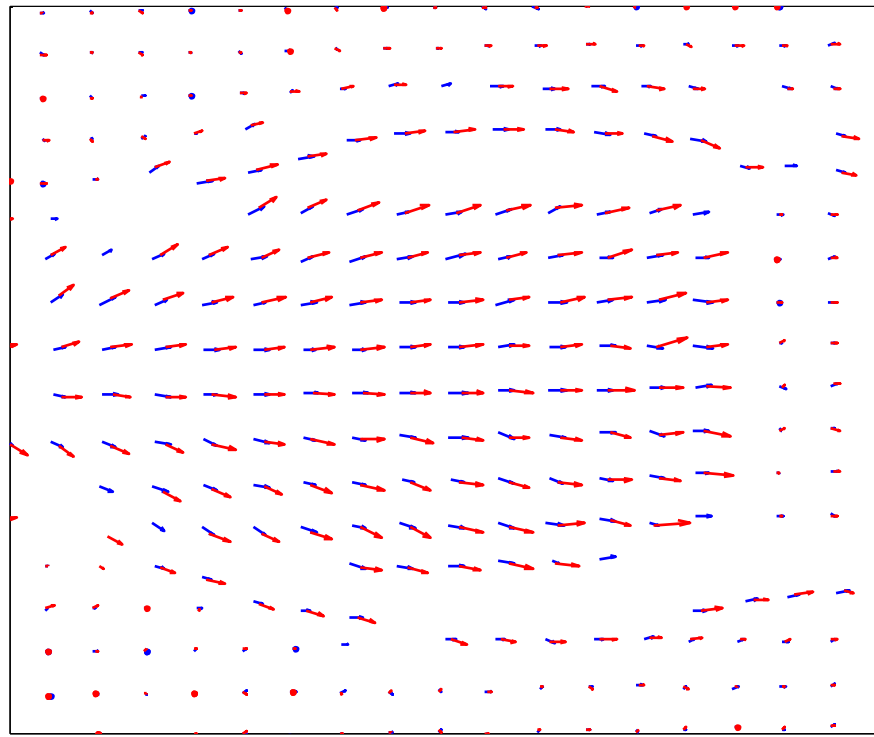


Fig. 6.1. Sequential velocity vectors in an underexpanded jet obtained by the current VENOM experimental setup.

The challenge is to demonstrate that the acceleration field measurement can be obtained with enough accuracy to correctly determine the pressure distribution field. Based on the current VENOM measurements discussed in chapters 4 and 5, the possibility of obtaining simultaneous velocity, temperature and pressure instantaneous

measurements is definitely feasible, and represents the next natural step in the development of further capabilities of the VENOM technique.

## VI.2 Stereoscopic VENOM Measurements

The VENOM system described in this work offers the capability of simultaneous planar measurements of instantaneous velocity and temperature fields. However, the following thoughts and questions are under current development in order to extend the capabilities of the VENOM system:

- \* Stereoscopic VENOM measurements - the measurement of the third velocity component (out-of-plane component,  $w$ ). This measurement would require a stereoscopic measurement system, which employs two cameras imaging a plane from different angles after  $\tau_1$ , and two more cameras to image the fluid after motion from different angles after  $\tau_2$ . This measurement can be also obtained by only two dual-shot cameras imaging the flow at different angles. Since the out of plane movement of an NO plane produced by a thick photolysis laser requires to be tracked, a probe beam thicker than the photolysis laser sheet is needed. The signal-to-noise constraints of a not fully focused probe beam need to be explored and the limitations clearly established. Figure 6.2 shows the setup required to perform an stereoscopic VENOM measurement.

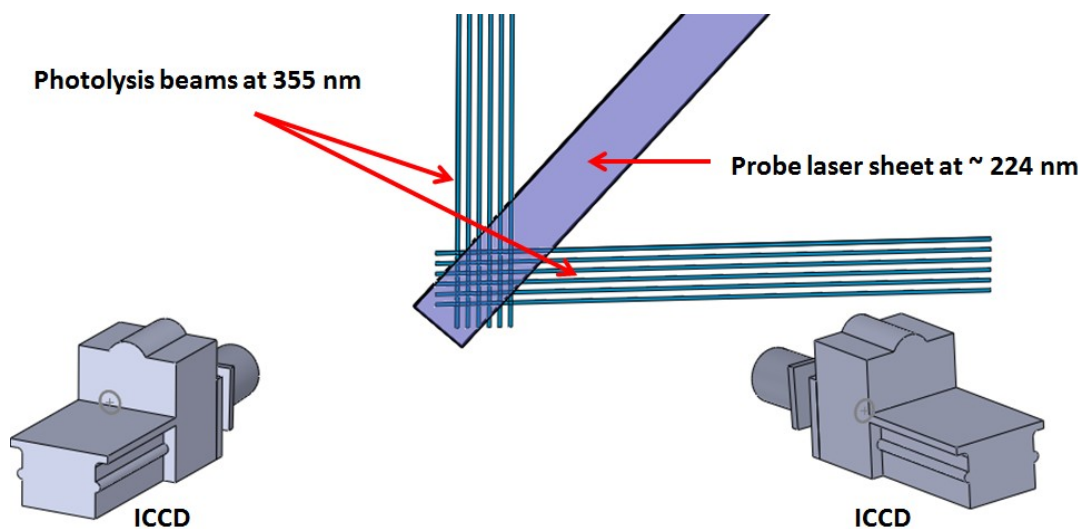


Fig. 6.2. Front view of the stereoscopic VENOM imaging of the flow

\* Dual-plane stereoscopic VENOM measurements. The objective of these measurements would be to not only obtain the out-of-plane velocity component as explained in the previous point, but also to track the complete deformation of the fluid elements in three dimensions. This configuration could be explored given that the out-of-plane flow tracking can be successfully obtained using the stereoscopic setup. The dual-plane imaging experiments require to duplicate the equipment employed for the stereoscopic imaging system. The dual-plane imaging setup is shown in figure 6.3.

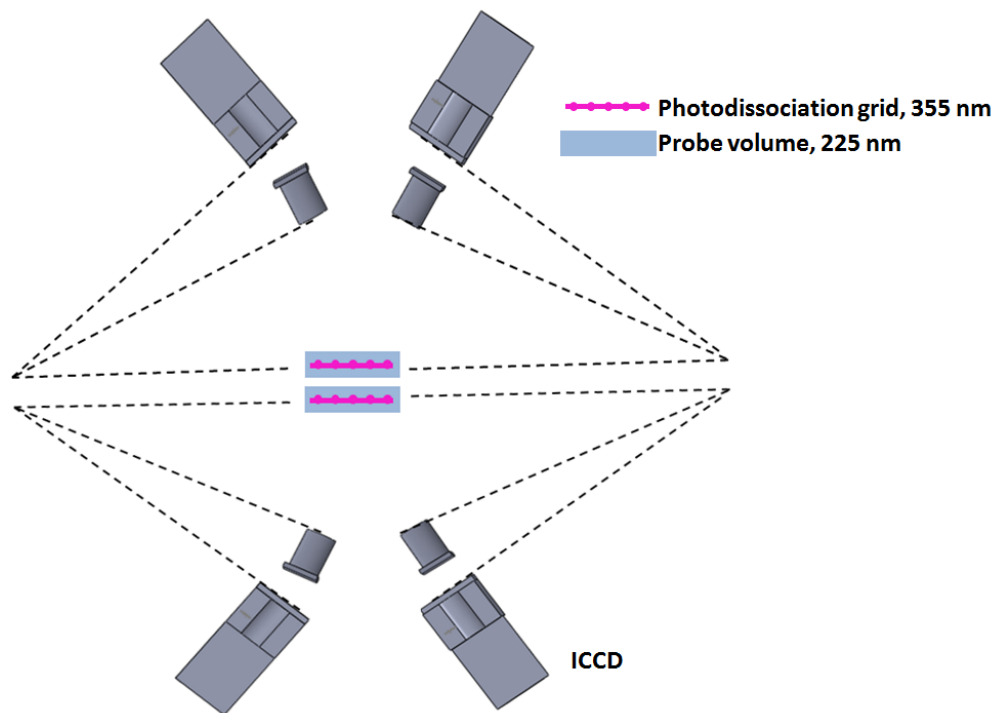


Fig. 6.3. Top view of the dual-plane stereoscopic VENOM imaging of the flow.

Figure 6.4 shows a schematic of the projected dual VENOM system, and consists of the same components of the VENOM system described in chapter 2, but duplicated. The volumetric flow mapping capability expected with this system will also require to develop the image processing algorithms necessary for more field of view

corrections between each camera pair looking at each image plane, as well as the calibration methods to detect and measure out-of-plane flow movement.

In addition to flow imaging in three dimensions, and 3-component velocimetry, tuning the different probe laser systems would still allow to measure rotational temperature as well as multiple species in more complex environments (such as ablation products or in combustion systems).

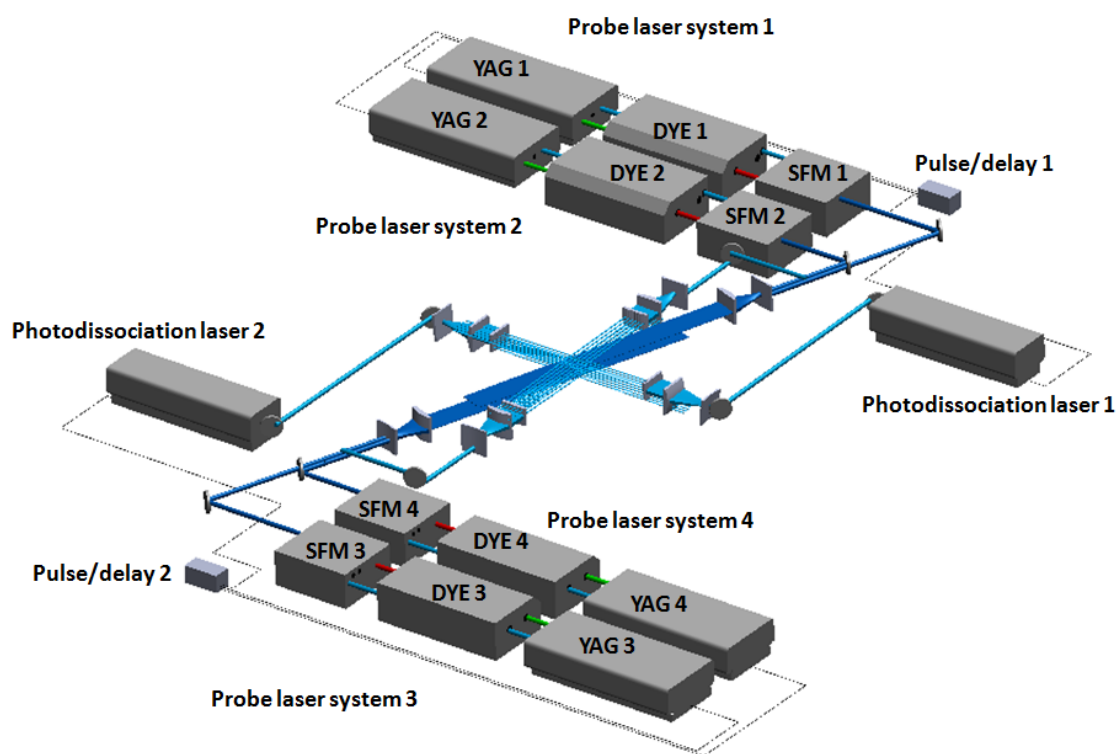


Fig. 6.4. Dual VENOM system.

## REFERENCES

1. R. D. W. Bowersox, "Combined laser doppler velocimetry and cross-wire anemometry analysis for supersonic turbulent flow," AIAA J. **34**, 2269-2275 (1996).
2. A. G. Hsu, R. Srinivasan, R.D.W. Bowersox, and S.W. North, "Two-component molecular tagging velocimetry utilizing NO fluorescence lifetime and NO<sub>2</sub> photodissociation techniques in an underexpanded jet flow field," Appl. Opt. **48**, 4414-4423 (2009).
3. B. R. Rowe, G. Dupeyrat, J. B. Marquette, and P. Gaucherel, " Study of the Reactions  $N_2^+ + 2N_2 \Rightarrow N_4^+ + N_2$  and  $O_2^+ + 2O_2 \Rightarrow O_4^+ + O_2$  from 20 to 160 K by the CRESU Technique," J. Chem. Phys. **80**, 4915-4921 (1984).
4. B. R. Rowe and J. B. Marquette, "CRESU studies of ion/molecular reactions," Int. J. Mass Spectrom. Ion Proc. **80**, 239-254 (1987).
5. P. L. James, I. R. Sims, I. W. M. Smith, M. H. Alexander, and M. Yang, "A combined experimental and theoretical study of rotational energy in collisions between NO( $X^2\Pi_{1/2}$ ,  $v=3,J$ ) and He, Ar and N<sub>2</sub> at temperatures down to 7 K," J. Chem. Phys., **109**, 3882-3897 (1998).
6. D. Chastaing, P. L. James, I.R. Sims, and I. W. M. Smith, "Neutral-neutral reactions at the temperature of interstellar clouds - rate coefficients for reactions of C<sub>2</sub>H radicals with O<sub>2</sub>, C<sub>2</sub>H<sub>2</sub>, C<sub>2</sub>H<sub>4</sub> and C<sub>3</sub>H<sub>6</sub> down to 15 K," Faraday Discuss. **109**, 165-181 (1998).
7. D. B. Atkinson and M. A. Smith, "Design and characterization of pulsed uniform supersonic expansions for chemical applications," Rev. Sci. Instrum. **66**, 4434-4446 (1995).
8. D. B. Atkinson and M. A. Smith, "Radical-molecule kinetics in pulsed uniform supersonic flows: termolecular association of OH + NO Between 90 and 220 K," J. Phys. Chem. **98**, 5797-5800 (1994).
9. D. B. Atkinson, V. I. Jaramillo, and M. A. Smith, "Low-temperature kinetic behavior of the bimolecular reaction OH + HBr (76 - 242 K) ," J. Phys. Chem. A **101**, 3356-3359 (1997).

10. B. Hansmann and B. Abel, "Kinetics in cold Laval nozzle expansions: from atmospheric chemistry to oxidation of biomolecules in the gas phase," *Chem. Phys. Chem.* **8**, 343-356 (2007).
11. S. Lee, R. J. Hoobler, and S. R. Leone "A pulsed Laval nozzle apparatus with laser ionization mass spectroscopy for direct measurements of rate coefficients at low temperatures with condensable gases," *Rev. Sci. Instrum.* **71**, 1816-1823 (2000).
12. A. B. Vakhtin, D. E. Heard, I. W. M. Smith, and S. R. Leone, "Kinetics of reactions of C<sub>2</sub>H radical with acetylene, O<sub>2</sub>, methylacetylene, and allene in a pulsed Laval nozzle apparatus at T = 103 K," *Chem. Phys. Lett.* **344**, 317-324 (2001).
13. A. B. Vakhtin, D. E. Heard, I. W. M. Smith, and S. R. Leone, "Kinetics of C<sub>2</sub>H radical reactions with ethene, propene and 1-butene measured in a pulsed Laval nozzle apparatus at T = 103 and 296 K," *Chem. Phys. Lett.* **348**, 21-26 (2001).
14. M. S. Tsurikov and N. T. Clemens, "Scalar / velocity imaging of fine scales in gas-phase turbulent jets," in *39th AIAA Aerospace Sciences Meeting and Exhibit*, AIAA-2001-0147 (AIAA, 2001).
15. J. E. Rehm and N. T. Clemens, "A PIV / PLIF investigation of turbulent planar non-premixed flames," in *35th AIAA Aerospace Sciences Meeting and Exhibit*, AIAA-1997-0250 (AIAA, 1997).
16. P.S. Kothnur, M.S. Tsurikov, N.T. Clemens, J.M. Donbar, and C.D. Carter, "Planar imaging of CH, OH and velocity in turbulent non-premixed jet flames," *P. Combust. Inst.* **29**, 1921-1927 (2002).
17. J. Sakakibara, K. Hishida, and M. Maeda, "Vortex structure and heat transfer in the stagnation region of an impinging plane jet (simultaneous measurement of velocity and temperature fields by DPIV and LIF)," *Int. J. Heat Mass Transfer*, **40**, 3163-3176 (1997).
18. H.G. Park, D. Dabiri, and M. Gharib, "Digital particle image velocimetry/thermometry and application to the wake of a heated circular cylinder," *Exp. Fluids* **30**, 327-338 (2001).
19. R. E. Huffman and G.S. Elliott, "An experimental investigation of accurate particle tracking in supersonic, rarefied axisymmetric jets," in *47th AIAA Aerospace Sciences Meeting and Exhibit*, AIAA-2009-1265 (AIAA, 2009).
20. H. Hu and M. Koochesfahani, "Molecular tagging velocimetry and thermometry technique and its application to the wake of a heated cylinder," *Meas. Sci. Technol.* **17**, 1269-1281 (2006).



21. M. Koochesfahani, R. Cohn, and C. MacKinnon, "Simultaneous whole-field measurements of velocity and concentration fields using combined MTV and LIF," *Meas. Sci. Technol.* **11**, 1289-1300 (2000).
22. A. Hsu, R. Srinivasan, R. Bowersox, and S. North, "Two-component molecular tagging velocimetry utilizing NO fluorescence lifetime and NO<sub>2</sub> photodissociation techniques in an underexpanded jet flowfield," *Appl. Opt.* **48**, 4414-4423 (2009).
23. M. Koochesfahani and D. G. Nocera, "Molecular tagging velocimetry," in *Handbook of Experimental Fluid Dynamics*, C. Tropea, A. L. Yarin, and J. F. Foss, Springer-Verlag, 362-381 (2007).
24. A. Hsu, R. Srinivasan, R. Bowersox, and S. North, "Molecular tagging using vibrationally excited nitric oxide in an underexpanded jet flowfield," *AIAA J.* **47**, 2597-2604 (2009).
25. C. Orlemann, C. Schulz, and J. Wolfrum, "NO-flow tagging by photodissociation of NO<sub>2</sub>. A new approach for measuring small-scale flow structures," *Chem. Phys. Lett.* **307**, 15-20 (1999).
26. P. Danehy, S. O'Byrne, F. Houwing, J. Fox, and D. Smith, "Flow-tagging velocimetry for hypersonic flows using fluorescence of nitric oxide," *AIAA J.* **41**, 263-271 (2003).
27. S. Nakaya, M. Kasahara, M. Tsue, and M. Kono, "Velocity measurements of reactive and non-reactive flows by NO-LIF method using NO<sub>2</sub> photodissociation," *Heat Tran. Asian Res.* **34**, 40-52 (2005).
28. N. Jiang, M. Nishihara, and W. Lempert, "Quantitative NO<sub>2</sub> molecular tagging velocimetry at 500 kHz frame rate," *Appl. Phys. Lett.* **97**, 221103 (2010).
29. B. F. Bathel, C. T. Johansen, P. M. Danehy, J. A. Inman, S. B. Jones, and C. P. Goyne, "Hypersonic boundary layer transition measurements Using NO<sub>2</sub> ==> NO photodissociation tagging velocimetry," in *41st AIAA Fluid Dynamics Conference and Exhibit*, AIAA-2011-3246 (AIAA, 2011).
30. G. Herzberg, *Molecular Spectra and Molecular Structure, I. Spectra of Diatomic Molecules* (D. Van Nostrand Company Inc, 1955).
31. R. Cattolica, "OH rotational temperature from two-line laser-excited fluorescence," *Appl. Opt.* **20**, 1156-1166 (1981).
32. R. K. Hanson, "Planar laser-induced fluorescence imaging," *J. Quant. Spectr. Radiat. Transfer* **40**, 343-362 (1988).

33. B. K. McMillin, J. M. Seitzman, and R. K. Hanson, "Comparison of NO and OH planar fluorescence temperature measurements in a scramjet model flow field," *AIAA J.* **32**, 1945-1951 (1994).
34. I. S. McDermid and J. B. Laudenslager, "Radiative lifetimes and electronic quenching rate constants for single-photon-excited rotational levels of NO( $A^2\Sigma^+$ ,  $v' = 0$ )," *J. Quant. Spectr. Radiat. Transfer*, **29**, 483-492 (1982).
35. H. Zacharias, J. B. Halpern, and K. H. Welge, "Two-photon excitation of NO( $A^2\Sigma^+$ ,  $v' = 0, 1, 2$ ) and radiation lifetime and quenching measurements," *Chem. Phys. Lett.* **43**, 41-44 (1976).
36. J. F. Burris, T. J. McGee, and J. Barnes, "Time-resolved fluorescence studies of the NO( $A^2\Sigma^+$ ,  $v' = 1$ ) state of nitric oxide: lifetimes and collisional deactivation rates," *Chem. Phys. Lett.* **121**, 371-376 (1985).
37. J. Luque and D. R. Crosley, *LIFBASE: Database and Spectral Simulation Program for Diatomic Molecules*, Version 2.0.64.
38. B. K. McMillin, "Instantaneous two-line PLIF temperature imaging of nitric oxide in supersonic mixing and combustion flow fields," Ph.D. dissertation (Stanford University, 1993).
39. A. G. Hsu, "Application of Advanced Laser Diagnostics Towards Non-Thermochemical Equilibrium Systems," Ph.D. dissertation (Texas A&M University, 2009).
40. B. F. Bathel, P. M. Danehy, J. A. Inman, S. B. Jones, C. B. Ivey, and C. P. Goyne, "Multiple velocity profile measurements in hypersonic flows using sequentially-imaged fluorescence tagging," in *48th AIAA Aerospace Sciences Meeting and Exhibit*, AIAA-2010-1404 (AIAA, 2010).
41. K. Liu, R. S. Fellers, M. R. Viant, R. P. McLaughlin, M. G. Brown, and R.J. Saykally "A long path length pulsed slit valve appropriate for high temperature operation: Infrared spectroscopy of jet-cooled large water clusters and nucleotide bases," *Rev. Sci. Instrum.* **67**, 410-416 (1996).
42. J. D. Anderson, *Modern Compressible Flow, A Historical Perspective* (Mc Graw Hill, 2003).
43. A. Pope and K. L. Goin, *High-Speed Wind Tunnel Testing*, (Robert E. Krieger Publishing Company, 1965).
44. D.W. Holder and R.J. North, *Schlieren methods*, (H.M. Stationery Off. London, 1963).

45. A. Shapiro, *The Dynamics and Thermodynamics of Compressible Fluid Flow*, (John Wiley and Sons, New York, 1953).
46. The General Aerodynamic Simulation Program - Users's Manual, AeroSoft, Inc., Blacksburg, VA, March (1997).
47. B. Leer, "Towards the ultimate conservative difference schemes V. A second order sequel to Godunov's method," J. Comput. Phys. **135**, 229-248 (1997).
48. P. L. Roe, "Approximate Riemann solvers, parameter vectors, and difference schemes," J. Comput. Phys. **43**, 357-372 (1981).
49. D. C. Wilcox, *Turbulence Modeling for CFD*. DCW Industries, (La Cañada, California, 1994).
50. F. R. Menter, "Two Equation Eddy Viscosity Turbulence Models for Engineering Applications," AIAA J. **32**, 1598-1605 (1994).
51. B. S. Baldwin and H. Lomax, "Thin Layer Approximation and Algebraic Model for Separated Turbulent Flows," in *16th AIAA Aerospace Sciences Meeting and Exhibit*, AIAA-1978-257 (AIAA, 1978).
52. B. McMillin, M. Lee, and R. K. Hanson, "Planar Laser-Induced Fluorescence Imaging of Nitric Oxide in Shock Tube Flows with Vibrational Nonequilibrium," in *21st AIAA Fluid Dynamics, Plasma Dynamics and Laser Conference*, AIAA-1990-1519 (AIAA, 1990).
53. M. P. Lee, B. K. McMillin, and R.K. Hanson, "Temperature measurements in gases by use of planar laser-induced fluorescence imaging of NO," Appl. Opt. **32**, 5379-5396 (1993).
54. B. K. McMillin, J. L. Palmer, and R. K. Hanson, "Temporally resolved, two-line fluorescence imaging of NO temperature in a transverse jet in a supersonic cross flow," Appl. Opt. **32**, 7532-7545, (1993).
55. Ames Research Staff, *Equations, tables, and charts for compressible flow*, NACA Report No. 1135 (1975).
56. A. G. Hsu, R. Srinivasan, R. D. W. Bowersox, and S. W. North, "Two-component molecular tagging velocimetry utilizing NO fluorescence lifetime and NO<sub>2</sub> photodissociation techniques in an underexpanded jet flow field," Appl. Opt. **48**, 4414-4423 (2009).

57. P. Danehy, S. O'Byrne, F. Houwing, J. Fox, and D. Smith, "Flow-Tagging Velocimetry for Hypersonic Flows Using Fluorescence of Nitric Oxide," *AIAA J.* **41**, 263-271 (2003).
58. L. A. Ribarov, J. A. Wehrmeyer, S. Hu, and R. W. Pitz, "Multiline hydroxyl tagging velocimetry measurements in reacting and nonreacting experimental flows," *Exp. Fluids* **37**, 65-74 (2004).
59. M. D. Lahr, R. W. Pitz, Z. W. Douglas, and C. D. Carter, "Hydroxyl-Tagging-Velocimetry Measurements of a Supersonic Flow over a Cavity," *J. Propul. Power* **26**, 790-797 (2010).
60. A. G. Hsu, R. Srinivasan, R. D. W. Bowersox, and S. W. North, "Molecular Tagging Using Vibrationally Excited Nitric Oxide in an Underexpanded Jet Flow field," *AIAA J.* **47**, 2597-2604 (2009).
61. R. Sanchez-Gonzalez, R. Srinivasan, R. D. W. Bowersox, and S.W. North, "Simultaneous Velocity and Temperature Measurements in Gaseous Flow Fields using the VENOM Technique," *Opt. Lett.* **36**, 196-198 (2011).
62. T. S. Shankara and A. K. Sreekanth, "Shock stand-off distance for a sphere," *J. Appl. Phys.* **48**, 1765 (1997).
63. M. D. Van Dyke and H. D. Gordon, *Supersonic flow past a family of blunt axisymmetric bodies*, NASA Tech. Rept. R-1, (1959).
64. T. B. Settersten, B. D. Patterson and W. H. Humphries, "Radiative lifetimes of NO  $A^2\Sigma^+(v' = 0,1,2)$  and the electronic transition moment of the  $A^2\Sigma^+ - X^2\Pi$  system," *J. Chem. Phys.* **131**, 104309, (2009).
65. M. Hunter, S. A. Reid, D. C. Robie, and H. Reisler, "The monoenergetic unimolecular reaction of expansion-cooled NO<sub>2</sub>: NO product state distributions at excess energies 0-3000 cm<sup>-1</sup>," *J. Chem. Phys.* **99**, 1093 – 1108 (1993).
66. L. A. Ribarov, J. A. Wehrmeyer, S. Hu, and R. W. Pitz, "Tagging velocimetry measurements in reacting and nonreacting experimental flows," *Exp. Fluids*, **37**, 65-74 (2004).
67. M. D. Lahr, R. W. Pitz, Z. W. Douglas, C. D. Carter, "Hydroxyl-tagging velocimetry measurements of a supersonic flow over a cavity," *J. Propul. Power*, **26**, 790-797 (2010) .

68. P. Danehy, A. F. P. Houwing, J. S. Fox, and D. R. Smith, "Flow-tagging velocimetry for hypersonic flows using fluorescence of nitric oxide," *AIAA J.* **41**, 263-271 (2003) .
69. D. C Robie, M. Hunter, J. L. Bates, H. Reisler, "Product state distributions in the photodissociation of expansion-cooled NO<sub>2</sub> near the NO( $X^2\Pi$ )  $v = 1$  threshold," *Chem. Phys. Lett.* **193**, 413-422 (1992).
70. S. I. Ionov, G. A. Brucker, C. Jaques, Y. Chen, and C. Wittig, "Probing the NO<sub>2</sub> + NO + O transition-state via time-resolved unimolecular decomposition," *J. Chem. Phys.* **99**, 3420-3435 (1993).
71. C. Wittig, I. Nadler, H. Reisler, M. Noble, J. Catanzarite, and G. Radhakrishnan, "Nascent product excitations in unimolecular reactions: the separate statistical ensembles method," *J. Chem. Phys.* **83**, 5581-5588 (1985).
72. H. P. Broda and T. Carrington, "Rotational, vibrational, and electronic energy transfer in the fluorescence of nitric oxide," *J. Chem. Phys.* **38**, 136-147 (1963) .
73. S. Lee, J. Luque, J. Reppel, A. Brown, and D. R. Crosley, "Rotational energy transfer in NO ( $A^2\Sigma^+$ ,  $v = 0$ ) by N<sub>2</sub> and O<sub>2</sub> at room temperature," *J. Chem. Phys.*, **121**, 1337-1382 (2004) .
74. T. Ebata, Y. Anezaki, M. Fujii, N. Mikami, and M. Ito, "Rotational energy transfer in NO ( $A^2\Sigma^+$ ,  $v = 0$  and 1) studied by two-color double-resonance spectroscopy," *Chem. Phys.* **84**, 151-157 (1984).
75. M. H. Kabir, I. O. Antonov, and M. C. Heaven, "Probing rotational relaxation in HBr( $v=1$ ) using double resonance spectroscopy," *J. Chem. Phys.* **130**, 074305 (2009).
76. M. Islam, I. W. M. Smith, and M. H. Alexander, "Rate constants for total relaxation from the rotational levels  $J = 7.5, 20.5, 31.5$  and  $40.5$  in NO( $X^2\Pi_{1/2}$ ,  $v = 2$ ) in collisions with He, Ar and N<sub>2</sub>: a comparison between experiment and theory," *Chem. Phys. Lett.* **305**, 311-318 (1999).
77. M. A., Woodmanesee, V. Iyer, J. C. Dutton, and R. P. Lucht, "Nonintrusive pressure and temperature measurements in an underexpanded sonic jet flow field," *AIAA J.* **42**, 1170-1180 (2004).
78. B. K. McMillin, J. L. Palmer, and R. K. Hanson, "Temporally resolved, two-line fluorescence imaging of NO temperature in a transverse jet in a supersonic cross flow," *Appl. Opt.* **32**, 7532-7545 (1993).

79. A. Y. Chang, M. D. DiRosa, and R. K. Hanson, "Temperature dependence of collision broadening and shift in the NO A  $\leftarrow$  X (0,0) band in the presence of argon and nitrogen," *J. Quant. Spectrosc. Radiat. Transfer* **47**, 375 - 390 (1992).
80. M. D. DiRosa and R. K. Hanson, "Collision broadening and shift of NO  $\gamma$ (0,0) absorption lines by O<sub>2</sub> and H<sub>2</sub>O at high temperatures," *J. Quant. Spectrosc. Radiat. Transfer* **52**, 515-529 (1994).
81. W. Z. Strang, R. F. Tomaro, and M. J. Grismer, "The defining methods of Cobalt60: a parallel, implicit, unstructured Euler/Navier-Stokes flow solver," in *37th AIAA Aerospace Sciences Meeting and Exhibit*, AIAA-1999-786 (AIAA, 1999).
82. S. K. Godunov, "A finite-distance method for the numerical computation of discontinuous solutions of the equations of fluid dynamics," *Mat. Sb.* **47**, 357-393 (1959).
83. F. R. Menter, "Zonal two-equation  $k$ - $\omega$  turbulence models for aerodynamic flows," in *23rd AIAA Fluid Dynamics, Plasmadynamics, and Lasers Conference*, AIAA-1993-2906 (AIAA, 1993).
84. B. W. van Oudheusden, F. Scarano, E. W. M. Roosenboom, E. W. F. Casimiri, and L. J. Souverein, "Evaluation of integral forces and pressure fields from planar velocimetry data for incompressible and compressible flows," *Exp. Fluids* **43**, 153-162 (2007).

## VITA

Rodrigo Sanchez-Gonzalez received his Bachelor of Science degree in Chemistry from Universidad Autonoma de Queretaro in Mexico in 2007. He entered the Chemistry graduate program at Texas A&M University in August 2007 and received his Doctor of Philosophy degree in May 2012. His research interests include Combustion and Laser Diagnostics.

Dr. Sanchez-Gonzalez may be reached at the Texas A&M University Chemistry Department, P.O. Box 30012, College Station, TX 77842. His email is [rodrigoundsag@gmail.com](mailto:rodrigoundsag@gmail.com).